Kinematic and dynamic characterization of the subduction seismic cycle in Northern and South-Central Chile: Modelling the Iquique 2014 Mw 8.1 and Maule 2010 Mw 8.8 GPS data and interpreting models alongside existing seismic catalogues.

Dissertation
Zur Erlangung des Grades eines
Doktors der Naturwissenchaften
Am Fachbereich Geowissenschaften
der Freien Universität Berlin.

Jonathan Bedford

February 2016

Kinematic and dynamic characterization of the subduction seismic cycle in Northern and South-Central Chile: Modelling the Iquique 2014 Mw 8.1 and Maule 2010 Mw 8.8 GPS data and interpreting models alongside existing seismic catalogues.

A Dissertation submitted in partial fulfilment of the requirements for the degree:

Doctor of Natural Sciences in the field of Earth Sciences

to the department of Geowissenschaften of the Freie Universität Berlin.

Author:

Jonathan Bedford.

Place and date of submission:

Berlin, August 13th 2015

Supervisor:

Professor Onno Oncken

Second Examiner:

Professor Serge Shapiro

Date of the Viva Voce / Defense:

Friday 4th December 2015

Acknowledgements

It has been just over four years since I embarked on my doctoral research at GFZ. From day one in Sektion 3.1, my colleagues have been most welcoming and helpful, and for that I am sincerely grateful. Special mentions must go out to Franziska Alberg for always making the time to help with all sorts of issues, Herr Herr for always swiftly sorting out my computer problems, and to Matthias Rosenau who helped me get settled in when I was a new arrival in Berlin. Thanks also to Christian Sippl for his invaluable help with the Unix operating system.

I would like to thank Onno Oncken and the rest of the recruiting board for taking a chance on me by offering me this opportunity to research at GFZ. Furthermore, I would like to acknowledge the DFG funding agency for the MARISCOS project MO/2310/1-1.

I have been fortunate to have received frequent and high quality feedback on my work, and I am especially grateful to Marcos Moreno, Onno Oncken, Dietrich Lange, Frederik Tilmann, Oliver Heidbach, Mike Bevis, Andrés Tassara, Gavin Hayes, Andreas Rietbrock and all colleagues of Sektion 3.1 for their fruitful academic discussions that have sharpened the scientific questions and arguments. Without the processed data I would have no project, so I am very thankful to Professor Juan Carlos Baez and Mitja Bartsch for providing me with their processed solutions. I would like to thank Shaoyang Li for always being available to talk about model concepts, meshing, and FEM solver issues.

I would like to thank my fellow PhD students, who have helped me both academically and socially.

Last but not least, the biggest thank you goes to Marcos Moreno for his daily guidance, trust, patience, and kindness. It has truly been a pleasure to work for you.

Dedication

For Anna and Charlotte, Oma Grete, Opa Willi, Oma Gabi, Opa Josef, Grandad, and Grandad Paul.

Abstract

The surface displacement measurements afforded in the new era of satellite geodesy have proven to be a valuable complimentary data set in addition to the seismic monitoring of active subduction margins. Being able to accurately measure the respective plate motions with high spatial and temporal frequency has inspired many modelling initiatives investigating both heterogeneous plate-interface kinematics and subduction zone seismic cycle dynamics. The isolation of plate interface kinematics from the surface signal and the robust modelling of the kinematic source provide the case-studies against which mechanical models of earthquake recurrence can be benchmarked, and is therefore of utmost importance for intermediate-long term hazard assessment of a subduction margin.

In this PhD thesis I present the investigations into the subduction zone seismic cycle plate-interface kinematics and viscoelastic dynamics of the subduction zone in response to the megathrust earthquake. I compare kinematic models to seismicity in order to gauge the heterogeneity in seismic efficiency across the plate interface in both the interseismic and postseismic phases of the earthquake cycle. I attempt to separate the various signals coming from simultaneous postseismic processes and explore and present a discussion of the non-uniqueness of the solution parameter space for the separated signals.

For these investigations I use the GPS data and published seismic catalogues from the Chile Maule 2010 Mw 8.8 and Pisagua-Iquique 2014 Mw 8.1 megathrust events.

From the Maule investigations, I find that afterslip is a dominant early postseismic process (decaying over 3-4 years) that is well captured due to the excellent coverage of near-field continuous GPS (cGPS). Afterslip spatiotemporal features are well resolved in certain regions and the comparison of afterslip to coseismic slip can reveal regions of the plate interface that are more likely to fail with large magnitude aftershocks. Postseismic processes can be separated if we make some assumptions about afterslip behaviour: To separate the simultaneous postseismic signals I develop the Postseismic Straightening method. The separation considers three postseismic processes: plate interface re-locking, afterslip, and viscoelastic relaxation. Plate re-locking is a traditionally neglected postseismic process that when modelled in combination with viscoelastic relaxation and afterslip significantly improves the model prediction fits to the time series. The effect of re-locking, when added to afterslip and viscoelastic relaxation, is to cause the horizontal displacements to veer with time. The afterslip separated using the Postseismic Straightening method has a normalized decay time function that is in good agreement with the normalized decay time function of the aftershocks over the first 3-4 years, suggesting that the spatiotemporal relation between afterslip and aftershocks persists long into the postseismic time period. The afterslip, however, is predominantly aseismic and puls-

ing in nature; leading to the interpretation of afterslip pulses on a postseismically weakened plate-interface being triggered by the larger magnitude aftershocks, and with the stress release of afterslip feeding back into the shear stress forcing of the aftershock sequence.

For the Pisagua-Iquique earthquake, I investigate the seismic efficiency of the preceding foreshock swarm and the source parameters of the largest foreshock that initiated this swarm. The cGPS motions leading up to the Mw 8.1 mainshock are mainly explained by seismic slip, although significant aseismic postseismic responses can be resolved for the larger earthquakes in the swarm. Similar to the interpretation of the Maule afterslip and aftershocks, I interpret the transient aseismic signals as being afterslip of the foreshocks.

While promising spatial relations exist between inter-, co-, and postseismic elastic dislocation kinematics, the degrees of freedom for the slip azimuth (rake) need to be further investigated, especially for the interseismic locking models which can be very sensitive to a constrained backslip azimuth.

(German version of the abstract can be found in the Appendix).

Contents

List of Figures

List of Tables

Foreword

Throughout my time undertaken as a PhD candidate I have been able to publish my work, both as a first author (3 papers; 2 published and 1 in final stages of internal review) and as a co-author (3 published, with 1 in submission). This PhD thesis is therefore an embellished concatenation of my contributions to this published work. Three chapters are re-formatted versions of my first-author papers. One chapter consists of results taken from a coauthored paper, accompanied by unsubmitted work that I felt was better included to fairly shape the final discussion. The first chapter covers the relevant background science and information about the study region and the two studied earthquakes. Further details on each earthquake are found in the respective chapters dealing with the earthquake data. The thesis is completed by a chapter that synthesises the findings of my PhD and presents the outstanding issues that I feel should be the objectives of future research proposals.

Chapter 1

Introduction, Methods, and Aims

Note

This chapter will first deal with the essential concepts of the subduction zone seismic cycle that are especially relevant to this body of work (section 1.1). I will introduce some of the ways in which geodetic data is utilized in the subduction zone modelling community, as well as how the insights from complimentary data sets and methods can help to constrain subduction zone mechanisms. In section 1.2 I will introduce the methods used in my research, with further details given in subsequent chapters. In section 1.3 I will give an overview of the 2010 Mw 8.8 and 2014 Mw 8.1 earthquakes that form the basis of my investigations, and finally in section 1.4 I will introduce the aims and objectives that have been tackled during my doctoral research.

1.1 Essential Concepts

1.1.1 The subduction zone seismic cycle

The simplest model describing the build up and release of stress in the subduction zone is the elastic-rebound theory (e.g. *Reid*, 1911) in which the mechanically coupled plate-interface between the subducting and overriding plate (the megathrust) accumulates stress due to the forces that drag, push, and pull the plates together (*Turcotte and Schubert*, 2014) until a threshold is reached and the stress is released in a sudden failure of the coupling. The plate interface is then re-coupled (re-locked) and the accumulation of stress begins again, completing the seismic-cycle. With such a basic model, the earthquake recurrence intervals can be crudely estimated by the magnitude of the previous large earthquake in the subduction zone segment and the rate of slip-deficit accumulated as the plates are locked together (e.g. *Bilham and Ambraseys*, 2005). The earthquake recurrence intervals at a particular segment of a subduction margin can also be estimated by looking into the written, archaeological, or geological record of megathrust events (e.g. *Clague and Bobrowsky*, 1994; *Mouslopoulou et al.*, 2011; *Melnick et al.*, 2009; *Satake et al.*, 1996; *Bilham et al.*, 2005), although such records are often incomplete or inadequate at accurately localizing the rupture extents. Furthermore, there exists the less frequent occurrence of *great* megathrust earthquakes (approximately Mw $\geqslant$ 8.8) which can run-away and rupture over multiple adjacent segments (*Rosenau and Oncken*, 2012). The most recent example of such a *great* event was the Tohoku Oki Mw 9.0 (*Tajima et al.*,

2013; *Simons et al.*, 2011) that swept over a region of segments that over the past 400 years have not hosted an earthquake greater than a Mw 8.5.

Key to better estimating the recurrence rate of such large earthquakes is a full understanding of the velocity- and state-dependent frictional behaviour of the plate interface (see *Scholz*, 1998): The testing of parameters in such friction models requires a reliable record of the relative plate motions as a function of time. Such records may comprise of:

- **kinematic models** which localize and quantify interseismic (before the earthquake) locking-patterns and slow-slip with slip distributions during (coseismic) and after the earthquake (postseismic).

- **seismic products** such as b-value which give a measure of the relative proportions of small to big earthquakes for a particular portion of the interface. Regions of the interface that are more prone to harbouring larger magnitude earthquakes (lower b-value) are more likely to adhere to a rate-weakening frictional behaviour, whereas the regions of the interface with a higher b-value indicate areas that are more prone to sliding with a rate-strengthening frictional behaviour.

Furthermore, modelling of the long-term plate-interface physical properties can be compared against the kinematic behaviour and tested for spatial correlations that would imply a certain frictional behaviour for some apparent physical properties. Such modelling of long-term features includes:

- **Interface anomaly identification** which can be achieved with various methods such as gravity (e.g. *Song and Simons*, 2003), magnetic surveys (e.g. *Yáñez et al.*, 2001), and seismic tomography of both active source seismic surveys and aftershock data (e.g. *Haberland et al.*, 2009; *Husen et al.*, 2000; *Hicks et al.*, 2012; *Groß et al.*, 2008; *Oncken et al.*, 2003).

- **Application of the critical taper theory** (e.g. *Dahlen*, 1990), which has been investigated in the analogue laboratory (e.g. *Lohrmann et al.*, 2003; *Santimano et al.*, 2015) and also with surface profiles from various subduction margins (e.g. *Cubas et al.*, 2013b,a). Such analysis can relate the topographic profile to the long term friction of the décollement (megathrust plate interface) and the activity of faults in the accretionary prism.

- **Geological Sampling** of ophiolites found in the field (e.g. *Angiboust et al.*, 2011, 2012) can characterize the long term deformation conditions in the vicinity of the plate interface. Currently, boreholes are being drilled in the Nankai Trough Seismogenic Zone Experiment (www.iodp.org/nantroseize) with the aim of returning rock samples from subduction plate interface. Laboratory measurements on the sliding features of fault rocks provide the basis for rate-dependent friction models (e.g. *Dieterich*, 1978).

In the next subsection I will present in more detail the concepts involved in ***kinematics and dynamics*** of the subduction zone seismic cycle, since that is the focus of my PhD research.

1.1.2 Subduction plate interface locking and slip, and the contamination from Viscoelastic Relaxation

The episodic slip and locking (coupling) on the subduction plate interface is generally constrained within a typical depth range of 0-70 km that is to a first-order controlled by the pressure temperature conditions and the depth-dependence of interface rock types (e.g. *Oleskevich et al.*, 1999). Below this zone, the plate interface slides stably due to thermal conditions and therefore slip-deficit is generally not accumulated. The seismogenic zone is found between the limits of slipping and locking zone, and this zone is generally narrower than the width of the slipping and locking zone, because the accretionary prism of sediments closer to the trench tends to facilitate a more weakly coupled interface (e.g. *Byrne et al.*, 1988). Such seismogenic zones are a product of the often azimuthally biased seismic networks: Offshore deployments of seismometers that can better map seismicity nearer to the trench are prohibitively expensive and are not usually deployed over long observation windows. Naturally there are a scarcity of deep and shallow (e.g. $>$ 70 km, $<$ 10 km) plate interface earthquakes that extend beyond the established seismogenic limits of a particular segment. Slip events (aseismic or seismic) along the slipping/locked zone have been characterized as tending to occur in certain failure domains (from the shallowest, A to the deepest, D) as suggested by the dependence of the frequency-time characteristics of the measured seismic waveforms as a function of depth (*Lay et al.*, 2012). While locking maps are useful the for estimating slip deficit and therefore the expected magnitudes and locations of imminent great earthquakes (e.g. *Moreno et al.*, 2010), the relationship between locking and failure across all domains, especially the assumed to be creeping shallowest (A domain), is not so clear-cut. Furthermore, the ability to map the locking within acceptable resolution diminishes as a function of distance to the nearest geodetic measurements, meaning that the locking at the trench (under the water and far from the land) is often very badly constrained by geodetic models. In many subduction zones, the occurrence of slow-slip events (predominantly aseismic slip that can be accompanied by seismic tremor) has been recognized by the deviation of the otherwise constant background interseismic locking velocities (e.g. *Rogers and Dragert*, 2003; *Wallace and Beavan*, 2010). This form of aseismic slip tends to occur in the deepest portion of the locking and slipping portion of the plate interface (D domain).

Locking of the subduction plate interface is represented by the measure of locking degree, a number between 0 and 1 that describes the state between fully uncoupled (0) and fully coupled (1) and this number is one minus the ratio of local sliding velocity to the incoming plate velocity. For example, if the incoming plate velocity of the subducting plate is 40 mm/yr, a portion of the plate interface with a locking degree of 0.75 will be locally sliding at a relative velocity of 10 mm/yr. The incoming plate velocity is defined as the velocity of the incoming plate with respect to the overriding plate and is measured at an arbitrary distance from the trench depending on the availability of any exposed landmasses on which to make the measurements.

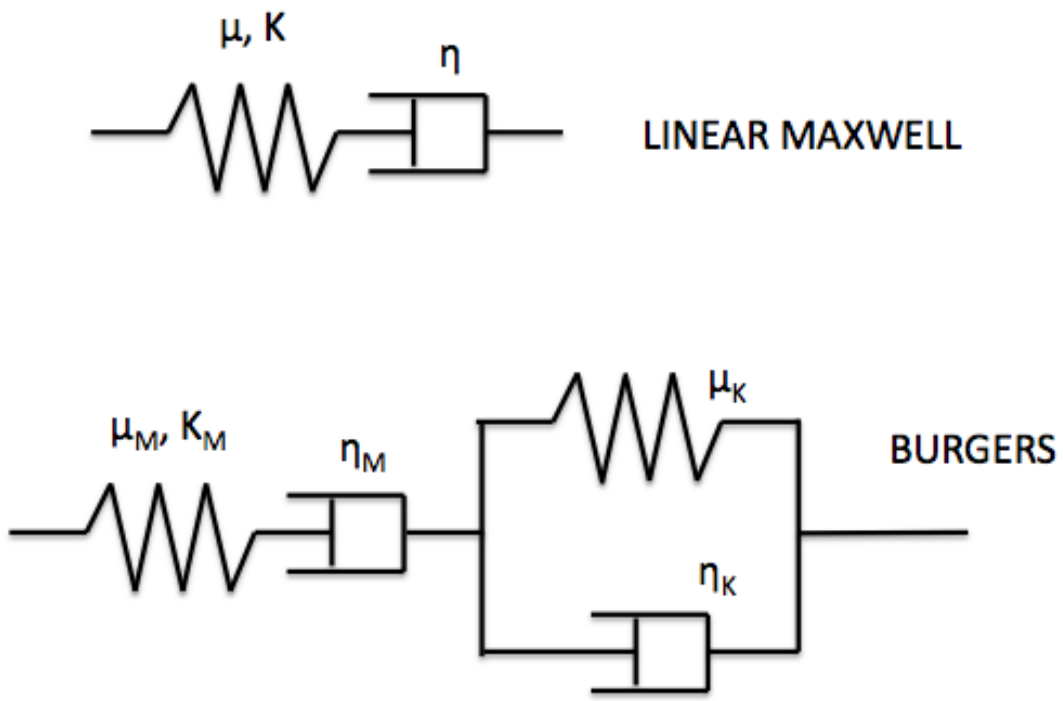

Figure 1.1: Figure shows the spring and dashpot schematic representations of two commonly used rheologies in subduction zone studies: Linear Maxwell, and Burgers viscoelasticity. The elastic parameters are given here by μ and K, representing shear modulus and stiffness respectively. The viscosity is represented by η. For a constant stress rate, the Linear maxwell model will produce a constant strain rate, and the Burgers model will produce an intially higher strain rate that decays in time to a constant strain rate (i.e. decays to Linear Maxwell behaviour). In my modelling of postseismic viscoelastic relaxation, I implemented the Linear Maxwell rheology.

Slip occurs on the plate interface rapidly in earthquakes, or more slowly as aseismic slip. Aseismic slip can occur as *afterslip* following an earthquake, or during the interseismic (locking phase) of the seismic cycle as *slow-slip*.

Viscoelastic relaxation of the subduction zone following large earthquakes was originally suspected due to long-term viscoelastic decay signals measured in the near and far-field (e.g. *Kanamori*, 1973; *Nur and Mavko*, 1974). The viscoelastic relaxation, if not removed from the data, can contaminate the plate interface afterslip model. Such contamination manifests itself as an unrealistically deep slip signal, and the motion on the plate interface is not able to produce fits to the far-field cumulative displacements. Viscoelastic behaviour is apparent in other geological settings such as Glacial Isostatic adjustment (GIA) (e.g. *James et al.*, 2000; *Larsen et al.*, 2005), whereby the viscosity has been estimated to be between $10^{18} - 10^{21}$ Pa.S. The influence of the viscoelastic relaxation in the subduction zone setting is hotly debated in the subduction zone research community: From being the dominant process recorded in both near- and far- field geodetic GPS measurements, to being a secondary process to the slipping signal coming from the plate interface. Viscoelastic relaxation models can consist of various rheologies, the most popular being the Burgers and Maxwell Linear viscoelastic rheologies. Figure 1.1 shows a schematic spring and dashpot representation of the Linear Maxwell and Burgers

rheologies. The arrangement in series or parallel of viscous (dashpots) and elastic (springs) elements determines the form of the differential equation that describes stress relaxation over time. The Burgers model exhibits an initially higher rate of strain for a constant applied stress which decays into a constant strain rate. The linear Maxwell viscoelastic model has a constant strain rate in response to a constant applied stress. For the purposes of addressing the aims of my research (see section 1.4), I chose the linear Maxwell model of viscoelasticity as an appropriate approximation for the behaviour of the viscoelastic bodies in my models. This rheology choice was based on a desire to reduce the number of parameters in a parameter search, and therefore simplify the consequent interpretation. For the viscoelastic relaxation models presented in this thesis we can consider the stress relaxation of the postseismic period as the relaxation of the stress imparted onto the viscoelastic body during the megathrust event. In terms of dashpots of strings, the stress imparted on the viscoelastic body by the coseismic slip can be represented by a sudden extension of a relaxed spring that is in series with a dashpot. During the postseismic the stress in the extended spring (with the extended end of the spring held at the point it was suddenly extended to) is relaxed over time by the viscous flow in the dashpot.

1.1.3 GPS measurements and feautures

The technology of satellite navigation systems such as Global Positioning System (GPS) and GLObal NAvigation Satellite System (GLONASS) have enabled the global monitoring of precise plate tectonic motions for over two decades (e.g. *Gordon and Stein*, 1992) revolutionising the science of earthquake cycle kinematics. Measurements can either be taken continuously (continuous GPS / cGPS) or by means of repeat measurements of survey (sGPS) points. Modern day technological advancements in antenna and receiver technology and the refinement of processing methods means that surface displacements can be measured within a precision of 1-2 mm, with daily repeatability of continuous measurements between 1-2 mm. In many subduction zones vast networks of cGPS and sGPS have been established that enable the capturing of the tectonic signal before, during, and after some of the largest earthquakes of the last century (e.g. *Sato et al.*, 2011; *Vigny et al.*, 2005). GPS displacements are used to locate the heterogeneity of motion between plates, and therefore the recorded surface displacements must be transformed into the correct reference frame whereby motion on the surface of the continental plate corrected for the long term pole of rotation of the plate on which they are measured (e.g. *Altamimi et al.*, 2011). Subduction zone plate motions can be explained simply with a trajectory model (from *Bevis and Brown*, 2014, modified to show the linear

background velocity variant):

$$\begin{aligned} x(t) &= a(t - t_R) \\ &+ \sum_{j=1}^{N_j} b_j H(t - t_j) \\ &+ \sum_{k=1}^{n_f} s_k \sin(\omega_k t) + c_k \cos(\omega_k t) \\ &+ \sum_{i=1}^{n_T} d_i \log(1 + \delta t_i / Ti) \end{aligned} \tag{1.1}$$

The component (east, north, or up) of the time series, $x(t)$ which starts at t_R, is described by a linear term, a; some Heaviside step functions where b_j is the coefficient of the Heavisides function, H, at time t_j; some coefficients of a Fourier series, s_k and c_k with k being the number of frequencies used (n_f, typically two); and a logarithmic decay function where d_i is the coefficient of the logarithmic decay described by a T_i decay constant and δt_i being 0 at the beginning of the postseismic decay. The Heavisides step functions describe sudden displacements from earthquakes or changes of antenna. The Fourier series describes the secular oscillations due to climactic effects on the ground or the atmosphere. The linear term describes the coupling of the incoming plate under the continent and the constant velocity of subduction.

In the studies presented in this thesis, we will deal with time series data from cGPS stations during the interseismic (the linear term from the 1.1 equation) the coseismic displacements (the Heavisides steps) and the postseismic motion (the decay term). We will model the processes causing these trajectories, challenging the assumptions of this trajectory model, as well as inferring processes for the transient deviations from the expected trajectories.

1.2 Methods: Using geodetic data to model subduction zone seismic cycle processes

1.2.1 Heterogeneous relative plate motion: Dislocation modelling

Okada (1985, 1992) provides the commonly used analytical Green's functions to model the recorded surface motions to the dislocation (fault motion) in an elastic half-space. For recorded slip events (earthquake slip, afterslip, or slow-slip) the slip distributions on a known fault geometry can be modelled by setting up a linear system of equations that relate the Okada Green's functions to the displacements. The matrix manipulation of this linear system of equations can solve for the slip values on each sub-patch in the fault geometry, and this process is known as a *slip-inversion*. Green's functions can also be calculated by forward modelling the surface deformations at the GPS station locations for unit slips on fault patches using the finite elements method (e.g. *Moreno et al.*, 2009; *Li et al.*, 2015).

Dislocation modelling is also used to model plate-interface locking, and this is achieved using the backslip assumption (*Savage*, 1983). In the backslip assumption, we can model locking on the plate interface as a dislocation in the opposite sense to the direction of the slip which would release such locking. *Kanda and Simons* (2010) showed the elastic plate subduction model as an alternative to backslip for modelling locking. It was demonstrated that the backslip model produces identical surface predictions to the elastic plate subduction model if the elastic plate thickness is zero. If the stresses in the subducting elastic plate due to plate flexure at the trench are not increasing over many seismic cycles then the backslip assumption is robust, regardless of elastic thickness of the subducting plate.

The resolution of the locking or slip model is subject to the number of measurements and their proximity to the plate-interface. Resolution can be visualized by means of a checkerboard test or analysis of the resolution matrix that is a product of the Green's function matrix (see *Page et al.*, 2009, for a good discussion on slip inversion resolution). Best practice is to either provide model resolution and sensitivity tests (checkerboard tests, bootstrap tests, etc.) or to adjust the patch size of the fault model so that each patch is nearly identically resolved (e.g. *Barnhart and Lohman*, 2010; *Atzori and Antonioli*, 2011). A common drawback of subduction zone locking and slip models is that the lack of measurements close to the trench means that the kinematic distribution near to the trench obtained by the inversion cannot be trusted as strongly as the distribution nearer to the coastline.

1.2.2 Application of the Finite Elements Method

In chapter 3 of this thesis I will apply the numerical method known as the Finite Elements Method (FEM) to model the postseismic viscoelastic flow below the assumed elastic thickness of the continental lithosphere as well as below the subducting slab. A rigorous explanation of the mathematical principles used in the FEM and the various approaches encompassed by this umbrella term *FEM* can be found in texts such as *Zienkiewicz and Taylor* (1994); here I will introduce the basic concepts of the FEM relevant to the understanding of the modelling in this thesis.

The application of the FEM to the subsequent rheological flow following a stress perturbation solves the equilibrium of forces equation (Poisson's equation) at time steps. The initial stress of the model, that will drive subsequent viscoelastic relaxation, is given by the relationship between the stress and strain (shown only the relationship between deviatoric tensors):

$$\sigma_{ij} = 2\mu\epsilon_{ij} \tag{1.2}$$

where i and j are the deviatoric combinations of rows and columns for the stress and strain tensors σ and ϵ, and μ is one of Lamé's parameters. For the dashpot representation of viscosity the Newtonian flow law (assuming here an incompressible fluid) relates deviatoric stress to deviatoric strain:

$$\sigma_{ij} = 2\eta\dot{\epsilon}_{ij} \tag{1.3}$$

where η is the viscosity. As the viscous flow proceeds in time, the stress is decreased, and so a system partial of differential equations explains the flow with time in all

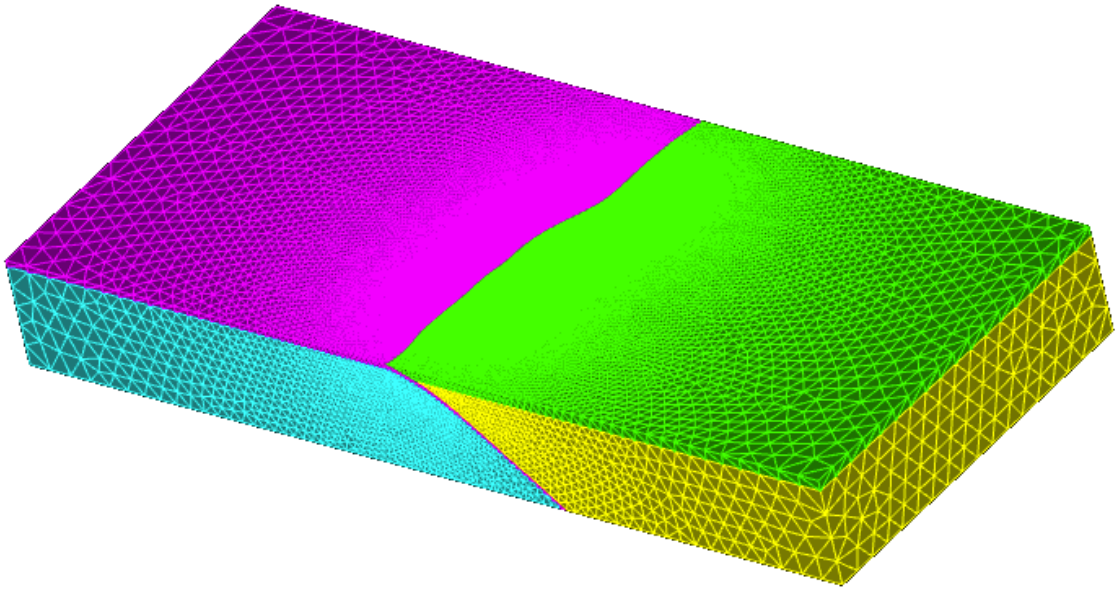

Figure 1.2: The mesh used in the finite element modelling of postseismic relaxation (chapter 3). Purple and green are the oceanic slab and continental crusts respectively. Blue and yellow are the oceanic and continental mantles respectively. Finer elements are used closer to the plate interface, since this region has the highest expected gradients of postseismic deformation. Model dimensions (drawn on figure 3.5) are 1800 km along strike, 500 km deep and 4000 km in the strike perpendicular direction. There are over 1.2×10^6 elements in this mesh.

directions. The solution to these partial differential equations is the undertaken with the FEM, and the solutions require the definition of boundary conditions. For each time step, the solution fields (e.g. displacement, stress change) are calculated at nodes in a mesh representing the model geometry. The arrangement of nodes determines the shape of the elements, and in my investigations I used tetrahedral elements. The elements must be more plentiful (i.e. smaller) in the regions where the largest solution field gradients are expected: this is to minimize the numerical artifacts related to interpolation (see fig. 1.2).

1.3 Introducing the Earthquakes of this study

1.3.1 Maule Mw 8.8, 2010

The Maule Mw 8.8 struck on the 27th February, 2010 with the hypocentre occuring offshore and north of of the coastal city of Concepción. Figure 1.3 shows the extents of the rupture zone, with most models being in agreement that the coseismic rupture extended with an along strike length of roughly 500 km (e.g. *Lorito et al.*, 2011; *Moreno et al.*, 2010; *Vigny et al.*, 2011; *Hayes et al.*, 2013; *Pollitz et al.*, 2011). This earthquake is the third largest earthquake ever recorded by satellite geodesy, behind the Sumatra 2004 Mw 9.2 and the Tohoku-Oki Mw 9.0 of 2011. The tsunami generated by the earthquake was responsible for 124 of the earthquake's 521 fatalities (*Fritz et al.*, 2011). This earthquake is considered to have released the majority, if not all, of the slip deficit since the last supposed rupture of this whole segment: The

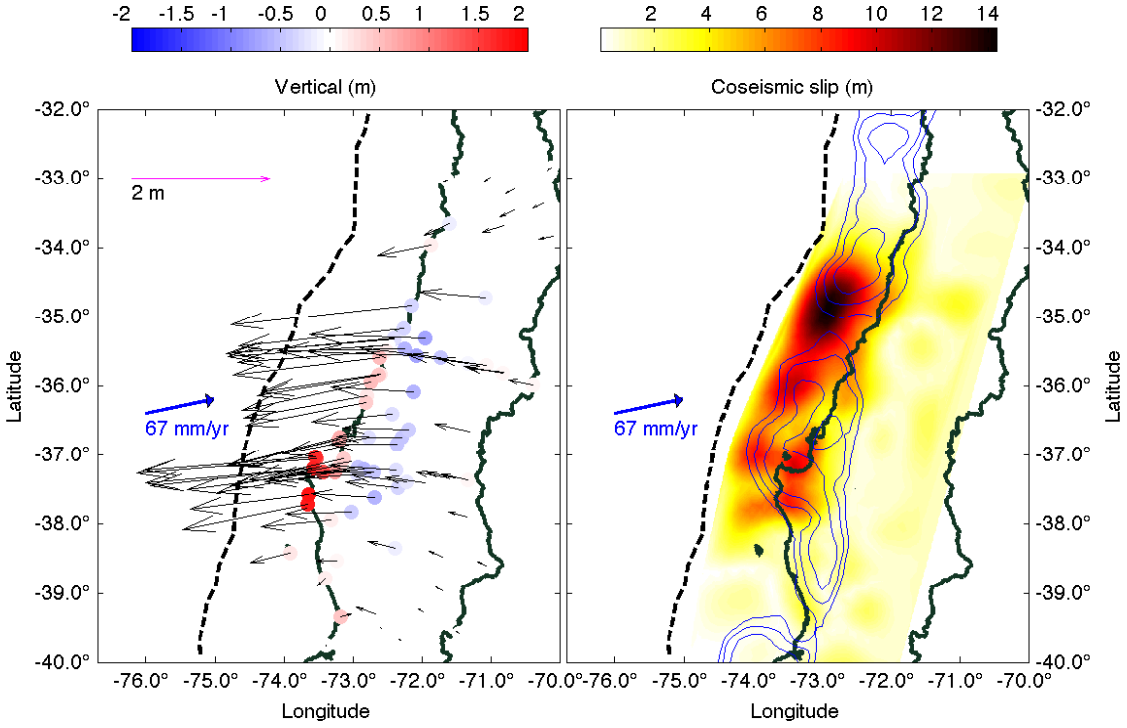

Figure 1.3: Both panels show a blue convergence vector and associated velocity representing the motion of the incoming Nazca oceanic plate with respect to the South American continental plate. The subduction trench is shown by the dotted black line, and both the Chilean coastline and border to Argentina are shown in dark green. The left hand panel shows the coseismic displacements (horizontal as vectors and vertical colour coded between blue and red). The hingeline is onshore up to approximately 35°S. There is uplift at the coastline with subsidence towards the volcanic-arc and a hint of uplift in the volcanic arc. Right hand side shows the coseismic slip distribution of *Bedford et al.* (2013) which was modelled using the data of the left hand plot (*Moreno et al.*, 2010; *Vigny et al.*, 2011). The interseismic locking degree (*Moreno et al.*, 2011) is shown with blue contours at 0.7, 0.8, and 0.9 locking degree. A locking degree of 1 would indicate a fully coupled interseismic plate interface.

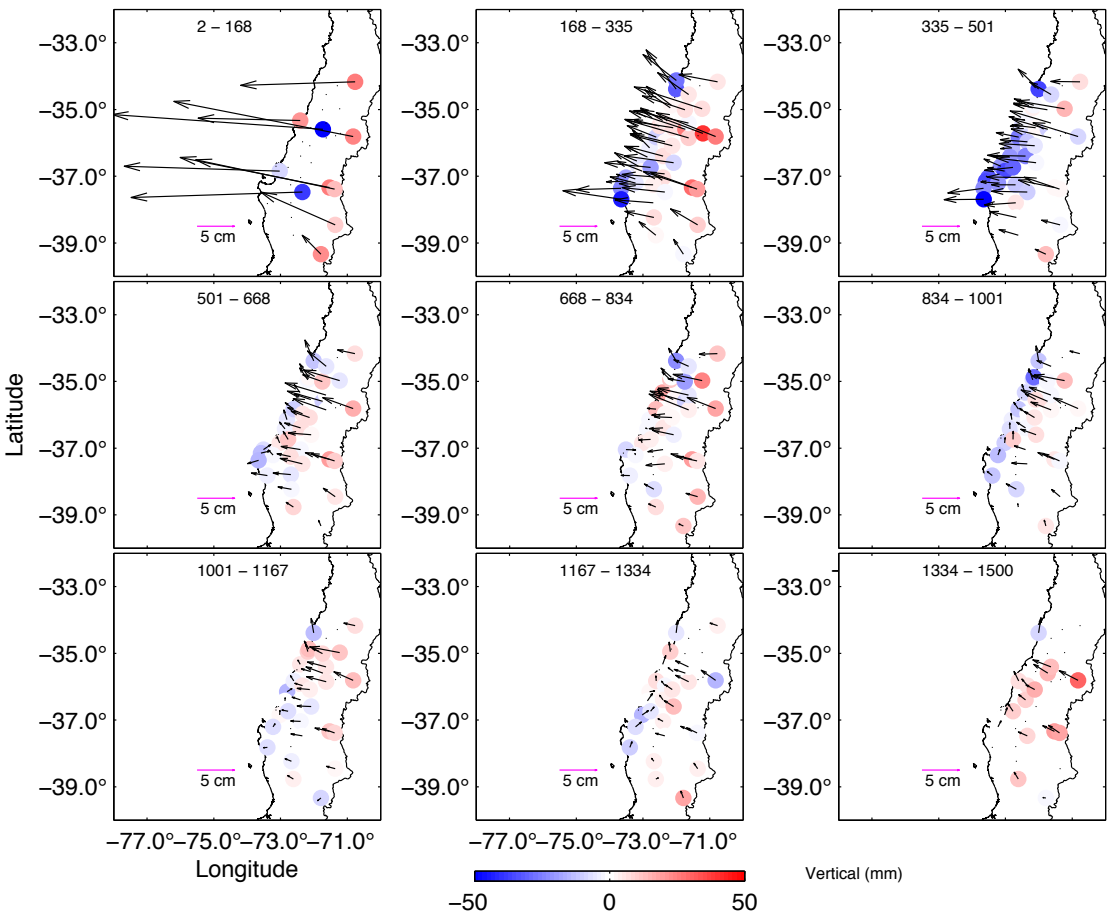

Figure 1.4: Equall length time windows of recorded postseismic displacements following the Maule Mw 8.8 of Feb. 27th 2010. Vectors show the horizontal displacements and colour scale shows the vertical displacements. Coastline and borders of Chile are plotted in black. The numbers in the top of each panel show the time window in postseismic days. Note that some time windows have better station availability than others.

Darwin Earthquake of 1835 (*Darwin*, 1851).

Figure 1.3 also shows the coseismic dispacements of the mainshock. The hinge-line of coseismic uplift and subsidence is onshore up to the latitude of approximately 35°S. Figure 1.4 shows the evolution of the 3 deformation components (east, north, and up) for the postseismic phase. These recorded motions, in particular the post-seismic, are modelled and discussed extensively in chapters 2 and 3.

1.3.2 Pisagua-Iquique Mw 8.1, 2014

The earthquake known both as the Iquique and the Pisagua earthquake of April 1st 2014 struck a portion of the plate interface that was extensively monitored in anticipation of the rupture of the mature seismic segment(s) - mature meaning that the slip-deficit is believed to be at the stage of imminent coseismic release. Figure 1.5 gives an overview of the coseismic rupture. So far, no models of postseismic deformation, either viscoelastic relaxation or afterslip, are available, although the late-interseismic activity measured by both cGPS and seismometers have revealed some extraordinary kinematic insights into the build up to the eventual Mw 8.1 failure (*Schurr et al.*, 2014; *Hayes et al.*, 2014; *Meng et al.*, 2015; *Ruiz et al.*, 2014;

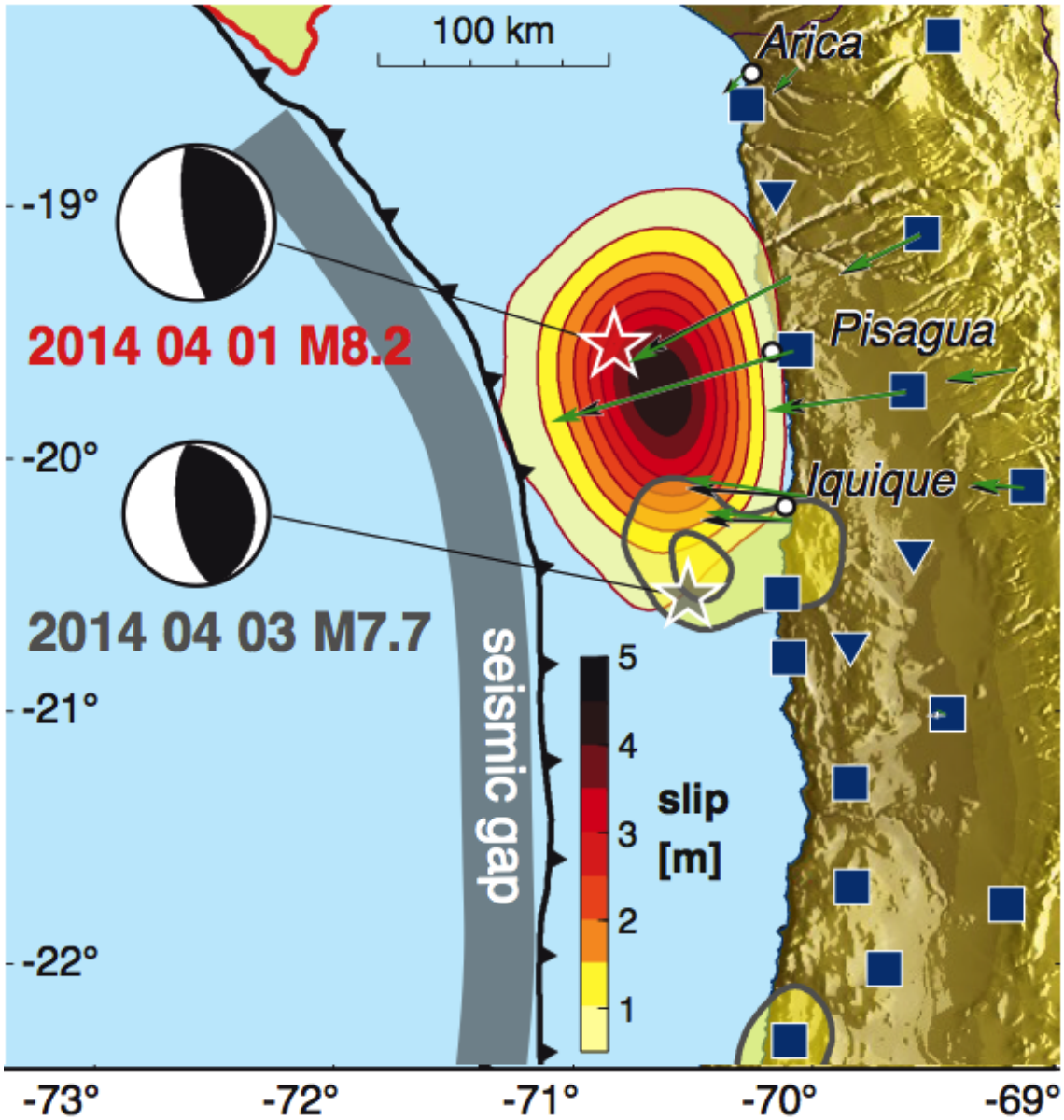

Figure 1.5: Figure modified from *Schurr et al.* (2014). Coseismic slips of the Mw 8.1/8.2 Pisagua-Iquique earthquake and the largest aftershock (Mw 7.6/7.7). Coseismic GPS vectors are shown in green (data) and black (model predictions). Epicentres are shown with stars and the focal mechanics of each earthquake are shown. Blue squares show the locations of broadband and strong motion seismometers together, and blue triangles show the locations of strong motion seismometers.

Kato and Nakagawa, 2014; *Bedford et al.*, 2015). The Mw 8.1 and the large Mw 7.6 aftershock that occurred two days later on April 3rd are thought to have released but a fraction of the total slip deficit of the North Chilean segment, with the potential of **at least** a Mw 8.5 remaining (*Schurr et al.*, 2014).

The seismo-tectonics of the late-interseismic build up to this event will be discussed in chapter 4.

1.4 Doctoral Research Aims and Objectives

The combination of extensive GPS surface motion records along with the seismicity catalogues of these earthquakes allows us to tackle some pertinent questions of subduction zone research spanning all phases of the seismic cycle (inter- co- and post-seismic). Relevant to both earthquakes and to both interseismic and postseismic data, there is the question of:

- **How are slip and seismicity related in space and time, and what are the respective magnitudes of seismic and aseismic moment release?**

For the Iquique-Pisagua earthquake, there existed some discord over the relative magnitude of seismic to aseismic slip preceding the mainshock. Chapter 4 (*Bedford et al.*, 2015) deals with this question, showing clearly the separation of aseismic and seismic signals in the cGPS through a novel approach of modelling the range of predicted GPS displacements due to uncertainties in the seismic parameter space. For the Maule earthquake, chapter 2 (*Bedford et al.*, 2013) provides some analysis into the relative magnitudes and distributions of seismic and aseismic slip. Furthermore, we relate the *seismic efficiency* to the remaining seismic hazard in the postseismic phase. Additionally, for the Maule earthquake we aim to discover how well the model of Coulomb Failure Stress explains both afterslip and aftershocks.

Relevant to just the Maule data, we would like to address the question of simultaneous postseismic processes, namely:

- **Can we separate the simultaneous postseismic processes and their magnitudes as a function of time following the earthquake.**

This question is addressed extensively in chapter 3 by means of a novel *Postseismic Straightening* methodology that teases apart the contributions of viscoelastic relaxation, afterslip, and plate interface re-locking signals. Implicit in this question of process separation is the question of how well we can parametrize each separated process.

For the case of the Maule earthquake, there is an opportunity to compare the co- post- and inter-seismic plate interface kinematics and answer the following:

- **How well do co-, post- and inter-seismic plate interface kinematics of the Maule earthquake adhere to the current understanding of frictional behaviour of subduction plate interface zones?**

As mentioned in section 1.1.1, the understanding of past and future earthquake occurrence is being investigated by a wide and integrated variety of geoscientific methods, and the insights of such studies should be tested against the observed and modelled kinematics of subduction zones such as those available for Maule.

In chapter 2, therefore, we include discussion into the likely long-term frictional behaviours of well resolved regions on the plate interface using the kinematics of the inter-, co- and postseismic.

In all the studies presented I try to address the limits of our interpretation in consideration of model resolution, measurement errors, and model assumption errors. In chapter 2, the resolution of the afterslip model is the limiting factor in our subsequent interpretations. In chapter 3, we frame the problem as a parameter search; giving a range of results and a discussion of whether or not some parameter combinations more credible than others. In chapter 4, a main aim of the study is to ascertain the validity of an aseismic-slip or a seismic-slip explanation for the transient cGPS signals, and this involves a thorough analysis of the model assumptions, and measurement errors. Finally, the discussion chapter 5 gives additional insights on plausible alternatives to the locking model of the Iquique Mw 8.1 (*Schurr et al.*, 2014), and forms the basis of an introductory discussion into the possibilities of future study into the validity of many common model assumptions used by the subduction zone locking/slip modelling community.

Chapter 2

A high-resolution, time-variable afterslip model for the 2010 Maule Mw = 8.8, Chile megathrust earthquake

Note

This chapter is a reformatted version of an EPSL paper (*Bedford et al.*, 2013). This thesis chapter of the paper includes some additional figures and text that were published in EPSL as supplementary material. The remaining supplementary material has been placed in the Appendix.

Abstract

The excellent spatial coverage of continuous GPS stations in the region affected by the Maule Mw = 8.8 2010 earthquake, combined with the proximity of the coast to the seismogenic zone, allows us to model megathrust afterslip on the plate interface with unprecedented detail. We invert post-seismic observations from continuous GPS sites to derive a time-variable model of the first 420 d of afterslip. We also invert co-seismic GPS displacements to create a new co-seismic slip model. The afterslip pattern appears to be transient and non-stationary, with the cumulative afterslip pattern being formed from afterslip pulses. Changes in static stress on the plate interface from the co- and post-seismic slip cannot solely explain the aftershock patterns, suggesting that another process – perhaps fluid related – is controlling the lower magnitude aftershocks. We use aftershock data to quantify the seismic coupling distribution during the post-seismic phase. Comparison of the post-seismic behaviour to interseismic locking suggests that highly locked regions do not necessarily behave as rate-weakening in the post-seismic period. By comparing the inter-seismic locking, co-seismic slip, afterslip, and aftershocks we attempt to classify the heterogeneous frictional behaviour of the plate interface

Highlights

- Continuous GPS maps the post-seismic subduction interface in unprecedented detail.
- Cumulative afterslip is formed from pulsing, non-migrating, slip patterns.
- Static stress transfer only seems to trigger the larger aftershocks.
- Plate interface mechanics interpreted from pre-, co-, and post-seismic kinematics.

2.1 Introduction

The period of time during which the subduction zone relaxes the stress induced by a megathrust earthquake is known as the post-seismic, which, depending on magnitude, can last for years or even decades (e.g. *Hu et al.*, 2004; *Wang et al.*, 2012). The post-seismic period presents an excellent opportunity to study subduction zone physics not only because the surface velocity is transient and much larger than before the earthquake, but also because it is accompanied by an increase in seismic activity that shows a similar time decay to the post-seismic surface displacements (*Hsu et al.*, 2006). Moreover, the transient character of the induced deformation allows testing of the time-dependent rheology of the Earth. However, interpreting post-seismic deformation is inherently non-unique and multiple physical mechanisms can explain the post-seismic surface displacements (e.g. *Freed et al.*, 2006; *Hergert and Heidbach*, 2006; *Hu and Wang*, 2012). Proposed primary mechanisms of stress relaxation following large earthquakes are afterslip (*Hsu et al.*, 2006; *Miyazaki et al.*, 2004; *Perfettini et al.*, 2010), poro-elastic rebound (*Wang*, 2000; *Hughes et al.*, 2010), and viscoelastic relaxation of stress (*Rundle*, 1978; *Hu et al.*, 2004; *Hergert and Heidbach*, 2006). Rapidly decaying deformation in the near-field of the rupture (lasting for days to 1–2 yr) is generally attributed to afterslip (*Hsu et al.*, 2006), which is characterized by aseismic slip on the plate interface surrounding the rupture as induced by co-seismic stress changes (e.g. *Marone et al.*, 1991). Afterslip has been inferred to be an important mechanism following recent great earthquakes (e.g. *Ozawa et al.*, 2011; *Vigny et al.*, 2011; *Hu and Wang*, 2012) and its distribution has been used to infer the frictional properties of the megathrust (e.g. *Miyazaki et al.*, 2004; *Marone*, 1998) and to investigate the trigger mechanism of aftershocks (*Helmstetter and Shaw*, 2009). The increased coverage of modern geodetic measurements allows us to observe the surface deformation field on finer spatial and temporal scales, adding further constraints to our models of post-seismic processes.

In this paper we will model the afterslip on the plate interface using the excellent spatio-temporal coverage of continuous GPS (cGPS) in the region of the great (Mw = 8.8) Maule, Chile earthquake of February 27th 2010. While we recognize that other physical processes are contributing to the surface deformation field, we assume afterslip to be the principal dominant contribution to the early post-seismic surface deformation pattern. This assumption is supported by the dominance of plate interface aftershocks in most of the rupture zone (e.g. *Lange et al.*, 2012; *Rietbrock et al.*, 2012; *Agurto et al.*, 2012). Deviations of the predicted (i.e. purely elastic) surface deformation from observed deformation is reasonably attributed to

and discussed in the framework of poro-elastic effects, viscoelastic stress relaxation as well as crustal faulting.

In previous studies investigating the spatio-temporal evolution of afterslip (*Segall et al.*, 2000; *Miyazaki et al.*, 2004; *Hsu et al.*, 2006, 2007) the spatial afterslip pattern was mostly not seen to significantly vary with time, i.e. it appeared stationary. However, these models lacked spatial resolution due to either the distance of cGPS stations from the slipping area (*Ozawa et al.*, 2011), or because only very few cGPS stations were available to constrain the model. Our afterslip model of the Maule 2010 earthquake highlights the transient and non-stationary character of afterslip in subduction megathrust settings and shows in detail how the afterslip varied in time and space during the first 14 months. We use our spatio-temporal model to distinguish different frictional behaviour at different regions of the plate interface, and discuss the implications for our understanding of the inter- and co-seismic behaviour of the Maule subduction segment.

The Mw = 8.8 Maule 2010 earthquake ruptured a 500 km long segment of the central Chile Forearc due to the subduction of the Nazca Plate beneath South America (Fig. 2.1). It occurred on a mature seismic gap, which presented a high degree of plate locking in the decade preceding the event (*Ruegg et al.*, 2009; *Moreno et al.*, 2010; *Metois et al.*, 2012). Strong motion in the near-field (shaking), tsunami run-up and inundation, as well as coastal uplift patterns show similarities to an earthquake in 1835 (Darwin, 1851), suggesting that both events ruptured an analogous segment of the plate boundary (*Moreno et al.*, 2012). Slip peaked at 16 m and back projection of teleseismic waveforms suggest a bilateral propagation of the rupture from the centrally located epicentre (*Kiser and Ishii*, 2011; *Wang and Mori*, 2011). There have been various models of co-seismic slip which have improved in resolution as more data have become available (e.g. *Delouis et al.*, 2010; *Vigny et al.*, 2011; *Pollitz et al.*, 2011; *Lorito et al.*, 2011; *Moreno et al.*, 2012). We compare our afterslip model with a co-seismic slip model obtained from inversion of 82 GPS measurements (described in detail in Section 3), which is similar in magnitude and distribution to the model of *Moreno et al.* (2012).

2.2 GPS Data

Following the Maule earthquake, a dense network of 67 cGPS stations (see Appendix A and Figs. 2.1, A.1) was deployed and maintained in a multinational effort (*Vigny et al.*, 2011). Data for all stations were organized in 24 h periods. Each observation was processed using the Bernese GPS Software (*Dach et al.*, 2007). Precise orbit and earth rotation parameters were used from IGS final products (*Dow et al.*, 2009). During the processing, the antenna phase centre was reduced using absolute calibration, and double differences were modelled in L3, using elevation masks of 10° and a sampling rate of 30 s. To form the single differences a phase strategy of maximum observations was used. No a-priori troposphere model was applied. The troposphere parameters were estimated in all steps of parameter estimation. Corrections of the troposphere zenith delay for each station were estimated every 2 h. We used a Neill mapping function to compute the correction in the wet and dry part. The elevation-dependent weighting was applied using the function $\cos(z)^2$. We stacked the free solutions in a normal equation file for each day. For the datum definition we used the minimum constraint approach, applying the No Net Rotation

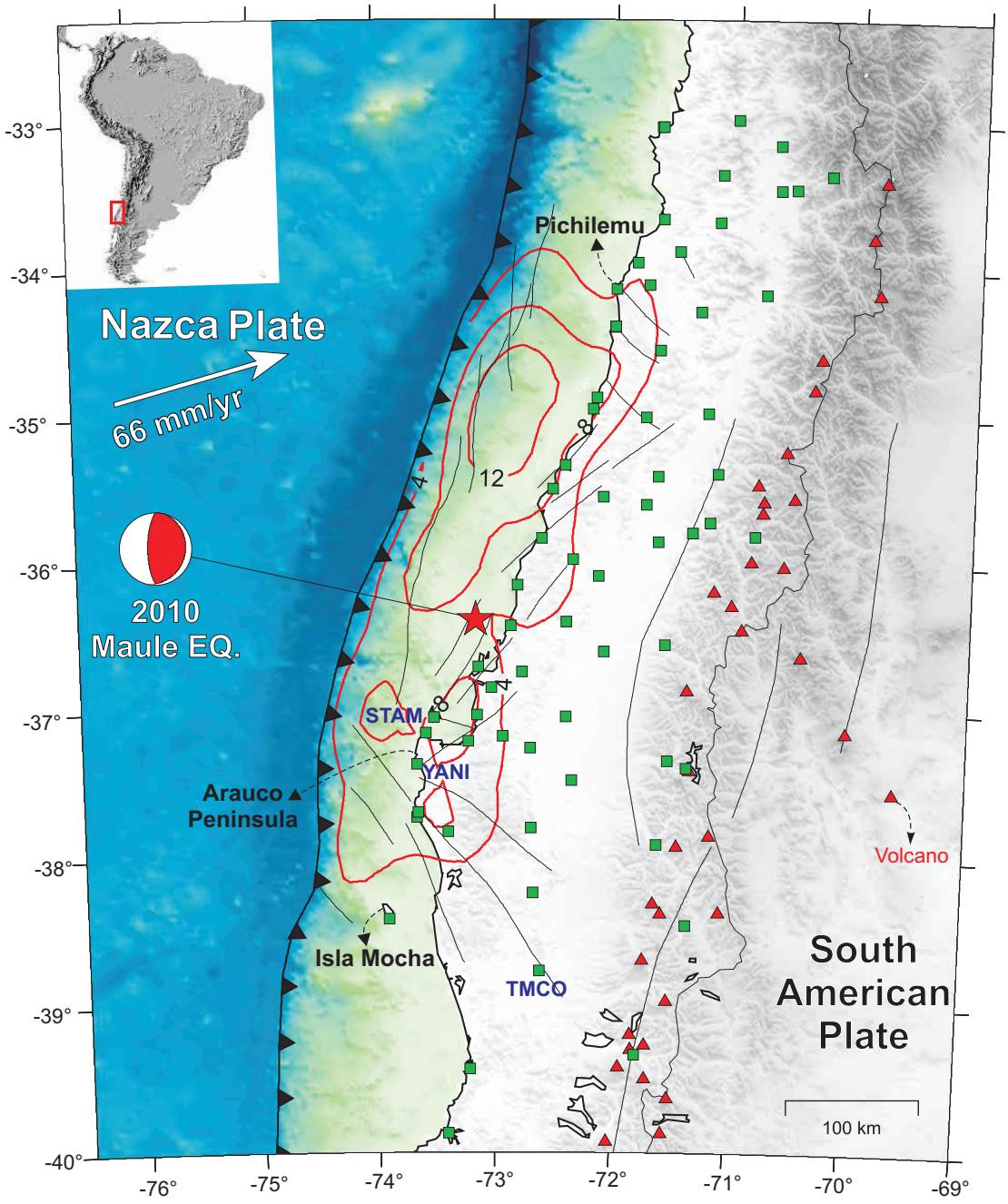

Figure 2.1: Tectonic setting for the Maule 2010 subduction earthquake. Green squares indicate locations of continuous GPS stations. Co-seismic slip contours of 4 m, 8 m, and 12 m are plotted in red. Mainshock hypocentre is given by the red star (*Vigny et al.*, 2011) and focal mechanism from the gCMT catalogue is shown. Crustal faults are indicated with black lines. Red triangles indicate Quaternary volcanoes.

(NNR) and No Net Translation (NNT) conditions for a group of selected reference stations (Table 2.1). Coordinates for each reference station were obtained from the global polyhedron weekly solution (*Dow et al.*, 2009). Our results are compatible with ITRF2005 (*Altamimi et al.*, 2007).

Station reference	Latitude(°)	Longitude(°)
CFAG	-31.60	-68.23
CHPI	-22.69	-44.99
COPO	-27.38	-70.34
CORD	-31.53	-64.47
COYQ	-45.51	-71.89
EISL	-27.15	70.62
IGM1	-34.57	-58.44
IQQE	-20.27	-70.13
ISPA	-27.12	70.65
LHCL	-38.00	-65.59
LPGS	-34.90	-57.93
OHI2	-63.32	-57.90
PARC	-53.13	-70.87
RIOG	-53.78	-67.75
SANT	-33.15	-70.66
UNSA	-24.72	-65.40
VBCA	-38.70	-62.26
RIO2	-53.78	-67.75
ANTC	-37.33	-71.53
AREQ	-16.46	-71.49
BRAZ	-15.94	-47.87
UFPR	-25.44	-49.23
FALK	-51.69	-57.87
VALP	-33.02	-71.62
RWSN	-43.29	-65.10

Table 2.1: List of reference stations and coordinates used for surface displacements.

The post-seismic signal after the Maule earthquake is evident by high rate trenchward (westward) movements and by the rapid decrease in the deformation rate (Fig. 2.2).We also see long and short period transient behaviour in the post-seismic signal, for example Fig. 2.2 shows peculiar accelerations in the North component of station YANI beginning at around post-seismic day 100. Sharp accelerations are usually related to large or nearby aftershocks (red lines on Fig. 2.2) and punctuate the decaying time series with step like features. The cGPS displacements for all stations can be found in Appendix A.

2.3 Kinematic Modelling

2.3.1 Afterslip

Afterslip is modelled as along strike and up-dip dislocations on 1344 triangular patches with an average patch size of 180 km^2, using Greens functions of dislocations

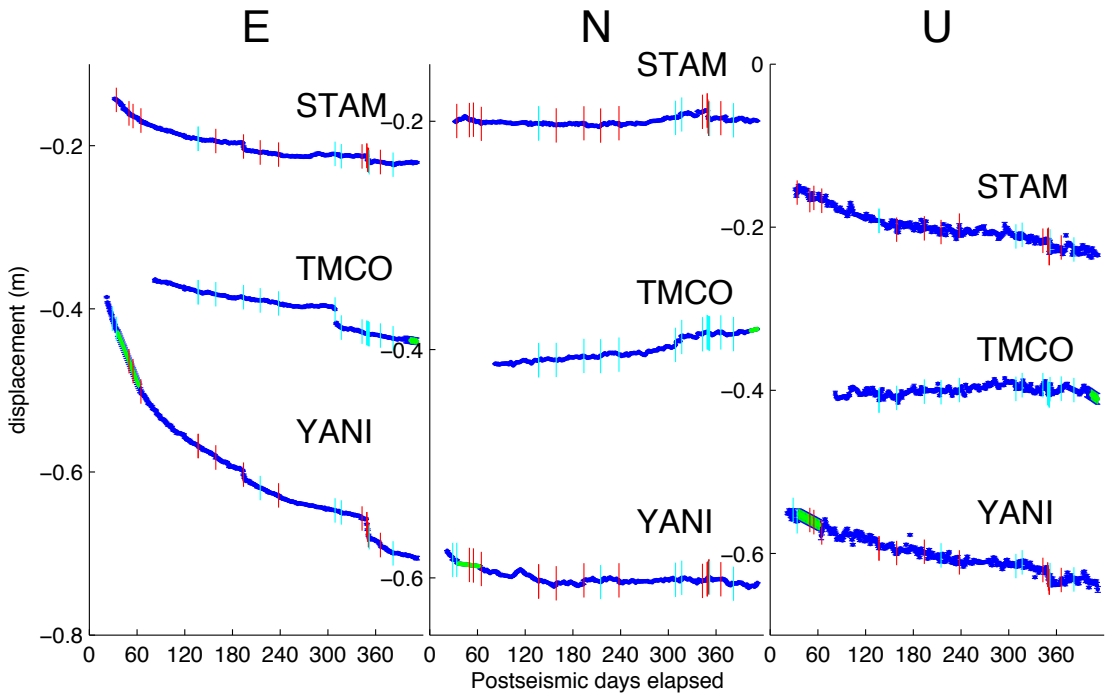

Figure 2.2: East, North, and Vertical components of the continuous GPS data for 3 stations. Blue time series points correspond to real data, and green points correspond to linearly interpolated data. Interpolated data has been given an error 3 times that of the average, so that it is weighted less in model. Vertical red lines indicate plate interface aftershocks with $M_w \geq 5.5$ (from catalogue of *Agurto et al.* (2012)) which have occurred within a lateral radius of 1°, and vertical cyan lines indicate earthquakes that have occurred further away. Aftershocks are often seen to line up with jumps and subsequent accelerations in the time series.

in an elastic halfspace (*Okada*, 1992). Rake is not constrained in the afterslip model, i.e. backslip is allowed to occur. The patches recreate the undulating plate interface, as modelled from gravity and seismicity by *Tassara and Echaurren* (2012), and extend from the trench to a depth of 100 km. The medium below the Earths surface is modelled as a perfectly elastic, homogeneous halfspace with a typical subduction zone shear modulus of 35 GPa and a Poissons ratio of 0.25 (Poissons ratio is based on the average Vp/Vs value in the local earthquake tomography study of *Haberland et al.*, 2009).

Spatio-temporal models of post-seismic afterslip in other studies have been created using either the Network Inversion Filter (NIF) (*Segall and Matthews*, 1997) or the Principal Components Analysis Method (PCAIM) (*Kositsky and Avouac*, 2010). To maximize the amount of data constraining our model, we split the data into non-overlapping 10 d periods (with a couple of exceptions; see station availability table in Appendix A), performed PCAIM on each period, before recombining the 10 d models to produce the total spatio-temporal model. This approach was necessary due to the significant gaps in the data; while PCAIM can handle small data gaps, for our model it was unable to produce reasonable results with too much missing data. To ensure a reasonable fit to the overall deformation at each station we interpolated data gaps linearly, but with the interpolated data weighted much less in the inversion than the real data. At two stations (MOCH and SOLD), we made special

interpolations to guide the model predictions along a reasonable deformation field (Appendix A Figs. **??**-**??**). This was because we have data missing from both before and after the large Mw = 7.1 aftershock of January 2nd 2011. At these two nearby stations we interpolated both forwards and backwards to the date of the aftershock and inferred the jump in the interpolated time series to be the displacement from the aftershock. Slip was regularized by a Laplacian smoothing operator, and the weight of the smoothing operator was chosen at the elbow of the L-curve between misfit and roughness. Edge effects from the smoothing were reduced by implementing a border of patches surrounding the 1344 interface patches, on which the slip was constrained to be zero. The border of patches extends all edges of the plate interface (even the trench), and is neglected in all plots because it does not physically exist.

On March 11th 2010, there were two large aftershocks (Mw = 6.9 and Mw = 7.0) on crustal faults close to Pichilemu (*Ryder et al.*, 2012; *Farías et al.*, 2011). Since we did not want to contaminate the interface model with these clearly crustal events and their immediate afterslip, we did not invert for afterslip between 10th–12th March. The afterslip model does include the afterslip between 10th–12th March, however we set the afterslip for this period to be zero everywhere on the interface. Therefore the predicted displacements for this period are also zero at all stations. For comparison of data and predictions we do not consider this period, and in the data time series the GPS positions are shown as constant for days March 10th, 11th, and 12th.

The PCAIM modelling generates daily afterslip solutions (see section 2.3.2 for more details of this method). However, this is not to say that the temporal resolution of the model is one day; since the signal to noise ratio in the data is decreasing in time (proportionally to the decay in surface GPS velocities) the daily afterslip solution accordingly becomes more noise dominated with time. For example, a two day period of the model early on in the post-seismic contains much more signal than a two day period later in the model.

2.3.2 PCAIM Modelling

PCAIM (e.g. *Kositsky and Avouac*, 2010) works by first decomposing the data time series, $X(t)$, into its n principle components using singular value decomposition:

$$X(t) = \sum_{k=1}^{n} U_k \; S_k \; V_k^T \tag{2.1}$$

where U is the spatial basis function, S is the weighting of the component, and V^T is the time evolution of the spatial basis function (time function). Once the spatial basis functions $U_1 \ldots, n$ have been found, they are treated as the 'data' matrix in a least squares minimization procedure to find the slip, L_k, on the plate interface. The spatial basis function, U_k, is related to slip, L_k, in the following way:

$$L_k = GU_k \tag{2.2}$$

where G is the matrix of Green's functions relating the surface displacements to dislocations at depth (e.g. *Okada*, 1992). After solving for L_k (regularization found in the PCAIM manual www.tectonics.caltech.edu/resources/pcaim) the time varying

model of slip is obtained by recombining the components according to their respective weights and time functions. Thus, the time varying slip model $L(t)$ is given by:

$$L_t = \sum_{k=1}^{n} L_k S_k V k' \tag{2.3}$$

Each 10 d inversion performed for the afterslip model used 3 components for the PCAIM. This choice of components gave us the least divergence of modelled and predicted time series (as discussed in sections 2.4 and 2.5.2) without being too computationally expensive.

2.3.3 Coseismic Slip

The co-seismic slip model was made using the same plate interface (including border) and regularization parameters as the post-seismic model. Vertical and horizontal displacements from 82 cGPS stations (Fig. 2.3) were inverted between 26th–27th February 2010, to produce the slip distribution of the megathrust earthquake. In addition to the published displacements (for processing details see *Vigny et al.*, 2011) we used more solutions for the day before and during the earthquake (February 26th and 27th 2010) which were processed as described in section 2.2.

2.3.4 Model resolution - What can we believe?

As is the case with any inversion model, certain model parameters are better constrained than others. Fig. 2.4 shows the diagonal elements of the model resolution matrix (*Menke*, 1989b). The best resolution is obtained on the interface closest to the stations, and these are the areas of our slip model that we can have the most confidence in. A checkerboard test (where one forward models the displacement field of a checkerboard slip pattern on the interface and then inverts for slip using the available station distribution (e.g. *Page et al.*, 2009), is a useful way to visualize limitations of our method in resolving afterslip. Figs. 2.4c–d show the inversions of noise-free and noisy synthetic data generated by a checkerboard slip on the plate interface. The resolution is best near the coastline where the approximately 80 km wide checkerboards are clearly resolved along the whole strike extent of the Maule rupture zone. The up-dip patches near the trench (extending to a depth of around 15 km) are not resolvable (Fig. 2.4a) due to their location far outside the network. On the landward side, good resolution extends about 60–70 km east of the coastline. However, the poorly resolved area in the east corresponds to slab depths of more than 60 km. A threshold of 0.1 for the resolution matrix value, based on the inspection of checkerboard tests, has been chosen to separate regions with high and low resolution (white line, Fig. 2.4a).

2.4 Results

Fig. 2.5 shows the cumulative afterslip of the spatio-temporal model 420 d after the mainshock along with selected predicted and observed time series. All observed and predicted time series can be found in Appendix A. An animated sequence for the cumulative and time windowed afterslip can be found in Appendix A. The model

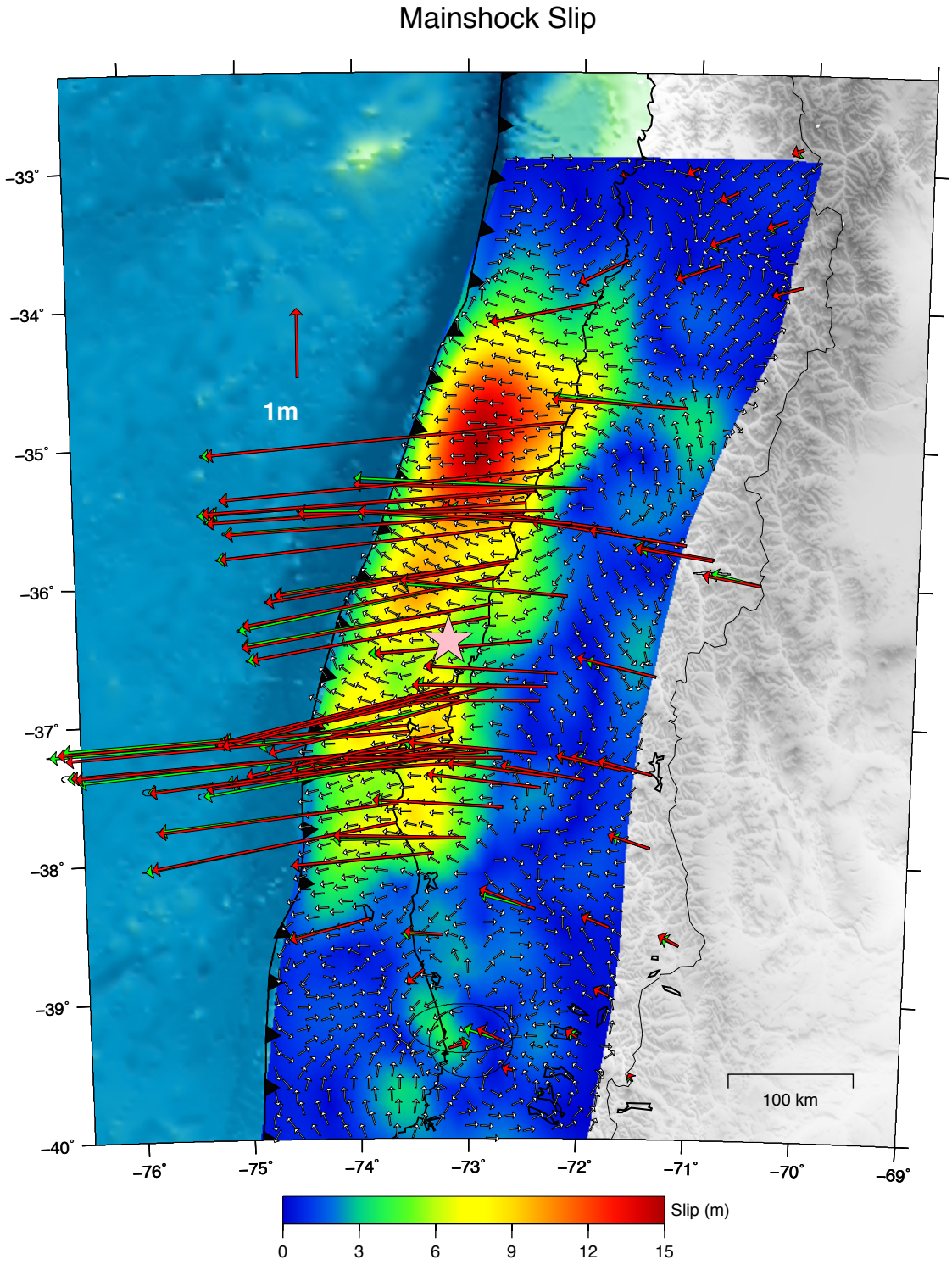

Figure 2.3: Co-seismic slip inversion using the 3 component GPS data from *Vigny et al.* (2011) and additional 3 component GPS data (82 stations in total). Horizontal data is shown in green, and horizontal predictions are shown in red.

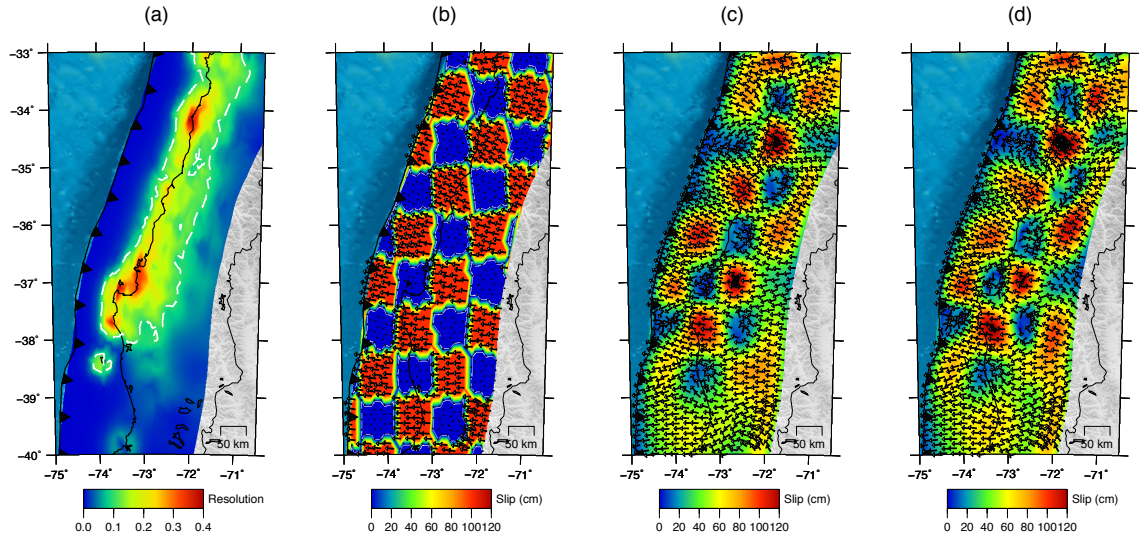

Figure 2.4: (a) The diagonal of the model resolution matrix, averaged for both up-dip and along-strike model parameters, and averaged over all the inversions that are summed to produce the model. Model resolution matrix, R , is equal to $(G^TG)^1G^TG$, where G is the matrix of Greens functions relating the dislocations in the elastic halfspace to the surface displacements (*Menke*, 1989b). Higher values indicate better model resolution. The white dashed line encloses the region of the interface with superior resolution (resolution > 0.1). (b) The input slip for the checkerboard test. Unit slip is implemented up-dip. (c) The inverted slip for the checkerboard test, using the synthetic displacements (without noise) at the 60 most commonly available cGPS station locations. (d) The inverted slip for the checkerboard test, using the synthetic displacements (with noise) at the 60 most commonly available cGPS station locations. Random uniformly distributed noise is added to each synthetic displacement, with the maximum noise being 20% of the maximum displacement.

fits the data well in most stations; however at some stations, particularly in the volcanic arc, we observe a divergence of the predicted time series from the observed time series, where the stations see more deformation than we can model.

Within the extent of co-seismic rupture, we see high afterslip regions elongated along strike, ocean-side of the coast between 36.5° and 34° S, and high afterslip regions south of the Arauco Peninsula towards the southern termination of the co-seismic rupture area (Fig. 2.5). The elongated afterslip bands north of the Arauco peninsula seem to have two main patches (at 34.5° and 36° S), but the one at 34.5° S might also be influenced by the Pichilemu cluster of seismicity (*Ryder et al.*, 2012). The densest cluster of the deep seismicity near 34.9° S and 71.8° W at approximately 50 km depth spatially coincides with cumulative afterslip of about 120 cm. The high afterslip patch of around 170 cm at 38.3° S, 73° W lies in a region of poor resolution. There are regions of low afterslip at the Arauco Peninsula and land-side of the coast at 35.3° S. We see low to moderate afterslip down-dip towards the lower limits of the seismogenic zone, with local minima at 37° and 34° S. Afterslip is also low or even backslip is seen along most of the interface near the trench, but we must be aware that the resolution is very poor at the trench and the results of the checkerboard test suggest that we are unlikely to recover even broad slip distributions here (Fig. 2.4). Down-dip of the co-seismic rupture we see apparently very high afterslip in the deepest parts of the model.

Compared to the co- and post-seismic models of other well observed megath-

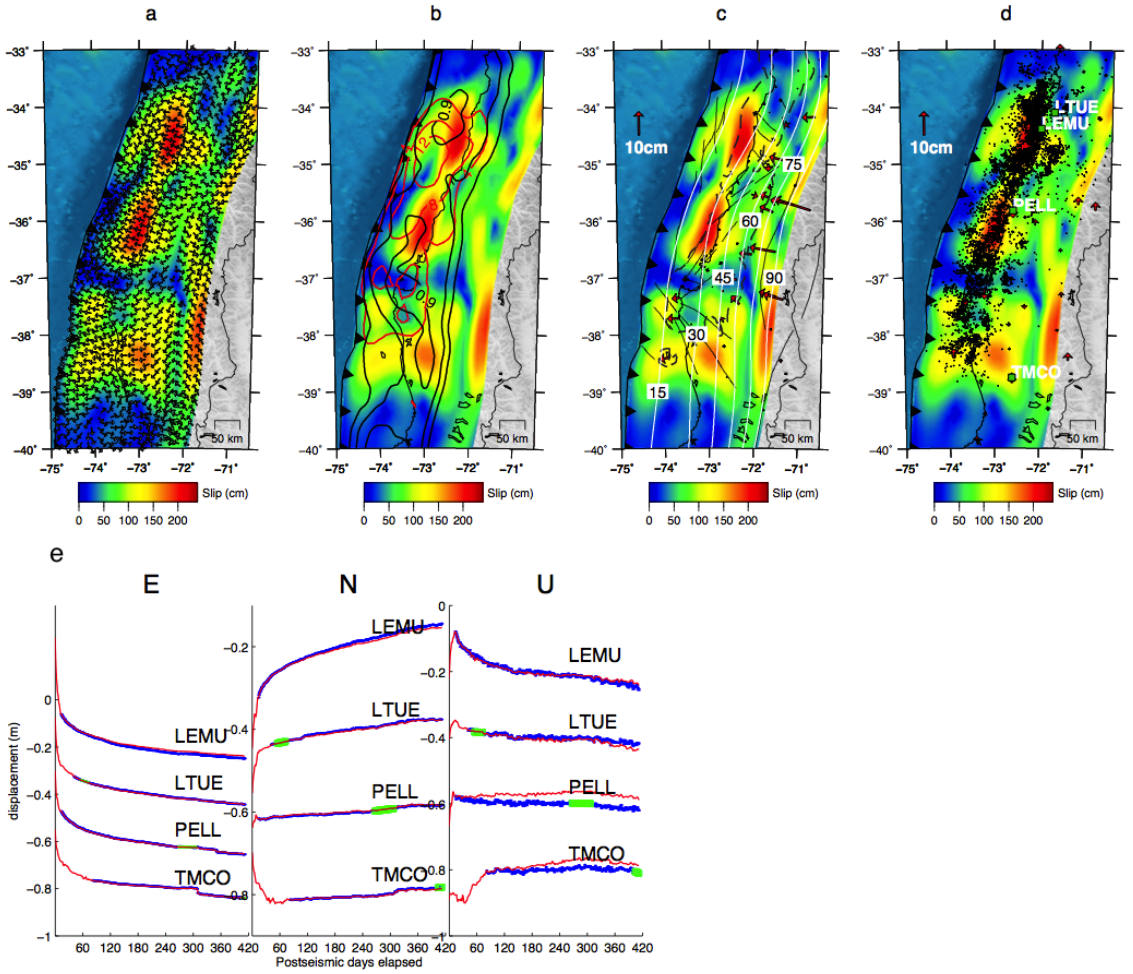

Figure 2.5: (a) Cumulative afterslip between February 27th 2010 (day of mainshock) and April 15th 2011. Arrows show direction of slip on the interface. (b) Afterslip model overlain with the red mainshock slip contours (4, 8, and 12 m) and the black interseismic locking degree contours (0.3, 0.6, and 0.9) (*Moreno et al.*, 2010). (c) Afterslip model and the horizontal misfit vectors (misfits are the data minus the predictions). Misfits are plotted rather than the data and prediction vectors because the data at certain stations are incomplete for the model duration. Misfit is calculated between the first and last days of available data. White lines represent depth contours of the plate interface, spaced in 15 km intervals (slab model: *Tassara and Echaurren*, 2012). Black dashed line encloses the region of the interface with superior resolution (resolution > 0.1). (d) Afterslip and the vertical misfit vectors. Black dots represent the aftershock seismicity from *Lange et al.* (2012). (e) Selected timeseries of model predictions and data. Blue, green, and red points represent the data, interpolated data, and the model predictions respectively.

rusts, the Maule earthquake behaves somewhat similarly to the Tohoku Mw = 9.0, Japan 2011 (*Ozawa et al.*, 2011) in that the afterslip mainly occurs down-dip of the mainshock peak slip. However, the drop off in resolution towards the trench means that we cannot rule out that high afterslip of the Maule event has occurred in the up-dip regions. As is seen for the Tokachi-Oki Mw = 8.3, Japan 2003 (*Miyazaki et al.*, 2004) and the Nias Mw = 8.7, Sumatra 2005 (*Hsu et al.*, 2006), high afterslip tends to occur outside the regions of peak co-seismic slip (Fig. 2.5b) with the exception of the northernmost high afterslip region.

2.5 Discussion

2.5.1 Transient afterslip features

The primary motivation to produce a spatio-temporal model of afterslip was to test different modes of spatio-temporal variability (for example pulsing) against stationarity of the afterslip pattern shown in other studies and to characterize the transient nature of slip accumulation in detail. In order to minimize artificial variability due to time-variable GPS availability we restricted our investigation of afterslip variability to the period between post-seismic days 82–292 during which the model relies on 58 common stations. Fig. 2.6 shows how the afterslip varies in consecutive 20 d time windows. One might argue that any variability seen in the afterslip model is mainly due to noise in the GPS. To test this possibility we performed a jackknife test in which the individual 10 d inversions were repeated with a varying station distribution to gather a variety of models. Each 10 d time window was inverted 10 times, and each inversion used 52 random stations from the 58 available. By taking the mean of the inversions (for each time window) we can reveal which features of the model are most stable (i.e. most prevalent) in all of the solutions. This analysis works on the assumption that the noise for most station combinations is very weakly correlated in time. When the difference in mean slip of consecutive time windows is greater than the sum of the standard deviations of the consecutive time windows we can consider the difference in slip for the consecutive windows as being robust. Due to the decaying nature of most time series we expect to see a decrease in slip with time. However, what we actually see are accelerations of slip (pulses) in various places within the regions releasing the most afterslip. Areas of pulsing for consecutive time windows are shown with contours in Fig. 2.6, along with a measure of robustness which is given by taking the ratio of slip difference to the sum of the standard deviations (1:1 is the minimum ratio for a pulse to be shown). Note that we only consider the up-dip component of the afterslip model since the regions of best resolution in the cumulative model exhibit predominantly up-dip slip. As discussed in Section 2.3.1, the signal to noise ratio will generally decay with time, so that the final 20 d window will be considerably more noise dominated than the first 20 d window. Therefore we also investigated the slip variability with each time window releasing the same moment in the shallowest 50 km of the plate interface, so that each time window should contain a similar amount of noise. Supplementary Fig. 2.7 demonstrates that for equal moment releases (each roughly equivalent to a seismic moment of Mw = 7.0) we also have considerable variation of afterslip pattern.

2.5.2 Misfit and slip vectors - secondary processes in action?

Although the model fits the data fairly well, and reproduces the transient signals within the post-seismic decay, it also produces considerable divergences between the observed and modelled cGPS time series at some stations. A plausible explanation for the divergence of fit could be viscoelastic relaxation of stress induced by the mainshock and poro-elastic rebound, both processes that are neglected in our model. *Hu and Wang* (2012) present similar misfit divergences from their model that simulates the post-seismic GPS data following the 2004 Sumatra megathrust, and achieve the best fit when they include both afterslip and viscoelastic stress relaxation. However, the fact that we do not see a long wavelength spatially coherent

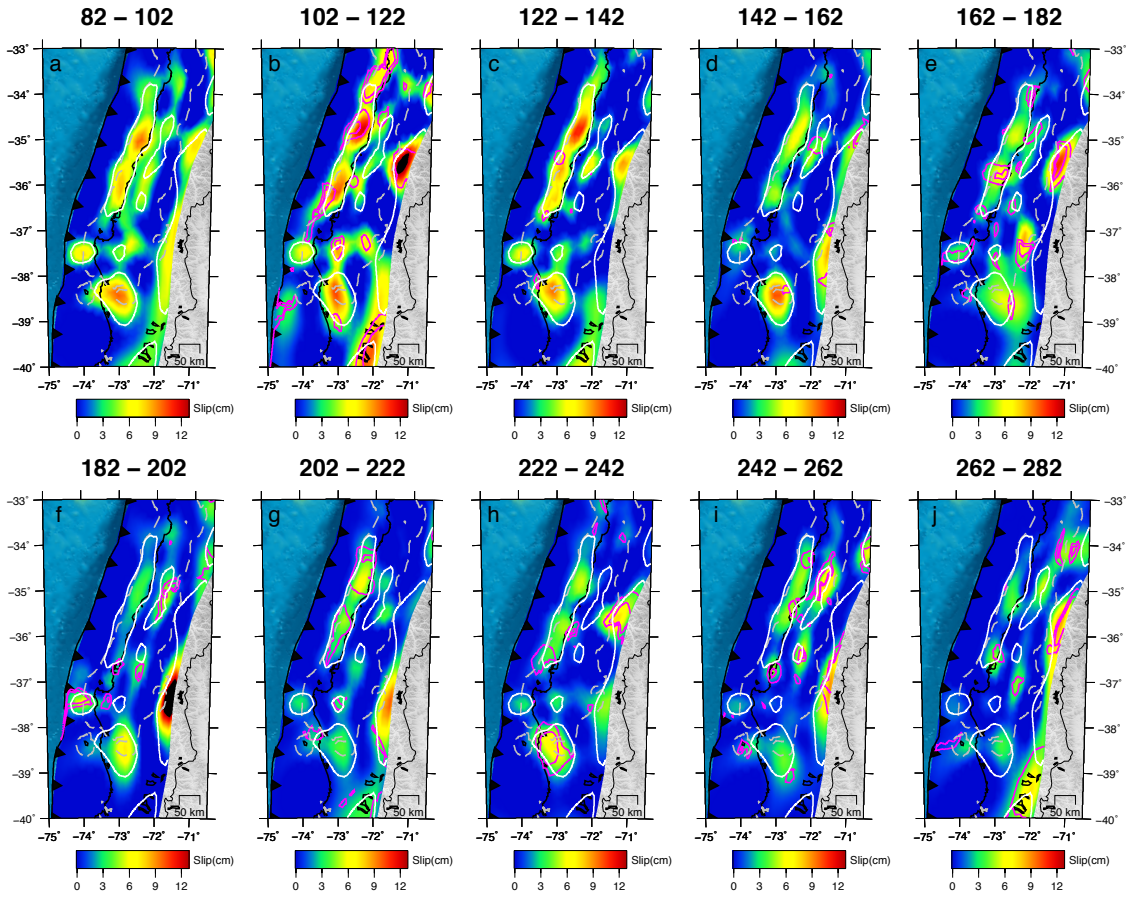

Figure 2.6: The panels (a)–(j) represent 20 day time windows of up-dip afterslip as averaged from the jackknife testing between days 82–282 of the post-seismic period. Pink contours indicate robustly identified pulses of afterslip, with the first contour representing the ratio (slip difference: standard deviation) of 1:1 and the second contour a ratio of 2:1. There are no contours on panel a because this is the first time window of the analysis. White contour represents the 25 cm contour of up-dip afterslip between post-seismic days 82–282. Light grey dashed contour encloses the region of the interface with superior resolution (resolution > 0.1).

pattern in the magnitude of misfit (as would be expected by viscoelastic relaxation and poro-elastic rebound which induce coherent long wave length deformation at the surface) suggests that certain regions of the surface could also be affected by local processes such as crustal faulting or gravitational mass movement (e.g. landslides). Crustal faulting in the overriding plate is a particularly likely candidate to explain the juxtaposition of vertical motion between Mocha Island and stations on the coast. Furthermore, large variations in magnitude and orientation of the misfit (Fig. 2.5c, d) in post-seismic decay at stations which are very close together make it difficult to fit the time series with such a simple plate interface model.

Further hints that crustal fault motions are contributing to the surface deformation field come from the slip vectors. The slip vectors (Fig. 2.5a) are generally showing the continental plate moving towards the trench, especially at regions of high afterslip and in regions of better resolution. However, there are some counter-intuitive slip directions, albeit in poorly resolved regions of the interface. Interestingly, when we constrain the rake of the slip to be up-dip, the overall slip distribution

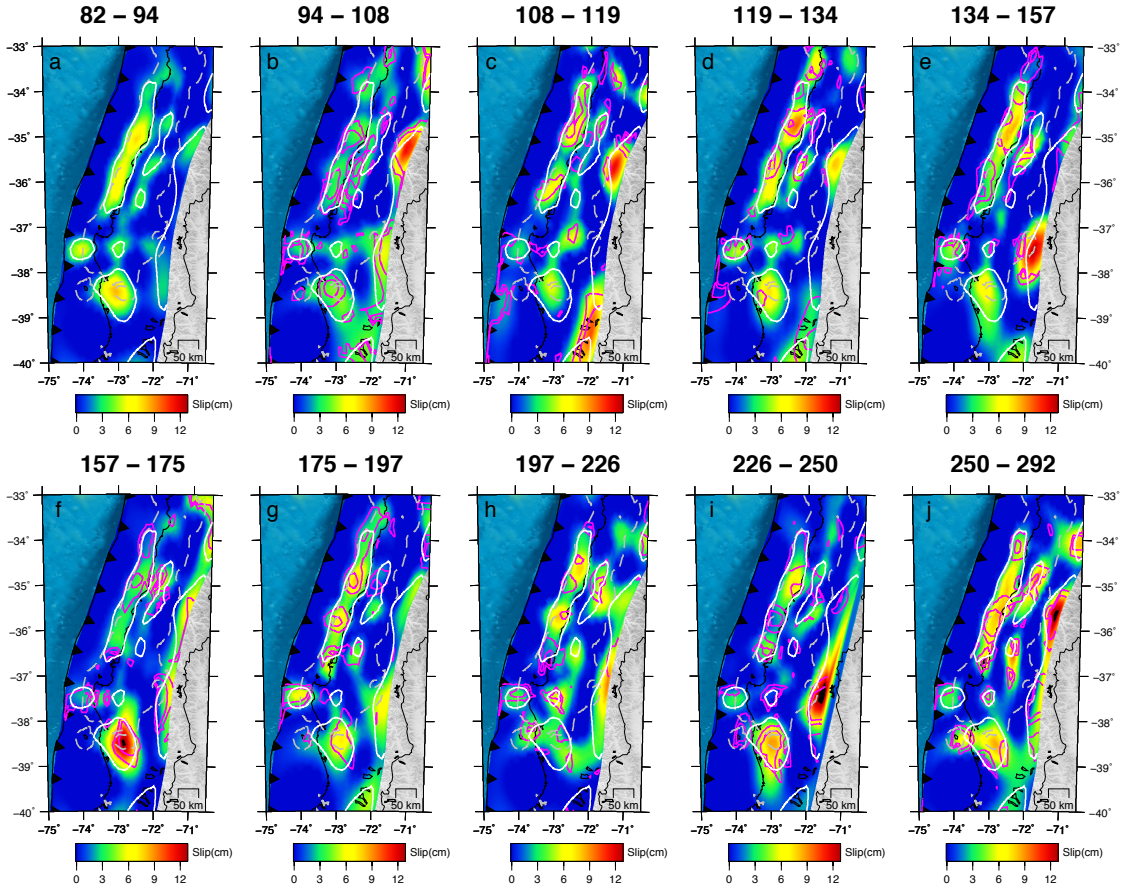

Figure 2.7: Time windows of slip (only up-dip slip since slip is predominantly up-dip in the well resolved regions). Each time window is chosen so that the moment released by up-dip slip in the top 50 km of the plate interface is the same for consecutive windows. Moment release for each time window is roughly equivalent to a Mw = 7 earthquake. Pink contours indicate both increases and decreases in slip between the current and previous panel which satisfy the criteria for robustness, with the first contour representing a ratio of slip difference to standard deviation of 1. The second contour represents a ratio of 2. Panel (a) has no contours of difference because it is the first time window in this analysis. The white contour represents slip of 25 cm between post-seismic days 82–292. The differences in slip for consecutive windows of near equal moment release do not show obvious migrations of afterslip, rather a non-stationary release of slip on the plate interface.

patterns of free and constrained rake are comparable in areas of better model resolution (Fig. 2.8); however, slip is much more concentrated and absolute slip values in the model with the constrained rake are smaller by a factor of about two. As could be expected, the misfit of the model with constrained rake is much larger than for that with unconstrained rake, demonstrating that rake variations are necessary to fit the data. The most striking difference between both models occurs in the poorly resolved near-trench region in the northernmost part of the rupture. In the constrained-rake model no afterslip is inferred for this region, whereas for the unconstrained-rake model highly oblique slip with a significant backslip component is seen.

Other non-trench-ward motions can be seen down-dip of the mainshock area, possibly due to crustal fault motion which is neglected in our model and would be projected onto the deep plate interface. Accordingly, there have been several strike

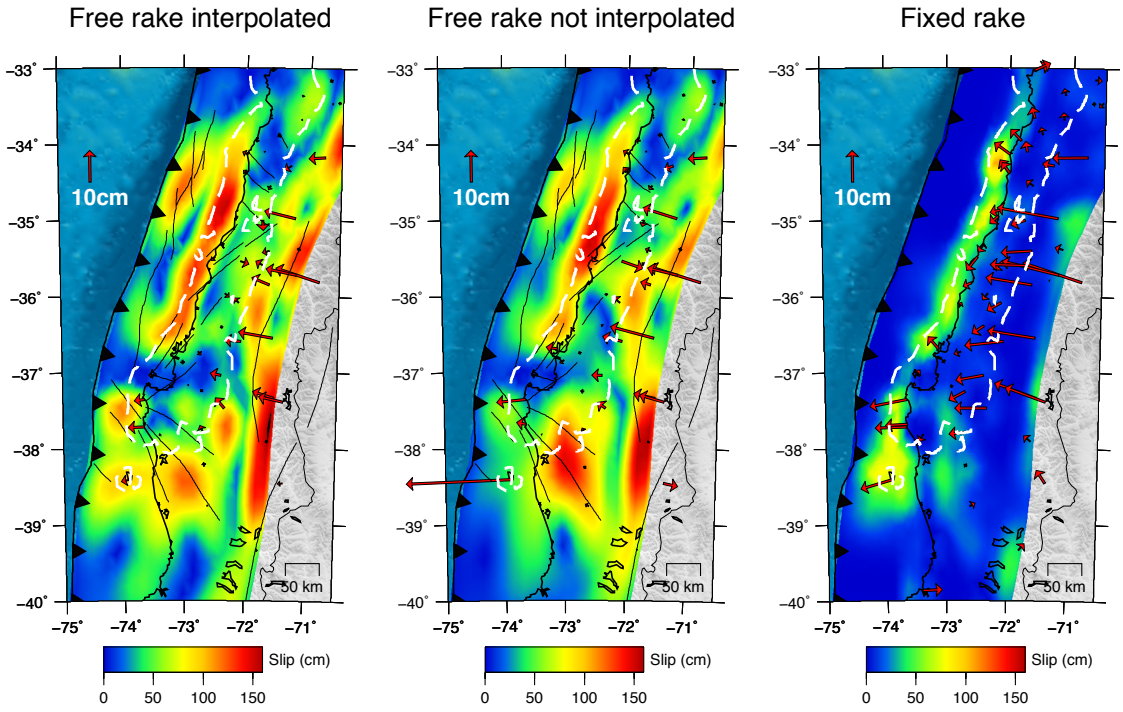

Figure 2.8: Left hand panel shows the slip magnitude using a free rake and interpolated data. The middle panel shows the slip magnitude using a free rake but without interpolated data. The right panel shows the constrained rake slip magnitude with interpolated data. All models span from post-seismic day 14–412. Red vectors represent the misfit between data and model predictions (data minus predictions). The pattern of afterslip for the three models are similar in the well resolved regions of the interface (see Fig. 2.4), although the fixed rake model tends to have lower slip magnitudes. Although the misfits for both free rake models are similar, the interpolated data model is preferred because misfits are calculated only for the time period that the data was used in the model. Therefore a low misfit can be misleading if the data was only used in one inversion. Black lines shown on the left and middle panels give locations of crustal faults. Each panel has a dark grey dashed line indicating the region of superior model resolution (i.e. diagonal of model resolution matrix > 0.1).

slip events in the volcanic arc (*Agurto et al.*, 2012), such as the recent strike slip event (Mw = 6.0) occurring at 10 km depth on 7th June 2012. However, we must be cautious with our interpretations in regions of the model with such poor resolution (Fig. 2.4). Also we expect the assumptions of our simple model of plate interface afterslip to break down as we pass the continental Moho.

Slip in the well resolved regions of the interface is predominantly in the up-dip direction, corresponding to the roughly trench-normal GPS vectors (see animation in Appendix A), and not opposite to the plate convergence direction as one might expect from a release of accumulated strain on the plate interface. The reason for this up-dip slip direction is not clear and will be investigated in future work.

2.5.3 Relation between aftershocks and Coulomb stress changes

Agurto et al. (2012) show how the larger magnitude plate interface aftershocks for

this megathrust have occurred at the fringes of the co-seismic slip distribution (Fig. 2.9a). This result is useful in terms of hazard assessment for identifying regions which

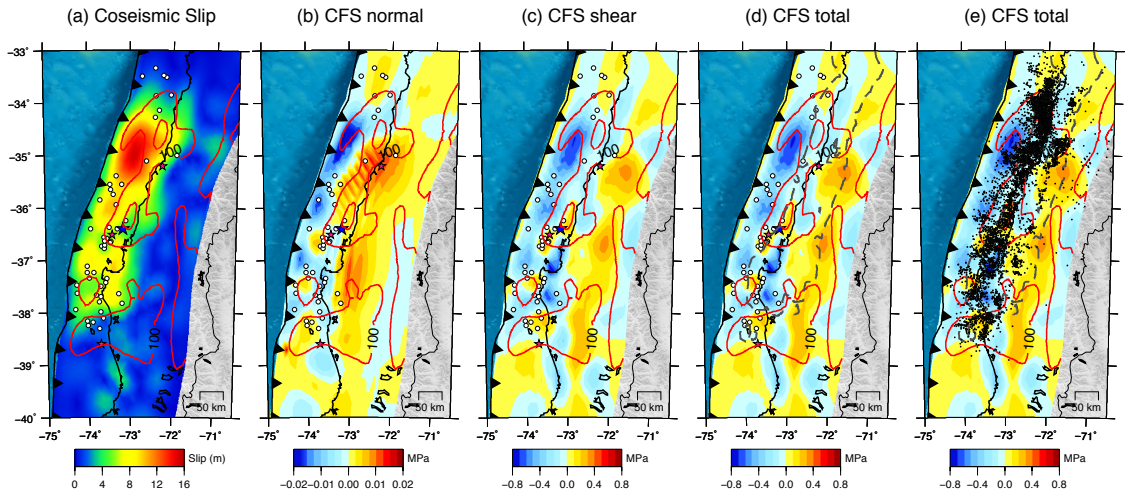

Figure 2.9: (a) Co-seismic slip. White circles are the plate interface thrust events larger than Mw = 5.5, pink stars are the largest aftershocks on the plate interface (from north to south Mw = 7.2, 6.8, 7.1), and the blue star is the epicentre of the mainshock (hypocentre from *Vigny et al.* 2011. All other epicentres from *Agurto et al.* 2012). Red contours represent 100 cm and 200 cm of afterslip (in any direction). (b) Normal component of the CFS calculation assuming a coefficient of friction mu = 0.1. Positive indicates a change in stress bringing the interface closer to failure. The circles, stars, and red contours indicate the same things stated for panel (a). (c) Shear component (in up-dip direction) of the ΔCFS calculation. Positive indicates a change in stress bringing the interface closer to failure. The circles, stars, and red contours indicate the same things stated for panels (a)–(b). (d) Total ΔCFS. Positive indicates a change in stress bringing the interface closer to failure. The circles, stars, and red contours indicate the same things stated for panels (a)–(c). The grey dashed line encloses the region of the interface with superior resolution (resolution > 0.1). (e) Total ΔCFS. Black dots represent the plate interface seismicity (events which are ± 5 km from the plate interface as defined by *Tassara and Echaurren* (2012). Seismicity from the catalogue of Lange et al. (2012). The red contours indicate the same things stated for panels (a)–(d). The grey dashed line encloses the region of the interface with superior resolution (resolution > 0.1).

are more likely to sustain larger aftershocks. However, it remains unclear by which mechanism these regions of the interface are triggered during the post-seismic phase, and why the larger aftershocks do not completely surround the co-seismic slip. If we assume the locations of aftershocks are controlled by static stress transfer expressed by a positive change of Coulomb Failure Stress (ΔCFS) (e.g. *King et al.*, 1994) then this raises the question as to whether the post-seismic afterslip is providing the additional static stress transfer to trigger these delayed aftershocks. The ΔCFS is calculated from the changes of the stress tensor with

$$\Delta\text{CFS} = \sigma_s - \sigma_n \cdot \mu \quad (2.4)$$

where μ is the coefficient of friction, σ_s is the change in shear stress (positive in up-dip direction) and σ_n is the change in normal stress (compression positive). Ac-

cording to the definition of ΔCFS the interface is brought closer to failure when ΔCFS is positive. The assumed failure direction needed for the shear component of the ΔCFS calculation was given by the up-dip direction for each patch of the model. Furthermore, we tested the sensitivity of the ΔCFS analysis results to the assumption of failure direction and it was found that within the range of failure directions captured by seismic centroid moment tensor (CMT) solutions the main findings of the analysis are unchanged (see section 2.5.4 for more details). Using the cumulative slip distribution from the mainshock and the time-varying post-seismic model (so that stress change is calculated only from slip preceding any particular aftershock) we calculated CFS for each aftershock in the catalogues of *Agurto et al.* (2012) and *Lange et al.* (2012). We combined these two catalogues (excluding redundant events) because the *Lange et al.* (2012) catalogue includes lower magnitude events but only spans post-seismic days 14–214, whereas the *Agurto et al.* (2012) catalogue has a larger magnitude cut-off but spans all the post-seismic days of our afterslip model. We also included the Mw = 7.2 event of March 25th 2012, even though this takes place almost one year after the termination of our afterslip model. The traction on the plate interface (needed for ΔCFS) is calculated from the displacement gradient in the lithosphere. The displacement gradient is calculated from analytical solutions of dislocations in an elastic halfspace (*Okada*, 1992) using the same elastic parameters for the halfspace as used in the inversion models. We chose a homogeneous effective coefficient of friction $\mu = 0.1$ (*Lamb*, 2006). We tested the sensitivity of the calculations to changes in friction coefficient and found no qualitative impact.

Fig. 2.9 shows the ΔCFS distribution (including both normal and shear components) and its relationship to the co-seismic slip, afterslip, and the aftershocks. Clearly, most of the lower magnitude events occur in areas of negative ΔCFS (Fig. 2.9e) and therefore static stress transfer does not seem to be the physical mechanism triggering these aftershocks. At the larger magnitudes (for example Mw > 5) although less data points are available, a tendency for the aftershocks to lie in the areas of negative ΔCFS seems to be the result (see fig. 2.9 and section 2.5.4). However, we must consider the effect of smoothing of the co-seismic inversion – it is likely that the larger magnitude events (shown as white circles in Fig. 2.9) are lying in positively stressed parts of the plate interface which are smeared over with negative ΔCFS from the smoothing. Two of the three plate interface aftershocks with Mw > 6.8 occur in regions of positive Coulomb stress but as all three events occur in areas of large CFS gradients, minor uncertainties in slip model or epicentral location could mean that all occurred in positive CFS regions.

Black contours in Fig. 2.9d show high afterslip (> 200 cm) in regions of positive co-seismic ΔCFS for the well resolved regions south–west of the Arauco Peninsula and south of the hypocentre. Conversely, high afterslip (> 200 cm) in the well resolved region north of the hypocentre (at around 34.6° S –72.3° W) coincides with a stress shadow (region of negative ΔCFS). It is intriguing as to why we observe the highest afterslip values in the stress shadow; one possible explanation is that this region has undergone a significant increase in pore fluid pressure to lithostatic or even supralithostatic levels following the mainshock. Such a mechanism might cause a large enough drop in effective normal stress allowing high afterslip in the presence of very low shear stresses. Alternatively, the initial (pre-mainshock) stress conditions of this region could be the reason for high afterslip: As the ΔCFS calculation only takes into account the change in stress due to the mainshock and afterslip, afterslip might

well release high shear stresses built up during the interseismic period preceding the mainshock. In that case a spatial correlation between afterslip and preseismic locking should be present. From Fig. 2.5b we see that regions of high afterslip (> 150 cm) overlap considerably with areas of high locking (> 0.9) and only moderate co-seismic slip (< 10 m) suggesting that relaxation of incomplete stress drops from the co-seismic rupture as a dominant mechanism driving afterslip.

2.5.4 Testing sensitivity of the CFS results to the assumption of failure direction

Using 122 CMT solutions for thrust events on the plate interface we calculated the horizontal component of the 3D slip vectors from the shallower nodal plane, using the equations relating slip direction to strike, dip, and rake (*Aki and Richards*, 2002):

$$x = \cos\lambda\cos\phi \; + \; cos\delta\sin\lambda\sin\phi \tag{2.5}$$

$$y = \cos\lambda\sin\phi \; - \; \cos\delta\sin\lambda\cos\phi \tag{2.6}$$

where ϕ, δ, and λ are strike, dip, and rake, respectively; x and y are the components of slip in the East and North directions. From the North and East slip components we plotted a rose-plot histogram of the horizontal slip direction (failure bearing) and compared this with a rose-plot of the failure bearings if all events were assumed to fail in the updip direction (Fig. 2.10). When comparing the failure directions in Fig. 2.10 one must remember that the majority of the CMT events are of larger magnitude (typically Mw > 5) whereas the ΔCFS analysis includes over 9000 events of all magnitudes (mostly lower because of the Gutenberg-Richter law). Based on the bearings shown in the rose-plots we decided to test failure at failure bearings ranging from 250 – 290° in 10 increments. For each test of failure bearing we defined the failure direction of each patch as the in-plane direction for which the horizontal component points in the direction of the failure bearing. Figure 2.11 compares the histograms of ΔCFS for various magnitude bands and failure bearings. From Figure 2.11, we can see that the conclusions of the ΔCFS analysis outlined in the maintext section 2.5.3 do not change significantly by varying the failure bearing. Figure 2.12 shows that the coseismic ΔCFS distributions do not vary significantly for the up-dip failure direction and the failure bearings between 250-290°.

2.5.5 Implications for mechanics of the subduction interface

Since we now have preseismic geodetic locking, co-seismic slip and afterslip models for the Maule event we can study this megathrust in terms of the pre-, co-, and post-seismic phases of the earthquake cycle, and speculate on the physical properties and stress field conditions that govern the kinematic and dynamic interface behaviour. The plate interface at regions of great subduction zone earthquakes is often thought to consist of interfingering areas of contrasting frictional properties, which are ultimately controlling the feedback of pre-, co- and post-seismic processes (*Kanamori and Brodsky*, 2004). The asperity model (*Lay and Kanamori*, 1981) describes the subduction interface as consisting of asperities which build up stress inter-seismically and fail suddenly while the surrounding interface creeps. The development of rate

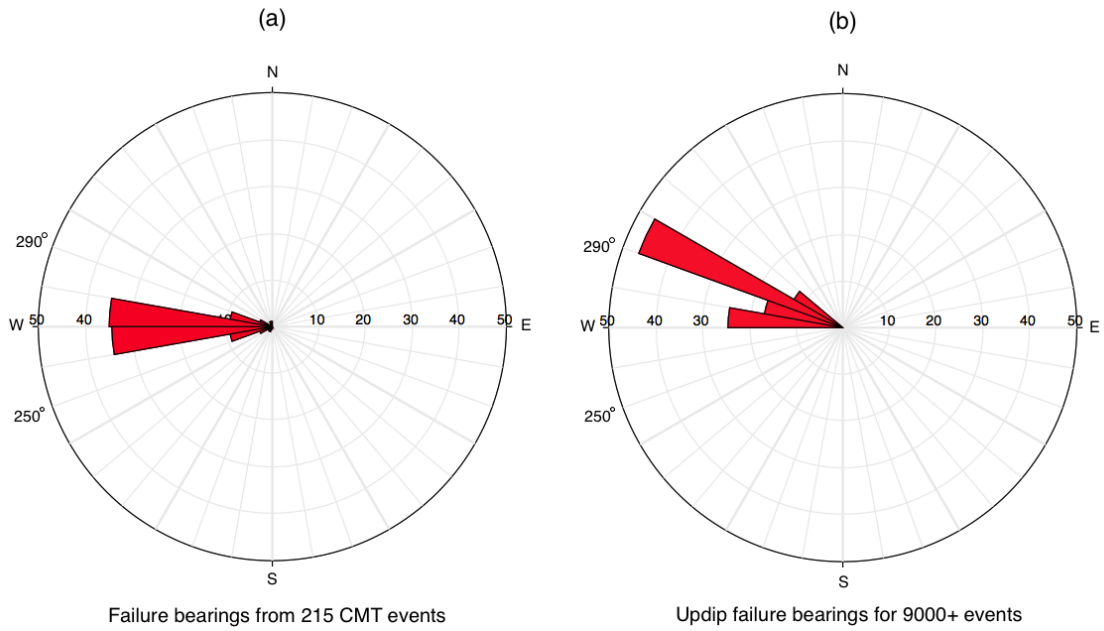

Figure 2.10: (a) Rose-plot histogram showing the horizontal direction (bearing) of the slip vectors derived from 122 CMT solutions of plate interface aftershocks. Corresponding aftershocks epicentres are plotted on Fig. 2.12b–d. Numbers moving radially outwards indicate percentage of events. (b) Rose-plot histogram showing the horizontal up-dip failure directions for all events used in the ΔCFS analysis. Numbers moving radially outwards indicate percentage of events.

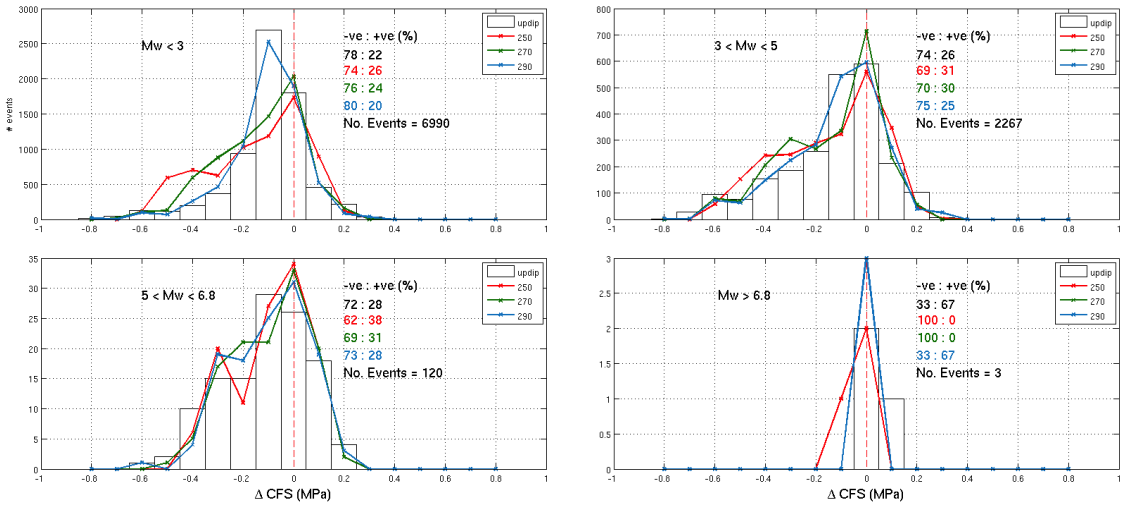

Figure 2.11: Histograms of ΔCFS (both co- and post-seismic) leading up to the plate interface aftershocks. Events are split into magnitude bands. Black bars represent the histograms for an up-dip failure, and red, green, and blue lines represent the histograms for 250°, 270°, and 290° respectively. Each of the four histograms is for a different seismic magnitude band, and the coloured ratios correspond to the non-triggered:triggered ratio for each failure bearing.

and state friction laws over the past decades (e.g. *Scholz*, 1998) describes how such asperity and creeping zones should behave when critically stressed (i.e. when a rupture front propagates into the zone). In rate-weakening zones, the frictional strength will decrease when slip rate increases leading to instability and increasing the likeli-

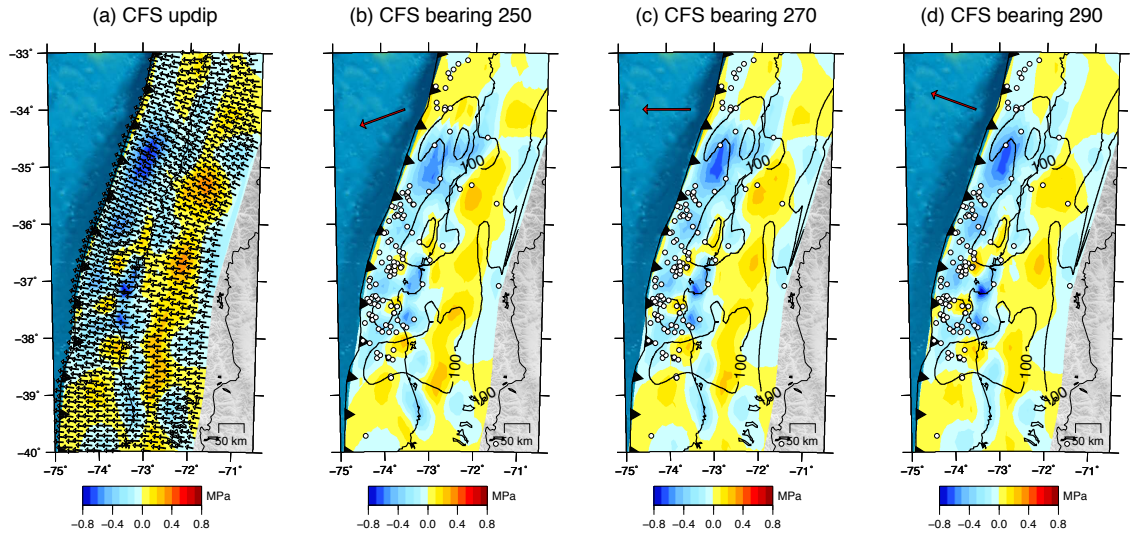

Figure 2.12: (a) Co-seismic ΔCFS distribution assuming failure direction to be up-dip. Vectors on each patch of the model indicate the up-dip direction. (b) Co-seismic ΔCFS distribution for a failure bearing of 250°. Red arrow gives the failure bearing direction and white circles are the hypocentre locations for the events with CMT solutions (Fig. 2.10c). (c) Same as (b) but for failure bearing of 270°. (d) Same as (b) but for failure bearing of 290°.

hood of continued rupture propagation. Zones of rate-strengthening friction behave in the opposite manner, increasing the friction during accelerated slip and strongly counteracting rupture propagation. It has often been assumed that the geodetically highly locked regions are acting as asperities and correspond to the rate-weakening friction zones, whereas the creeping regions correspond to rate-strengthening friction zones. However, this simplistic binary view is inconsistent with observations of post-seismic creep on supposed asperities following the great Tohoku-Oki megathrust of 2011 (*Johnson et al.*, 2012).

In order to analyse the frictional behaviour in more detail, we compared afterslip to slip from aftershocks by calculating the post-seismic seismic efficiency (PSE) (*Tilmann et al.*, 2010); i.e. the percentage of slip which is released seismically during the post-seismic observation period. By forward modelling the expected slip and rupture area from scaling relationships (*Wells and Coppersmith*, 1994) for aftershock events that occurred on the plate interface during the time period of our afterslip model (*Agurto et al.*, 2012) then inverting the displacement field using our time varying station coverage, we produced an approximation of the seismic contribution to the cumulative afterslip model (i.e. the seismic coupling coefficient during accelerated slip) and hence we quantified the percentage of seismic slip captured in our model. The slip in the forward modelling is assumed to be in the local up-dip direction and is performed on a finer mesh with an average patch area of 11 km^2. The forward modelled slip for each earthquake is consistent with the equation for seismic moment:

$$SD \sum_{j=1}^{n} A_j \tag{2.7}$$

where S is the shear modulus of the faulted material, Aj is the area of each patch

in the rupture area, D is the average slip on the rupture, and n is the number of subpatches of the fault used in the forward calculation of the displacements. First we selected a suitable source area for each aftershock by selecting the closest patch(es) to the hypocentre. The number of patches was determined by the minimum misfit between theoretical rupture area and cumulative area of patches. Then we adjusted the slip to satisfy the moment according to Eq.(2.7). For lower magnitude events the rupture areas are unrealistically large with very low values of slip which, even in such high frequency, have a negligible effect on the surface displacement field. Therefore we only consider the largest plate interface aftershocks as presented in the paper of *Agurto et al.* (2012). Inversion of the synthetic data is performed using the same regularization and model parameters that were used in the afterslip inversion. PSE appears to be negative in regions where we have backslip in the cumulative afterslip model but this only appears in poorly resolved regions of the plate interface, allowing us to disregard the negative regions in the subsequent discussion. In general PSE is relatively low (<10% for most areas), although we must consider that the seismic slip is smeared during both the forward modelling and the regularization of the inversion. In reality PSE values are likely to be larger, and so values of PSE should only be interpreted relatively. Furthermore, the smearing of the inversion puts seismic slip onto regions of the interface which may in reality have very little seismicity, and this effect is exacerbated with larger events. Nevertheless, this method is useful for showing differences in mode of afterslip release over broad spatial scales.

Figs. 2.13a-c show the PSE (clipped at 5% for clarity) versus the co-seismic slip, afterslip and interseismic locking distributions. There seems to be no obvious correlation between co-seismic slip and PSE (Fig. 2.13a) although we see high PSE together with moderately high co-seismic slip at the Arauco Peninsula (a region where the co-seismic model also has good resolution due to good station coverage; see Fig. 2.3). Also in this region we see high interseismic coupling. From Fig. 2.13b we see that most regions of high afterslip are aseismic with the exception of the region near Mocha Island, where the Mw = 7.1 occurred on January 2nd 2011.

Under rate-and-state physics, the more highly seismically efficient regions of the plate interface should correspond to the rate-weakening zones because the stress is being released more suddenly. Therefore it seems that the Arauco peninsula is behaving as a rate-weakening asperity which becomes highly locked in the interseismic, releases large slip co-seismically, and has a relatively high PSE to surrounding regions. Heading North along the coastline there seems to be a transition from a rate-weakening into a rate-strengthening region with peak afterslip centred at 73° W 36.2° S, and this transition in from high to low PSE coincides with the termination of a very highly preseismically locked slither (Fig. 2.13c). This region has undergone a strong increase in ΔCFS due to the mainshock (Fig. 2.9d) yet it releases this stress with predominantly aseismic afterslip and was locked to a lesser degree (i.e. creeping more) than the Arauco peninsula during the interseismic. The gradual release of mainly aseismic slip centred at 73° W 36.2° S is of stark contrast to the also positive ΔCFS region nearby to the southwest at 73.6° W 36.7° S (Fig. 2.9d) which releases stress with some of the largest plate interface aftershocks. As the high afterslip region extends Northwards along the coast towards 34° S it becomes less straightforward to characterize the frictional properties of the plate interface. As discussed in Section 2.5.3, we see high afterslip in a region with a negative ΔCFS which could be due to a slip-deficit, expulsion of fluids onto the interface, or a com-

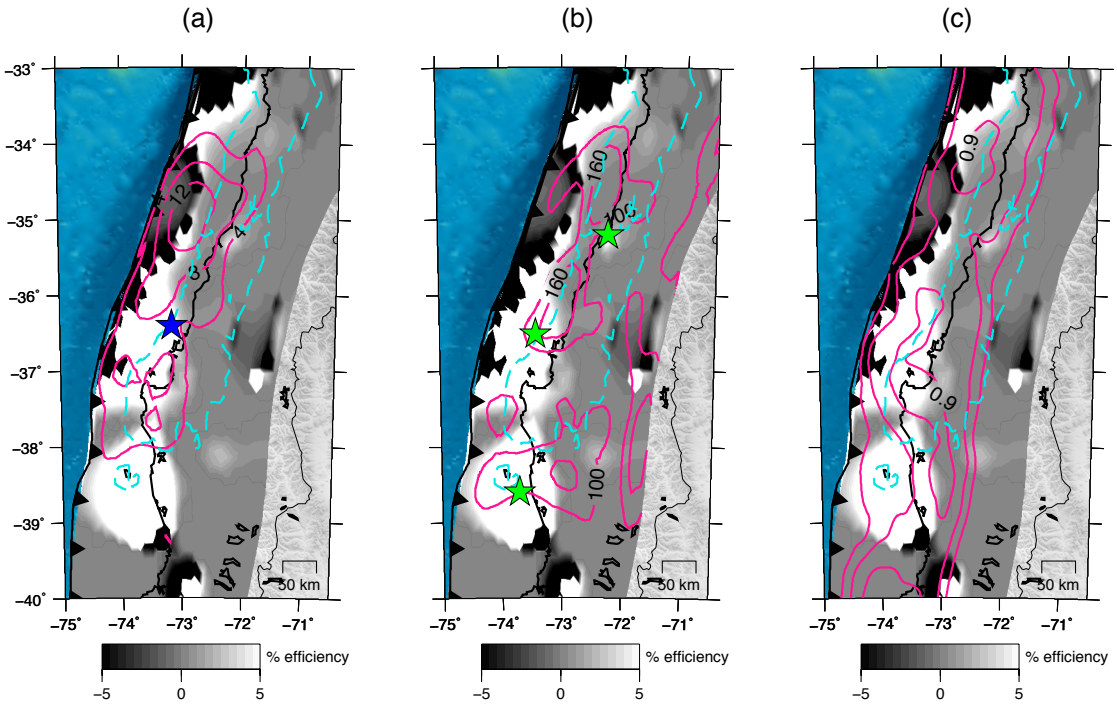

Figure 2.13: (a) Post-seismic Seismic Efficiency (PSE) with magenta contours of co-seismic slip (4, 8, and 12 m). Blue star is the mainshock hypocentre (*Vigny et al.*, 2011). The blue dashed line encloses the region of the interface with superior resolution (resolution > 0.1). (b) PSE with magenta contours of afterslip (100 and 160 cm). Green stars are the largest aftershocks on the plate interface (pink stars in figure 2.9). The large aftershock at 35.2°S happens over one year later – it is not included in the calculation of PSE. The blue dashed line encloses the region of the interface with superior resolution (resolution > 0.1). (c) PSE with contours of interseismic locking degree (contour intervals: 0.3, 0.6, and 0.9). The blue dashed line encloses the region of the interface with superior resolution (resolution > 0.1).

bination of both these effects. This region of low PSE afterslip lies in an area of high co-seismic slip (> 8 m) – a colocation that we would not expect if this region behaved with purely rate-weakening mechanics. From the low PSE one might be inclined to say this is a rate-strengthening region, however this seems incompatible with the high afterslip at regions of very high interseismic locking. In the context of conditional stability this behaviour can only be reconciled by assuming that pore pressures increased at these locations during or shortly after the mainshocks. We therefore interpret the creep which we see on the supposed asperity as due to a transient elevation in pore fluid pressure. If an increase in fluids on the interface is facilitating the large afterslip of this region then perhaps it is also facilitating the high density of low magnitude events in this region.

Interestingly, anomalously high PSE compared to surrounding regions at 72.2° W 35.2° S coincides with the hypocentre of one of the largest plate interface aftershocks (Mw = 7.1) that occurred on March 25th 2012 (for PSE calculation we only used events until April 11th 2011).

2.6 Conclusions

The proximity of cGPS to the seismogenic plate interface and the excellent spatial coverage has allowed us to model the spatio-temporal changes of afterslip with unprecedented resolution. We have found that afterslip accumulates in pulses in specific regions on the plate interface, rather than decaying with a stationary pattern or migrating (see animation in Appendix A). While most of the afterslip is aseismic (Fig. 2.13), the plate interface aftershocks tend to line up over regions of high afterslip (Fig. 2.5d). We have shown that most of the plate interface aftershocks (which are of low magnitude) are not triggered by the transfer of co- and post-seismic static stresses, and from this result we can speculate on other possible mechanisms controlling aftershocks. If we assume that poro-elastic rebound and visco-elastic stress relaxation would only result in a long-wavelength pattern of the post-seismic GPS signals then these processes would also not explain the locations or decay of the aftershocks. Since our model captures most of the post-seismic signal we hypothesize that the processes that control the strength are mainly due to pore pressure diffusion due to pathways opened at the interface by the mainshock (e.g. *Shapiro et al.*, 2003). This might result in significant decrease of the effective normal stress, i.e. an increase of positive ΔCFS. However, pore pressure changes (particularly when they occur locally) would not leave an imprint on the GPS signal. The hypothesis of pore pressure diffusion could also explain the high afterslip and pulsing behaviour, both for areas with positive and negative ΔCFS. Additionally, we have demonstrated that the simple rate-and-state friction based models to explain locking, asperities, co-seismic rupture and afterslip distribution do not seem to hold for this megathrust, with the Maule 2010 afterslip occurring in both highly preseismically locked zones and in zones of lower preseismic locking. Since both afterslip pulses and the majority of aftershocks are possibly both linked to fluid effects, a sensible next step would be to establish whether a spatio-temporal relation exists between afterslip pulses and aftershocks.

Chapter 3

Separating Simultaneous postseismic processes: an application of the postseismic straightening method

Note

This chapter is a reformatted version of a paper under internal review entitled **"Rapid re-locking of the 2010 Maule Mw 8.8 captured by curvature in postseismic cGPS motion.** Additional supplementary material has been placed in the Appendix.

Abstract

The postseismic deformation captured with continuous Global Positioning System (cGPS) monitoring following many recent mega-thrust events has been shown to be a signal composed of two processes: afterslip on the plate interface (*Miyazaki et al.*, 2004; *Chlieh et al.*, 2007) and viscoelastic relaxation of the continental and oceanic mantles in response to the coseismic stress perturbation (*Wang et al.*, 2012). Following the South-Central Chile 2010 Maule Mw 8.8 earthquake, the postseismic cGPS network has captured a curvature in the pathway of the horizontal motion that is not easily fit by a stationary decaying pattern of afterslip in combination with viscoelastic relaxation. Here we show that with realistic assumptions about the long-term decay of the afterslip signal, the postseismic signal can be decomposed into three first-order contributing processes: plate interface re-locking, plate interface afterslip, and mantle viscoelastic relaxation. From our analyses we conclude that the plate interface recovers its interseismic locking state rapidly (in a negligible amount of time compared to the length of the megathrust seismic cycle) supporting experimental evidence. Re-locking is the main cause of the curvature in the cGPS signal, and this study provides the first ever quantification of geodetic re-locking rates following a megathrust earthquake.

3.1 Introduction

Geodetic monitoring is a powerful tool for constraining physical properties and mechanical behavior of the subduction plate interface. By using analytical functions describing surface motions due to dislocation in an elastic halfspace (*Okada*, 1985), we can mosaic the subduction zone plate interface kinematics according to the recorded surface displacements for all phases of the megathrust earthquake seismic cycle (*Simons et al.*, 2011). These kinematic patterns, if correctly mapped, are crucial for better estimating the remaining seismic potential (slip-deficit) of a margin segment (*Moreno et al.*, 2012). The estimation of afterslip - which can release as much as 30% of the coseismic moment on the interface and is therefore an important consideration in the slip-deficit calculation (*Perfettini et al.*, 2010) - is complicated by the presence of other postseismic processes in the signal, with the most commonly investigated simultaneous postseismic process being viscoelastic relaxation. In this study we are dealing with the near-field cGPS data for the first four years following the 2010 Maule Mw 8.8 earthquake of South-Central Chile with the aim of distinguishing the major contributing postseismic processes in the cGPS time series.

Figure 3.1 shows the selection of cGPS used in this study, with the stations covering an area approximately 100-300 km from the trench. This station coverage is near enough to capture the plate interface kinematics and extends far enough to capture the mantle relaxation processes. The Maule earthquake ruptured a segment of the plate boundary between the Nazca and South American plates and the features of the main earthquake have been well documented, with most models in agreement for the main features of the coseismic rupture (*Delouis et al.*, 2010; *Vigny et al.*, 2011; *Moreno et al.*, 2010; *Bedford et al.*, 2013). Until now, the Maule postseismic data has been modeled with purely elastic assumptions to give a preliminary diagnosis of the afterslip pattern and spatiotemporal characteristics (*Bedford et al.*, 2013; *Vigny et al.*, 2011). However, questions remain as to the validity of such purely elastic models when the viscoelastic response is neglected. Comparisons of afterslip, coseismic slip, and aftershocks have yielded promising spatial relations that suggest a predominance of afterslip contributing to the captured near-field cGPS (*Bedford et al.*, 2013), especially since there is a clear linear relation between the local number of plate interface aftershocks and local cGPS motion and that location of modeled afterslip and majority of aftershocks is in good agreement (*Lange et al.*, 2014).

This study uses postseismic horizontal motions (fig. 3.1) that have been captured over the first four years following the earthquake. At many stations the postseismic motion in space is curved, with the curvature occuring in a clockwise direction. Curvature in the anti-clockwise sense is not observed. Postseismic processes that could be combining to produce this spatial curvature in time would be (1) megathrust plate interface afterslip, (2) viscoelastic relaxation of the mantle, and (3) the re-locking of the megathrust plate interface. The aim of this study is to investigate the relative contribution of these candidate postseismic processes in the signal. We use simple models to model each process while assuming that the curvature in the signal is due to a combination of a spatially straight afterslip signal with one of: (a) viscoelastic relaxation, (b) re-locking, or (c) both viscoelastic relaxation and re-locking.

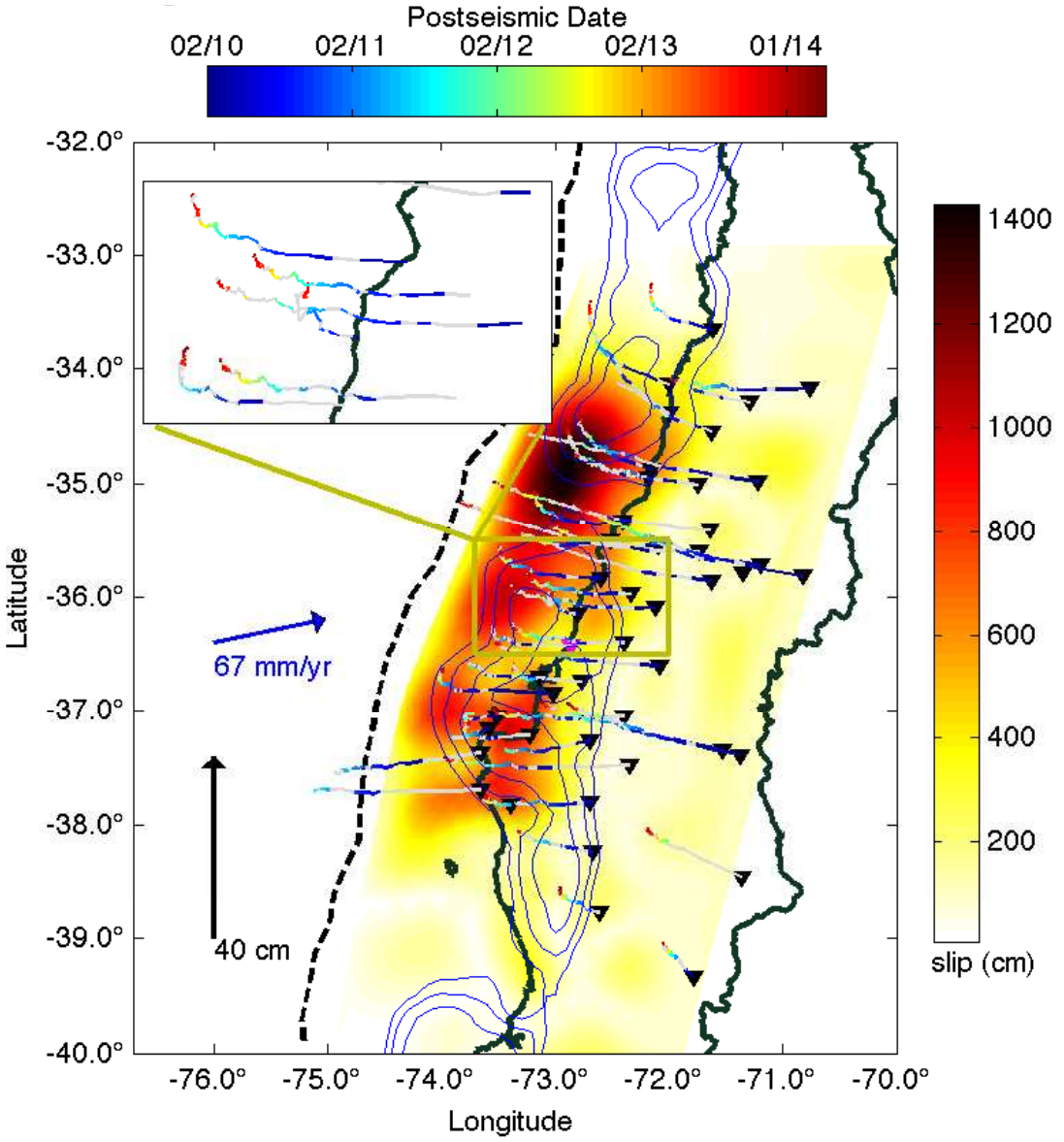

Figure 3.1: Plot of the study area. Black dashed line is the trench where the subducting Nazca plate meets the overriding South American plate. Thick black lines show the Chilean coastline and the border with Argentina. Blue contours show the interseismic locking model (*Moreno et al.*, 2011) with contour intervals at 0.7, 0.8, and 0.9 locking degree (1 and 0 would indicate a fully locked and fully de-coupled plate interface respectively). The coloured distribution shows the coseismic slip distribution (*Bedford et al.*, 2013). The black triangles indicate the location of the postseismic continuous GPS stations used in this study. Colour scale shows the evolution of the horizontal pathway at each station. Curvature can clearly be seen at most stations. The inset shows a zoom in of postseismic horizontal deformation pathways for the region enclosed by the gold box.

3.2 Methods

3.2.1 Isolating afterslip signal with a straightness assumption

Curvature in the spatial pathway of the postseismic cGPS motions is due to either a single postseismic process that produces curved motions, or a combination of process with different decay rates and azimuthal tendencies. While slip on the subduction plate interface has been shown on occasions to produce spatially curved predictions in time (e.g. *Radiguet et al.*, 2011), this curvature is associated with a migration of the slip location with time. In the case of spatiotemporal models of megathrust afterslip on the plate interface, slip migration has not been apparent (*Bedford et al.*, 2013; *Shirzaei et al.*, 2014), and these models exhibit a predominantly stationary afterslip pattern that decays with time. Cumulative afterslip on the plate interface has been shown to be linearly related to the cumulative aftershock number (e.g. *Perfettini and Avouac*, 2007; *Lange et al.*, 2014) meaning that an independent indicator of the extent of afterslip migration is the difference between normalized cumulative aftershock decay along-strike of the rupture: Figure 3.2 shows the normalized cumulative aftershock time functions along-strike of the Maule rupture zone for the seismic catalogue of *Hayes et al.* (2013). Here we see that the normalized decay in number of aftershocks along-strike with time is very similar. If the aftershocks and afterslip are temporally related as suggested by *Perfettini and Avouac* (2007) and *Lange et al.* (2014), then the relative magnitudes of the afterslip pattern are likely to be constant with time, giving a non-migrating afterslip pattern.

Proceeding with the assumptions that the afterslip following the Maule megathrust is stationary and decaying, with relative magnitudes of afterslip constant through time, we can attempt to isolate the afterslip signal based on the characteristic cGPS predictions of such an afterslip model. With the commonly used model of afterslip as a dislocation in an elastic half-space (*Okada*, 1985), the cGPS signals of such an afetrslip model have the following characteristics:

(1) - A spatially straight, non-veering, motion as a function of time.

(2) - Identical normalized time functions of cumulative motions at all prediction locations on the surface.

The characteristic of *spatial straightness* in the afterslip surface signal is explained by considering the individual components of cGPS signal. For simplicity, we will consider the horizontal components (East and North), although this explanation would hold for a consideration all three components of the signal. The individual East and North afterslip signals are:

$$E(t) = C_E \log(1 + \delta t/T) \tag{3.1}$$

$$N(t) = C_N \log(1 + \delta t/T) \tag{3.2}$$

where C_E and C_N are impulse responses from the the elastic dislocation Green's functions relating the particular afterslip pattern to the surface motion, and the

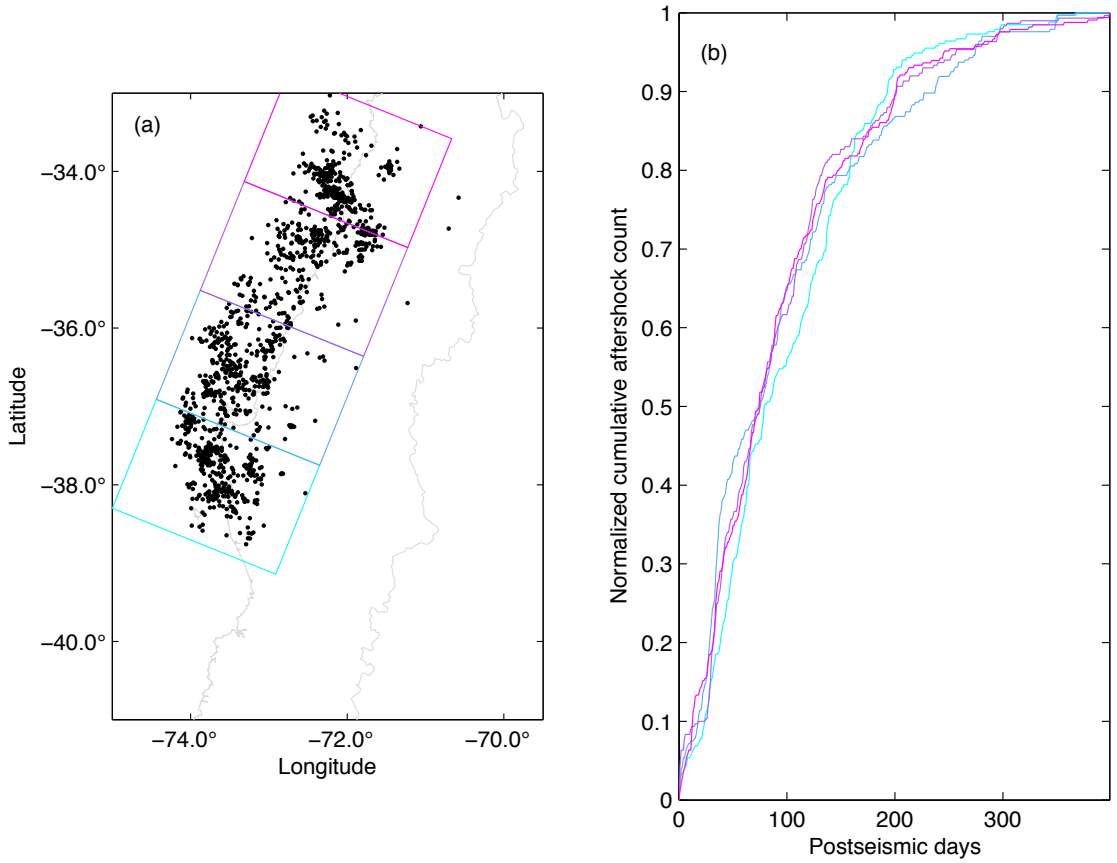

Figure 3.2: Maule plate interface aftershocks are shown in black (*Hayes et al.*, 2013). The coastline and political borders are shown in grey. The zones for the along-strike analysis of cumulative aftershock number are the boxes, with the colours corresponding to the lines plotted in (b). Aftershocks greater than 10 km from the plate interface geometry model (*Tassara and Echaurren*, 2012) have been discarded in this analysis. (b) The normalized cumulative aftershock count for the zones of panel (a).

logarithmic term is a typical function used in long-term plate trajectory models (e.g. *Bevis and Brown*, 2014) that characterizes the postseismic decay. Azimuth of the horizontal motion as a function of time can be found by taking the arc-tangent of equation 3.1 divided by 3.2, giving:

$$\phi_{afterslip} = \arctan\left(\frac{C_E}{C_N}\right) \tag{3.3}$$

where $\phi_{afterslip}$ is the azimuth of surface motion due to afterslip with the discussed assumptions. Afterslip azimuth is clearly independent of time, and therefore produces straight motion in the cGPS, without any veering. From equations 3.1 and 3.2 it follows that the cumulative horizontal motion as a function of time is:

$$H(t) = \left(\sqrt{C_E^2 + C_N^2}\right) \log(1 + \delta t/T) \tag{3.4}$$

Given that the logarithmic term is dependent on the decay of the afterslip pattern, and that C_E and C_N are the impulse response of the stations from the calculations of the Green's functions for that particular afterslip pattern, then we can rewrite equation 3.4 as:

$$H_i(t) = X_i \log(1 + \delta t/T) \tag{3.5}$$

where X_i is a constant multiplier unique to each station. If we normalize $H_i(t)$ for each station by dividing by the final horizontal cumulative displacement, the X_i term at each time step is cancelled out and we are left with the normalized logarithmic time function at each station - the same normalized time function at each station (see figure 3.3). Note that the time function of afterslip decay does not have to take the logarithmic form as written in the above equations: the straightness and identical normalized time functions of the surface signal would also be valid with a linear or power law decay of the afterslip signal.

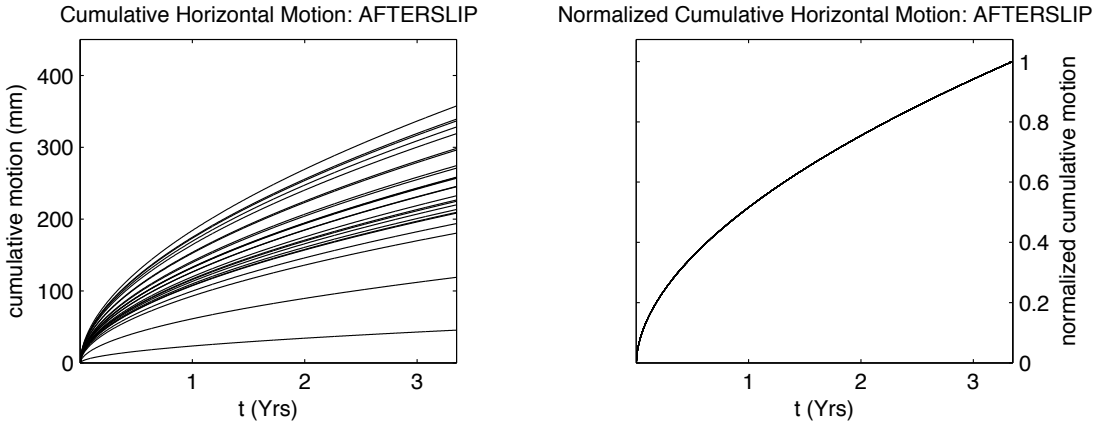

Figure 3.3: Left panel shows the cumulative horizontal displacements as function of time at a cGPS network. Displacements are predicted from a stationary afterslip pattern that decays at the same relative rate along the whole dimensions of the slipping zone. The right panel shows the normalized horizontal displacement time functions of the left panel. Here we demonstrate that all cumulative horizontal displacement histories collapse to the same normalized time function if they are coming from a stationary pattern of decaying slip, where the relative magnitudes of adjacent slip patches are constant.

With our assumptions of afterslip behaviour and the characteristics of the consequential surface signal, we can isolate the afterslip signal by removing simultaneous postseismic processes that cause the horizontal motion to deviate (veer) from a straight course. Figure 3.4 shows schematically the combination of simultaneous postseismic processes (afterslip, re-locking, and viscoelastic relaxation) in producing the measured cGPS signal.

By subtracting viscoelastic relaxation and re-locking (known as backslip in the geodetic modelling community) signals from the measured signal we leave behind the afterslip signal. On this premise we construct a parameter search method to explore the parameter space describing re-locking rate, and mantle viscosities below the elastic limits of the oceanic and continental crusts. The best fitting parameters of re-locking and viscoelastic relaxation produce a signal, that when subtracted from the data, leave behind a straight horizontal motion in the cGPS and similar normalized time functions. The first stage of the parameter search is to ***straighten*** the data by subtracting the viscoelastic relaxation and/or re-locking predictions (see sections 3.2.4 and 3.2.3 for details of the prediction methods and ranges in these parameter spaces). For each combination of re-locking and/or viscoelastic relaxation parameters we subtract the predicted signals from the data (equations 3.6 & 3.7)

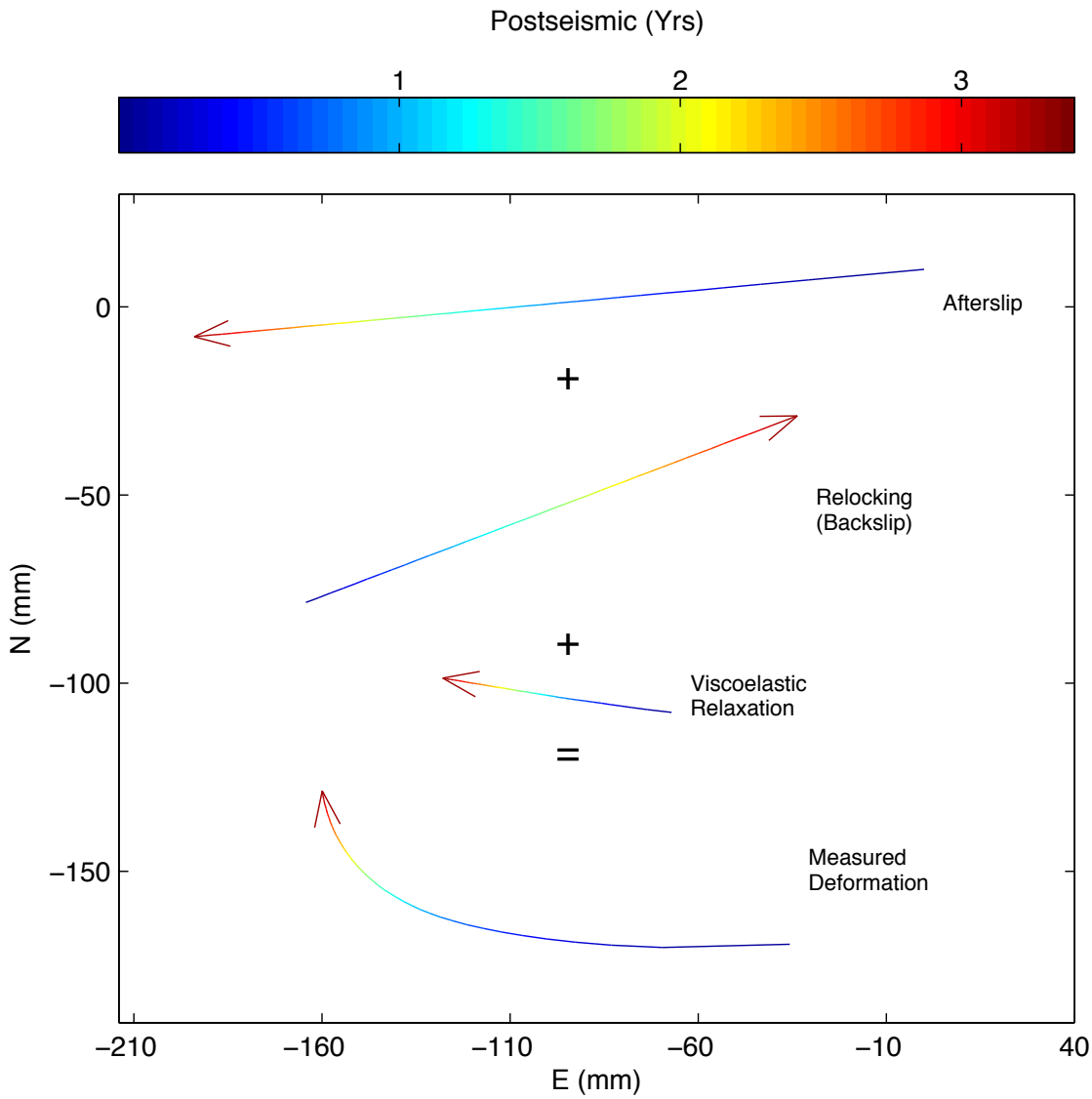

Figure 3.4: A schematic example of the simultaneous surface signals of afterslip, re-locking (backslip) and viscoelastic relaxation which contribute to the measured signal in East-North space. Colours correspond to the elapsed time (shown in the colourbar at the top of the figure).

and fit a linear trend to the remaining signal with a least squares minimization of equation 3.8 to find the gradient, m:

$$A^i_E(t) = D^i_E(t) -_p V^i_E(t) -_p B^i_E(t) \tag{3.6}$$

$$A^i_N(t) = D^i_N(t) -_p V^i_N(t) -_p B^i_N(t) \tag{3.7}$$

$$A^i_E(t)m = A^i_N(t) \tag{3.8}$$

where $D^i_E(t)$, $D^i_N(t)$, $A^i_E(t)$, $A^i_N(t)$, ${}_pV^i_E(t)$, ${}_pV^i_N(t)$, ${}_pB^i_E(t)$, ${}_pB^i_N(t)$ are the east and north components of displacement as a function of time for the measured signal (**D**ata), assumed remaining **A**fterslip, predicted **V**iscoelastic relaxation, and predicted **B**ackslip (re-locking) for each station, i. By multiplying the east component

of the remaining signal, $A^i_E(t)$, by the gradient, m, we can create predictions for the north motion, ${}_pA^i_N(t)$ (equation 3.9) and we can evaluate the fit of the predicted north motion to the actual north motion at all stations, i, by taking the sum of the squared residuals (equation 3.10):

$$ {}_pA^i_N(t) = mA^i_E(t) \tag{3.9} $$

$$ S_m = \sum_{n=1}^{i} \sum_{t=f_i}^{l_i} \sqrt{(A^i_{tN} -_p A^i_{tN})^2} \tag{3.10} $$

where for each station, i, the start and end times f_i and l_i are determined by data availability (gaps in the data between available epochs are not considered in the summation). A straightness misfit S_m is thus calculated for all m model parameter combinations.

Following the straightening, the remaining signals that are assumed to be afterslip ($A^i_E(t)$ and $A^i_N(t)$) are fed into an inversion for cumulative afterslip (see section 3.2.4 for details on inversion). For this step we must have data available for as many stations as possible and for as long an epoch as possible. We choose, therefore, the epoch between 4th April 2010 and 7th August 2013 and take the cumulative displacements from the $A^i_E(t)$ and $A^i_N(t)$ signals as the static displacements for the afterslip inversion. Inverting the cumulative afterslip signals produces a set of cumulative afterslip predictions. To create a time series of afterslip predictions (${}_pA^i_E(t)$ and ${}_pA^i_N(t)$) we multiply the cumulative predictions by the mean of the normalized cumulative horizontal displacement of the isolated afterslip signals (e.g. 3.3). This multiplication assumes that the cumulative isolated afterslip signals can be fit well by an afterslip model and that the isolated afterslip signals have very similar time functions. Isolated afterslip signals that do not adhere to these assumptions result in a poor fit to the time series upon combination of the predicted afterslip signals with the viscoelastic relaxation and re-locking time series predictions:

$$ \chi^2_m = \sum_{n=1}^{i} \sum_{t=f}^{l} \sqrt{(D^i_{tE} -_p A^i_{tE} -_p B^i_{tE} -_p V^i_{tE})^2 + (D^i_{tN} -_p A^i_{tN} -_p B^i_{tN} -_p V^i_{tN})^2} \tag{3.11} $$

where χ^2_m is the measure of misfit for the whole data set for each of the m model parameter combinations of the parameter search, f and l are the first and last days of the time series between the epoch considered for the inversion of the afterslip model.

The results of the parameter search are separated into three ensembles (see Results section 3.3):

1. Afterslip + Viscoelastic Relaxation + Backslip (AS+BS+VR / BS+VR straightening).
2. Afterslip + Viscoelastic Relaxation (AS+VR / VR-only straightening).
3. Afterslip + Backslip (AS+BS / BS-only straightening).

where the process we call *backslip* can be also referred to as *re-locking*.

3.2.2 Data processing

Following the Maule earthquake, a dense network of 67 cGPS stations was deployed and maintained in a multinational effort (e.g. *Vigny et al.*, 2011). In this study we use 44 stations for which to perform the data straightening and 25 stations for the afterslip inversion and final time series misfits evaluation. The unfortunate discarding of some stations is due to the incomplete record at some stations making the time series unsuitable for our modelling efforts in this study. Data for all stations were organized in 24 hour periods. Each observation was processed using the Bernese GPS Software 5.2 (*Dach et al.*, 2007). Precise orbit and earth rotation parameters were used from IGS final products (*Dow et al.*, 2009). During the processing, the antenna phase centre was reduced using absolute calibration, and double differences were modelled in L3, using elevation masks of 10 and a sampling rate of 30 seconds. To form the single differences a phase strategy of maximum observations was used. No a-priori troposphere model was applied. The troposphere parameters were estimated in all steps of parameter estimation. Corrections of the troposphere zenith delay for each station were estimated every 2 hours. We used a Vienna Mapping Function (*Boehm et al.*, 2006), to compute the correction. The elevation-dependent weighting was applied using the function . We stacked the free solutions in a normal equation file for each day. For the datum definition we used the minimum constraint approach, applying the No Net Rotation (NNR) and No Net Translation (NNT) conditions for a group of selected reference stations (see table 3.1). Coordinates for each reference station were obtained from the global polyhedron weekly solution (*Dow et al.*, 2009). Our results are compatible with ITRF2008 (*Altamimi et al.*, 2011). The horizontal cGPS data are corrected for sudden displacements attributed to large aftershocks by means of a step detection algorithm based on a canny filter. Steps were removed by subtraction of the displacement between the consecutive points of the confirmed sudden displacement.

Station name	Latitude(°)	Longitude(°)
SANT	-33.15	-70.67
AREQ	-16.47	-71.49
LPGS	-34.91	-57.93
UNSA	-24.73	-65.41
IQQE	-20.27	-70.13
COPO	-27.38	-70.34
COYQ	-45.51	-71.89
PARC	-53.14	-70.88
RIO2	-53.79	-67.75
FALK	-51.69	-57.87
VBCA	-38.70	-62.27
CHPI	-22.69	-44.99
BRAZ	-15.95	-47.88
UFPR	-25.45	-49.23
ISPA	-27.12	70.66

Table 3.1: Reference stations used in the processing of the Maule postseismic time series.

3.2.3 Modelling Viscoelastic Relaxation

Modelling of surface motions due to viscoelastic relaxation is conducted using the finite element method (FEM). The model neglects the curvature of the Earth's surface and consists of four material blocks: oceanic crust, oceanic mantle, continental crust, and continental mantle (figure 3.5).

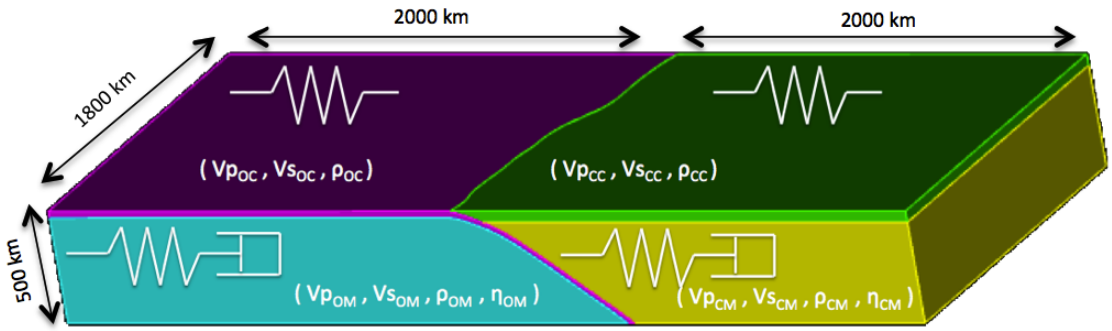

Figure 3.5: The geometry and division of materials for the finite element method (FEM) modelling of postseismic viscoelastic response. We consider an elastic oceanic crust with elastic thicknesses of 30 km (purple) and an elastic continental crust with an elastic thickness of 50 km (green). Below the oceanic and continental crusts we have isotropic linear Maxwell viscoelastic mantle units (continental and oceanic mantles). In each forward model of postseismic viscoelastic response, we assign a different combination of viscosities to the two mantles. List of fixed elastic parameters can be found in Table 3.2

Material Block	Shear Modulus (GPa)	Poisson's Ratio
Continental Crust	40	0.27
Oceanic Crust	46	0.3
Continental Mantle	78	0.25
Oceanic Mantle	78	0.25

Table 3.2: Elastic parameters used in the FEM simulation

The continental crust extends to a uniform Moho depth of 50 km, and the subducting slab has an elastic thickness of 30 km. Both oceanic and continental crusts are assumed to be perfectly elastic bodies (see table 3.2 for list of elastic parameters), whereas the two mantles are assigned linear Maxwell viscoelastic behaviour with the elastic parameters constrained from gravity and tomography studies (*Hicks et al.*, 2012; *Tassara and Echaurren*, 2012). The plate interface is defined by the gravity and seismicity studies (*Tassara and Echaurren*, 2012) and the mesh extends approximately 2000 km both east and west from the trench, and the along strike length of the mesh is 1800 km. The depth of the mesh is 500 km; therefore there is ample distance in all directions from coseismic rupture zone to the bounds of the mesh to avoid boundary artifacts. We employed controlled meshing to mesh the tetrahedral elements more finely at the zone of interest in the vicinity of the rupture, and the mesh size expands towards the volume boundary to save on computational expense. The mesh consists of over 1.2×10^6 elements. The bottom of the mesh is free to slide laterally on its plane, as are the east and west boundaries. The north and south

boundaries are unconstrained. FEM simulation is run using the open source solver PyLith (*Aagaard et al.*, 2013). The coseismic rupture distribution and magnitude is taken from *Bedford et al.* (2013). Combinations of oceanic and continental mantle viscosities are varied for each simulation between 1×10^{19} and 1×10^{20} Pa.S for the continental mantle, and between 1×10^{19} and 2.5×10^{20} Pa.S for the oceanic mantle.

Figure 3.6 shows an example of the predicted time evolution of surface motions due to different combinations of oceanic and continental mantle viscosities. The veering of the horizontal motion can be both in a clockwise and anti-clockwise sense for the isolated viscoelastic relaxation signal.

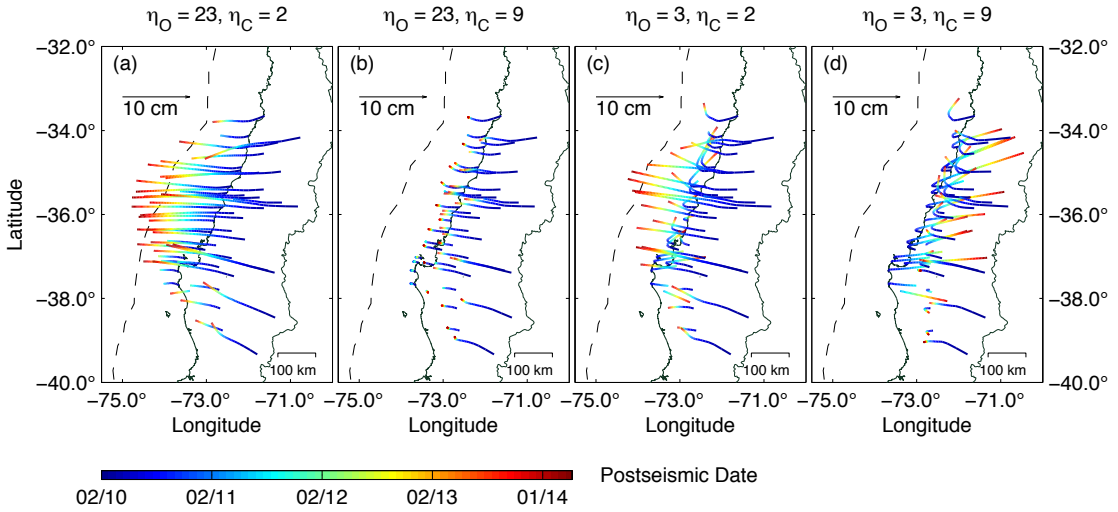

Figure 3.6: Panels a-d show different surface prediction evolutions (colour bar shows corresponding date) for different combinations of oceanic and continental mantle viscosities. Above each panel the viscosities are specified and are multiples of $1\text{x}10^{19} Pa.S$.

3.2.4 Modelling Re-locking

Surface motions due to plate interface re-locking are forward modelled using the backslip assumption, whereby the surface motions due to locking on the plate interface can be modelled from dislocations on the plate interface in the direction of plate convergence. Most of our input time functions correspond to the power law equation:

$$L(t) = at^b \tag{3.12}$$

where L is the fraction of original locking degree as a function of time, t (in days), and a and b are variables of the time function. Other time functions take a flat rate of the form:

$$L(t) = c \tag{3.13}$$

where c is the assumed fraction of locking degree and the locking degree is independent of time. All time functions are listed in a supplementary table in Appendix B.

For each time function of re-locking, L(t), we produce a suite of horizontal surface predictions at the cGPS locations by multiplying the time function with the locking

map of (*Moreno et al.*, 2011) (see fig. 3.1) and predicting the evolution of displacements with the Green's functions relating surface motion due to dislocations in an elastic half-space. The calculation of Green's functions assumed elastic parameters of 0.25 for Poisson's ratio and 35 GPa for shear modulus. These parameters were derived using average values of forearc V_s and density, using seismic tomography and gravity studies of the region (*Hicks et al.*, 2012; *Tassara and Echaurren*, 2012). Backslip direction was assumed to be in line with the azimuth of plate convergence (*DeMets et al.*, 1994) and the plate interface was represented with the same geometry as that used in the construction of the finite element modelling. The horizontal surface displacements calculated predicted with the backslip models produces N-E pointing landwards signals that are are spatially straight since the relative magnitude in the backslip pattern is constant for all time functions (e.g. equations 3.1 - 3.3). The maximum locking rate allowed in the backslip time functions is set as 2× the interseismic rate (*Ruegg et al.*, 2009) which allows for super-interseismic backslip in case of an increase in subduction velocity during the early postseismic - a phenomenon postulated by *Heki and Mitsui* (2013).

3.2.5 Modelling afterslip

The afterslip models are produced by inversion of surface motion for slip on the plate interface. The plate interface geometry used for the inversion is the same as the one used for the previous modelling steps. The forward problem is set out by the following equation:

$$GX = A$$

where G is the matrix of Green's functions relating unit motions on the plate interface to the elastically predicted surface motions at the cGPS stations, X is the vector containing slip magnitude at each patch, and A is the vector containing the surface displacements that we are inverting (the assumed isolated afterslip cumulative displacements). We apply a Laplacian smoothing constraint on the slip distribution (e.g. *Bedford et al.*, 2013) and for consistency this smoothing constraint is kept constant for both the inversion of the curved and straightened data. The azimuth of the horizontal component of the slip vector is constrained to be within 240 to 300° to avoid solutions with spurious slip directions. The Laplacian weighting factor is chosen by means of a subjective trade-off selection between model roughness (*Menke*, 1989a) and misfit of the predicted displacements. The patches of the fault model extend to a maximum depth of 70 km. Displacements used in the inversion are the cumulative time series displacements between 4th April 2010 and 7th August 2013. This time period was chosen to maximise the number of stations with cumulative displacement coverage. Afterslip models for all favoured parameter combinations of the three model ensembles are discussed in section 3.3.4.

3.3 Results

3.3.1 Straightening of Horizontal Motion

Figure 3.7 shows the result of the straightness misfit of the signals following the subtraction of the predicted viscoelastic relaxation and/or backslip signal from the data plotted as normalized straightness misfits. We normalize the straightening mis-

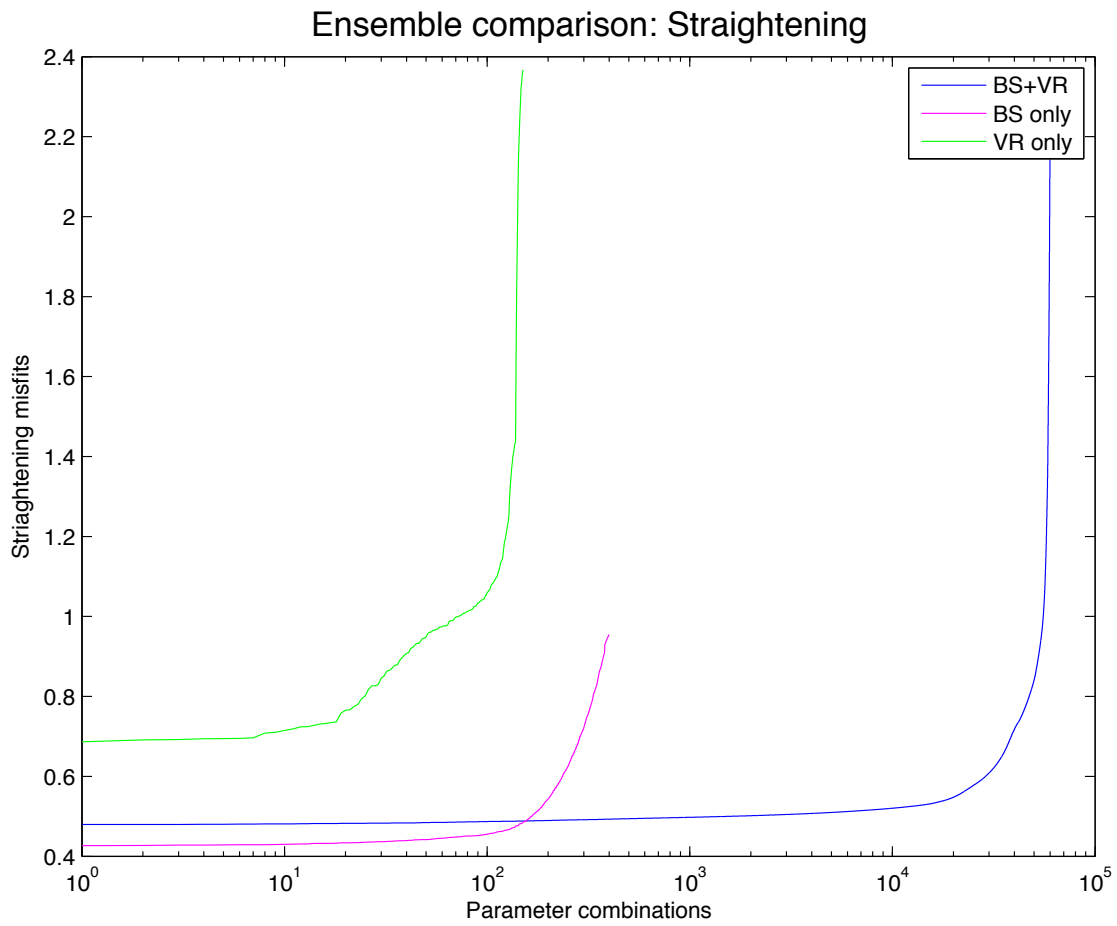

Figure 3.7: Comparison of the straightness for all ensemble types (legend in the top right corresponds to colours of ensemble type). Straightening misfit is the y-axis, where the straightening misfit is normalized by the straightness misfit of the non-straightened data. The x-axis shows the number of parameter combinations considered, and is on a logarithmic scale. The re-locking-only (BS only) straightening ensemble achieves the straightest horizontal motions, closely followed by the re-locking and viscoelastic relaxation (BS + VR) ensemble. The viscoelastic relaxation only (VR only) ensemble performs the most poorly for straightening the horizontal motion. While there are roughly 100 re-locking only models that straighten the motions data with near equal success, there are over 10,000 combinations of re-locking and viscoelastic relaxation parameters that straighten the data with a near equal success.

fit of the corrected signals by dividing by the straightening misfit of the uncorrected signals. The BS-only correction results in the straightest signals, with the best normalized straightness misfit being approximately 0.43. Over 100 of the 400 input time functions of backslip in the BS-only straightening result in a similar success in straightening. For the BS+VR straightening, the best straightened signal has a misfit of 0.48. This model ensemble has up to 10,000 out of 60,000 parameter combinations that straighten the signal to a similar success. The worst performing ensemble for straightening the signal is by VR-only, which has a normalized straightening misfit of 0.69. If we assume the assumptions of the straightness for the afterslip model are valid (section 3.2.1) and that the assumptions of viscoelastic rheology is not too over-simplified, then from figure 3.7 it can be stated that the backslip is the dominant process causing the curvature in the time series. The non-

uniqueness of the straightening performance in each ensemble type strongly depends on the sampling interval of the parameter space; i.e. there are many more locking time functions (600) than viscoelastic relaxation models (150) and therefore the non-uniqueness of the solution space could be decreased considerably by discarding the many of the similar locking time functions.

3.3.2 Time Series Misfits following Afterslip inversion

Figure 3.8 shows the result of the time series fits following the inversion for afterslip and the recombination of the predicted afterslip time series with the backslip and/or viscoelastic relaxation signals. We can clearly see that the ensemble of three processes (AS+BS+VR) produces the best fits to the time series data (see 3.3.5 for more details and examples of the time series). The time series misfit decreases by 22% when the backslip process is considered in addition to the afterslip and viscoelastic relaxation. Interestingly, the neglecting of a viscoelastic response, with just a model of backslip and afterslip (AS+BS), can fit the data slightly better than a model with just afterslip and viscoelastic response There exists some non-uniqueness in the solutions for all ensemble types (see section 3.3.3), although this non-uniqueness is not as pronounced as for the straightening results. This is because there are some combinations of parameters that will straighten the horizontal motions very well, yet the remaining signals will have too much of a variation in their time functions, and/or the remaining signals will not be fit so well with a least squares minimization of the afterslip on the plate interface.

3.3.3 Best fitting parameters

Figure 3.9 shows the best fitting time functions and viscosity combinations for each ensemble of the parameter search. We can see that the best (AS+BS+VR) models have locking time functions that indicate a recovery of interseismic locking rate within one year. Also in the locking time function solution space for this ensemble are super-interseismic locking rates. The parameter space of the parameter search includes super-interseismic rates since this has been postulated by *Heki and Mitsui* (2013) based on the postseismic velocity change of locked segments adjacent to ruptured segments. The non-uniqueness of the solution means that we cannot distinguish between flat-rates and power-law time functions of locking. The best fitting viscosity combinations of the oceanic and continental mantles for the 3 processes (AS+BS+VR) model indicate a more viscous oceanic mantle than continental mantle. The oceanic mantle viscosity is between the ranges of 4×10^{19} and 2.5×10^{20} Pa.S and the continental mantle viscosity is between the ranges of 2×10^{19} and 3×10^{19} Pa.S, therefore the fitting of the time series with the 3 process model is more sensitive to the continental mantle rather than the oceanic mantle viscosity, so long as the oceanic mantle viscosity is greater than 4×10^{19} Pa.S. The range of locking time functions that produce the best time series fits in the two process model of afterslip and re-locking (AS+BS) is similar to the solution space of the 3 process model. The difference being locking rates of the AS+BS model after 1 year of postseismic time tend to be greater than 1.4 the interseismic rate, compared to 1.1 for the 3 processes model. For the model ensemble of viscoelastic relaxation and afterslip (VR+AS) the oceanic mantle viscosity tends to be less than the continental

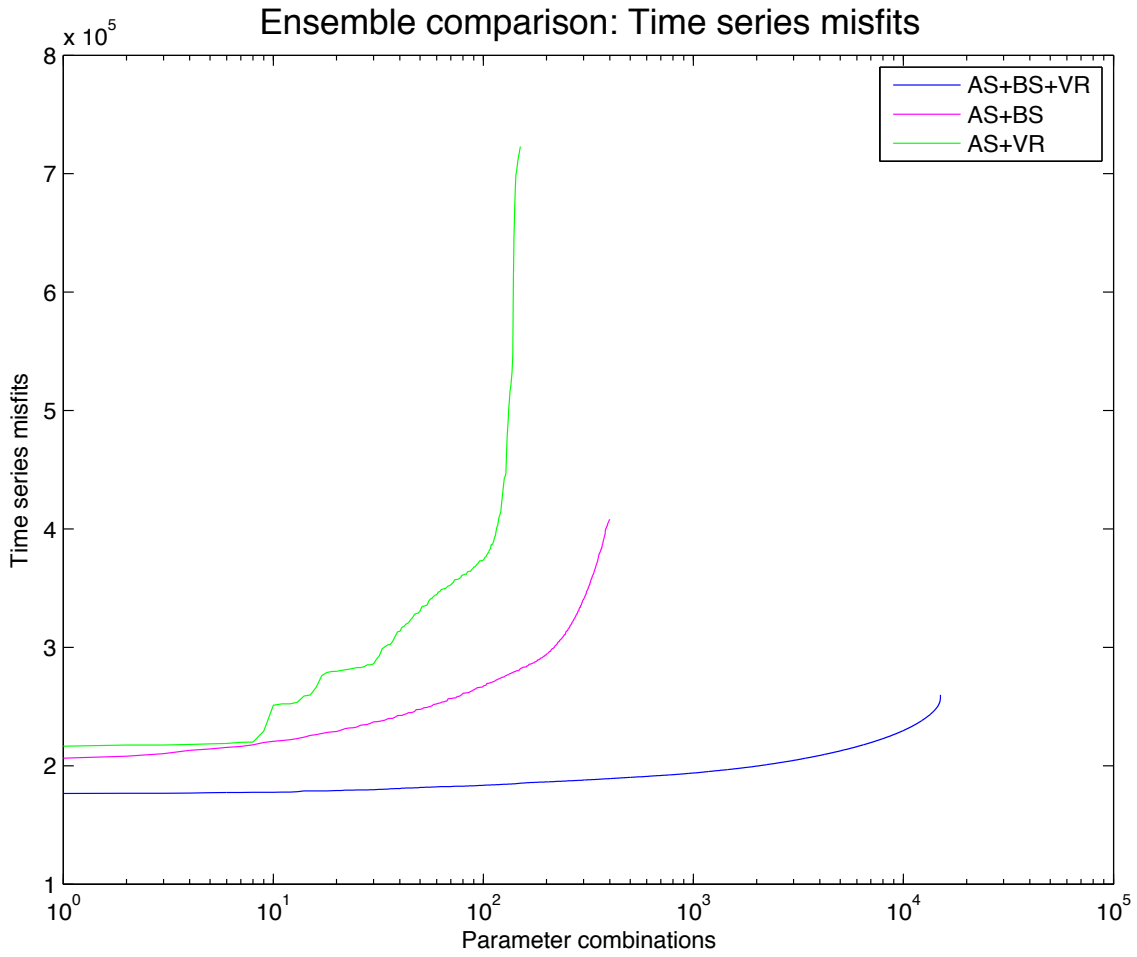

Figure 3.8: Comparison of the total misfit to the time series after the combination of the straightened signals with their respective with afterslip decay signals (y-axis). X axis shows the number of parameter combinations. Ensemble type is indicated by the legend in the top right. The inclusion of re-locking (backslip/BS) in the modelling of postseismic time series significantly increases the fit to the time series. However, there is considerable non-uniqueness in the solution space (see figure 3.9)

mantle viscosity. The oceanic mantle viscosity is 3×10^{19} Pa.S and the continental mantle viscosity is between the ranges of 2×10^{19} and 1×10^{20} Pa.S, therefore the fits of this model ensemble are more sensitive to the viscosity of the oceanic, rather than the continental, mantle.

3.3.4 Comparing afterslip models

As explained in section 3.2.1, the predicted afterslip signals are obtained by inverting the cumulative displacements before recombining with the mean of the normalized time functions of the time series between the start and the end of the epoch of cumulative displacement. A comparison of the assumed cumulative afterslip before and after straightening (before and after the correction for viscoelastic relaxation and/or backslip) is shown in figure 3.10. Here we can see the effects of the corrections on the cumulative signal of the data for each model ensemble. Note that for each ensemble we use the model parameters that result in the best fit to the time

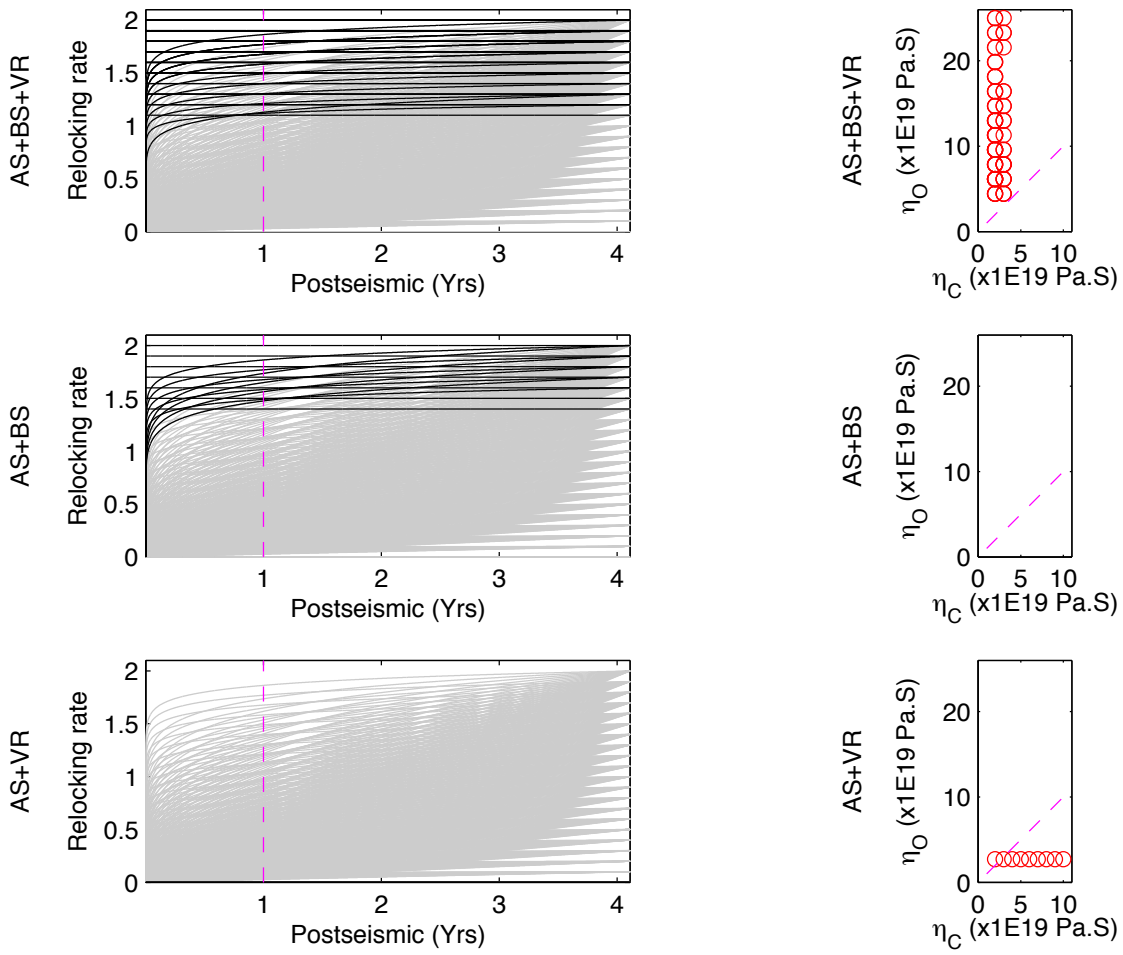

Figure 3.9: The left column shows re-locking rates (in grey are all the re-locking rates in the parameter space, and in black are the best-performing re-locking rates of the parameter search). The right column shows the best-performing combinations of oceanic and continental linear Maxwell viscosities. The top row corresponds to the combined afterslip, re-locking, and viscoelastic relaxation model (AS+BS+VR) and shows the top 30 parameter combinations. The middle row corresponds to the afterslip and re-locking model (AS+BS) and shows the top 10 parameter combinations. The bottom row corresponds to the afterslip and viscoelastic relaxation model (AS+VR) and shows the top 9 parameter combinations. Most re-locking rates indicate a return to interseismic locking degree or higher within one year following the earthquake. Note, the top model parameter combinations in each case are determined by examining the distribution of misfits to the time series. The cut-off choice for the top model combinations tends to be between the minimum and approximately 5% of the misfit range for each ensemble.

series after inversion for afterslip and combination of all predictions. For the model of BS+AS, the straightening from BS-only adds a significant south-westerly displacement at all stations in the network meaning that the cumulative displacement assumed to be afterslip is more consistent with the azimuth of plate convergence. For the three processes model, the straightening affects the cumulative signal as a function of distance to the trench. In the nearfield the displacements are increased in the south-westerly direction. At 70-100 km inland the cumulative displacements are increased in the south direction, and further towards the back-arc the cumulative displacements are shortened in an east-south-easterly correction. The straightening

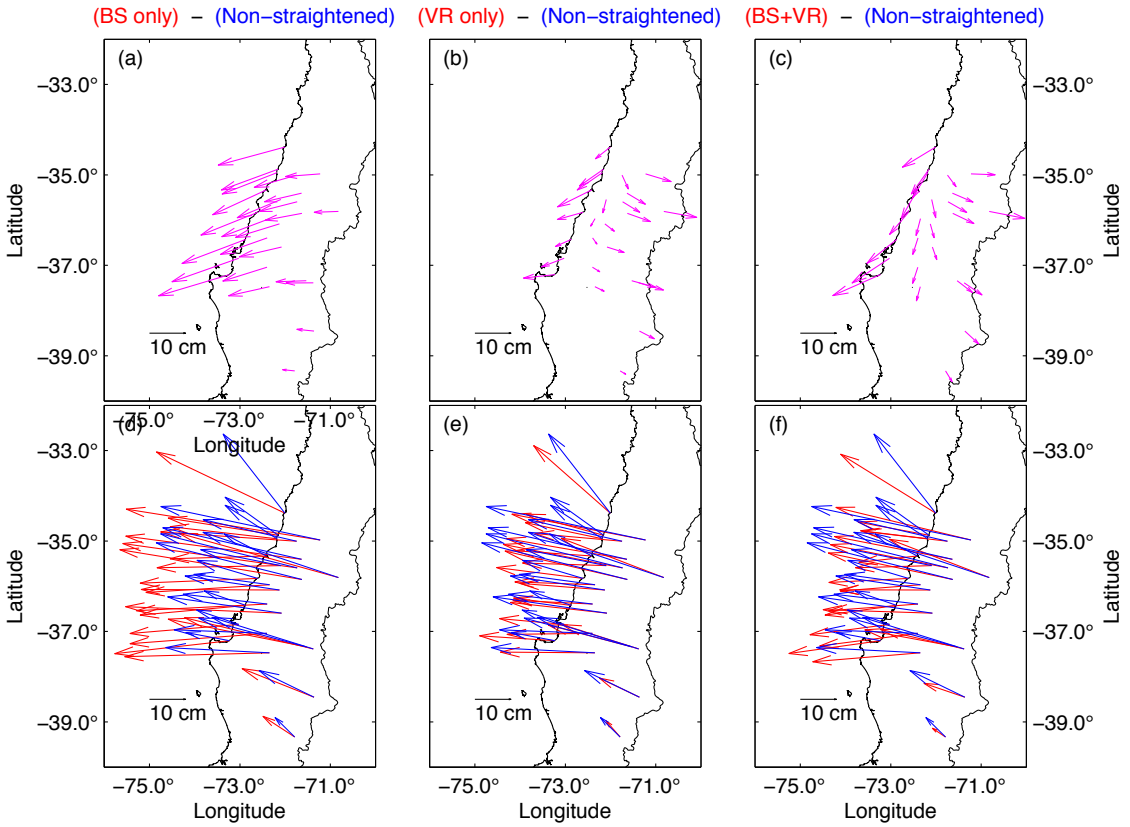

Figure 3.10: Panels **(a)-(c)** on the top row show the differences between the straightened and non-straightened cumulative displacements for each model ensemble. The re-locking and viscosity parameters for each ensemble are chosen from the best fitting time series after inversion for afterslip on the plate interface. Panels **(d)-(f)** on the bottom row show the straightened cumulative displacements (red) in comparison to the non-straightened displacements (blue) for each ensemble type indicated at the top of the column. Straightened displacements seen here can be interpreted as the afterslip signal for each ensemble type. From comparison of **(d)-(f)** we can see that the purely elastic re-locking and afterslip model (AS+BS) needs a much larger afterslip signal than the models that include viscoelastic relaxation. The afterslip signals for the viscoelastic relaxation and afterslip (AS+VR) and the 3 processes (AS+BS+VR) ensembles are very similar in magnitude, but with considerable differences in the azimuth of the cumulative afterslip signal: The afterslip signals for the 3 processes model tend to be rotated more towards the plate convergence azimuth. The differences between afterslip signals of the 3 ensembles are shown in 3.11.

corrections of the AS+VR ensemble (VR-only straightening) are similar to those of the BS+VR straightening, but with slightly less of a southerly magnitude. The differences between straightening corrections and cumulative afterslip signals for the three model ensembles can be seen in figure 3.11. Figure 3.12 shows the results of the inversion of the cumulative afterslip signal for each model ensemble, and also for the data that has not been straightened. As also shown by *Bedford et al.* (2013), an afterslip model for the data that has not been corrected for other postseismic processes results in a large misfit in the back-arc and an unrealistically deep afterslip. All of the correction ensembles (3.12b-d) show a clear improvement in the fit of an afterslip model compared to the non-straightened data, with the AS+BS+VR

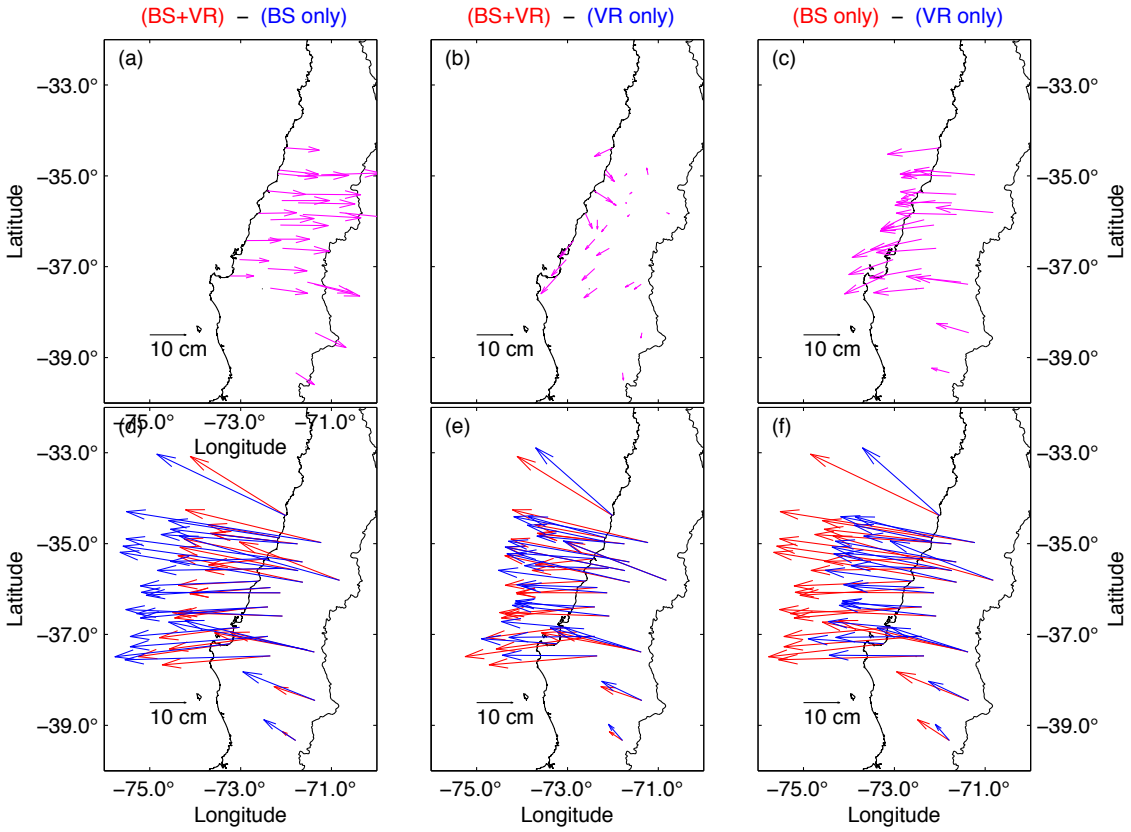

Figure 3.11: Panels **(a)-(c)** on the top row show the differences between the cumulative straightened (afterslip) signals for each combination of the 3 model ensembles. The relocking and viscosity parameters for each ensemble are chosen from the best fitting time series after inversion for afterslip on the plate interface. Panels **(d)-(f)** on the bottom row show the straightened cumulative displacements of each model type (indicated by the colour in the title at the top of each column).

and AS+VR ensembles showing roughly the same 67-68% decrease in misfit, and the AS+BS ensemble having a 55% decrease in misfit. Misfit is slightly larger in the back-arc for the AS+BS ensemble, and the afterslip is of higher magnitude and extends deeper than for the other model ensembles. All of the afterslip models fit poorly the station at 71°W 36°S. Important to note is that these afterslip patterns are not to be interpreted in a mechanical framework of patchwork plate interface frictional heterogeneity since the inclusion of the vertical signal will probably shift the afterslip up-dip as shown in *Bedford et al.* (2013).

3.3.5 Comparing time series fits

Figures 3.13-3.15 show examples of the misfits at cGPS locations at various distances from the coseismic rupture zone. The time series discussed in this section use the model parameters that best fit the time series for that particular model ensemble. From these examples and from the rest of the fits (see animation in Appendix C) we can see that certain ensembles do produce better fits at certain stations, but in general the best fitting ensemble overall is the ensemble of three postseismic processes. For example at the station CONZ (fig. 3.13) the AS+BS+VR and the AS+BS ensemble result in the best time series fits, while at the station ANTC (fig.

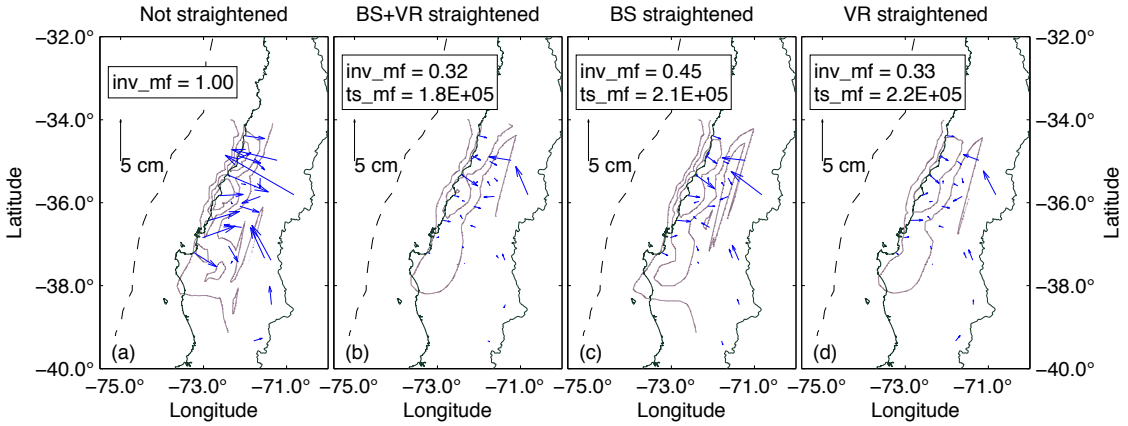

Figure 3.12: Each panel **(a)-(d)** shows the misfit vectors (data minus predictions) following the inversion for afterslip on the plate interface (blue vectors) and the afterslip distribution on the plate interface (contours show 1 m intervals increasing from 1 m). The title of each panel shows the straightening method applied to the data before inversion. The re-locking and viscosity parameters for each ensemble are chosen from the best fitting time series after inversion for afterslip on the plate interface. Inversion misfit (**inv_misf**) and misfit of the time series after recombination of afterslip with the other processes in the model ensemble are (**ts_misf**) are shown in the boxes inset. The inversion misfit is normalized by the misfit of the non-straightened data. The afterslip model from the cumulative displacement is greatly improved after corrections of additional processes (re-locking and/or viscoelastic relaxation), particularly in the back-arc. The inversion misfits for the BS+VR and VR-only straightening are very similar, whereas the BS-only straightening results a slightly larger misfit in the back-arc stations. All straightening ensembles result in a poor fit to easternmost station. The models that neglect viscoelasticity (i.e. panels **(a) and (c)**) tend to have a deeper, higher magnitude afterslip.

3.15), the AS+BS+VR and the AS+VR model ensembles result in the best fits.

3.3.6 Checking assumptions of afterslip model

We revisit our assumptions from section 3.2.1 to check if the time functions of the assumed remaining afterslip signal share a similar normalized time function. Figure 3.16 shows the time functions and their normalized forms for the data before and after straightening for the AS+BS+VR ensemble. The normalized time functions before the straightening corrections are quite dissimilar, and there is a substantially stronger similarity in the normalized time functions following straightening. There are a couple of stations that deviate with their normalized time functions considerably even after straightening. However, the majority of normalized time functions are grouped tightly, and therefore adhere to the expected behaviour of the assumed afterslip model (as discussed in section 3.2.1).

Furthermore, we can compare the normalized afterslip time functions to the normalized cumulative aftershock number. Figure 3.17 shows that decay in time of the seismicity has a similar normalized time function as the isolated afterslip signal. Such an agreement allows us to state that an independent measure of the normalized decay of megathrust afterslip for the Maule earthquake is, to a good approximation, the decay in the number of cumulative aftershocks.

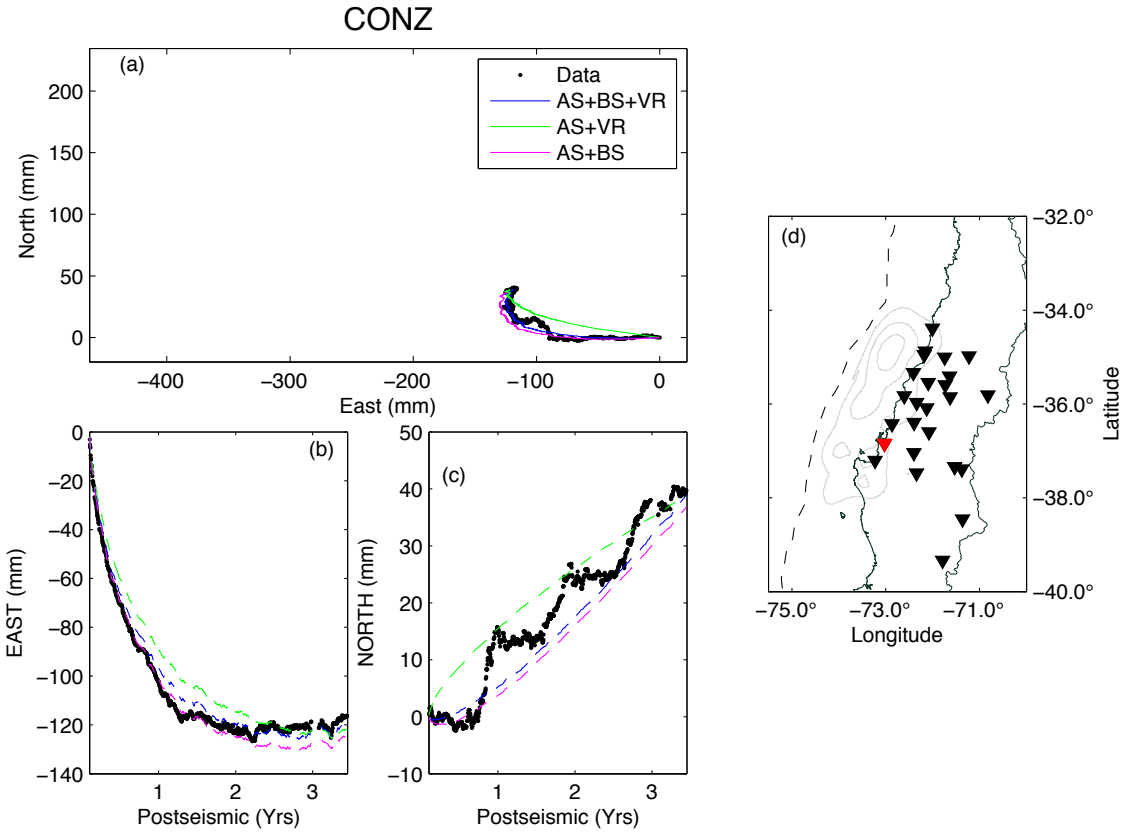

Figure 3.13: Panel **(a)** shows the horizontal displacement pathway of the data and the predictions from the model ensembles (colours denoted in the legend). Panel **(d)** shows the location of the station (red triangle) in the cGPS network (black triangles) and with respect to the coseismic slip distribution (grey contours). Panels **(b)-(c)** show the east and north displacements as a function of time for the data and predictions.

3.3.7 Relative surface signal magnitudes of the simultaneous postseismic processes

Figures 3.18 - 3.20 show the relative magnitudes and time histories of the simultaneous signals that have been separated by the parameter search. Each model is representative of the model parameters that create the best time series misfits after recombination of all processes in the ensemble. The three processes model (fig. 3.18) shows the opposing east and west motions of the backslip and viscoelastic relaxation signals. At the coastline, the imbalance of the magnitudes of these signals leads to a slight increase in cumulative displacement magnitude when the backslip and viscoelastic relaxation signals are removed from the data. Compared to the viscoelastic signal, the magnitude of afterslip is generally much larger, with the difference in relative magnitudes decreasing with distance from the rupture zone. For the AS+VR model ensemble, the isolated afterslip signal is visibly less straight than in the three processes model. The viscoelastic relaxation model creates landwards motion at the coastline, with the hingeline of trenchwards displacement at around 70 - 100 km inland. For the AS+BS model ensemble, the removal of the large backslip signal from the data leaves a cumulative afterslip magnitude that is much larger than for the AS+VR and AS+BS+VR afterslip magnitude.

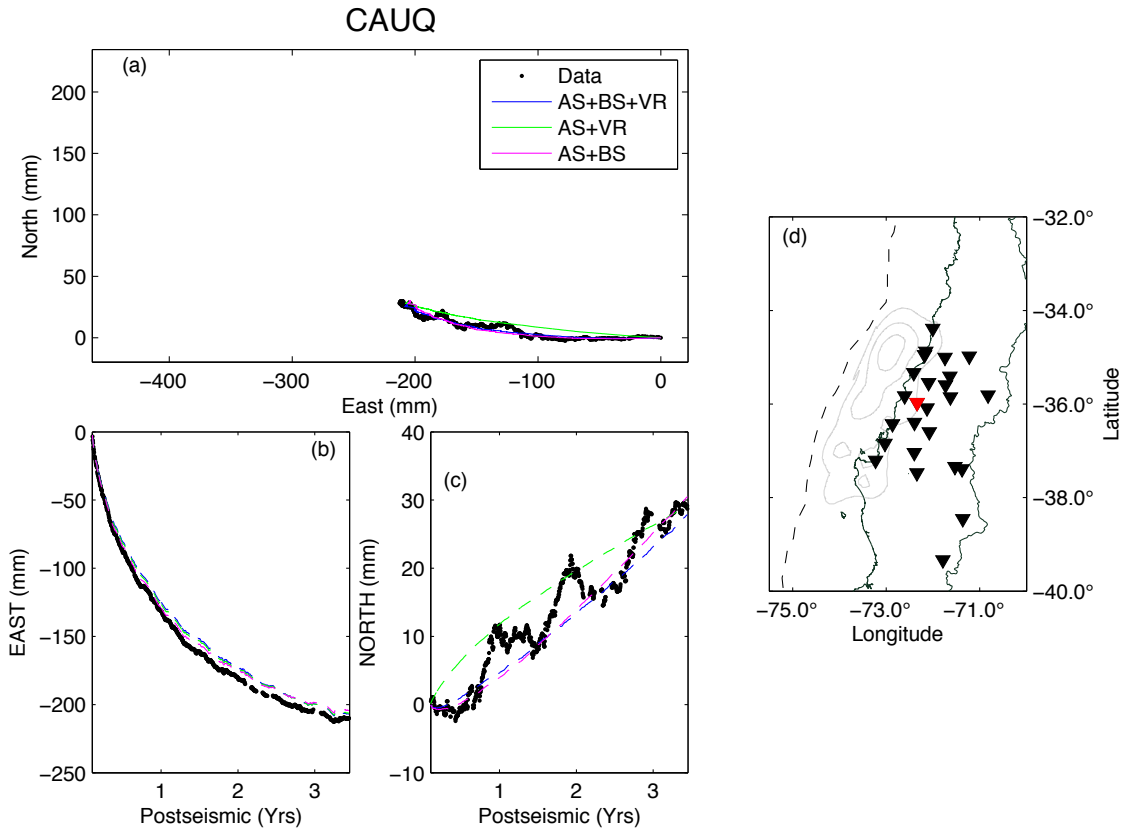

Figure 3.14: Panel **(a)** shows the horizontal displacement pathway of the data and the predictions from the model ensembles (colours denoted in the legend). Panel **(d)** shows the location of the station (red triangle) in the cGPS network (black triangles) and with respect to the coseismic slip distribution (grey contours). Panels **(b)-(c)** show the east and north displacements as a function of time for the data and predictions.

3.4 Discussion and Conclusions

3.4.1 Discussion

The deduction of the best combination of simultaneous postseismic processes depends on the expectations of the sensible ranges of model parameters, the expectation of the features of the isolated signals of each process, and the measures of fit for each model ensemble. The three processes ensemble (AS+BS+VR) results in the best fit to the time series, having a 15% lower misfit value than the minimum of the other two ensembles. The realistic spatial distribution and good fit of the afterslip model, as well as the azimuthal agreement of the cumulative isolated afterslip signal with the plate convergence direction strongly support the credibility of the three processes model. The AS+VR and AS+BS models both result in a significantly larger misfit to the time series, with the AS+BS model having an unrealistic afterslip distribution consisting of high magnitude slip at great depths. The isolated afterslip signal of the best-fitting AS+VR model exhibits the most veering, and the combinations of mantle viscosities are opposite to what would be expected based on the probable pressure-temperature and compositional conditions either side of the downgoing slab (*Billen and Gurnis*, 2001). Additionally, these viscosity combinations do not agree with viscosities obtained in other subduction zone

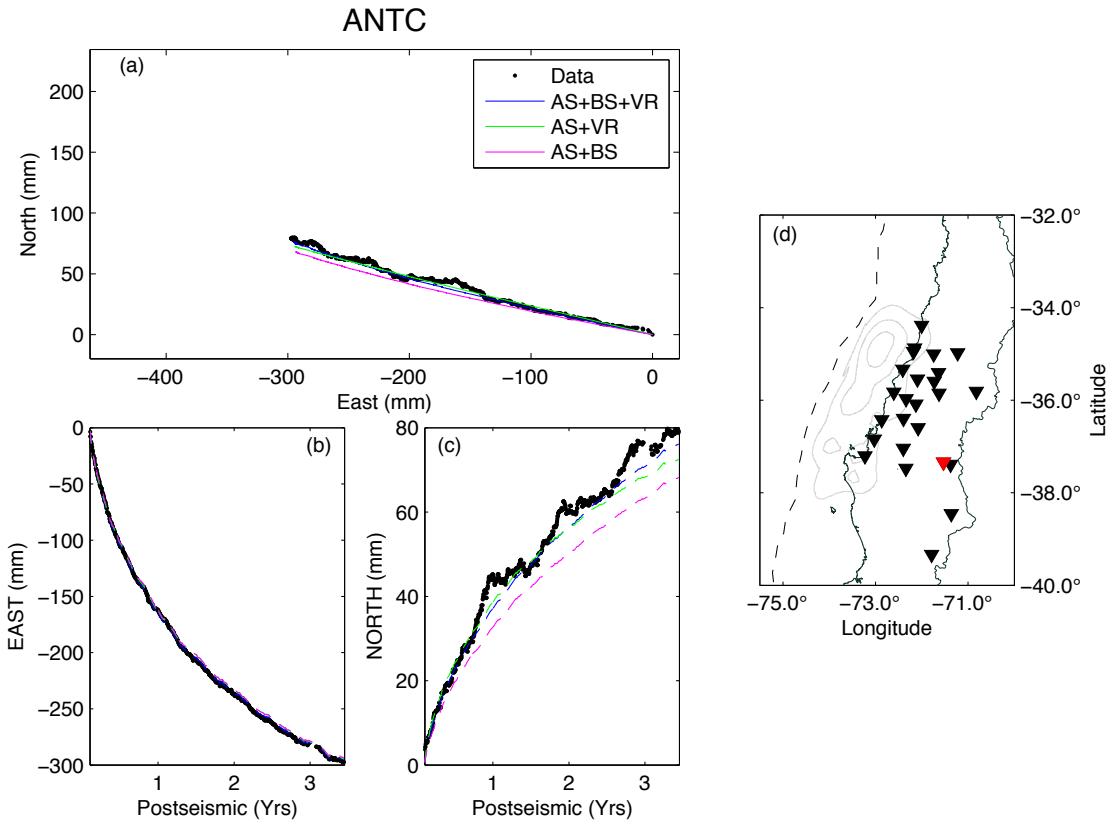

Figure 3.15: Panel **(a)** shows the horizontal displacement pathway of the data and the predictions from the model ensembles (colours denoted in the legend). Panel **(d)** shows the location of the station (red triangle) in the cGPS network (black triangles) and with respect to the coseismic slip distribution (grey contours). Panels **(b)-(c)** show the east and north displacements as a function of time for the data and predictions.

postseismic viscoelastic studies (e.g. *Hu and Wang*, 2012). Therefore our favoured model ensemble is the three processes model.

This study provides the first estimates of plate re-locking rate following a megathrust subduction event, and as such has some important implications for the future of seismic cycle research in similar margins. The rapid re-locking time (< 1 year) with respect to the interseismic period means that the current assumption in slip-deficit modelling - that the re-locking is instantaneous - is a valid one. By monitoring seismic velocity recovery in strike slip faults, *Li et al.* (2006) suggested that gradual strength recovery occurred in the years following the 2004 Parkfield earthquake. Experimental studies exploring recovery at stresses and temperatures relevant to plate interface faulting have shown that slide-hold tests indicate rapid recovery within minutes at the experimental scale (*Tenthorey et al.*, 2003) with a slowing rate following rapid initial healing due to mechanisms such as crack closure and solution processes (*Yao et al.*, 2013). These initially rapid and subsequently decaying rates are supported by our results suggesting that geodetic observations are appropriate for constraining postseismic strength recovery.

The rate of backslip for the best AS+BS+VR parameter combinations can (but not in all solutions) exceed the interseismic rate. From the continued monitoring of this backslip rate we hope to determine the mechanism for such an acceleration, such as the relaxation of a thin low viscosity layer beneath the slab (*Naif et al.*, 2013;

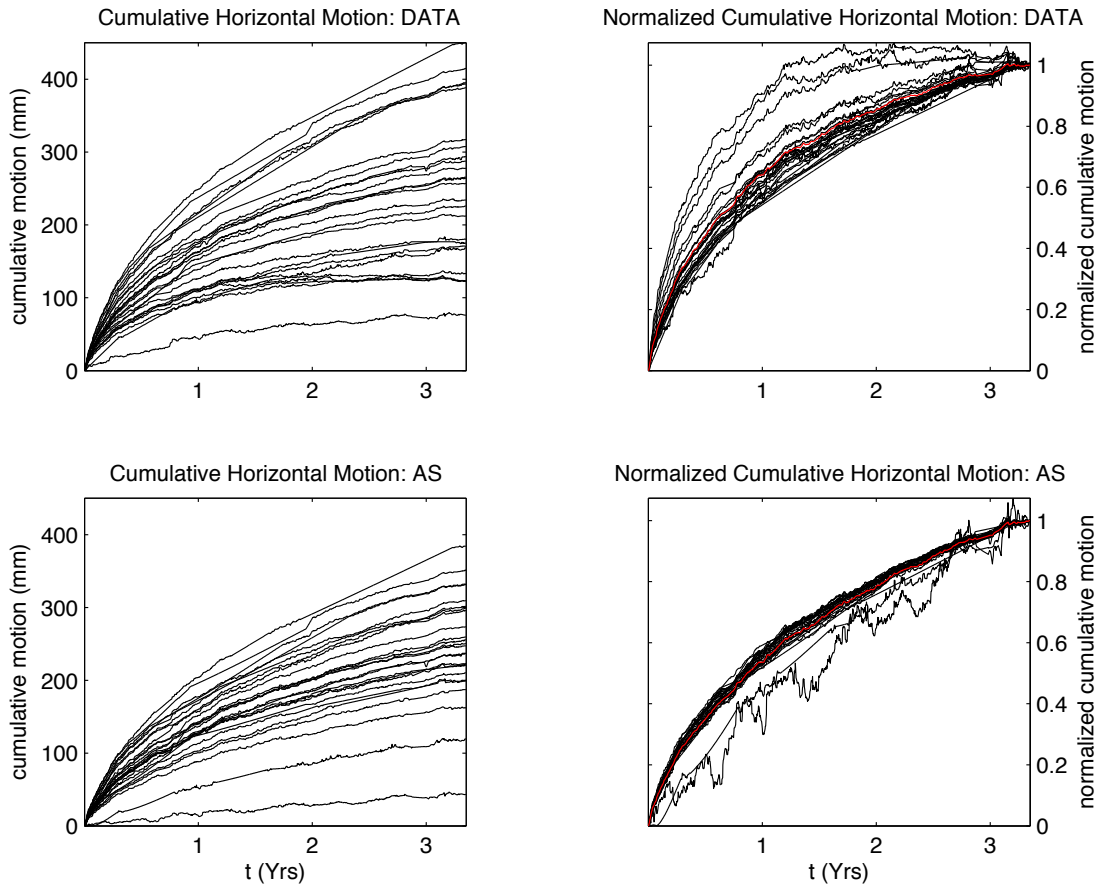

Figure 3.16: Left column shows the cumulative horizontal displacements as function of time and the right column shows the normalized cumulative horizontal displacement time functions, with the mean of the time functions plotted in red. The top row shows the data time functions before and after normalization. The bottom row shows the remaining afterslip signals following the straightening of the data with the re-locking and viscoelastic relaxation (parameters of re-locking and viscosities are taken from the model with the best fitting time series following afterslip inversion). The normalized time functions of the straightened (afterslip) signals are much more tightly packed around the mean (red) than in the case of the non-straightened data, with the exception of a couple of stations.

Heki and Mitsui, 2013). Continuing to monitor the Maule postseismic segment will allow the possibility to track the backslip rate with time, and could constrain the relaxation time parameters of any viscous process that could be facilitating a super-interseismic subduction velocity. However, the consideration of a low viscosity layer under the slab would require a re-designing of the parameter search, such that the sensitivity of the results so that the impact of such a viscoelastic layer under the slab on the total viscoelastic relaxation signal can be fully understood.

There is some discord between the Maule near-field observations and the near-field 2011 Japanese Tohoku-Oki Mw 9.0 observations. Following Tohoku-Oki, the landward motion well exceeds the background interseismic rate (*Sun et al.*, 2014) suggesting that another process, other than or in addition to plate interface re-locking, is producing such displacements in the near-field. One possible explanation is that the offshore GPS stations monitoring the postseismic deformation of Tohoku-Oki are moving in response to a postseismic crustal fault afterslip following

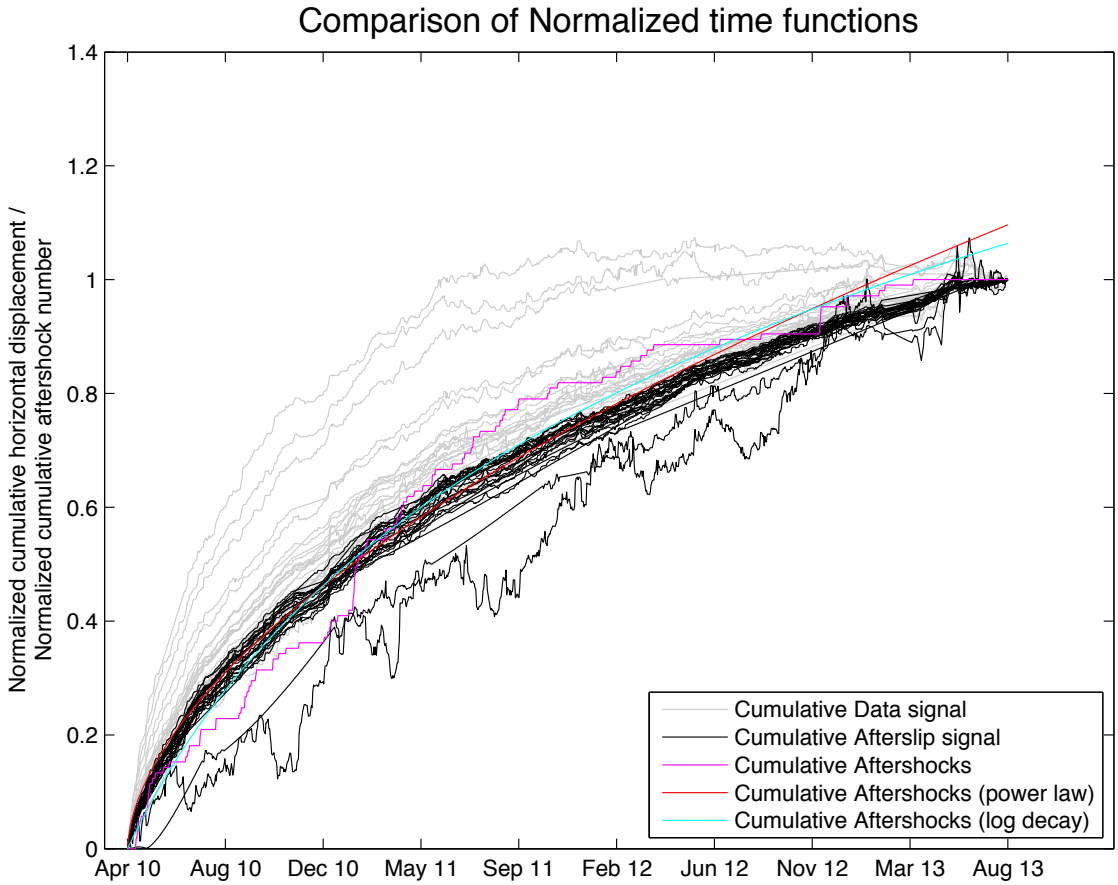

Figure 3.17: Comparison of the normalized time functions for cumulative aftershock number (events with Mw > 5 taken from the IRIS catalogue www.ds.iris.edu) shown by the pink line. Red line shows the power law fit to the pink decay. Normalized time functions of cumulative horizontal motion due to afterslip (straightened data) are shown by the black lines. The normalized time functions of the non-straightened data are shown in grey. The time functions of cumulative aftershock number and cumulative afterslip are strikingly similar, in agreement with the observations of *Perfettini and Avouac* (2007) and *Lange et al.* (2014).

the activation of crustal faults during coseismic rupture (*McKenzie and Jackson*, 2012; *Tsuji et al.*, 2011). The magnitude and pattern of viscoelastic response depends on the magnitude and location of coseismic slip as well as the viscosities and rheologies (*Sun and Wang*, 2015). In this sense it is conceivable that such a relocking signal as seen for Maule 2010 event may not be so distinguishable in the data for a larger earthquake such as Tohoku Oki. Furthermore, we recognize that the ongoing efforts to instrument and more frequently measure the submerged surface of the overriding plate will allow a better discrimination between dislocation and viscoelastic relaxation as a cause for curved postseismic motions (*Bürgmann and Chadwell*, 2014).

The separation of the afterslip signal from the other postseismic processes by deducing and removing the veering effect of the simultaneous processes is obviously better constrained by a longer time series. Following a megathrust earthquake, the large aftershocks that can follow can be potentially as destructive as the larger magnitude mainshock, depending on the location, building standards, and regional

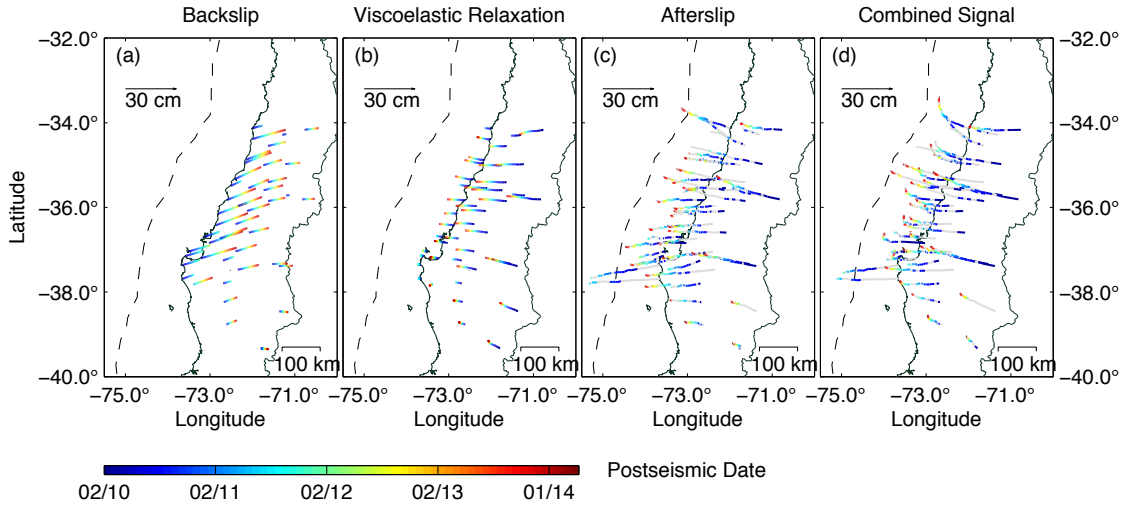

Figure 3.18: Separation of the relative magnitudes of postseismic processes for best fitting time series model in the ensemble of afterslip, re-locking, and viscoelastic relaxation (AS+BS+VR). Panels **(a)-(b)** show the contribution of backslip and viscoelastic relaxation processes from the optimal model that uses BS+VR straightening. Panel **(c)** shows the remaining signal after straightening of the data, and this signal can be considered as mainly afterslip. Panel **(d)** shows the original data before decomposition into the three processes **(a-c)**. Colours of horizontal deformation pathways in each panel correspond to the time evolution in the colourbar. The deformation pathways in panel **(c)** are clearly much straighter that in panel **(d)**. Furthermore, the nearfield stations after straightening have an increased tendency to move towards the plate convergence azimuth, rather than to the **W-N-W** as in the non-straightened dataset. This rotation of azimuth in the straightened data further suggests that the straightened data is the afterslip signal, since these azimuths are reasonable for afterslip opposite to the general direction of plate-convergence.

geology of the nearest human populations. In terms of a short term hazard assessment, the slip-deficit can be compared with the afterslipping regions on the plate interface: regions with both a high remaining slip-deficit and low afterslip are naturally the zones of highest immediate likelihood of harbouring a large aftershock. Future studies must focus on the effects of non-afterslip signal removal on our modelled afterslip: in other words, we should investigate whether or not neglecting non-afterslip processes significantly alters the afterslip model thereby producing assessment of zones that are at most risk of a high magnitude aftershock on the plate interface. An example of the ability to identify regions at high risk of large magnitude plate interface aftershocks with the afterslip model would be the subsequent rupture of the March 25th Constitución 2012 Mw 7.0 aftershock on the plate interface (*Ruiz et al.*, 2013) inside the along strike rupture extents of the Maule 2010 Mw 8.8. This aftershock, occuring over two years after the mainshock, occured in the pocket of low afterslip (fig. 3.21) that had been identified by a model that assumed afterslip as the sole postseismic process contributing to the surface signal (*Bedford et al.*, 2013). This zone was at a similar depth to adjacent after-slipping zones and aftershock releasing zones and so could be considered as within the seismogenic depth limits. With the basic assumption that all but the highly slipping coseismic zones have the potential to harbour some significant slip-deficit, then this zone of low afterslip and relatively low coseismic slip could have been considered

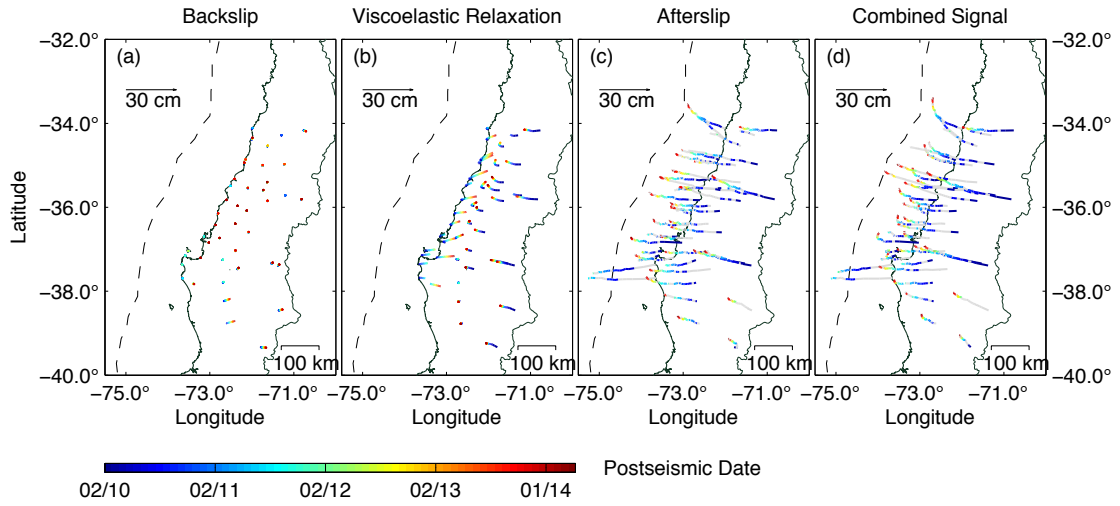

Figure 3.19: Separation of the relative magnitudes of postseismic processes for the best fitting time series model in the ensemble of afterslip and viscoelastic relaxation (AS+VR). Layout is as in the previous figure. The coastline viscoelastic response is landwards with the hinge-line lying around approximately 50-100 km inland. The remaining straightened signal (afterslip) following the removal of viscoelastic relaxation points generally to the **W-N-W** and is notably more curved than the afterslip signal following the removal of both re-locking and viscoelastic relaxation (also see fig.3.7), 3.18.

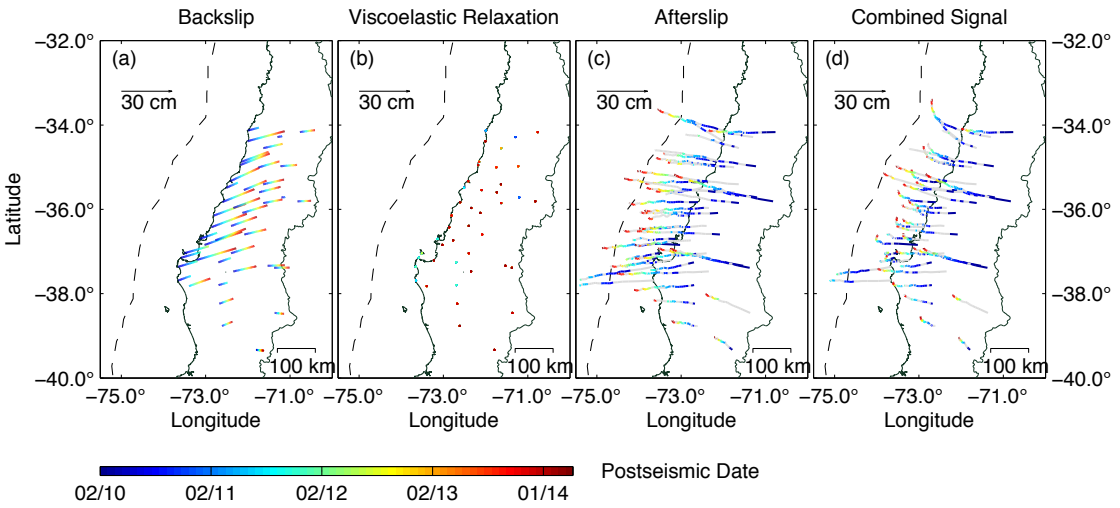

Figure 3.20: Separation of the relative magnitudes of postseismic processes for best fitting time series model in the ensemble of afterslip and re-locking (AS+BS). Layout is as in the previous figure. Cumulative afterslip (straightened signal) magnitudes are greatly increase in comparison to the other model ensembles.

to have a high seismic potential. Furthermore, the afterslip model is based on the first year of surface deformation, meaning that with quick enough data retrieval and modelling, this region could have been highlighted as especially prone to a large aftershock in advance of it's occurrence. In this case, it seems the contaminating presence of viscoelastic relaxation and backslip in the postseismic surface signal did not significantly affect the ability to model the heterogeneity in the plate interface postseismic kinematics.

The ability to separate the simultaneous postseismic processes in the case study of Maule 2010 is due to the convenient spread of cGPS locations with respect to the ruptured interface. The magnitude of the veering is larger at stations nearer to the coseismic rupture, and a longer range of distances to the rupture zone makes it easier to distinguish between backslip related veering and viscoelastic relaxation related veering.

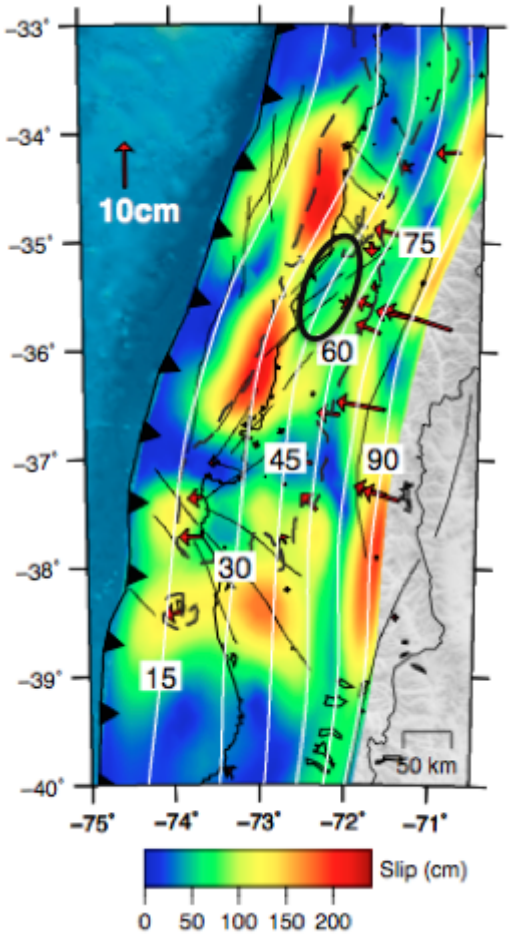

Figure 3.21: Afterslip map between March 2010 and April 2011 taken from (*Bedford et al.*, 2013) with the addition of a black ring showing the rupture location of the future March 2012 Mw 7.0 aftershock (*Ruiz et al.*, 2013). Vectors shown the afterslip misfit in the horizontal component. Note that the afterslip model puts slip further up-dip than the models in this study, because the modelling of *Bedford et al.* (2013) has included the vertical component of the postseismic signal.

3.4.2 Conclusions

- We have presented a novel approach for separating the relative contributions of simultaneous postseismic processes, and have explored the parameter space for different combinations (ensembles) of these processes.
- Following the well founded assumption that decaying afterslip distribution has a constant relative magnitude, backslip is the dominant process responsible for the postseismic veering of the cGPS.

- Rapid re-locking rates of our favoured models are consistent with healing rates that have been shown in lab experimental results and inferred from postseismic seismic velocity observations of strike-slip faults.

- Inclusion of backslip (re-locking and possible super-interseismic subduction velocity) along with viscoelastic relaxation results in approximately 15% decrease in the fit to the time series.

- Isolation of afterslip from straightening method and subsequent fitting of time series leaves behind a time function of afterslip that is in better agreement with the time function of cumulative aftershock number.

- Afterslip distribution is far more realistic (i.e. less deep afterslip needed to fit the data) and produces a much improved data fit when considering viscoelastic relaxation in addition to the afterslip.

- Afterslip is dominant in the near-field signal in comparison to the viscoelastic relaxation. The credibility of a purely elastic afterslip model is, to a first order, acceptable and useful for immediate hazard monitoring. However, for this situation one needs to have a cGPS network with near enough station distances to the rupture zone.

Chapter 4

Investigating the final seismic swarm before the Iquique-Pisagua 2014 Mw 8.1 by comparison of continuous GPS and seismic foreshock data.

Note

This chapter is a reformatted version of the published Geophysical Research Letters paper (*Bedford et al.*, 2015) with the same title as this chapter. Additional supplementary material has been placed in the appendix of this thesis.

Abstract

Pre-existing networks of seismometers and continuous GPS in Northern Chile successfully captured surface motions and seismicity leading up to the April 1st Mw 8.1. Here, we compare cGPS with predictions of seismic dislocations for the final foreshock swarm, beginning with the March 16th Mw 6.7. Results show that the cumulative cGPS motion can be largely explained by seismic slip because evolutions of cGPS positions for most stations stay within the ranges of seismic predictions (given sensible ranges of assumed source errors). However, cGPS motions between 18th-21st and 25th-31st March outpace seismic predictions, supporting the existence of aseismic transients that were most probably the afterslip from preceding bursts of seismicity. A parameter search reveals that the March 16th Mw 6.7 cGPS displacements can be recreated with a fault plane significantly rotated anticlockwise from the strike of the plate interface, suggesting that failure was on a structure other than the plate interface.

4.1 Introduction

The Mw 8.1 Iquique-Pisagua earthquake of April 1st 2014 was exceptionally well monitored by the Integrated Plate Boundary Observatory Chile (IPOC: www.ipoc-

network.org) with various geophysical instrumentations already in place due to the expected failure of a mature seismic gap on the Andean subduction margin (*Comte and Pardo*, 1991; *Chlieh et al.*, 2011). This earthquake ruptured only a small portion of this seismic gap leaving a remaining slip-deficit to potentially harbour an earthquake of Mw > 8.9 (*Schurr et al.*, 2014). Of particular interest to the community researching this margin is the occurrence of foreshock clusters in the year leading up to the mainshock, with the ultimate and most active cluster lasting from March 16th (when it was initiated by a Mw 6.7) until the onset of the mainshock (Figure 4.1). This final foreshock cluster was accompanied by a transient continental surface

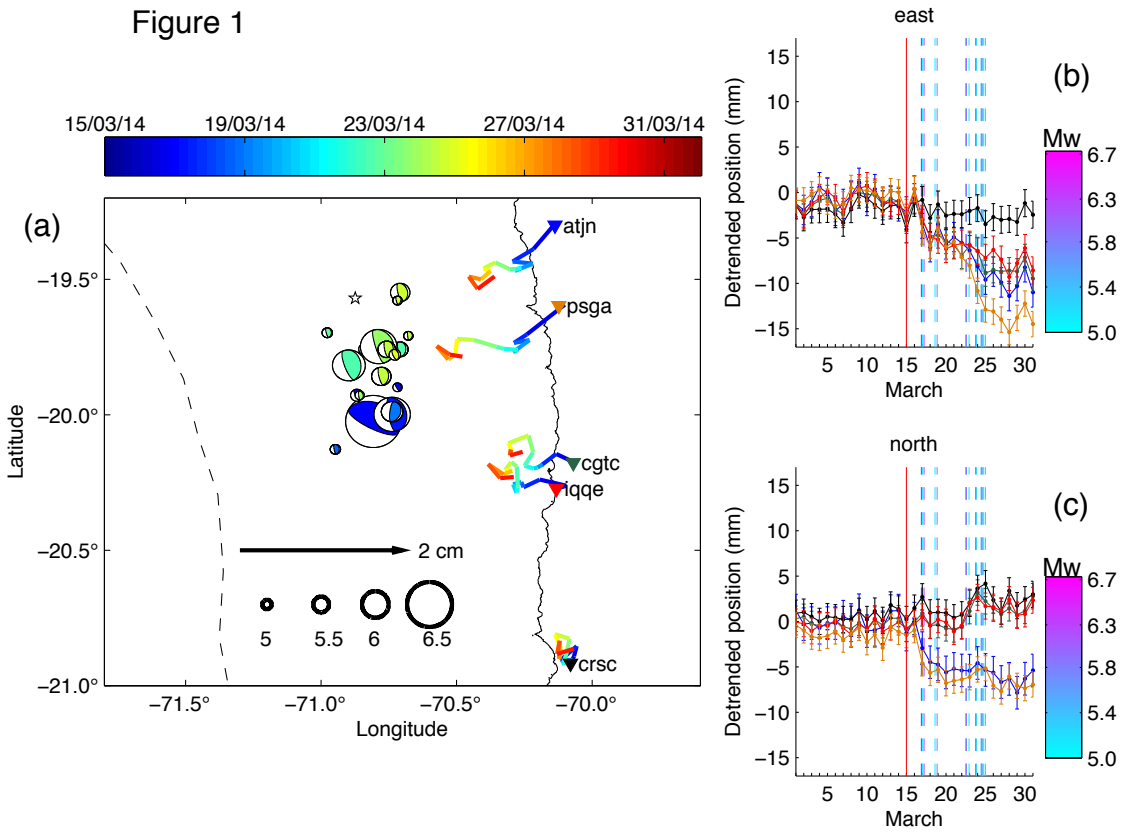

Figure 4.1: **(a)** Map view of the subduction zone. Dashed black line represents the subduction trench and solid black line is the coastline of Chile. Small white star is the location of the April 1st 2014 Mw 8.1 epicentre. Focal mechanisms (geofon.gfz-potsdam.de) shown are for the foreshock sequence beginning on March 16th and are chronologically colour coded, corresponding to the colour bar above. Size of plotted focal mechanisms corresponds to the magnitudes shown by the radii of the black circles and these sizes correspond to the extents of the event if it were to fail in a circular pattern. Stations of interest in the analyses of seismic motion are shown on the plot as coloured triangles. The colours of these triangles correspond to the colours shown on panels (b) and (c). The coloured lines originating from the station locations represent the time evolutions of transient motion (available for download in supplementary information) and are colour coded in the same way as the focal mechanisms. **(b)** Plot of the March 2014 eastwards deformation at the cGPS locations shown on panel (a). Colours correspond to the colours of the triangular station markers on panel (a). **(c)** Same as panel (b) but for the north component. Data shown (b) and (c) has been de-trended and common mode filtered.

deformation recorded on land by the IPOC continuous GPS (cGPS) network (*Schurr*

et al., 2014; *Ruiz et al.*, 2014). Hence, the spatial-temporal pattern of seismicity and deformation leading up to the Iquique-Pisagua earthquake is of particular interest regarding precursory activity and may provide insights for improving earthquake hazard assessment based on future margin activity.

There currently exists some discord as to whether the transient deformation recorded by the continuous GPS (cGPS) can be explained by seismic or aseismic slip of the plate interface. Some studies have suggested slow-slip as a significant tectonic process during the final foreshock cluster, with evidence presented from either cGPS records (*Ruiz et al.*, 2014) or the recognition of repeating earthquakes (*Kato and Nakagawa*, 2014; *Meng et al.*, 2015). By contrast, the cumulative preseismic GPS displacements have been reproduced with predicted earthquake slip based on location, mechanism and magnitude from scaling relations (*Schurr et al.*, 2014); in this case the centroid of slip for each event was assumed to be at the hypocentre (from the catalogue produced by GEOFON (geofon.gfz-potsdam.de), and the failure directions of all events were assumed to be opposite to the azimuth of plate convergence, the latter obviously not always being true. Particularly as the largest foreshock (Mw 6.7) apparently was not on the plate interface (*Schurr et al.*, 2014; *Hayes et al.*, 2014) but was modeled as such by *Schurr et al.* (2014) when predicting its deformation. The Mw 6.7 foreshock is suspected to have occurred in the upper plate, due to the peculiar rotation of the shallowest nodal plane of the focal mechanism with respect to the slab geometry (*Hayes et al.*, 2014), although there is some variability in the moment tensor solutions (Table 4.1) leading to some uncertainties in the most likely location and tectonics of this event.

The primary aim of this study is to contribute to the discussion concerning competing hypotheses of aseismic and seismic failure during the final 16 days leading to the earthquake. This will be achieved by producing a range of time-dependent predicted positions for the cGPS by considering the errors in the seismic catalogue. This approach allows for the respective evolutions of actual and predicted positions to be compared while also considering the errors in both data and prediction domains. To investigate the seismic efficiency of the slip leading up to the Iquique-Pisagua earthquake, we will analyze the evolution of the surface deformation predictions at the cGPS locations modelled from the dislocations of the foreshock events. We focus on the progression of 16 days before the mainshock. For each event in the foreshock catalogue we consider a sensible range of errors in the focal mechanisms and hypocentral locations to produce **P**robability **D**ensity **F**unctions (PDF) of predicted displacement at each cGPS location. These PDFs are transformed into the temporal format of the daily cGPS data so that the transient behaviour of data and predictions can be compared on a daily basis. Additionally, the methodology for predicting seismic displacements is reversed to conduct a parameter search for the Mw 6.7 foreshock of March 16th with the aim of constraining the focal mechanism of this event. Finally we interpret the results in the framework of the known plate kinematics that have been monitored at this segment.

4.2 Methods

4.2.1 Modelling seismic predictions

We model surface predictions of deformation using analytical solutions for dislocations in an elastic half-space (*Okada*, 1985), with the elastic parameters $G = 3.5E9$ Pa and $Poisson's ratio = 0.25$ deduced from seismic tomography and gravity studies (*Husen et al.*, 2000; *Tassara and Echaurren*, 2012). For all events considered by our forward modelling we set the length and width of each rectangular source according to the scaling relations between seismic magnitude and source dimensions in subduction zones (*Strasser et al.*, 2010). The parameters varied for each event are the hypocentral location (x, y, z), strike, dip, slip azimuth, and magnitude of uniform slip. The strike, dip, and slip azimuth for each event are taken from focal mechanisms (geofon.gfz-potsdam.de). Slip azimuth comes from the horizontal component of the slip vector given by equations 4.1-4.3 (*Aki and Richards*, 2002) applied to the strike, dip, and rake of the focal plane:

$$north = \cos(rake)\cos(strike) + \cos(dip)\sin(rake)\sin(strike) \tag{4.1}$$

$$east = \cos(rake)\sin(strike) - \cos(dip)\sin(rake)\cos(strike) \tag{4.2}$$

$$z = -\sin(rake)\sin(dip) \tag{4.3}$$

The uniform slip magnitude for each event satisfies the equation from *Brune* (1968):

$$M_0 = \mu AD \tag{4.4}$$

where M_0 is the known seismic moment, μ is shear modulus of the elastic medium in the vicinity of the slipping region, A is the assumed area of the source region (already defined by seismic scaling relations), and D is the uniform slip magnitude. Since there is some uncertainty of the shear modulus value and its heterogeneity at the plate interface we calculate a probability distribution of μ using randomly selected combinations of parameters from a range of Chilean subduction plate interface densities (2700-3000 kgm^{-3}), Vp wavespeeds (6250-7000 ms^{-1}), and V_p to V_s ratios (1.8-2.0) (*Tassara and Echaurren*, 2012; *Husen et al.*, 2000; *Hicks et al.*, 2012). The parameter ranges of density, Vp and $V_p : V_s$ were discretized so that there were 100 values of each, and a value from each parameter range was taken pseudo-randomly before being combined in the following equation for shear modulus:

$$\mu = V_s * \rho \tag{4.5}$$

Where Vs is the shear wave speed determined by the randomly selected Vp and $Vp : Vs$ ratio, and ρ is the randomly selected density. This process was repeated until we produced a stable histogram (probability distribution) of shear modulus values (Fig. 4.2). The a priori probability distributions of uniform slip magnitudes for each forward modeled event in the foreshock series were calculated according to the probability distribution of shear moduli, using Brune's equation to calculate the slip values (equation 4.4). Therefore our modelling approach assumes a single shear modulus, G, of 35 GPa for the calculation of surface motions due to elastic dislocations, and a log-normal probability distribution of shear moduli, μ, at the

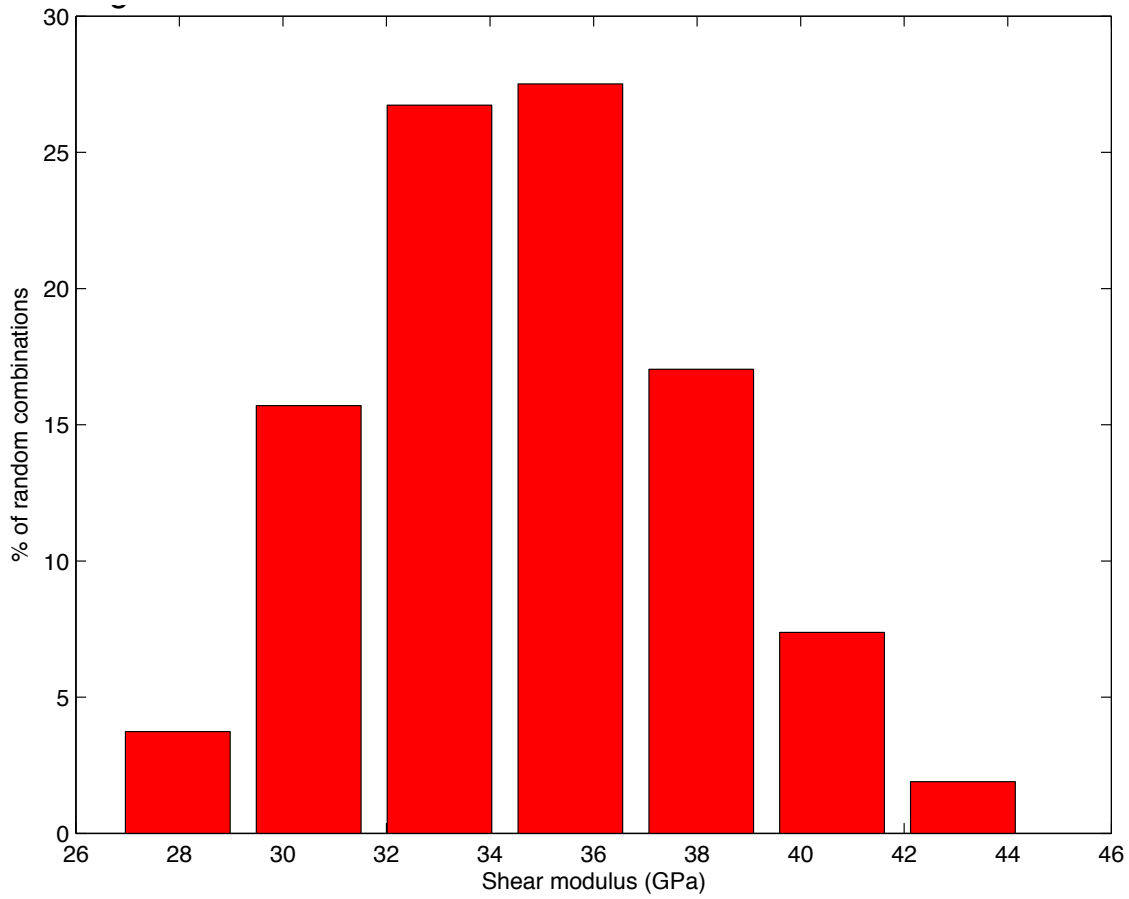

Figure 4.2: Probability distribution of the shear moduli that are used to generate an a priori probability distribution of uniform slip magnitude for each forward modeled event.

plate interface between 28 and 44 GPa 4.2) which are solely used to calculate the range and a priori probability distribution of uniform slip for each modelled event. The sensitivity of the Greens functions to the uncertainty of the Poisson's ratio and shear modulus (G) for the elastic half-space is negligible and so we do not include this variability in our forward modelling.

For the forward modelling of seismic predictions of the foreshock sequence, strike, dip, and slip azimuths are varied $\pm 15°$, $\pm 10°$, and $\pm 15°$ respectively from the central values derived from focal mechanisms. Hypocentres are varied $\pm 15km$, $\pm 15km$, and $\pm 10km$ in the East, North, and Vertical directions respectively. This variability in source parameters is in keeping with the variation observed in available focal mechanisms and hypocentres from various sources (e.g. Table 4.1).

source	lat(°)	lon(°)	z	strike1	dip1	rake1	strike2	dip2	rake2	centroid z	method
GEOFON	-19.97	-70.84	23	131	73	99	283	19	63	9	regional waves
GEOFON	-19.96	-70.66	12	117	66	91	294	25	87	20	body waves
gCMT	-19.94	-70.92	-	144	69	106	284	26	54	12	LP waves
USGS	-19.98	-70.7	20	127	74	108	258	24	44	15	body waves
USGS	-19.98	-70.7	20	126	74	98	277	18	63	15	w-phase
This study	-20.02	-70.81	-	-	-	-	237	11	12	17	GPS search

Table 4.1: Comparison of March 16th Mw 6.7 source parameters form seismic catalogues and GPS parameter search of this study

For the Mw 6.7 parameter search, the parameter space is sampled more finely and with a wider range of variability in all parameters. Strike, dip, and slip azimuths are varied between $-135°$ and $45°$ for strike, between $4°$ and $25°$ for dip, and between $-200°$ and $20°$ for slip azimuth. The hypocentre is varied $\pm 20km$ in both East and North directions and between 5 and 25 km in depth. Due to computational speed, we do not vary slip magnitude in the Mw 6.7 parameter search, assuming slip of all parameter combinations to be in agreement with the mean value of the distribution, 35 GPa. The average of the best solutions for the Mw 6.7 is then assumed for the default parameters for this event in the modelling of the evolution of seismic predictions of the whole foreshock series. We neglect events with a magnitude of less than Mw 5 since we generally did not have focal mechanisms for these events.

4.2.2 GPS data

Figure 4.1b-c shows the de-trended daily solutions at the cGPS stations closest to the foreshock activity. A common mode filter (CMF) is applied to this data to remove network-correlated noise *Wdowinski et al.* (1997). The common mode filtered cGPS data used in this study are identical to those presented in *Schurr et al.* (2014). The effects of common mode filtering can be seen in figure 4.3. The common mode filter is applied with the aim of removing the network-correlated noise. Figure 4.4 shows the stations used to form the average signal and the stations of interest from which this average signal is subtracted. Since the station coverage is not uniform in time there are certain periods in the time series in which the common mode filter is constrained by more or less stations. For times when the minimum amount of stations required to form an average signal (8 stations) is not possible, the common mode filter cannot be estimated and therefore there is a gap in the filtered time series. Figure 4.5 shows the availability of stations in the network as a function of time. Stations used for the stacked signal near to the rupture zone of the Mw 8.1 are not online during the final 16 days leading up to the mainshock, therefore the correction at the stations of interest in this study is not influenced by signals near-field stations, and therefore any transient signals that exist at the stations of interest are not quashed by this method. The zero positions of the data are assigned as the mean North and East station positions of the de-trended data between 1st and 15th March 2014. Since there is no significant transient deformation apparent in the cGPS and no significant seismic activity between 1st-15th March, we can evaluate the noise in the signal during this epoch. Consequently, errors at each station are defined by the standard deviations of the East and North components in this time period.

For the parameter search of the 16th March Mw 6.7 we fit the displacement obtained by the cGPS between 15th-17th March. This is due to the daily format of the cGPS solutions: The daily position of the GPS is the mean position, and the Mw 6.7 occurred late in the day, meaning that the cumulative displacement of this event is more apparent in the cGPS positions on the following day, 17th March. There is some contamination of the fitted signal by a subsequent Mw 6.3 on the 17th March contributing in total to 20% of moment release (M_0 release) captured in this epoch, therefore we removed the prediction of this event from the displacements of this epoch. This was achieved by finding the mean predicted displacements of this event and subtracting these from the data. Predicted displacements of the Mw 6.3 were

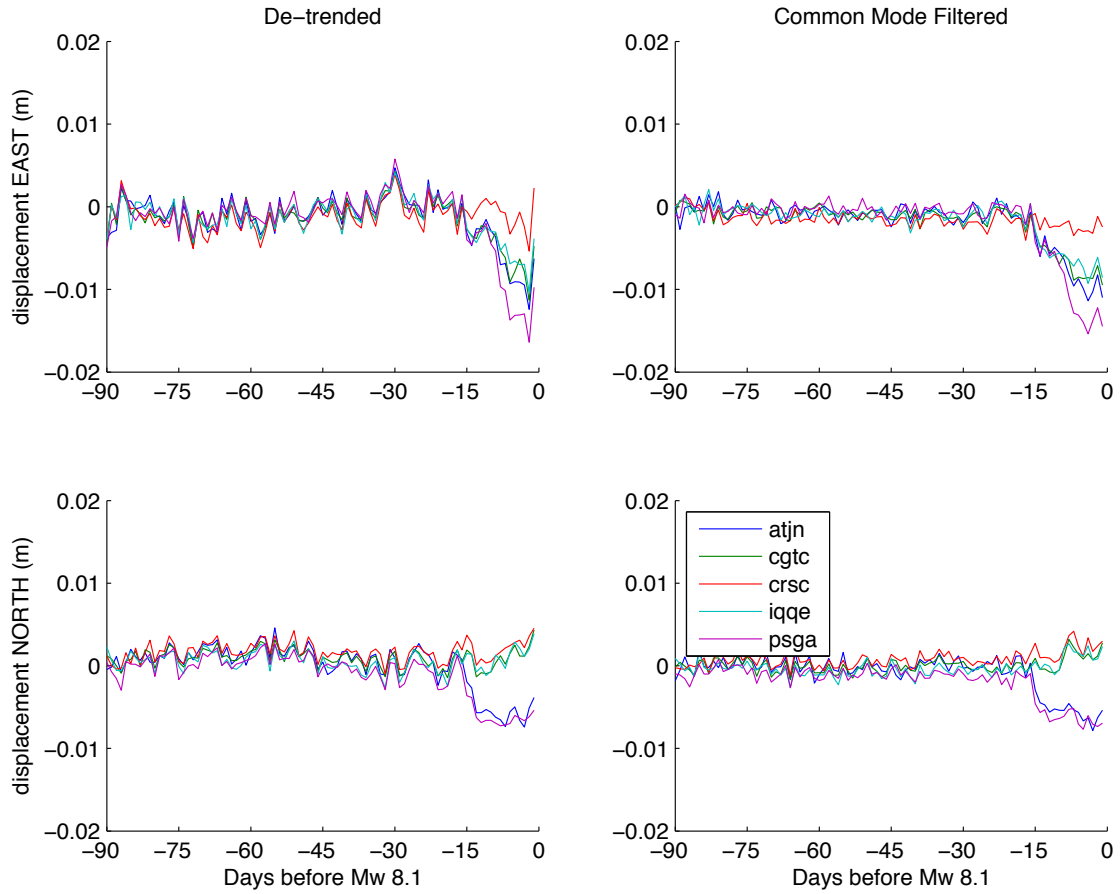

Figure 4.3: Left hand side shows the East and North components of the de-trended cGPS time series at the stations of interest (shown figure 4.2). Right hand side shows this de-trended data after the application of a common mode filter. The common mode filter does a good job of removing both the long and short wavelength noise. Colours of time series correspond to the stations written in the legend.

obtained by repeatedly forward modelling the Mw 6.3 source within its assumed uncertainties (see section 4.2.3) and taking the mean positions of these probability density functions in North-East model space. The Mw 6.3 displacements were then weighted by the time of occurrence of this event and subsequently subtracted. The predictions of lower magnitude events during this epoch were not subtracted because they were negligible in magnitude in comparison to those of the Mw 6.7 and Mw 6.3. The parameter search for the Mw 6.7 event includes data from the station pb11 (shown on figure 4.4). In this case, the common mode filter was changed to include this station in the list of corrected stations rather than the list of stacked stations. The reason we do not include pb11 in the seismic motion analysis is that it was offline for the majority of the period of interest between 16th and 31st March.

4.2.3 cGPS predictions: Probability density functions

The suite of cGPS displacement predictions for each event in the foreshock series is sampled into a probability density function in the East and North prediction manifold. These PDFs are then chronologically cascaded so that for each consecutive event the PDF is added X amount times to the positions of the prior PDF, with

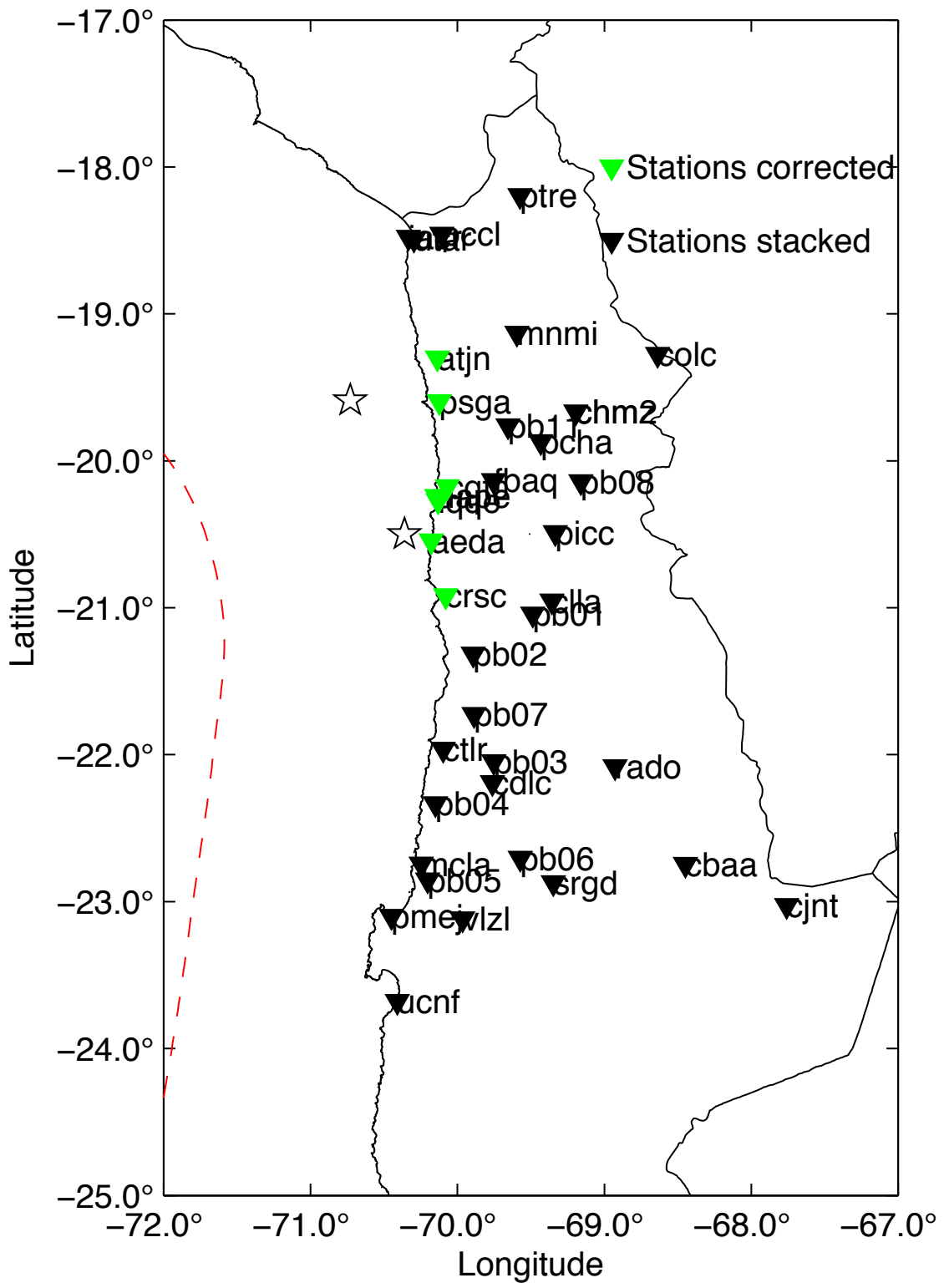

Figure 4.4: Map of the stations used to make the common mode filtered time series. The de-trended positions of the stations in black are averaged and this average signal is subtracted from the de-trended time series of the stations in green. Of the stations shown in green, we use 5 in our analyses of seismic motion. This is due to the gaps in temporal coverage in the period of interest making some of the stations in green unsuitable for this study.

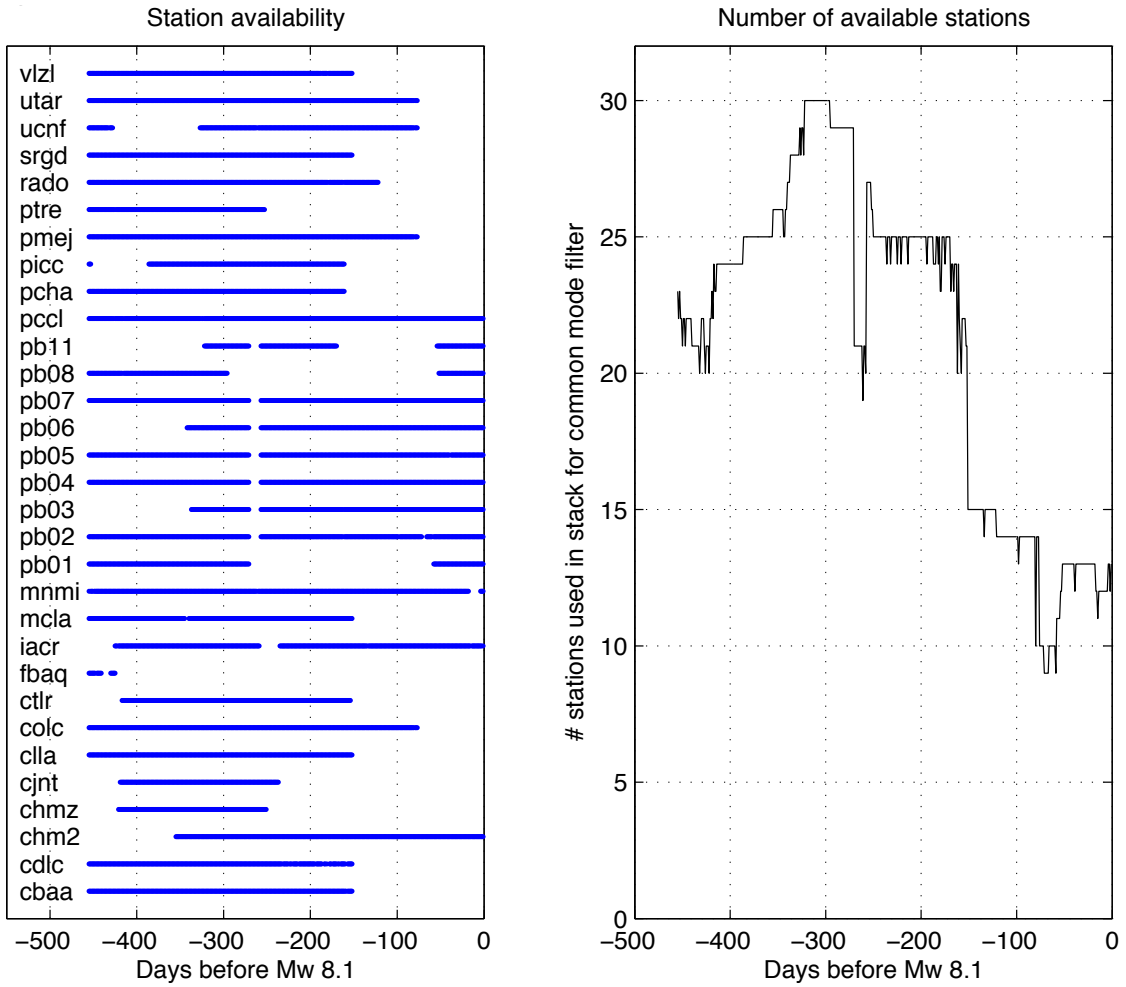

Figure 4.5: Temporal availability of the cGPS stations used to make the common mode filter (black stations of figure 4.3). Blue crosses on the left hand plot indicate days when the station was available. Right hand plot shows the number of stations available to form the common mode filter at each day in the time series.

X depending on the PDF value at each particular position of the prior PDF. After the PDFs have been cascaded, we obtain a daily PDF for each day of the foreshock series by sampling and appropriately weighting the cascaded PDFs according to the time that each event occurred on the particular day. For the daily PDF calculation, a point from each cascaded PDF is sampled randomly before a new point is calculated by weighting the sampled points by the fraction of the day that each event has been representative of that day's cumulative seismic motion. This creation of new points by random sampling and time weighting is repeated until we have a new cloud of points thereby creating a daily PDF.

The calculations of the PDFs are performed on a binned grid in the North-East model space with each bin a square of size 0.5 mm^2 and the grid extending between -3.0 and 1.0 cm in the East direction and -2.5 and 2.5 cm in the North direction. Choice of bin size determines the sensitivity of the method to the magnitude of seismic prediction. The trade off between sensitivity to seismic magnitude prediction and speed of computation has determined our bin size in this study. In evaluating

the daily position PDF we must randomly sample the cascaded PDFs and weight according to the time of the event in the day under consideration. This is achieved by multiplying each cascaded PDF, P, by a discretization factor, f:

$$Q = Pf \tag{4.6}$$

Then each point in the multiplied PDF is put into a list q amount of times where $q(i)$ is the rounded value of $Q(i)$ and i is the amount of elements in the PDF. The list of points, L, is shuffled with a pseudo-random re-sorting algorithm and truncated at a specified number, n. Each event, $(1tok)$, considered in the daily position will have its own list of points and its own weighing factor, w, so that the new list of points, L_{new}, takes the form:

$$L_{new} = w(1)L(1) + w(2)L(2) + \ldots..w(k)L(k) \tag{4.7}$$

Finally the daily PDF is obtained by binning the cloud of points in L_{new} into the discretized grid and scaling so that the sum of each element in the PDF equals 1. In this study we chose a discretization factor, f, of 1.5×10^4 and a truncation number, n, of 1×10^4. The choice of these parameters was made considering the computation speed. Such parameter choices have an effect of the lowest probability extents of the calculated PDFs but do not significantly alter the shape of the PDF in the higher probability zones. In the discussion of our results we have subjectively chosen a bound of $P = 0.004$ when considering the most probable predicted displacements.

4.3 Results

4.3.1 Parameter search for the source characteristics of the March 16th Mw 6.7

The best fitting solutions are defined by those solutions that produce predictions within the error ellipses of the data at one standard deviation. Figure 4.6a,c-d shows the mean parameters of all the best fitting models found in the parameter search. This average model represented by the mean of each best fitting parameter has a strike of -123°, dip of 11°, and a rake of 12°, giving a slip azimuth roughly in line with the direction of plate convergence). The centroid of the average model lies in the upper plate, although the centroid location of best fitting solutions can vary significantly, to a similar order of that of the seismically determined centroids (the maximum distance between best fitting centroids of the parameter search being 26 km and the largest distance between seismic centroids being 21 km). The centroid locations of the parameter search are in the vicinity of the range of centroids from seismic estimations (fig. 4.7). The average fault plane dips to the Northwest, and the focal mechanism for failure on such an oriented fault would be a highly oblique thrust (fig. 4.6b). Figure 4.8 shows the variability of the strikes, dips and rakes of the various planes that fit the data. The strikes of the best fitting planes vary between -90° and -135°, dip is constrained between 5° and 17.5°, and slip azimuth is constrained between 215° and 270°. Figure 4.9 shows the best-fitting suite of focal mechanisms output by the parameter search and figure 4.10 compares the mean solution to the seismically determined focal mechanisms. We find that the mean fault plane solution is most similar to that of the USGS using body waves (earthquakes.usgs.gov).

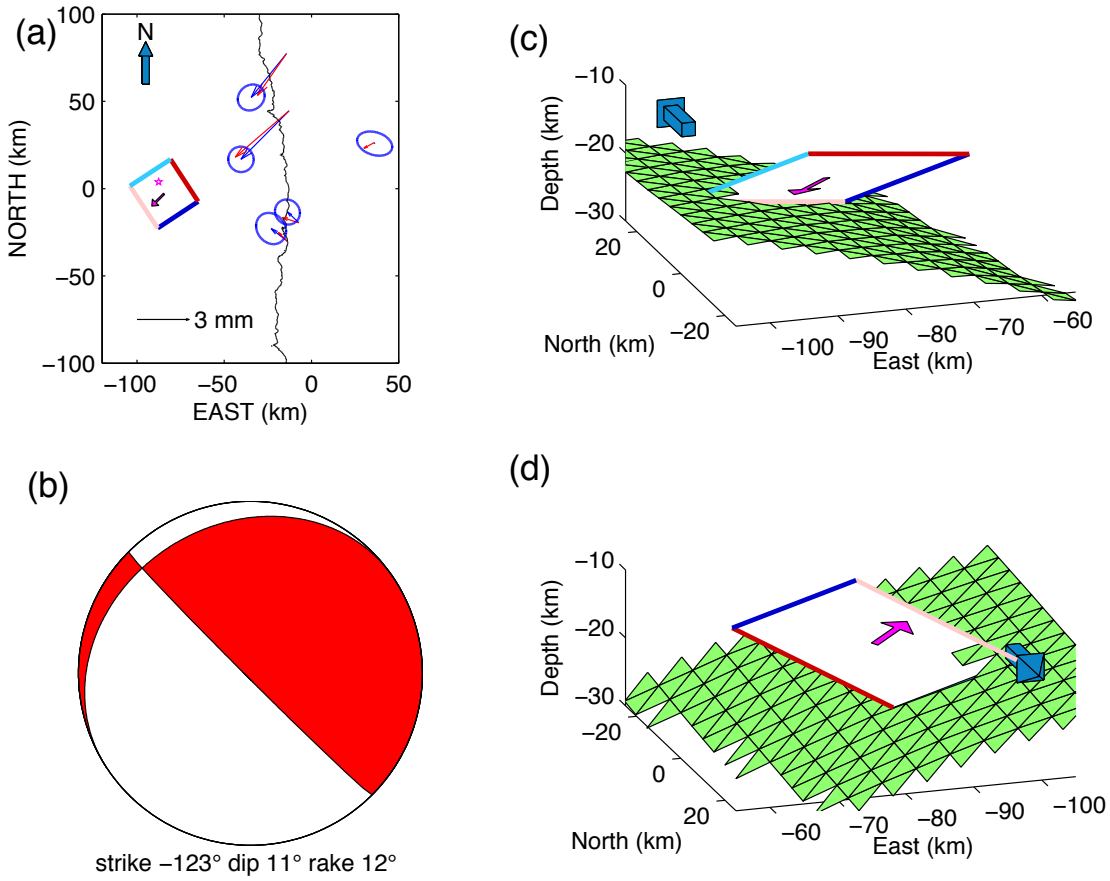

Figure 4.6: (a) Plan view of the GPS data and predictions for the average solution of the parameter search for the March 16th Mw 6.7. Blue vectors and ellipses represent the data displacements estimations for this event with 67% confidence. Red vectors are the predictions. Black line represents the Chile coastline. Average of the best-fitting fault planes is shown along with a failure vector plotted from the centre (centroid) of the fault plane. Colours of each side of the fault plane are repeated in panels (c) and (d). Plot is in cartesian coordinate system with origin at 70°W and 20°S. Magenta star is the epicentre from the GEOFON regional waves seismic solution (Table 4.1). **(b)** Focal mechanism of the average of the best fitting fault planes of the parameter search. **(c)** Average fault plane plotted with the plate interface from a South-Westerly look angle. North arrow is plotted to help clarify the look angle. Fault plane is plotted as a mesh of green triangles. **(d)** Same as (c) but from a North-East look angle.

4.3.2 Foreshock sequence

Figure 4.11-4.15 show comparisons between seismic prediction evolutions and GPS data evolution for the stations used in our analysis (these figures are animated in animations found in Appendix C). At psga, the data position and its associated uncertainty ellipse stays within the most likely predicted positions as both the mean data and prediction positions move towards the epicentres of the foreshock clusters with time (animation of plan view seismic predictions and GPS data can be found in Appendix C). At the other stations we see this spatiotemporal overlap between data uncertainty and prediction range, except for the northernmost station, atjn, where we see a divergence in time between data uncertainty and prediction range

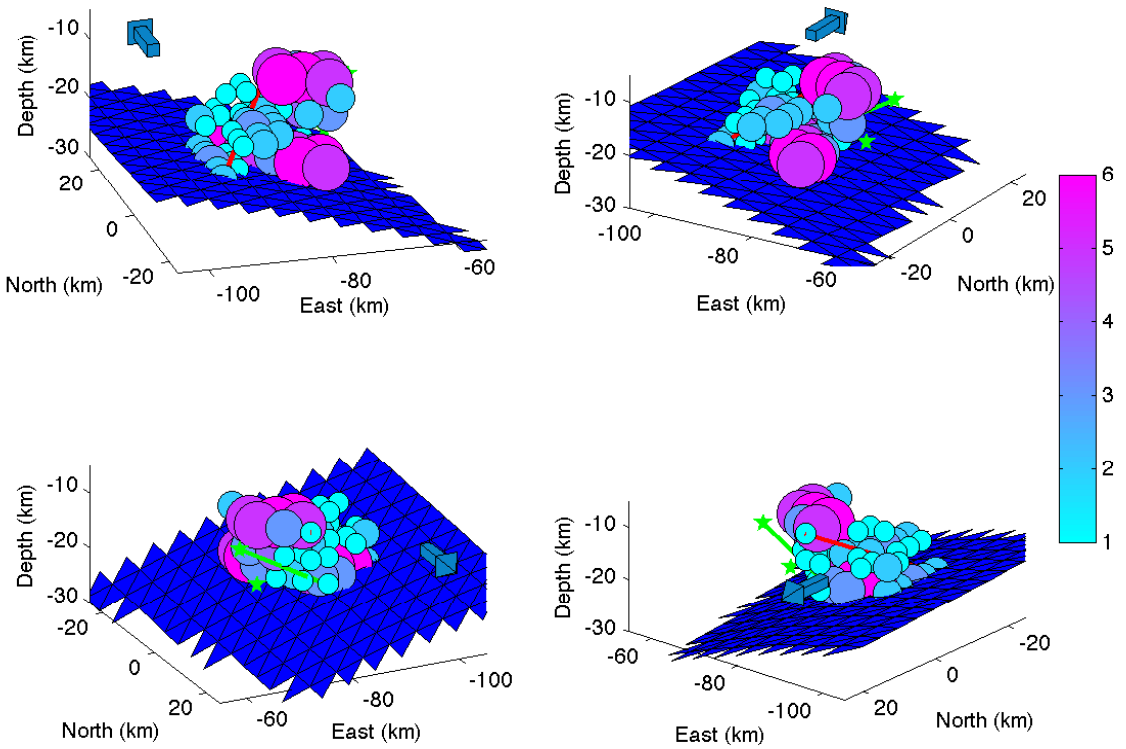

Figure 4.7: Panels show different look angles of the best fitting locations for the fault plane centroid of the Mw 6.7 parameter search. North arrow is plotted to help clarify the look angle. The blue triangular patches make the plate interface. Colours and size of the circles indicate the number of solutions at each particular centroid. Green stars are the locations of the seismically determined centroids (Table 4.1), and the green line is plotted between the two most distant seismic solutions. Red line is plotted between the two most distant centroids from the parameter search. Best fitting centroid locations are located in the vicinity of the seismically determined centroids and the spatial range of GPS centroids is of a similar order to the spatial range of seismic centroids.

(fig. 4.12).

Since the data generally stay within the bounds of the most likely locations predicted by forward modelling of seismic sources, it can be stated that the cumulative surface deformation of these stations can be, with the exception of atjn, explained by the surface displacements associated to the cluster of seismic events. Of course this statement is subject to the consideration of the assumed errors in the seismic source parameters: Naturally, wider and narrower ranges of input variability in the seismic parameters would result in a broadened and restricted region of predicted cGPS position in the PDF, respectively, meaning that the cGPS motions fall within the range of seismic predictions if the ranges of input parameters for each event are wide enough.

Another pertinent comparison to make between data and prediction is the comparison of the rate of change in displacement magnitude. Figure 4.16 shows the evolution of total displacement magnitude for both predictions and data for the common mode filtered data. In this analysis we are interested in the gradient of the cross-plotted rates of data and prediction magnitude: the greater the gradient decrease from 1, the more likely that the motion of the GPS station is explained by aseismic activity (assuming that all other seismic activity that is neglected by

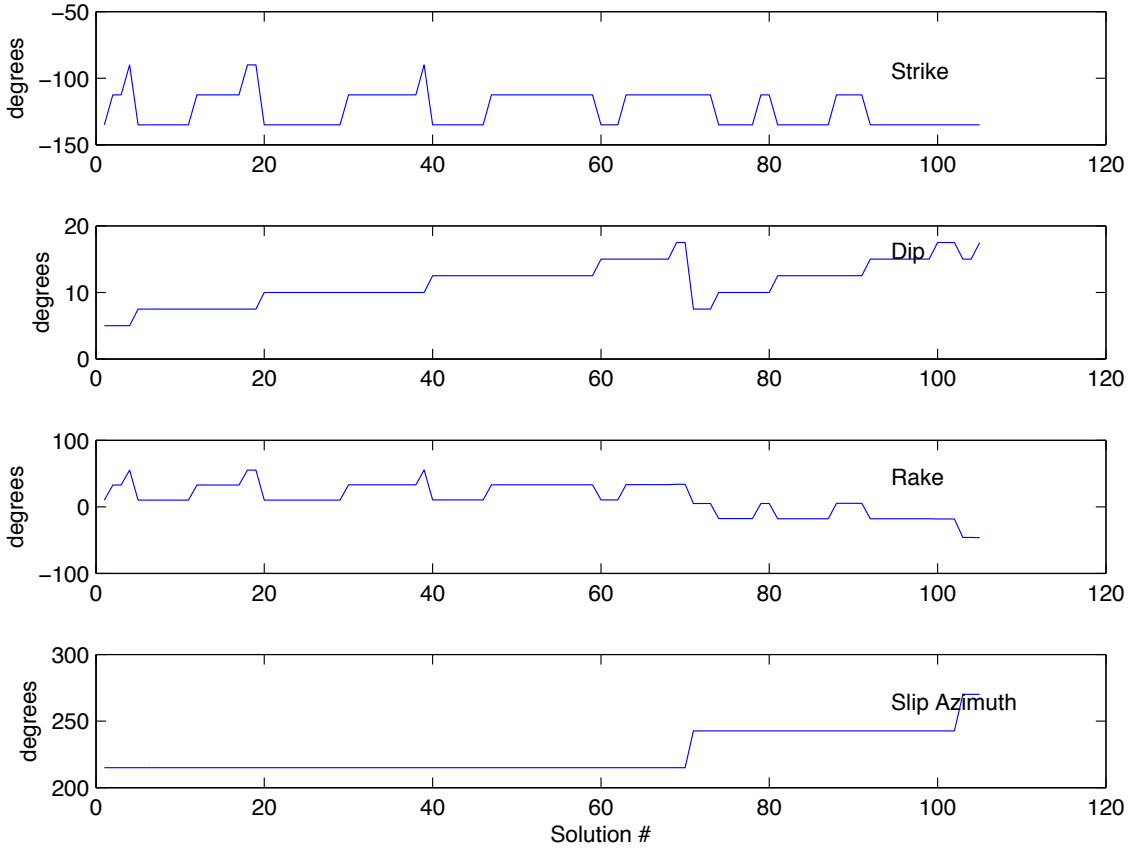

Figure 4.8: Panels show the variation of fault plane parameters, strike, dip, and rake (slip azimuth is a function of these parameters) for the best fitting planes of the Mw 6.7 parameter search.

our event magnitude cut off is not responsible for the extra GPS motion). An over prediction of GPS motion would result in a gradient greater than 1. Since we do not see significant displacement in either prediction or data at the station crsc we neglect this station for this analysis. At the four closest stations cgtc, iqqe, and psga, and atjn we see an initial gradient of slightly less than 1 indicating an in-concert evolution between mean prediction and data positions. Between the times of 18th-21st March we suspect aseismic motion most strongly at atjn and slightly at psga. All stations exhibit some noise at the end of the time series from 25th March onwards and that manifests itself as a horizontal right-to-left motion on the cross plots (as the noise occurs and corrects itself). However, despite this noise, there is an indication that aseismic motion has occurred some time between 25th and 31st March at all stations due to the pronounced flattening of the gradient in all the cross-plots during this period. In summary, we can state that the cumulative motion of the surface matches the cumulative motion of the most probable predicted positions within the assumed error distribution of source parameters for all stations except atjn. However this statement is subject to the confidence in our assumed errors in our input source parameters. Furthermore, the magnitude of the mean data predicted position initially increases at a similar rate before the data outpaces the predictions at two stations between March 18th – 21st and at all stations on or after March 25th, suggesting the detection of two aseismic slip transients.

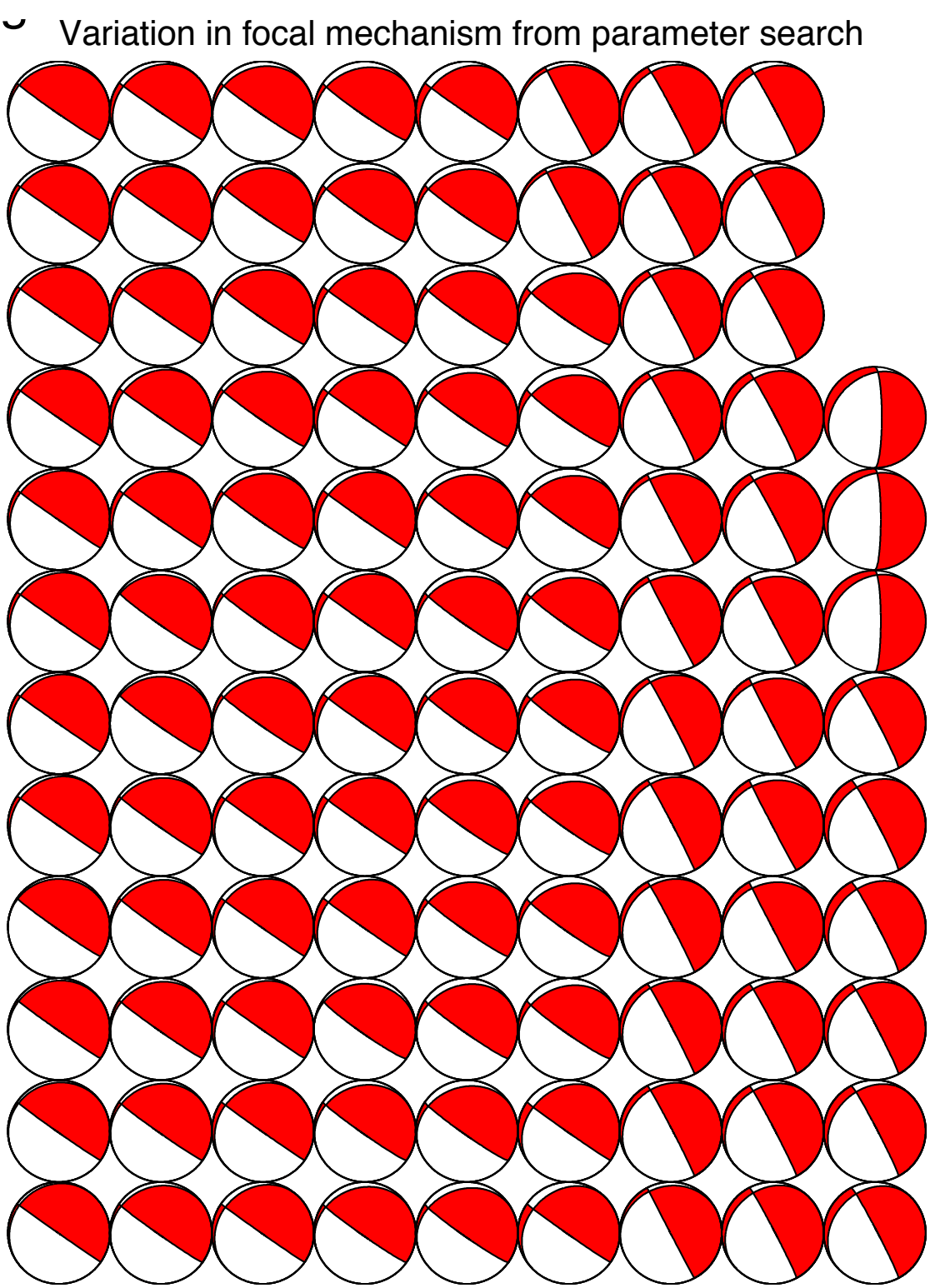

Figure 4.9: Plot of the focal mechanisms to show the variation in fault plane parameters, strike, dip, and rake, for the best fitting planes of the Mw 6.7 parameter search.

4.4 Discussion

The results of the parameter search and forward modelling approaches presented in this study must be considered within the limitations of the assumptions made in the modelling. While we can estimate the bounds of error for input parameters

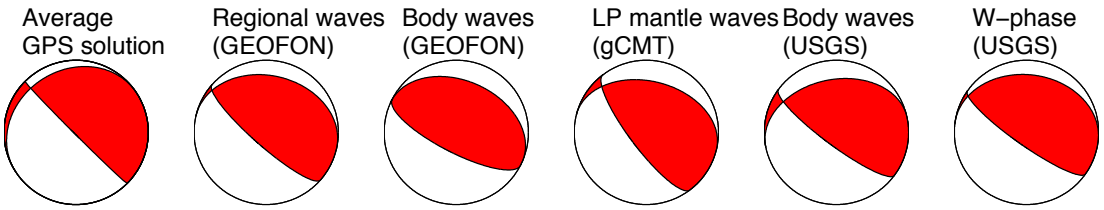

Figure 4.10: Comparison of focal mechanisms (from Table 4.1) for seismically determined solutions and the average solution of the best fitting fault planes from the GPS data

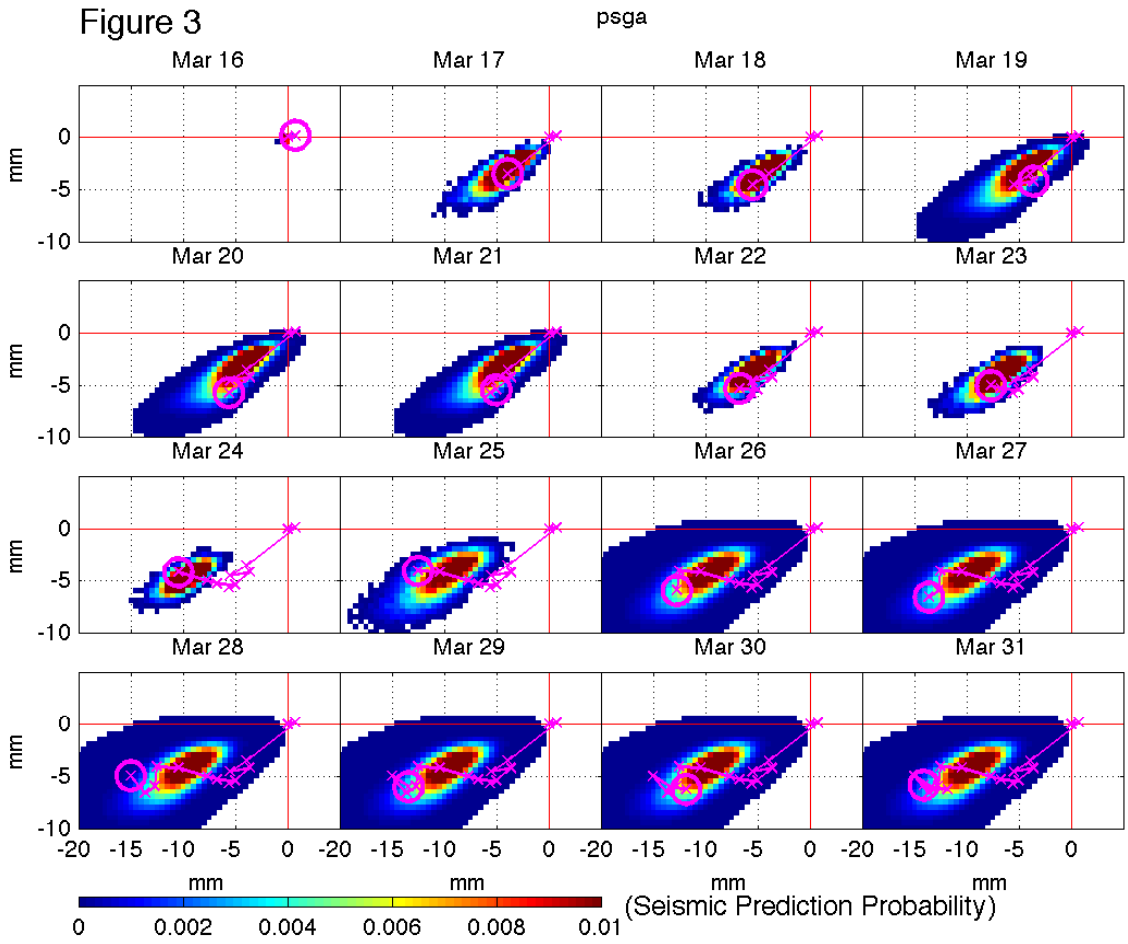

Figure 4.11: Chronological evolution of the seismic predictions of station position and the actual station position from cGPS for psga. Time increase is given by the data above each panel. X and Y axes correspond to East and North motion. Colours represent the probability distribution of the seismically predicted station position. The growing magenta line represents the cumulative cGPS data motion and the ellipse at the end of this line represents the 95% error range of this cumulative displacement. At this particular station we see that the most probable predicted positions of the cGPS follow the data, with perhaps the data growing at a slightly greater rate than the range of most likely predictions.

using the variability found in independently obtained seismic hypocentral locations and focal mechanism solutions, it is unknown what kind of probability distribution these co-dependent errors should take. Sources of these errors come from oversimplified velocity models used in hypocentral and moment tensor inversions, noise in

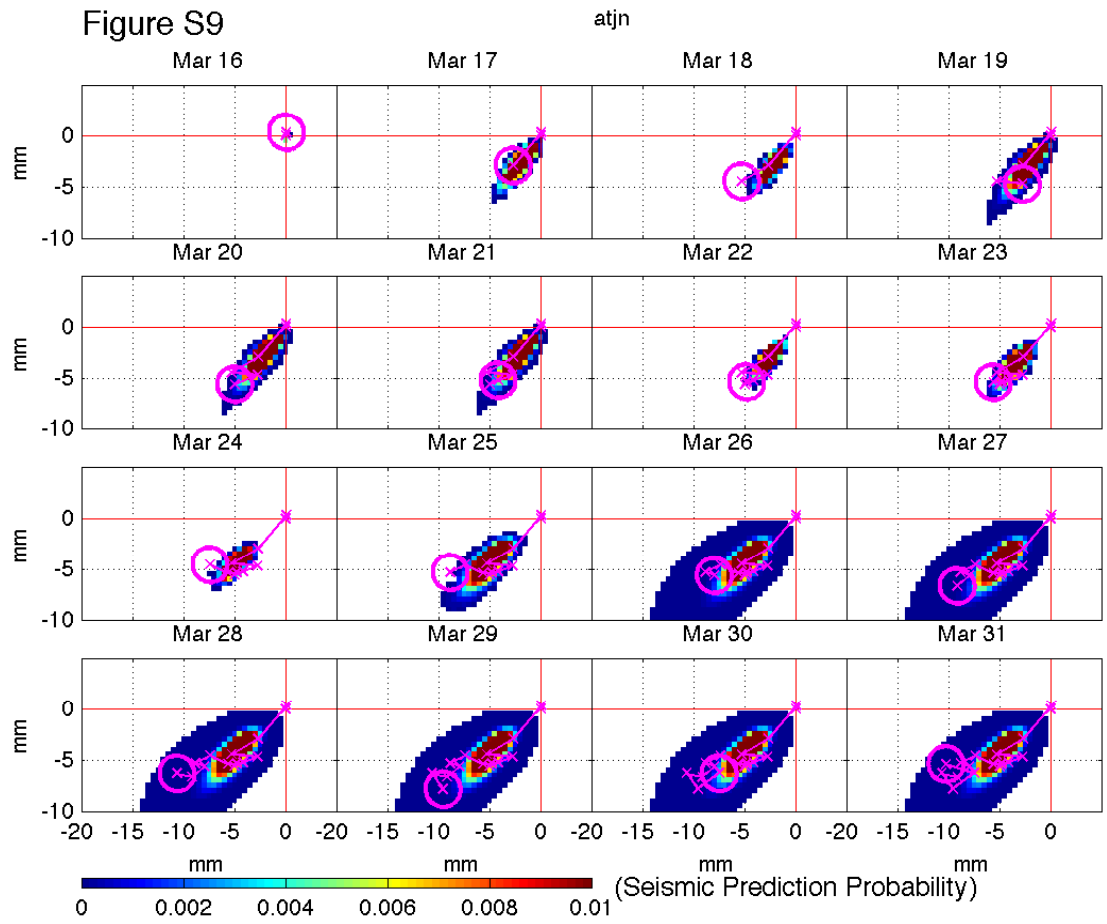

Figure 4.12: Same as figure 4.11, but for station atjn.

the seismic data, as well as artifacts introduced by the processing of moment tensor solutions. An example of the variability of a seismic event is found by comparing independently derived solutions from the Mw 6.7 foreshock (Table 4.1 figure 4.10). Nevertheless, even with conservative estimates of source parameter errors we can state that the cumulative transient in the data is mostly explained by the cumulative displacement along the plate interface from the foreshocks. Only at the northernmost station (atjn) do we see an evolution of cGPS position that exceeds the range of most probable predicted positions.

Given that the modelled seismic-slip can reproduce most of the cumulative signal in the data within given error considerations, we must then ask what spatiotemporal role the aseismic slip plays during the foreshock sequence. Certainly, the outpacing of the data over the prediction in mean magnitude evolution, evident both between 18-21st March and following March 25th leading to the mainshock on April 1st, strongly suggests the occurrence of aseismic slip. However, the increased noise levels in the data concurrent with this suspected aseismic motion in the final week leading to the mainshock slightly decreases our confidence in occurrence of the second transient.

Detection of repeating events (*Kato and Nakagawa*, 2014; *Meng et al.*, 2015) has been taken as an additional indication of slow slip. However, neither these repeating events, nor indeed the microseismicity have occurred with a high enough frequency or regularity during the final 16 days leading to the Mw 8.1 mainshock to support the case of a background slow slip forcing seismicity. Furthermore, it remains to

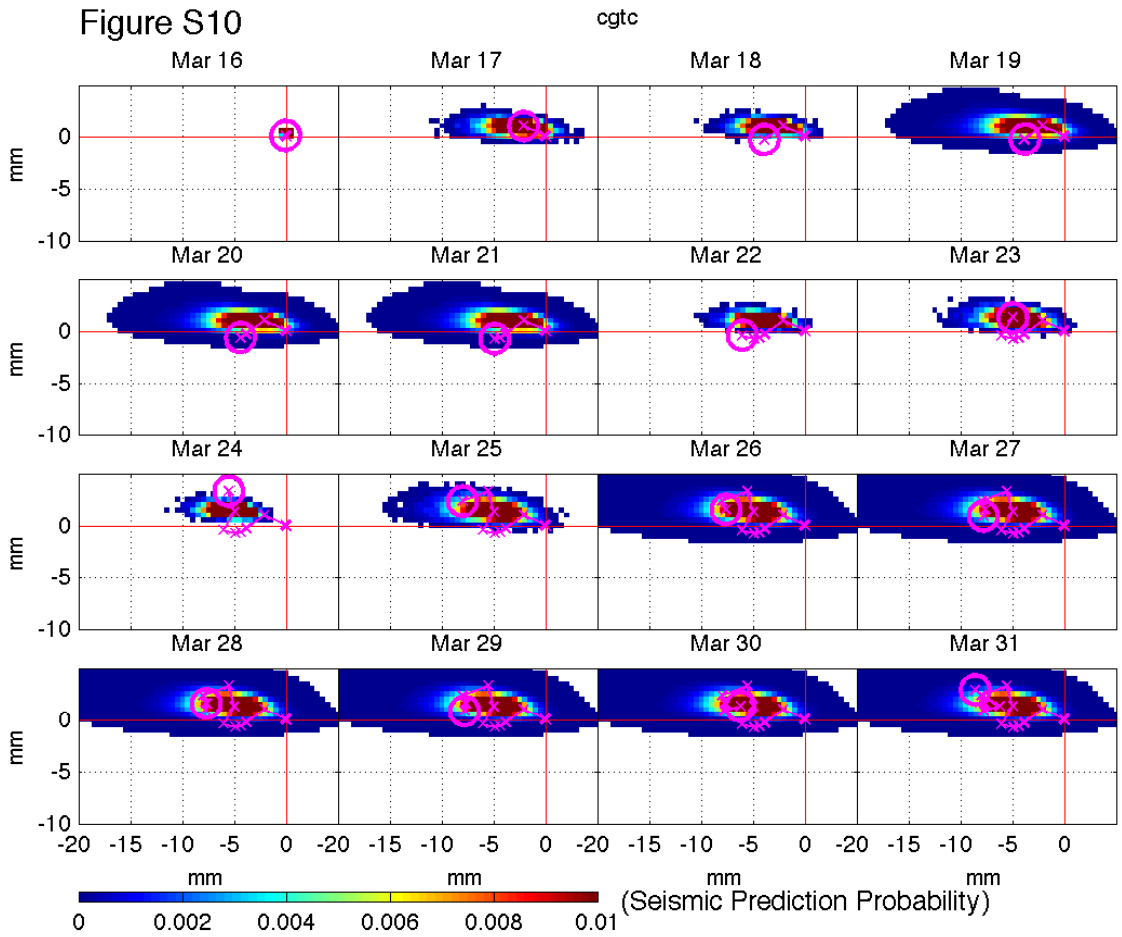

Figure 4.13: Same as figure 4.11, but for station cgtc.

be demonstrated whether these repeating events did indeed break the exact same patches, based on the source dimensions and location uncertainties. Even if the repeating events have occurred on the same patches, forcing mechanisms other than slow slip (for instance fluid pressure change) could explain the seismicity. Therefore the proposed slow-slip associated with the repeating events may have occurred, but this slow-slip is certainly not the main process contributing to the transient cGPS motion captured during this final foreshock sequence beginning on March 16th. If such a slow slip has occurred concurrent with repeating events, then the surface signal is not detectable above the level of data noise. Moreover, the aseismic deformation transients that we have detected are not strongly correlated in time to the repeating events. Figure 4.1 shows how the largest events occur in two bursts, the first southerly sequence occurring between 16th and 18th March and the second northerly sequence occurring between 22nd and 25th March. Indeed, the identification of aseismic motion following both of these seismic bursts strongly supports the scenario of a postseismic response to foreshocks, most likely in the form of aseismic afterslip. The time series are too noisy to provide a reliable inverted location of aseismic slip, although the difference in mean data and prediction displacements leaves a signal that generally points towards the location of the foreshock activity.

The Mw 6.7 of March 16th is seen as the point at which the foreshock series intensified and therefore its source parameters are of particular interest in trying to understand the runaway process leading up to the mainshock. From the results of

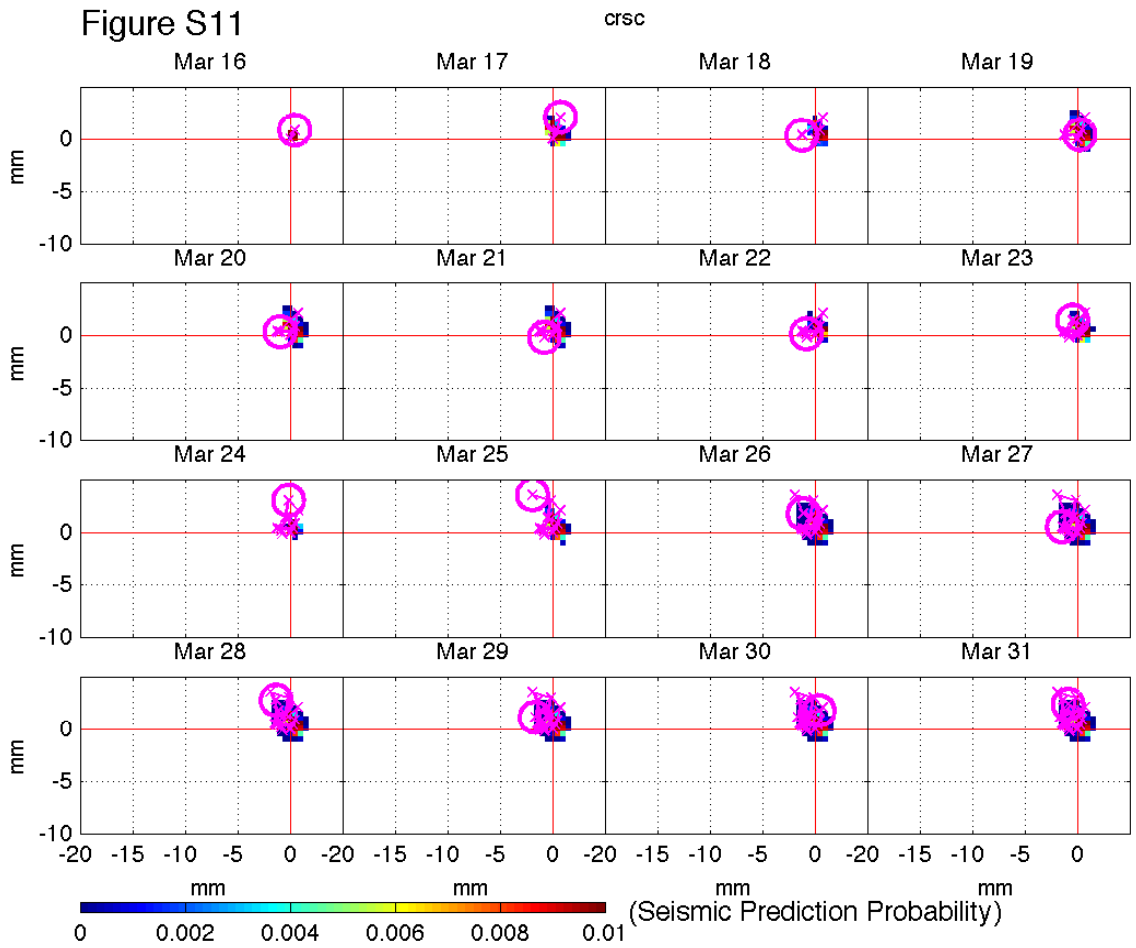

Figure 4.14: Same as figure 4.11, but for station crsc.

our parameter search we show that the final foreshock sequence was triggered by a fault plane striking between -135° and -90°. This result is significant in that it indicates a failure on a plane other than the megathrust, which would have a more northerly-rotated strike. For other parameters of the parameter search (hypocentral location, dip, and rake) we do not see an improvement in constraint compared to those given by initial seismic estimations. Therefore, while our method indicates failure on an unconventional fault plane, it does not show if such fault plane is in contact with the plate interface or is sitting higher in the upper crust.

The significance of an intra-plate Mw 6.7 in facilitating this accelerated unlocking of the interface remains unclear: If this event had happened on the plate interface then the subsequent foreshock series may still have resulted in the final rupture of the Mw 8.1. If the location and mechanism of the Mw 6.7 fault is significant then we could speculate that this event allowed the release and migration of upper plate fluids onto the plate interface. In this scenario, an increased fluid pressure on the plate interface would reduce the effective normal stress thereby promoting a decrease of the locking degree (*Audet and Schwartz*, 2013; *Moreno et al.*, 2014). In an alternative scenario, an increase in permeability in the vicinity of the Mw 6.7 rupture could have drawn fluids away from the plate interface, thereby strengthening the interface and pushing it into a state more susceptible to rate weakening and therefore seismic failure.

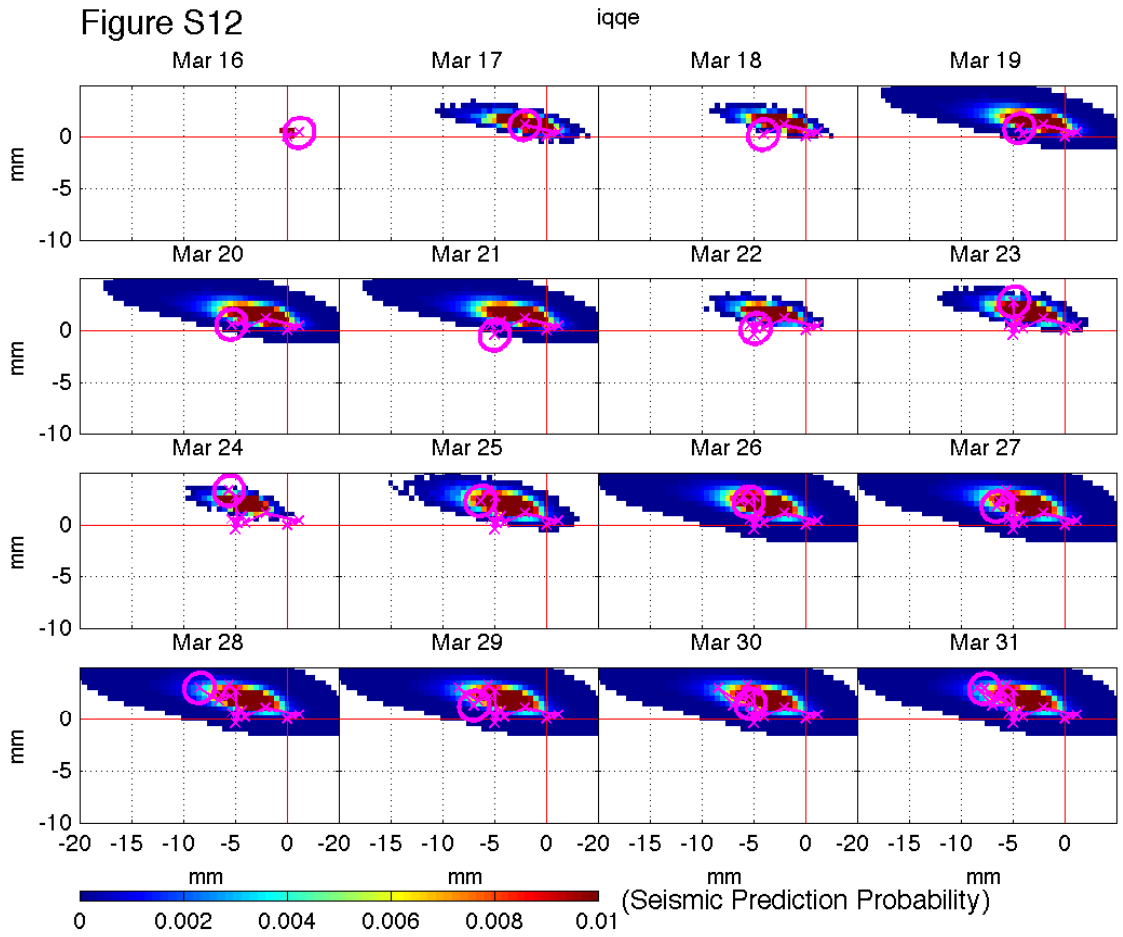

Figure 4.15: Same as figure 4.11, but for station iqqe.

4.5 Conclusions

This study has shown that the transient signal in cGPS data following and including the March 16th Mw 6.7 foreshock leading up to the Mw 8.1 mainshock of April 1st can be largely explained by seismic-slip, given a realistic range of foreshock source parameter uncertainties. With the exception of the northernmost station, atjn, and with the consideration of noise, the evolution of a transient signal in the data does not fall outside of the bounds of the probable seismic prediction locations, although the time dependent rates of mean data and prediction magnitude evolution have revealed possible periods of aseismic motion between 18th - 21st March and between 25th - 31st March. Due to noise levels in the data we cannot rule out the possibility of a very low-rate background aseismic slip that could be forcing the seismicity and repeating events. However, the aseismic slip that we can detect is most likely to be a response to the foreshocks in the form of afterslip.

The methods demonstrated in this paper have a strong potential to be applied to other scenarios where there exists both dense cGPS and seismometer networks to identify the contribution of seismic displacements to the transient signals recorded in the GPS. Improvement of the forward modelling of seismic prediction PDFs could be obtained by improving our knowledge of the a priori probability distributions of the seismically obtained parameters. By comparing the seismically obtained parameters of the March 16th Mw 6.7 to that of our parameter search, we see that the

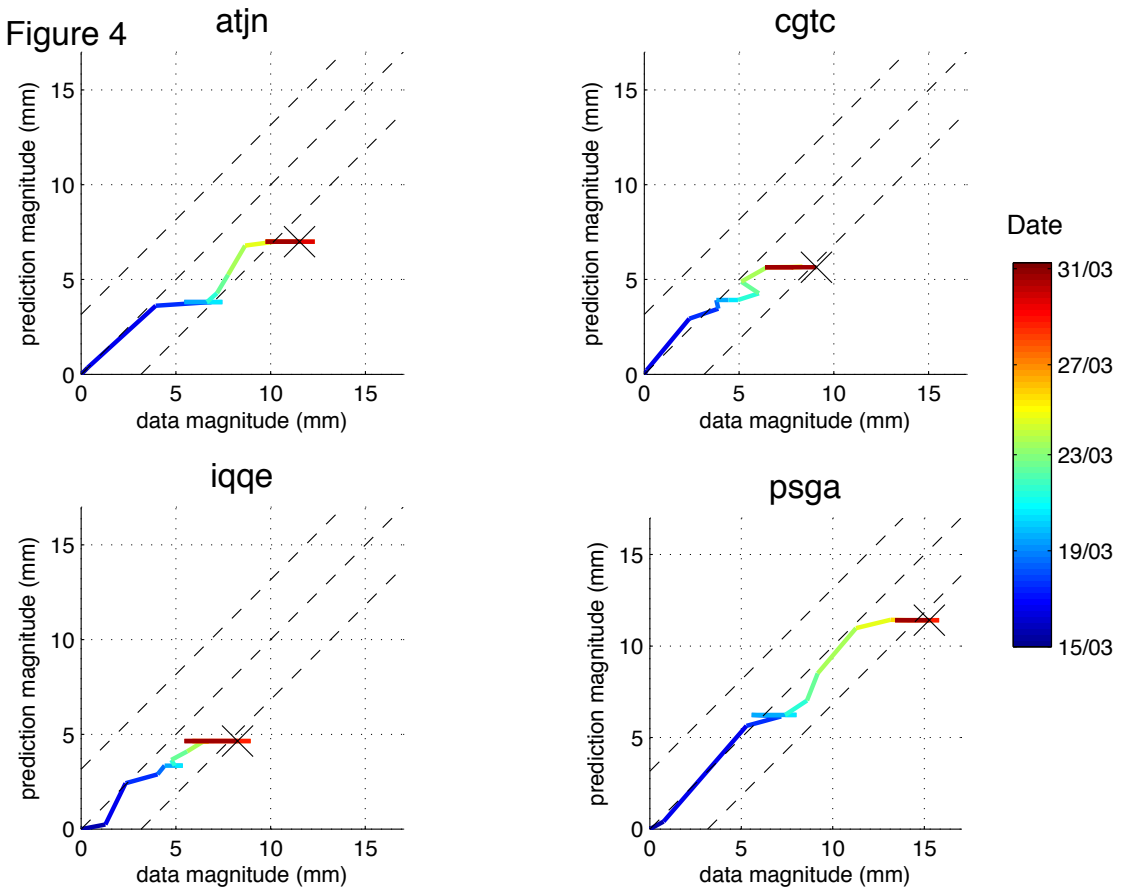

Figure 4.16: Cross-plots of the cumulative mean data magnitudes and mean prediction magnitudes are shown on each panel, with the time corresponding to the location on the cross plot given by the colour bar. Dashed black lines represent a gradient of 1. At stations atjn and psga do we see most clearly two decreases in gradient, suggesting two times when the cGPS motion was not seismically explained, most probably due to aseismic afterslip following the preceding bursts of foreshock activity. At all stations the days from March 25th onwards are characterized by a horizontal motion in the cross plots partially due to noise and partially suspected to be aseismic motion (see plan-view movie in Appendix C). Final mean magnitudes on March 31st are plotted with a black cross.

GPS displacements better constrain the strike of the event, although constraints on hypocentral location, dip, and azimuth of seismic failure are not improved.

Chapter 5

Synthesis and Conclusions

Note

This chapter contains a summary of the results from the chapters 2-4 in relation to the research aims highlighted in section 1.4. In addition to the results of the preceding chapters, I also present in this chapter the relevant results from papers that I have been involved in as a co-author (*Schurr et al.*, 2014; *Li et al.*, 2015; *Lange et al.*, 2014).

5.1 Re-cap of aims and objectives

Chapter 1 detailed the foundations and reasons for addressing the following research questions:

- **How are slip and seismicity related in space and time, and what are the respective magnitudes of seismic and aseismic moment release?**
- **Can we separate the simultaneous postseismic processes and their magnitudes as a function of time following the earthquake?**
- **How well do co-, post- and inter-seismic plate interface kinematics of the Maule earthquake adhere to the current understanding of frictional behaviour of subduction plate interface zones?**

The subsequent sections further discuss and summarise the findings of our work with relation to these questions.

5.2 Seismicity And Slip

In my studies of both earthquakes, I was able to compare the seismic efficiency of the slip. For the Iquique foreshock series, the seismic efficiency was very high, with most of the cGPS motion being explained by seismic slip, and with the aseismic slip being interpreted as afterslip of the larger foreshocks. For the Maule earthquake, the seismic efficiency for the majority of the regions of high afterslip was deemed to be quite low. Nevertheless, the majority of aftershocks (lower magnitude events due to Gutenberg-Richter law) were co-located with zones of high afterslip. *Lange et al.*

(2014) showed that the cumulative aftershock numbers nearby to cGPS stations produced a linear relationship with the cumulative displacement in time (fig. 5.1). A similar result for the linear relationship between cumulative aftershock number and cumulative afterslip displacement was found in chapter 3, but for a longer time period of over 3 years and a Mw of completeness > 5. This finding alone brings us no closer to answering whether aftershocks drive afterslip, or vice-versa. Rather, this finding further establishes the temporal link between the two postseismic phenomena. The **spatio**temporal link between aftershocks and afterslip pulses was not established but is a good candidate for further research with the time-varying afterslip model and the aftershock catalogue. For example, if the cumulative number larger aftershocks (e.g. Mw > 5) are decaying at a similar rate to the cumulative afterslip, then the whole Maule afterslip could in fact be a sequence of triggered afterslip events of the aftershocks: the additional stress release from the afterslips feeding-back into triggering more events in addition to the traction forces on the interface due to the viscoelastic relaxation.

The seismicity can also show where afterslip is not on the plate interface, i.e. on splay faults or upper crustal extensional faults (*Lieser et al.*, 2014). Unfortunately time constraints and priorities of other research targets meant that the investigation of afterslip magnitude on crustal faults was not undertaken within this PhD project. Furthermore, since most of the splay-fault seismicity occurred offshore, the occurrence of afterslip on non-plate-interface structures may not even be resolvable from most of the on-land cGPS network. The unclear spatial relations of locking, afterslip, and coseismic slip in the Northern portion of the Maule segement may be due to the contamination of the afterslip signal with a continued crustal motion on the Pichilemu extensional fault system, which recorded a clear extensional signal during the Pichilemu aftershock series of 12th March 2010 (*Ryder et al.*, 2012), and which likely had a significant postseismic phase of its own.

The triggering of the aftershocks and afterslip by stress transfer of the coseismic slip and ensuing afterslip was tested in chapter 2. We found that the ΔCFS model of aftershock triggering is more valid for larger magnitude events: i.e. larger magnitude aftershocks are quite likely to be in plate interface regions that were postively stressed by the mainshock. Also, the coseismic slip from teleseismic finite fault solutions (*Hayes et al.*, 2013) provides a better agreement with the ΔCFS model than the coseismic slip model from GPS. The afterslip triggering by the coseismic ΔCFS was less conclusive, probably due to the smearing of the slip distributions from regularizing smoothing constraints used in the inversions.

5.3 Separation of postseismic processes

The separation of postseismic processes was achieved for the horizontal displacements but the methodology is subject to the assumptions of afterslip behaviour and also subject to the intrinsic assumptions of the subsurface elastic and viscoelastic structure and parameters. The follow-on research from this study will need to incorporate the vertical signal in the Postseismic Straightening method. Use of the vertical signal may warrant the exploration of additional rheology laws (e.g. Burgers) or alternatively, the early postseismic may be omitted from the analysis so that the solution is only a function of the steady state viscosity. Furthermore, the assumption of the relative locking distribution being the same before and after the

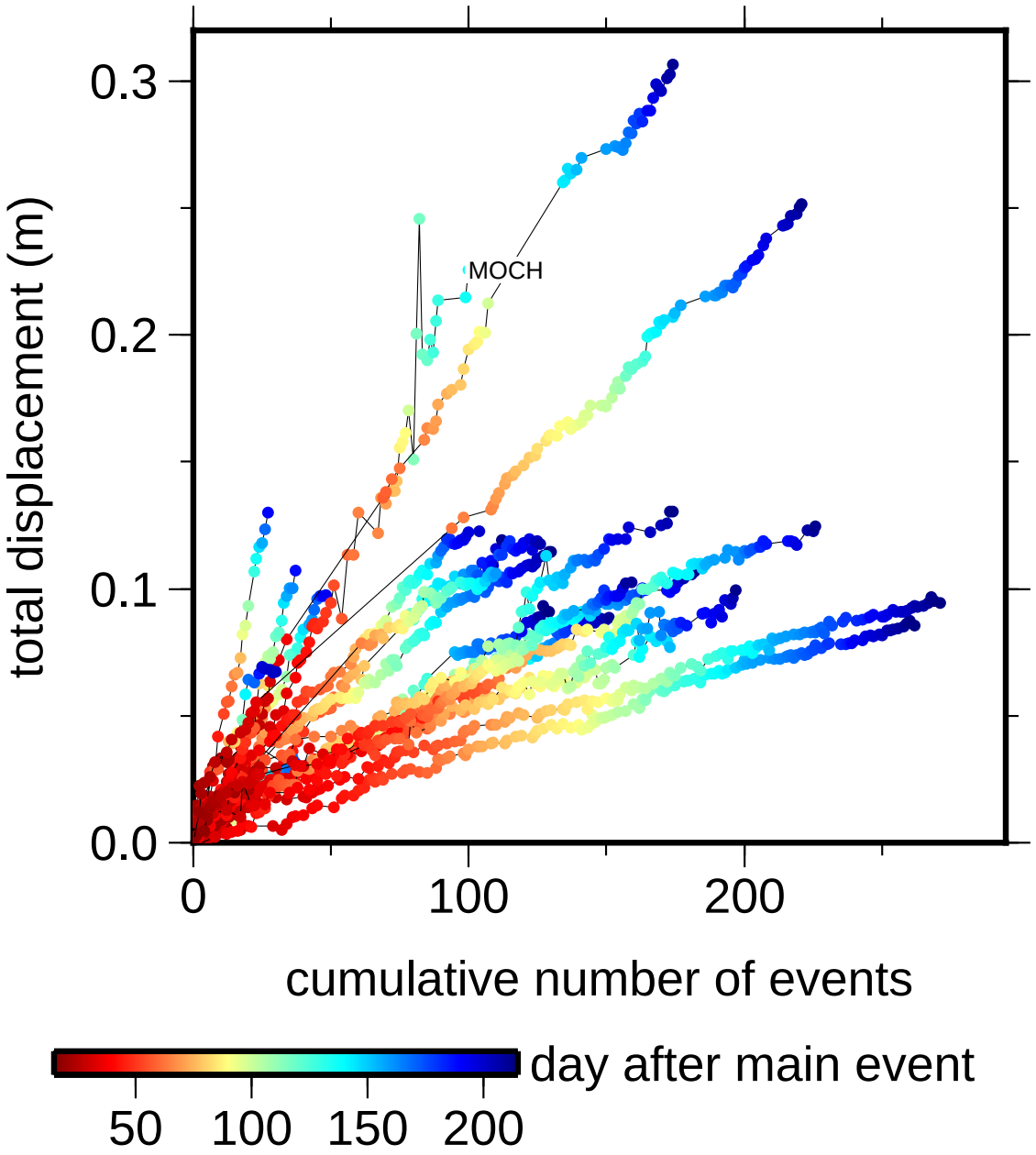

Figure 5.1: Figure taken from *Lange et al.* (2014). Total GPS displacements for the Maule 2010 earthquake plotted versus the cumulative number of aftershocks (*Lange et al.*, 2012) occurring within 50-km radius around the GPS stations and for events with moment magnitudes larger than 3.5. Note that the local seismicity catalogue begins 21 days after the mainshock and ends 2010 September 30: the cumulative displacement was set to zero on the first day that an event occurred within the search radius of the station in order to make it easy to compare the slopes of the different lines.

earthquake could be improved by giving the locking model more degrees of freedom. The computational expense of exploring the solution space was a major constraint over the methodology, one which needs to be considered carefully in future parameter search efforts using the vertical signal.

As for the results, the main message must be that including a rapid re-locking in the postseismic model significantly improves the model prediction fits to the time series, and that the parameterization of the locking signal requires a cGPS

network close enough to the ruptured interface to capture in detail the veering of the postseismic displacments. The inclusion of locking has a significant impact on the range of best-fitting oceanic and continental linear Maxwell viscosities. An intriguing result is the super-interseismic locking rates in the solution space for the three processes model. While the extent of super-interseismic subduction is not ideally constrained (it can vary between 1 - 1.8 the interseismic subduction velocity) postseismic increases in subduction velocity have been suggested for other subduction margins (e.g. *Heki and Mitsui*, 2013). Our results suggest a competition between viscoelastic relaxation and locking magnitude in fitting the veering signals at the coastline, so it is not clear whether the super-interseismic rates are just artifacts of of the non-uniqueness of the solution space. Hopefully the inclusion of the vertical signal will narrow down the locking parameter space. Another way of testing the validity of such a super-interseismic subduction velocity would be to test the change in velocity of signals at segments adjacent to the Maule zone to determine whether such a velocity change is explained by viscoelastic relaxation or by the increase in subduction velocity. If a postseismic subduction velocity change were to be found, then the next stage would be to look at the physical models that would enable such a change. Therefore, the plate trajectory model (equation 1.1) may be wrongly assuming the continuation of a constant linear component either side of the mainshock, and will need to be revised if the subduction velocity is found to increase following the rupture of a large enough portion of the segment.

The agreement of the cumulative aftershock decay time function with the cumulative afterslip decay time function can be tested further by repeating the analysis with multiple independent seismic catalogues. If shown to be a robust for other catalogues, this temporal relationship may be assumed in other postseismic margins to assess what proportion of the signal is related to afterslip. The magnitude dependence of the Omori-decay should also be considered, along with the magnitude of completeness of each catalogue, since the tempoal relationship with afterslip might only be valid above a certain magnitude.

5.4 Seismic cycle interface kinematics

The data captured by the dense survey and continuous mode GPS instrumentation, both in the Maule and Pisagua rupture zones, has proved invaluable for probing the plate interface mechanical behaviour. As discussed in chapter 2, the resolution of plate interface properties is a function of the distance of the surface measurement to the plate interface, therefore the spatial resolution of such large megathrust earthquakes captured by the dense near-field coseismic and postseismic networks of cGPS has yielded unprecedented insights into the small scale heterogeneities in plate interface behaviour. The data from these segments are especially useful because we have a record of the inter-, co-, and post- seismic phases of the seismic cycle. Therefore, by continuing to monitor these segments from the gradual transition from post- to inter- seismic, we are able to improve our understanding of how the heterogeneity of the plate interface properties is linked to the distinct mechanical behaviours of adjacent plate-interface regions during the different stress conditions.

To be able to confidently divide the plate interface into mechanically distinct regions requires an implementation the current friction laws (i.e. rate-and-state friction) in a numerical modelling of the short- and long- term behaviour of such het-

erogeneous adjacent regions (e.g. *Barbot et al.*, 2012; *Kazemian et al.*, 2015) with the aim of reproducing the kinematic behaviours captured by the dislocation modelling and seismic catalogues. While I have touched on the discussion of rate-dependent friction in the discussion of the Maule elastic dislocation modelling (section 2.5.5) there is certainly scope to test the perceived plate interface frictional heterogeneity of this segment by means of numerical modelling approaches. Time dependent dislocation models (both for back-slip/locking and slip) therefore play a crucial role in our improved understanding of plate interface properties, and the better establishment of the robustness of these dislocation solutions is necessary to narrow down the physical parameter space on the plate interface. For the both earthquakes, it has been possible to make spatial comparisons between interseismic locking distribution and the coseismic slip (*Moreno et al.*, 2010; *Bedford et al.*, 2013; *Schurr et al.*, 2014; *Li et al.*, 2015). From the spatial correlations of models, one first order observation is that the coseismic slip releases the interseismically stored stress (slip-deficit) on the plate interface, and this spatial relation is most striking for the model of *Li et al.* (2015) (Fig.5.2) which considers the viscous flow in the subduction zone as a contributing signal to the measured interseismic surface deformation.

Moreno et al. (2010) argue for such a slip-deficit release at the highly locked patches by comparing the coseismic slip and interseismic coupling models. The spatial correlation between interseismic locking and coseismic slip does not substantially improve following the update of the Maule coseismic model (*Bedford et al.*, 2013) with the newest model including the data from both *Vigny et al.* (2011) and *Moreno et al.* (2010). Accordingly, a clear spatial correlation or anti-correlation is also lacking between afterslip and interseismic locking. In the south of the Maule rupture coseismic model, near to the Arauco peninsula, there is a prominent anti-correlation between coseismic slip and afterslip. At this peninsula, the model resolution is superior to other portions of the segment, and therefore such a spatial pattern that fits with the assumed frictional model of coseismically slipping, rate-weakening asperities, transferring stress to rate-strenghtening/conditionally stable surrounding regions that is released in a gradual aferslip decay is a convincing explanation of the model results. Such an anti-correlation is not so prominent nearer to the high afterslip patch in the north of the ruptured segment, although this could be due to some contamination of the co- and post-seismic signal with crustal tectonic signal, or due to an exceptional role of fluids transiently altering the frictional behaviour at this region, as supported by the considerable VpVs anomaly at this portion of the plate interface *Farías et al.* (e.g. 2011).

One outstanding issue that I feel that warrants immediate scrutiny is the sensitivity testing of our elastic dislocation modelling assumptions. The common limit of scrutiny paid to the dislocation model is the resolution testing with methods such as checkerboard analysis, adaptive patch size based on the resolution matrix (e.g. *Atzori and Antonioli*, 2011; *Barnhart and Lohman*, 2010), and experimentation with the effects of different inversion regularization approaches (e.g. *Johnson et al.*, 2012; *Evans and Meade*, 2012). In subduction zone dislocation models, a common practice is to allow freedom in the rake direction of slip on the individual patches, with the final rake direction of the slip on each patch often omitted from figures with the leader left to guess as to the respective rakes of each slip patch. Initial investigations into the sensitivity of the interseismic locking pattern to the constrained backslip azimuth show some striking differences within 15° of assumed

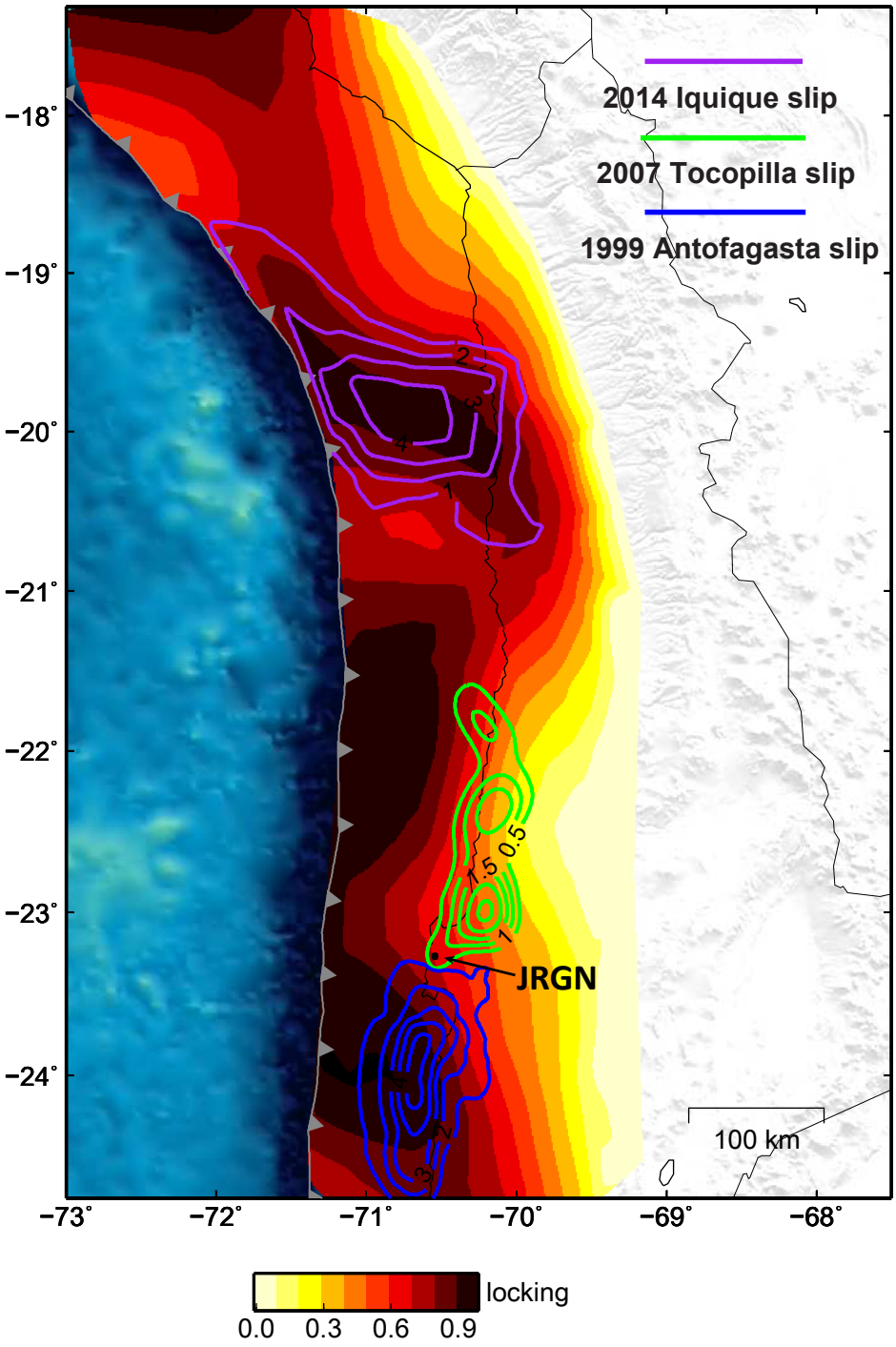

Figure 5.2: Figure taken from *Li et al.* (2015) showing the locking map that has considered the interseismic viscous flow of the subduction zone in the surface signal. The slip contours for recent earthquakes are shown overlain.

plate interface backslip azimuth (azimuth being the horizontal component of the 3-D backslip vector on each patch of the fault). Figure 5.3 show a slight change in the assumed azimuth can change the interpretation of rupture extents and it's relation to locking. For example, with a backslip azimuth fixed to 77.5° the peak rupture of the Pisagua-Iquique earthquake can be interpreted as being inhibited by the locked zone; i.e. the locked zone is acting as a barrier (*Aki*, 1984) in preventing a wider rupture on the interface. Conversely, for a backslip azimuth of 85°, the co-location of rupture and high locking suggests that the locked patch has ruptured as an asperity. Certainly, the ambiguity in the locking models due to freedom of the

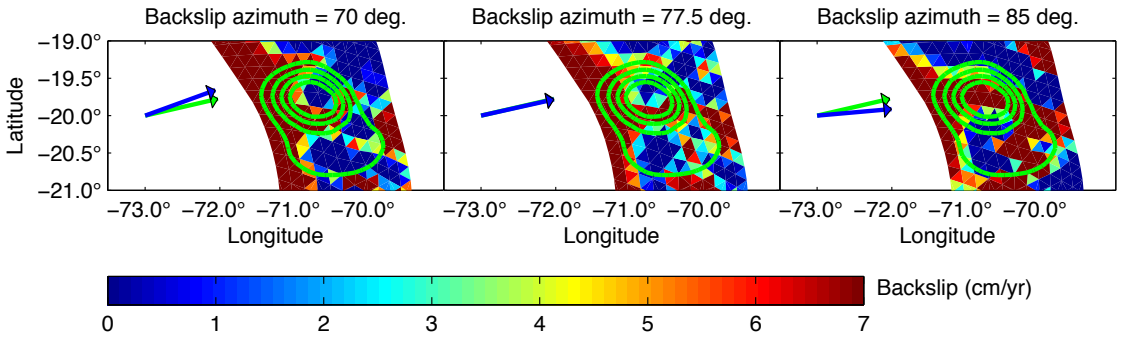

Figure 5.3: Locking in the Pisagua-Iquique Mw 8.1 2014 segment for three different constrained backslip azimuths. Locking pattern is sensitive to the backslip azimuth, which is often unconstrained in the inversion, and allowed to vary from patch to patch. Green contours show slip of the Mw 8.1 and largest aftershock (Mw 7.6) in 1 m intervals.

backslip rake is a research challenge that should be tackled as soon as possible, since many interpretations of the seismic cycle plate interface kinematics could change significantly with rakes of elastic dislocation better constrained.

In Chapter 3 we applied an azimuth constrained slip inversion, with azimuths constrained between 240-300°. The wide range of azimuths was allowed in this instance because the direction of afterslip is not well understood, especially since the best fitting range of parameters for simultaneous processes of re-locking and viscoelastic relaxation is non-unique. Evidence suggesting that such a range of slip azimuths for the inversion is valid can be found by looking at the range of failure azimuths of the aftershocks (fig 2.10). The better constraining of afterslip azimuth can help us to understand the interplay (respective dominance) of forces at the plate interface during different phases of the seismic cycle.

5.5 Conclusions

The main messages of the thesis can be summed up in the following list:

- **Postseismic processes can be separated if we make some assumptions about afterslip behaviour. We have called this approach the *Postseismic Straightening* method.**
- **Afterslip is a dominant early postseismic process (1-3 years) that is well captured due to the nearfield cGPS along the Maule 2010 Mw 8.8 segment. It's spatiotemporal features are well resolved in certain**

regions: afterslip is released as non-migrating pulses to produce the cumulative afterslip pattern. The comparison of afterslip to coseismic slip can reveal regions of the plate interface that are more likely to fail with large magnitude aftershocks.

- **Plate re-locking is a process that when modelled in combination with viscoelastic relaxation and afterslip significantly improves the model fits to the time series. Re-locking, when added to afterslip and viscoelastic relaxation, causes the horizontal displacements to veer with time.**
- **For most regions on the Maule segment plate interface, the moment release of aftershocks is much less than the moment release of afterslip, therefore the afterslip is predominantly aseismic.**
- **The Maule 2010 afterslip, separated using the Postseismic Straightening method, has a normalized decay time function that is in good agreement with the decay time function of the aftershocks.**
- **For the foreshock sequence before the Iquique-Pisagua Mw 8.1, the transient surface deformation is mostly explained by seismic slip. Nevertheless, we are able to distinguish bursts of aseismic slip which are interpreted to be the postseismic responses (probably afterslip) to the foreshocks.**
- **ΔCFS model for the spatial distribution of Maule 2010 aftershocks works better for larger magnitude aftershocks.**
- **While promising spatial relations exist between inter-, co-, and postseismic elastic dislocation kinematics, the degrees of freedom for the slip azimuth (rake) need to be further investigated, especially for the interseismic locking models which can be very sensitive to a constrained backslip azimuth.**
- **Viscoelastic relaxation becomes more of a dominant postseismic process with increasing time and with increasing distance from the rupture zone. For the 2010 Maule earthquake, the assumption of a purely elastic afterslip model works well in the first year due to the favourable locations of the cGPS network, with many stations close enough to pick up the dominating afterslip signal.**

5.6 Outlook and Recommendations

The insights from this study have only been possible due to the unprecedented cGPS measurement density and proximity to the rupture zones, as well as the availability of extensive seismic catalgues due to the excellent network of pre-existing and deployed seismometers. The separation of simultaneous postseismic processes would not have been feasible with a network as far away from the trench such as in the Japanese Tohoku Oki 2011 segment, due to the fact that such curvature in the signal diminishes with distance to the rupture zone. The recent advances in sea-floor

geodesy (e.g. *Bürgmann and Chadwell*, 2014; *Sun et al.*, 2014) are allowing us to take measurements even closer to the plate interface thereby improving our ability to model the plate interface kinematics and better constraining the rheological behaviour due to the availability of data close to the trench as well as in the far-field. The geodetic modelling community is moving towards an increased complexity of materials in the subduction zone model (e.g. *Hu et al.*, 2014) especially in an attempt to fit the vertical component of the postseismic data with a viscoelastic signal. I feel that significant progress needs to be made in the ways that we can efficiently explore the parameter space, taking into consideration run-times of FEM viscoelastic relaxation simulations and the non-uniqueness of parameter combinations.

In linking inter-, co-, and post-seismic kinematics a review of the many geophysical models, datasets, and data-products for the Maule earthquake could yield some additional insights and promising relationships between independently derived models and observations. Better understanding of the often significant differences in modelling results of independent research groups needs additional scrutiny: i.e. we must really understand "Why does my slip model look different to yours?". For the Pisagua-Iquique 2014 earthquake, the agreement within the independent research sections at GFZ was to use the same plate interface geometry in all modelling efforts presented between the research sections, thereby eliminating one potential source of model differences. The excellent data set for the Pisagua-Iquique 2014 earthquake spanning all phases of the seismic cycle (inter-, co-, and post-seismic) should allow a similar analysis of the plate interface kinematics and subduction zone seismic cycle processes, and will prove a useful case study to compare and contrast against the Maule 2010 research insights.

Bibliography

Aagaard, B. T., M. G. Knepley, and C. A. Williams (2013), A domain decomposition approach to implementing fault slip in finite-element models of quasi-static and dynamic crustal deformation, *Journal of Geophysical Research: Solid Earth*, *118*(6), 3059–3079.

Agurto, H., A. Rietbrock, I. Ryder, and M. Miller (2012), Seismic-afterslip characterization of the 2010 mw 8.8 maule, chile, earthquake based on moment tensor inversion, *Geophysical Research Letters*, *39*(20).

Aki, K. (1984), Asperities, barriers, characteristic earthquakes and strong motion prediction, *Journal of Geophysical Research: Solid Earth (1978–2012)*, *89*(B7), 5867–5872.

Aki, K., and P. G. Richards (2002), *Quantitative seismology*, vol. 1.

Altamimi, Z., X. Collilieux, J. Legrand, B. Garayt, and C. Boucher (2007), Itrf2005: A new release of the international terrestrial reference frame based on time series of station positions and earth orientation parameters, *Journal of Geophysical Research: Solid Earth (1978–2012)*, *112*(B9).

Altamimi, Z., X. Collilieux, and L. Métivier (2011), Itrf2008: an improved solution of the international terrestrial reference frame, *Journal of Geodesy*, *85*(8), 457–473.

Angiboust, S., P. Agard, H. Raimbourg, P. Yamato, and B. Huet (2011), Subduction interface processes recorded by eclogite-facies shear zones (monviso, w. alps), *Lithos*, *127*(1), 222–238.

Angiboust, S., P. Agard, P. Yamato, and H. Raimbourg (2012), Eclogite breccias in a subducted ophiolite: A record of intermediate-depth earthquakes?, *Geology*, *40*(8), 707–710.

Atzori, S., and A. Antonioli (2011), Optimal fault resolution in geodetic inversion of coseismic data, *Geophysical Journal International*, *185*(1), 529–538.

Audet, P., and S. Y. Schwartz (2013), Hydrologic control of forearc strength and seismicity in the costa rican subduction zone, *Nature Geoscience*, *6*(10), 852–855.

Barbot, S., N. Lapusta, and J.-P. Avouac (2012), Under the hood of the earthquake machine: Toward predictive modeling of the seismic cycle, *Science*, *336*(6082), 707–710.

Barnhart, W., and R. Lohman (2010), Automated fault model discretization for inversions for coseismic slip distributions, *Journal of Geophysical Research: Solid Earth (1978–2012)*, *115*(B10).

Bedford, J., M. Moreno, J. C. Baez, D. Lange, F. Tilmann, M. Rosenau, O. Heidbach, O. Oncken, M. Bartsch, A. Rietbrock, et al. (2013), A high-resolution, time-variable afterslip model for the 2010 maule mw= 8.8, chile megathrust earthquake, *Earth and Planetary Science Letters*, *383*, 26–36.

Bedford, J., M. Moreno, B. Schurr, M. Bartsch, and O. Oncken (2015), Investigating the final seismic swarm before the iquique-pisagua 2014 mw 8.1 by comparison of continuous gps and seismic foreshock data, *Geophysical Research Letters*.

Bevis, M., and A. Brown (2014), Trajectory models and reference frames for crustal motion geodesy, *Journal of Geodesy*, *88*(3), 283–311.

Bilham, R., and N. Ambraseys (2005), Apparent himalayan slip deficit from the summation of seismic moments for himalayan earthquakes, 1500–2000, *Current Science*, *88*(10), 1658–1663.

Bilham, R., R. Engdahl, N. Feldl, and S. Satyabala (2005), Partial and complete rupture of the indo-andaman plate boundary 1847-2004, *Seismological Research Letters*, *76*(3), 299–311.

Billen, M. I., and M. Gurnis (2001), A low viscosity wedge in subduction zones, *Earth and Planetary Science Letters*, *193*(1), 227–236.

Boehm, J., B. Werl, and H. Schuh (2006), Troposphere mapping functions for gps and very long baseline interferometry from european centre for medium-range weather forecasts operational analysis data, *Journal of Geophysical Research: Solid Earth (1978–2012)*, *111*(B2).

Brune, J. N. (1968), Seismic moment, seismicity, and rate of slip along major fault zones, *Journal of Geophysical Research*, *73*(2), 777–784.

Bürgmann, R., and D. Chadwell (2014), Seafloor geodesy, *Annual Review of Earth and Planetary Sciences*, *42*, 509–534.

Byrne, D. E., D. M. Davis, and L. R. Sykes (1988), Loci and maximum size of thrust earthquakes and the mechanics of the shallow region of subduction zones, *Tectonics*, *7*(4), 833–857.

Chlieh, M., J.-P. Avouac, V. Hjorleifsdottir, T.-R. A. Song, C. Ji, K. Sieh, A. Sladen, H. Hebert, L. Prawirodirdjo, Y. Bock, et al. (2007), Coseismic slip and afterslip of the great mw 9.15 sumatra–andaman earthquake of 2004, *Bulletin of the Seismological Society of America*, *97*(1A), S152–S173.

Chlieh, M., H. Perfettini, H. Tavera, J.-P. Avouac, D. Remy, J.-M. Nocquet, F. Rolandone, F. Bondoux, G. Gabalda, and S. Bonvalot (2011), Interseismic coupling and seismic potential along the central andes subduction zone, *Journal of Geophysical Research: Solid Earth (1978–2012)*, *116*(B12).

Clague, J. J., and P. T. Bobrowsky (1994), Tsunami deposits beneath tidal marshes on vancouver island, british columbia, *Geological Society of America Bulletin*, *106*(10), 1293–1303.

Comte, D., and M. Pardo (1991), Reappraisal of great historical earthquakes in the northern chile and southern peru seismic gaps, *Natural hazards*, *4*(1), 23–44.

Cubas, N., J. Avouac, Y. Leroy, and A. Pons (2013a), Low friction along the high slip patch of the 2011 mw 9.0 tohoku-oki earthquake required from the wedge structure and extensional splay faults, *Geophysical Research Letters*, *40*(16), 4231–4237.

Cubas, N., J.-P. Avouac, P. Souloumiac, and Y. Leroy (2013b), Megathrust friction determined from mechanical analysis of the forearc in the maule earthquake area, *Earth and Planetary Science Letters*, *381*, 92–103.

Dach, R., U. Hugentobler, P. Fridez, M. Meindl, et al. (2007), Bernese gps software version 5.0, *Astronomical Institute, University of Bern*, *640*, 114.

Dahlen, F. (1990), Critical taper model of fold-and-thrust belts and accretionary wedges, *Annual Review of Earth and Planetary Sciences*, *18*, 55.

Darwin, C. (1851), *Geological observations on coral reefs, volcanic islands, and on South America: Being the geology of the voyage of the Beagle, under the command of Captain Fitzroy, RN, during the years 1832 to 1836*, Smith, Elder.

Delouis, B., J.-M. Nocquet, and M. Vallée (2010), Slip distribution of the february 27, 2010 mw= 8.8 maule earthquake, central chile, from static and high-rate gps, insar, and broadband teleseismic data, *Geophysical Research Letters*, *37*(17).

DeMets, C., R. G. Gordon, D. F. Argus, and S. Stein (1994), Effect of recent revisions to the geomagnetic reversal time scale on estimates of current plate motions, *Geophysical research letters*, *21*(20), 2191–2194.

Dieterich, J. H. (1978), Time-dependent friction and the mechanics of stick-slip, *Pure and applied geophysics*, *116*(4-5), 790–806.

Dow, J. M., R. Neilan, and C. Rizos (2009), The international gnss service in a changing landscape of global navigation satellite systems, *Journal of Geodesy*, *83*(3-4), 191–198.

Evans, E. L., and B. J. Meade (2012), Geodetic imaging of coseismic slip and postseismic afterslip: Sparsity promoting methods applied to the great tohoku earthquake, *Geophysical Research Letters*, *39*(11).

Farías, M., D. Comte, S. Roecker, D. Carrizo, and M. Pardo (2011), Crustal extensional faulting triggered by the 2010 chilean earthquake: The pichilemu seismic sequence, *Tectonics*, *30*(6).

Freed, A. M., R. Bürgmann, E. Calais, and J. Freymueller (2006), Stress-dependent power-law flow in the upper mantle following the 2002 denali, alaska, earthquake, *Earth and Planetary Science Letters*, *252*(3), 481–489.

Fritz, H. M., C. M. Petroff, P. A. Catalán, R. Cienfuegos, P. Winckler, N. Kalligeris, R. Weiss, S. E. Barrientos, G. Meneses, C. Valderas-Bermejo, et al. (2011), Field survey of the 27 february 2010 chile tsunami, *Pure and Applied Geophysics*, *168*(11), 1989–2010.

Gordon, R. G., and S. Stein (1992), Global tectonics and space geodesy, *Science*, *256*(5055), 333.

Groß, K., U. Micksch, S. Team, T. R. Group, et al. (2008), The reflection seismic survey of project tipteq—the inventory of the chilean subduction zone at 38.2 s, *Geophysical Journal International*, *172*(2), 565–571.

Haberland, C., A. Rietbrock, D. Lange, K. Bataille, and T. Dahm (2009), Structure of the seismogenic zone of the southcentral chilean margin revealed by local earthquake traveltime tomography, *Journal of Geophysical Research: Solid Earth (1978–2012)*, *114*(B1).

Hayes, G. P., E. Bergman, K. L. Johnson, H. M. Benz, L. Brown, and A. S. Meltzer (2013), Seismotectonic framework of the 2010 february 27 mw 8.8 maule, chile earthquake sequence, *Geophysical Journal International*, p. ggt238.

Hayes, G. P., M. W. Herman, W. D. Barnhart, K. P. Furlong, S. Riquelme, H. M. Benz, E. Bergman, S. Barrientos, P. S. Earle, and S. Samsonov (2014), Continuing megathrust earthquake potential in chile after the 2014 iquique earthquake, *Nature*, *512*(7514), 295–298.

Heki, K., and Y. Mitsui (2013), Accelerated pacific plate subduction following interplate thrust earthquakes at the japan trench, *Earth and Planetary Science Letters*, *363*, 44–49.

Helmstetter, A., and B. E. Shaw (2009), Afterslip and aftershocks in the rate-and-state friction law, *Journal of Geophysical Research: Solid Earth (1978–2012)*, *114*(B1).

Hergert, T., and O. Heidbach (2006), New insights into the mechanism of postseismic stress relaxation exemplified by the 23 june 2001 mw= 8.4 earthquake in southern peru, *Geophysical research letters*, *33*(2).

Hicks, S. P., A. Rietbrock, C. A. Haberland, I. Ryder, M. Simons, and A. Tassara (2012), The 2010 mw 8.8 maule, chile earthquake: Nucleation and rupture propagation controlled by a subducted topographic high, *Geophysical Research Letters*, *39*(19).

Hsu, Y.-J., M. Simons, J.-P. Avouac, J. Galetzka, K. Sieh, M. Chlieh, D. Natawidjaja, L. Prawirodirdjo, and Y. Bock (2006), Frictional afterslip following the 2005 nias-simeulue earthquake, sumatra, *Science*, *312*(5782), 1921–1926.

Hsu, Y.-J., P. Segall, S.-B. Yu, L.-C. Kuo, and C. A. Williams (2007), Temporal and spatial variations of post-seismic deformation following the 1999 chi-chi, taiwan earthquake, *Geophysical Journal International*, *169*(2), 367–379.

Hu, Y., and K. Wang (2012), Spherical-earth finite element model of short-term postseismic deformation following the 2004 sumatra earthquake, *Journal of Geophysical Research: Solid Earth (1978–2012)*, *117*(B5).

Hu, Y., K. Wang, J. He, J. Klotz, and G. Khazaradze (2004), Three-dimensional viscoelastic finite element model for postseismic deformation of the great 1960 chile earthquake, *Journal of Geophysical Research: Solid Earth (1978–2012)*, *109*(B12).

Hu, Y., R. Bürgmann, J. T. Freymueller, P. Banerjee, and K. Wang (2014), Contributions of poroelastic rebound and a weak volcanic arc to the postseismic deformation of the 2011 tohoku earthquake, *Earth, Planets and Space*, *66*(1), 1–10.

Hughes, K. L., T. Masterlark, and W. D. Mooney (2010), Poroelastic stress-triggering of the 2005 m8. 7 nias earthquake by the 2004 m9. 2 sumatra–andaman earthquake, *Earth and Planetary Science Letters*, *293*(3), 289–299.

Husen, S., E. Kissling, and E. R. Flueh (2000), Local earthquake tomography of shallow subduction in north chile: A combined onshore and offshore study, *Journal of Geophysical Research: Solid Earth (1978–2012)*, *105*(B12), 28,183–28,198.

James, T. S., J. J. Clague, K. Wang, and I. Hutchinson (2000), Postglacial rebound at the northern cascadia subduction zone, *Quaternary Science Reviews*, *19*(14), 1527–1541.

Johnson, K. M., J. Fukuda, and P. Segall (2012), Challenging the rate-state asperity model: Afterslip following the 2011 m9 tohoku-oki, japan, earthquake, *Geophysical Research Letters*, *39*(20).

Kanamori, H. (1973), Mode of strain release associated with major earthquakes in japan, *Annual Review of Earth and Planetary Sciences*, *1*, 213.

Kanamori, H., and E. E. Brodsky (2004), The physics of earthquakes, *Reports on Progress in Physics*, *67*(8), 1429.

Kanda, R. V., and M. Simons (2010), An elastic plate model for interseismic deformation in subduction zones, *Journal of Geophysical Research: Solid Earth (1978–2012)*, *115*(B3).

Kato, A., and S. Nakagawa (2014), Multiple slow-slip events during a foreshock sequence of the 2014 iquique, chile mw 8.1 earthquake, *Geophysical Research Letters*, *41*(15), 5420–5427.

Kazemian, J., K. Tiampo, W. Klein, and R. Dominguez (2015), Foreshock and aftershocks in simple earthquake models, *Physical review letters*, *114*(8), 088,501.

King, G. C., R. S. Stein, and J. Lin (1994), Static stress changes and the triggering of earthquakes, *Bulletin of the Seismological Society of America*, *84*(3), 935–953.

Kiser, E., and M. Ishii (2011), The 2010 mw 8.8 chile earthquake: Triggering on multiple segments and frequency-dependent rupture behavior, *Geophysical Research Letters*, *38*(7).

Kositsky, A., and J.-P. Avouac (2010), Inverting geodetic time series with a principal component analysis-based inversion method, *Journal of Geophysical Research: Solid Earth (1978–2012)*, *115*(B3).

Lamb, S. (2006), Shear stresses on megathrusts: Implications for mountain building behind subduction zones, *Journal of Geophysical Research: Solid Earth (1978–2012)*, *111*(B7).

Lange, D., F. Tilmann, S. E. Barrientos, E. Contreras-Reyes, P. Methe, M. Moreno, B. Heit, H. Agurto, P. Bernard, J.-P. Vilotte, et al. (2012), Aftershock seismicity of the 27 february 2010 mw 8.8 maule earthquake rupture zone, *Earth and Planetary Science Letters*, *317*, 413–425.

Lange, D., J. Bedford, M. Moreno, F. Tilmann, J. Baez, M. Bevis, and F. Krüger (2014), Comparison of postseismic afterslip models with aftershock seismicity for three subduction-zone earthquakes: Nias 2005, maule 2010 and tohoku 2011, *Geophysical Journal International*, *199*(2), 784–799.

Larsen, C. F., R. J. Motyka, J. T. Freymueller, K. A. Echelmeyer, and E. R. Ivins (2005), Rapid viscoelastic uplift in southeast alaska caused by post-little ice age glacial retreat, *Earth and Planetary Science Letters*, *237*(3), 548–560.

Lay, T., and H. Kanamori (1981), An asperity model of large earthquake sequences, *Earthquake Prediction*, pp. 579–592.

Lay, T., H. Kanamori, C. J. Ammon, K. D. Koper, A. R. Hutko, L. Ye, H. Yue, and T. M. Rushing (2012), Depth-varying rupture properties of subduction zone megathrust faults, *Journal of Geophysical Research: Solid Earth (1978–2012)*, *117*(B4).

Li, S., M. Moreno, J. Bedford, M. Rosenau, and O. Oncken (2015), Revisiting viscoelastic effects on interseismic deformation and locking degree: a case study of the peru-north chile subduction zone, *Journal of Geophysical Research: Solid Earth*.

Li, Y.-G., P. Chen, E. S. Cochran, J. E. Vidale, and T. Burdette (2006), Seismic evidence for rock damage and healing on the san andreas fault associated with the 2004 m 6.0 parkfield earthquake, *Bulletin of the Seismological Society of America*, *96*(4B), S349–S363.

Lieser, K., I. Grevemeyer, D. Lange, E. Flueh, F. Tilmann, and E. Contreras-Reyes (2014), Splay fault activity revealed by aftershocks of the 2010 mw 8.8 maule earthquake, central chile, *Geology*, *42*(9), 823–826.

Lohrmann, J., N. Kukowski, J. Adam, and O. Oncken (2003), The impact of analogue material properties on the geometry, kinematics, and dynamics of convergent sand wedges, *Journal of Structural Geology*, *25*(10), 1691–1711.

Lorito, S., F. Romano, S. Atzori, X. Tong, A. Avallone, J. McCloskey, M. Cocco, E. Boschi, and A. Piatanesi (2011), Limited overlap between the seismic gap and coseismic slip of the great 2010 chile earthquake, *Nature Geoscience*, *4*(3), 173–177.

Marone, C. (1998), Laboratory-derived friction laws and their application to seismic faulting, *Annual Review of Earth and Planetary Sciences*, *26*(1), 643–696.

Marone, C. J., C. Scholtz, and R. Bilham (1991), On the mechanics of earthquake afterslip, *Journal of Geophysical Research: Solid Earth (1978–2012)*, *96*(B5), 8441–8452.

McKenzie, D., and J. Jackson (2012), Tsunami earthquake generation by the release of gravitational potential energy, *Earth and Planetary Science Letters*, *345*, 1–8.

Melnick, D., B. Bookhagen, M. R. Strecker, and H. P. Echtler (2009), Segmentation of megathrust rupture zones from fore-arc deformation patterns over hundreds to millions of years, arauco peninsula, chile, *Journal of Geophysical Research: Solid Earth (1978–2012)*, *114*(B1).

Meng, L., H. Huang, R. Bürgmann, J. P. Ampuero, and A. Strader (2015), Dual megathrust slip behaviors of the 2014 iquique earthquake sequence, *Earth and Planetary Science Letters*, *411*, 177–187.

Menke, W. (1989a), Geophysical data analysis: Discrete inverse theory, *International Geophysics Series, New York: Academic Press, 1989, Rev. ed.*, *1*.

Menke, W. (1989b), Geophysical data analysis:"discrete inverse theory" 1989, *Orlando, Fla.: Academic Press. xii*, *260*.

Metois, M., A. Socquet, and C. Vigny (2012), Interseismic coupling, segmentation and mechanical behavior of the central chile subduction zone, *Journal of Geophysical Research: Solid Earth (1978–2012)*, *117*(B3).

Miyazaki, S.-i., P. Segall, J. Fukuda, and T. Kato (2004), Space time distribution of afterslip following the 2003 tokachi-oki earthquake: Implications for variations in fault zone frictional properties, *Geophysical Research Letters*, *31*(6).

Moreno, M., J. Bolte, J. Klotz, and D. Melnick (2009), Impact of megathrust geometry on inversion of coseismic slip from geodetic data: Application to the 1960 chile earthquake, *Geophysical Research Letters*, *36*(16).

Moreno, M., M. Rosenau, and O. Oncken (2010), 2010 maule earthquake slip correlates with pre-seismic locking of andean subduction zone, *Nature*, *467*(7312), 198–202.

Moreno, M., D. Melnick, M. Rosenau, J. Bolte, J. Klotz, H. Echtler, J. Baez, K. Bataille, J. Chen, M. Bevis, et al. (2011), Heterogeneous plate locking in the south–central chile subduction zone: Building up the next great earthquake, *Earth and Planetary Science Letters*, *305*(3), 413–424.

Moreno, M., D. Melnick, M. Rosenau, J. Baez, J. Klotz, O. Oncken, A. Tassara, J. Chen, K. Bataille, M. Bevis, et al. (2012), Toward understanding tectonic control on the m w 8.8 2010 maule chile earthquake, *Earth and Planetary Science Letters*, *321*, 152–165.

Moreno, M., C. Haberland, O. Oncken, A. Rietbrock, S. Angiboust, and O. Heidbach (2014), Locking of the chile subduction zone controlled by fluid pressure before the 2010 earthquake, *Nature Geoscience*, *7*(4), 292–296.

Mouslopoulou, V., D. Moraetis, and C. Fassoulas (2011), Identifying past earthquakes on carbonate faults: Advances and limitations of the 'rare earth element'method based on analysis of the spili fault, crete, greece, *Earth and Planetary Science Letters*, *309*(1), 45–55.

Naif, S., K. Key, S. Constable, and R. Evans (2013), Melt-rich channel observed at the lithosphere-asthenosphere boundary, *Nature*, *495*(7441), 356–359.

Nur, A., and G. Mavko (1974), Postseismic viscoelastic rebound, *Science*, *183*(4121), 204–206.

Okada, Y. (1985), Surface deformation due to shear and tensile faults in a half-space, *Bulletin of the seismological society of America*, *75*(4), 1135–1154.

Okada, Y. (1992), Internal deformation due to shear and tensile faults in a half-space, *Bulletin of the Seismological Society of America*, *82*(2), 1018–1040.

Oleskevich, D., R. Hyndman, and K. Wang (1999), The updip and downdip limits to great subduction earthquakes: Thermal and structural models of cascadia, south alaska, sw japan, and chile, *Journal of Geophysical Research: Solid Earth (1978–2012)*, *104*(B7), 14,965–14,991.

Oncken, O., G. Asch, C. Haberland, J. Metchie, S. Sobolev, M. Stiller, X. Yuan, H. Brasse, S. Buske, P. Giese, et al. (2003), Seismic imaging of a convergent continental margin and plateau in the central andes (andean continental research project 1996 (ancorp'96)), *Journal of Geophysical Research: Solid Earth (1978–2012)*, *108*(B7).

Ozawa, S., T. Nishimura, H. Suito, T. Kobayashi, M. Tobita, and T. Imakiire (2011), Coseismic and postseismic slip of the 2011 magnitude-9 tohoku-oki earthquake, *Nature*, *475*(7356), 373–376.

Page, M. T., S. Custódio, R. J. Archuleta, and J. Carlson (2009), Constraining earthquake source inversions with gps data: 1. resolution-based removal of artifacts, *Journal of Geophysical Research: Solid Earth (1978–2012)*, *114*(B1).

Perfettini, H., and J.-P. Avouac (2007), Modeling afterslip and aftershocks following the 1992 landers earthquake, *Journal of geophysical research*, *112*(B7).

Perfettini, H., J.-P. Avouac, H. Tavera, A. Kositsky, J.-M. Nocquet, F. Bondoux, M. Chlieh, A. Sladen, L. Audin, D. L. Farber, et al. (2010), Seismic and aseismic slip on the central peru megathrust, *Nature*, *465*(7294), 78–81.

Pollitz, F. F., B. Brooks, X. Tong, M. G. Bevis, J. H. Foster, R. Bürgmann, R. Smalley, C. Vigny, A. Socquet, J.-C. Ruegg, et al. (2011), Coseismic slip distribution of the february 27, 2010 mw 8.8 maule, chile earthquake, *Geophysical Research Letters*, *38*(9).

Radiguet, M., F. Cotton, M. Vergnolle, M. Campillo, B. Valette, V. Kostoglodov, and N. Cotte (2011), Spatial and temporal evolution of a long term slow slip event: the 2006 guerrero slow slip event, *Geophysical Journal International*, *184*(2), 816–828.

Reid, H. F. (1911), *The elastic-rebound theory of earthquakes*, University Press.

Rietbrock, A., I. Ryder, G. Hayes, C. Haberland, D. Comte, S. Roecker, and H. Lyon-Caen (2012), Aftershock seismicity of the 2010 maule mw= 8.8, chile, earthquake: Correlation between co-seismic slip models and aftershock distribution?, *Geophysical Research Letters*, *39*(8).

Rogers, G., and H. Dragert (2003), Episodic tremor and slip on the cascadia subduction zone: The chatter of silent slip, *Science*, *300*(5627), 1942–1943.

Rosenau, M., and O. Oncken (2012), Fault synchronization and the likelihood of giant earthquakes along subduction megathrusts, in *AGU Fall Meeting Abstracts*, vol. 1, p. 2481.

Ruegg, J., A. Rudloff, C. Vigny, R. Madariaga, J. De Chabalier, J. Campos, E. Kausel, S. Barrientos, and D. Dimitrov (2009), Interseismic strain accumulation measured by gps in the seismic gap between constitución and concepción in chile, *Physics of the Earth and Planetary Interiors*, *175*(1), 78–85.

Ruiz, S., R. Grandin, V. Dionicio, C. Satriano, A. Fuenzalida, C. Vigny, E. Kiraly, C. Meyer, J. C. Baez, S. Riquelme, et al. (2013), The constitución earthquake of 25 march 2012: A large aftershock of the maule earthquake near the bottom of the seismogenic zone, *Earth and Planetary Science Letters*, *377*, 347–357.

Ruiz, S., M. Metois, A. Fuenzalida, J. Ruiz, F. Leyton, R. Grandin, C. Vigny, R. Madariaga, and J. Campos (2014), Intense foreshocks and a slow slip event preceded the 2014 iquique mw 8.1 earthquake, *Science*, *345*(6201), 1165–1169.

Rundle, J. B. (1978), Viscoelastic crustal deformation by finite quasi-static sources, *Journal of Geophysical Research: Solid Earth (1978–2012)*, *83*(B12), 5937–5945.

Ryder, I., A. Rietbrock, K. Kelson, R. Bürgmann, M. Floyd, A. Socquet, C. Vigny, and D. Carrizo (2012), Large extensional aftershocks in the continental forearc triggered by the 2010 maule earthquake, chile, *Geophysical Journal International*, *188*(3), 879–890.

Santimano, T., M. Rosenau, and O. Oncken (2015), Intrinsic versus extrinsic variability of analogue sand-box experiments–insights from statistical analysis of repeated accretionary sand wedge experiments, *Journal of Structural Geology*, *75*, 80–100.

Satake, K., K. Shimazaki, Y. Tsuji, and K. Ueda (1996), Time and size of a giant earthquake in cascadia inferred from japanese tsunami records of january 1700, *Nature*, *379*(6562), 246–249.

Sato, M., T. Ishikawa, N. Ujihara, S. Yoshida, M. Fujita, M. Mochizuki, and A. Asada (2011), Displacement above the hypocenter of the 2011 tohoku-oki earthquake, *Science*, *332*(6036), 1395–1395.

Savage, J. (1983), A dislocation model of strain accumulation and release at a subduction zone, *J. geophys. Res*, *88*(6), 4984–4996.

Scholz, C. H. (1998), Earthquakes and friction laws, *Nature*, *391*(6662), 37–42.

Schurr, B., G. Asch, S. Hainzl, J. Bedford, A. Hoechner, M. Palo, R. Wang, M. Moreno, M. Bartsch, Y. Zhang, et al. (2014), Gradual unlocking of plate boundary controlled initiation of the 2014 iquique earthquake, *Nature*.

Segall, P., and M. Matthews (1997), Time dependent inversion of geodetic data, *Journal of Geophysical Research: Solid Earth (1978–2012)*, *102*(B10), 22,391–22,409.

Segall, P., R. Bürgmann, and M. Matthews (2000), Time-dependent triggered afterslip following the 1989 loma prieta earthquake, *Journal of Geophysical Research: Solid Earth (1978–2012)*, *105*(B3), 5615–5634.

Shapiro, S., R. Patzig, E. Rothert, and J. Rindschwentner (2003), Triggering of seismicity by pore-pressure perturbations: permeability-related signatures of the phenomenon, *Pure and applied geophysics*, *160*(5-6), 1051–1066.

Shirzaei, M., R. Bürgmann, N. Uchida, Y. Hu, F. Pollitz, and T. Matsuzawa (2014), Seismic versus aseismic slip: Probing mechanical properties of the northeast japan subduction zone, *Earth and Planetary Science Letters*, *406*, 7–13.

Simons, M., S. E. Minson, A. Sladen, F. Ortega, J. Jiang, S. E. Owen, L. Meng, J.-P. Ampuero, S. Wei, R. Chu, et al. (2011), The 2011 magnitude 9.0 tohoku-oki earthquake: Mosaicking the megathrust from seconds to centuries, *science*, *332*(6036), 1421–1425.

Song, T.-R. A., and M. Simons (2003), Large trench-parallel gravity variations predict seismogenic behavior in subduction zones, *Science*, *301*(5633), 630–633.

Strasser, F. O., M. Arango, and J. J. Bommer (2010), Scaling of the source dimensions of interface and intraslab subduction-zone earthquakes with moment magnitude, *Seismological Research Letters*, *81*(6), 941–950.

Sun, T., and K. Wang (2015), Viscoelastic relaxation following subduction earthquakes and its effects on afterslip determination, *Journal of Geophysical Research: Solid Earth*, *120*(2), 1329–1344.

Sun, T., K. Wang, T. Iinuma, R. Hino, J. He, H. Fujimoto, M. Kido, Y. Osada, S. Miura, Y. Ohta, et al. (2014), Prevalence of viscoelastic relaxation after the 2011 tohoku-oki earthquake, *Nature*, *514*(7520), 84–87.

Tajima, F., J. Mori, and B. L. Kennett (2013), A review of the 2011 tohoku-oki earthquake (mw 9.0): Large-scale rupture across heterogeneous plate coupling, *Tectonophysics*, *586*, 15–34.

Tassara, A., and A. Echaurren (2012), Anatomy of the andean subduction zone: three-dimensional density model upgraded and compared against global-scale models, *Geophysical Journal International*, *189*(1), 161–168.

Tenthorey, E., S. F. Cox, and H. F. Todd (2003), Evolution of strength recovery and permeability during fluid–rock reaction in experimental fault zones, *Earth and Planetary Science Letters*, *206*(1), 161–172.

Tilmann, F., T. Craig, I. Grevemeyer, B. Suwargadi, H. Kopp, and E. Flueh (2010), The updip seismic/aseismic transition of the sumatra megathrust illuminated by aftershocks of the 2004 aceh-andaman and 2005 nias events, *Geophysical Journal International*, *181*(3), 1261–1274.

Tsuji, T., Y. Ito, M. Kido, Y. Osada, H. Fujimoto, J. Ashi, M. Kinoshita, and T. Matsuoka (2011), Potential tsunamigenic faults of the 2011 off the pacific coast of tohoku earthquake, *Earth, planets and space*, *63*(7), 831–834.

Turcotte, D. L., and G. Schubert (2014), *Geodynamics*, Cambridge University Press.

Vigny, C., W. J. Simons, S. Abu, R. Bamphenyu, C. Satirapod, N. Choosakul, C. Subarya, A. Socquet, K. Omar, H. Abidin, et al. (2005), Insight into the 2004 sumatra–andaman earthquake from gps measurements in southeast asia, *Nature*, *436*(7048), 201–206.

Vigny, C., A. Socquet, S. Peyrat, J.-C. Ruegg, M. Métois, R. Madariaga, S. Morvan, M. Lancieri, R. Lacassin, J. Campos, et al. (2011), The 2010 mw 8.8 maule megathrust earthquake of central chile, monitored by gps, *Science*, *332*(6036), 1417–1421.

Wallace, L. M., and J. Beavan (2010), Diverse slow slip behavior at the hikurangi subduction margin, new zealand, *Journal of Geophysical Research: Solid Earth (1978–2012)*, *115*(B12).

Wang, D., and J. Mori (2011), Frequency-dependent energy radiation and fault coupling for the 2010 mw8. 8 maule, chile, and 2011 mw9. 0 tohoku, japan, earthquakes, *Geophysical Research Letters*, *38*(22).

Wang, H. (2000), *Theory of linear poroelasticity with applications to geomechanics and hydrogeology*, Princeton University Press.

Wang, K., Y. Hu, and J. He (2012), Deformation cycles of subduction earthquakes in a viscoelastic earth, *Nature*, *484*(7394), 327–332.

Wdowinski, S., Y. Bock, J. Zhang, P. Fang, J. Genrich, et al. (1997), Southern california permanent gps geodetic array: spatial filtering of daily positions for estimating coseismic and postseismic displacements induced by the 1992 landers earthquake, *Journal of Geophysical Research-Part B-Solid Earth-Printed Edition*, *102*(8), 18,057–18,070.

Wells, D. L., and K. J. Coppersmith (1994), New empirical relationships among magnitude, rupture length, rupture width, rupture area, and surface displacement, *Bulletin of the Seismological Society of America*, *84*(4), 974–1002.

Yáñez, G. A., C. R. Ranero, R. Huene, and J. Díaz (2001), Magnetic anomaly interpretation across the southern central andes (32–34 s): The role of the juan fernández ridge in the late tertiary evolution of the margin, *Journal of Geophysical Research: Solid Earth (1978–2012)*, *106*(B4), 6325–6345.

Yao, L., T. Shimamoto, S. Ma, R. Han, and K. Mizoguchi (2013), Rapid postseismic strength recovery of pingxi fault gouge from the longmenshan fault system: Experiments and implications for the mechanisms of high-velocity weakening of faults, *Journal of Geophysical Research: Solid Earth*, *118*(8), 4547–4563.

Zienkiewicz, O., and R. Taylor (1994), *The Finite Element Method*, McGraw Hill.

Appendices

Appendix A

Afterslip model appendix

- Shown in this appendix chapter is the map of station locations (corresponding to the table of station usage), and the time series fits of the models.
- Table of afterslip model station usage "*Afterslip_model_station_usage.xlsx*" can be found on the CD provided and also can be downloaded from this link. The table shows which stations were used in the inversion each inversion (labeled in calendar days starting at January 1st 2010) contributing to the total afterslip model. Red background and '1' indicate the station was used, whereas white background and '0' indicate that the station was not used. Green background and '2' indicate that a station was used but the data contained interpolated points.
- Animation of the afterslip model can be found on the CD provided and can also be downloaded from this link. The animation shows time windows of slip updip (left panel) and cumulative slip updip (right panel) for the afterslip model between postseismic days 20-412. Each time window has a moment release in the top 50km of the plate interface equivalent to an Mw range of 7.3-7.6. Horizontal data vectors are show in magenta and the modelled vectors are shown in green. Only prediction vectors are shown on the cumulative model since the data availability of the model varies with time.

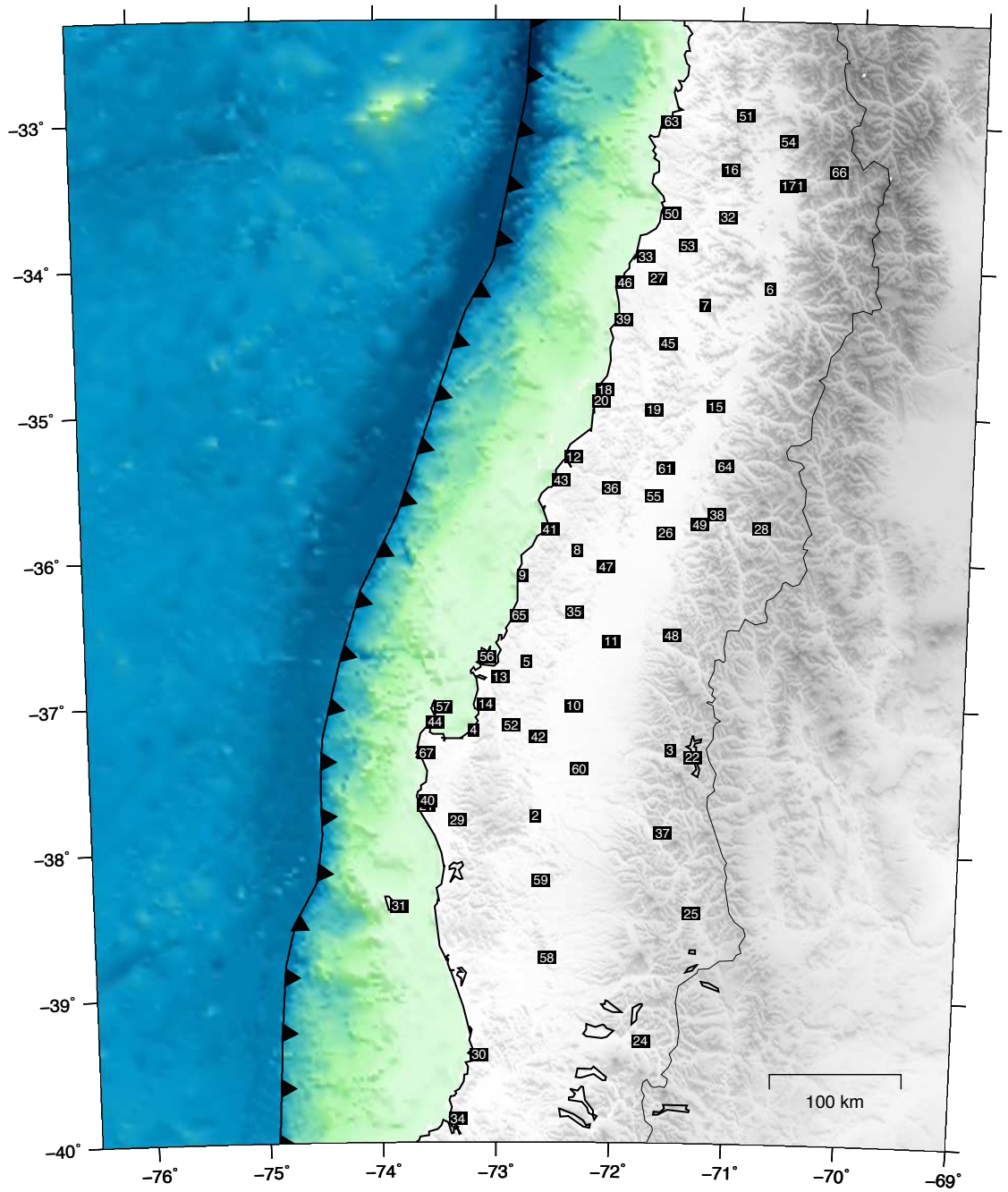

Figure A.1: Map of cGPS stations. Numbers correspond to the stations numbered in the first column of the table in file "*Afterslip_model_station_usage.xlsx*".

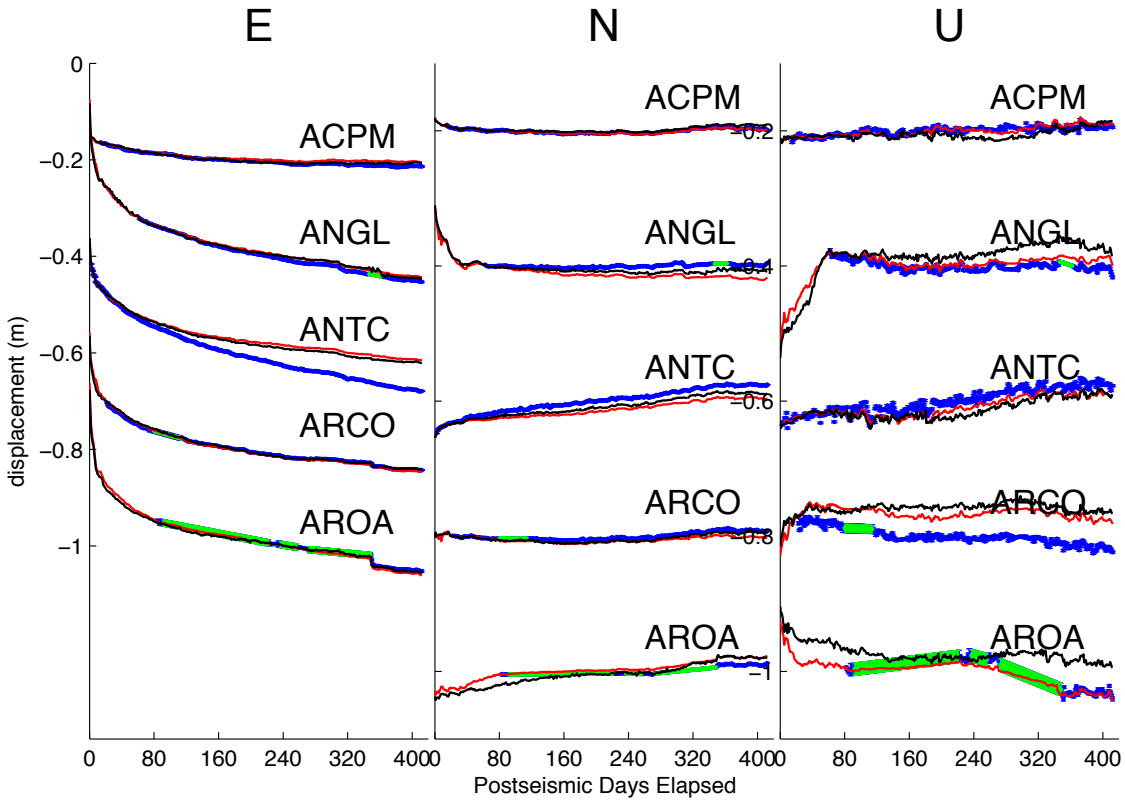

Figure A.2: Alphabetically listed timeseries of model predictions and data. Blue, green, and red points represent the data, interpolated data, and the model predictions respectively. Black line represents the model fit to the data when the interpolated points (green) are omitted from the inversion.

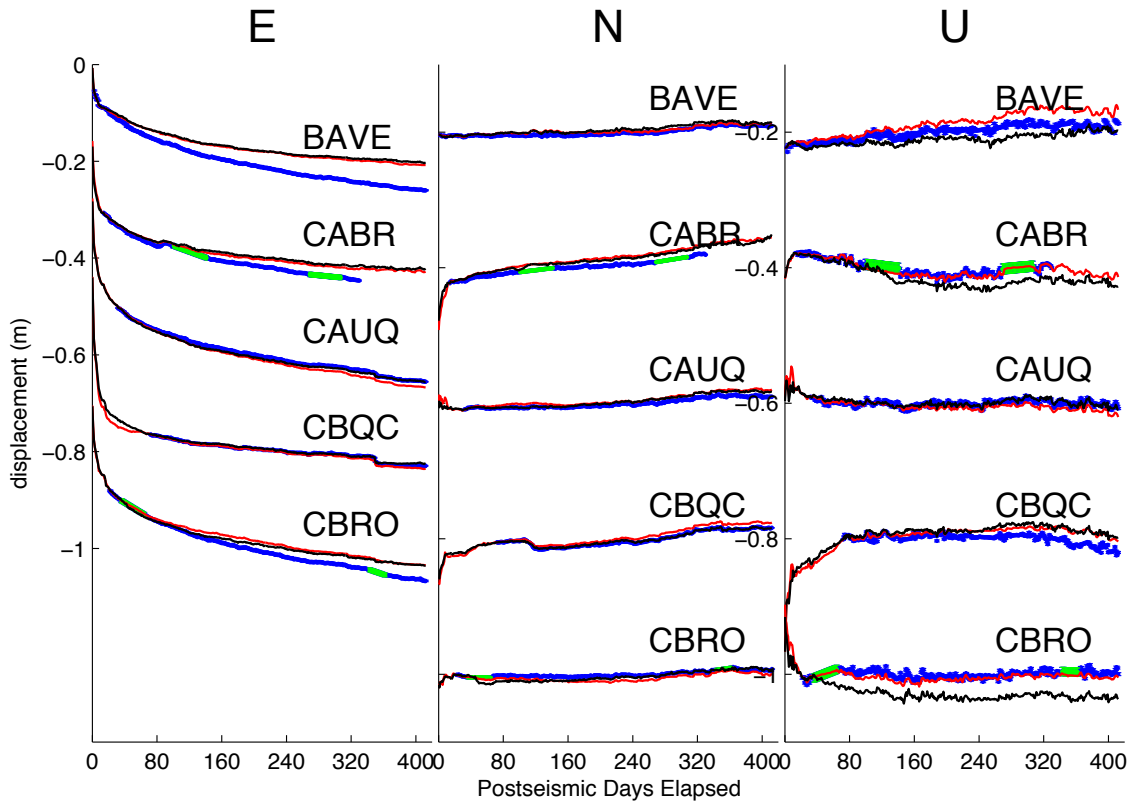

Figure A.3: Continuation of the alphabetically listed timeseries of model predictions and data. Blue, green, and red points represent the data, interpolated data, and the model predictions respectively. Black line represents the model fit to the data when the interpolated points (green) are omitted from the inversion.

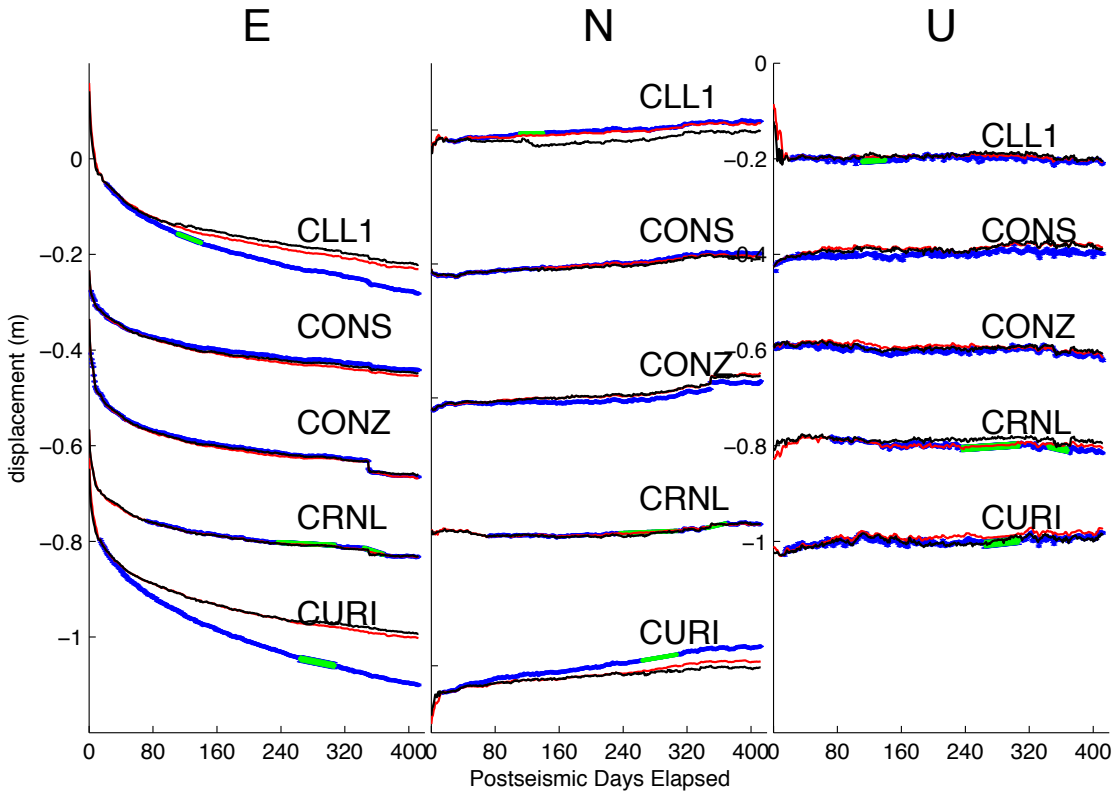

Figure A.4: Continuation of the alphabetically listed timeseries of model predictions and data. Blue, green, and red points represent the data, interpolated data, and the model predictions respectively. Black line represents the model fit to the data when the interpolated points (green) are omitted from the inversion.

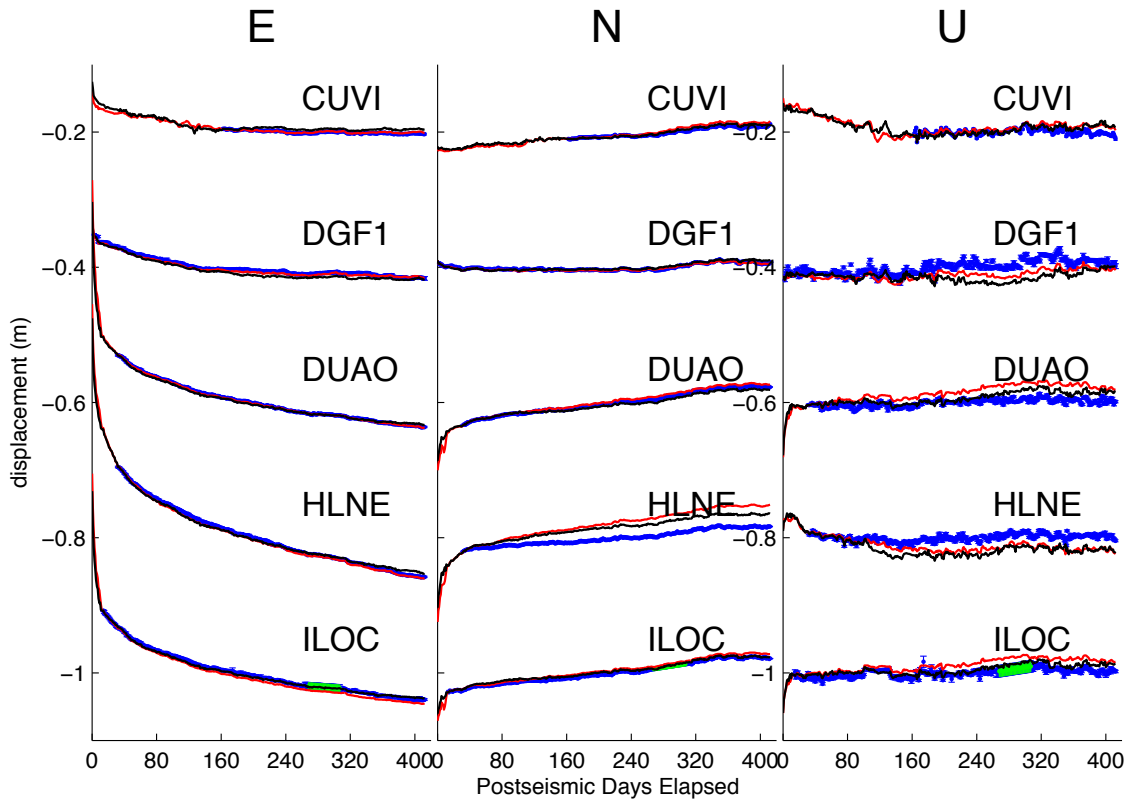

Figure A.5: Continuation of the alphabetically listed timeseries of model predictions and data. Blue, green, and red points represent the data, interpolated data, and the model predictions respectively. Black line represents the model fit to the data when the interpolated points (green) are omitted from the inversion.

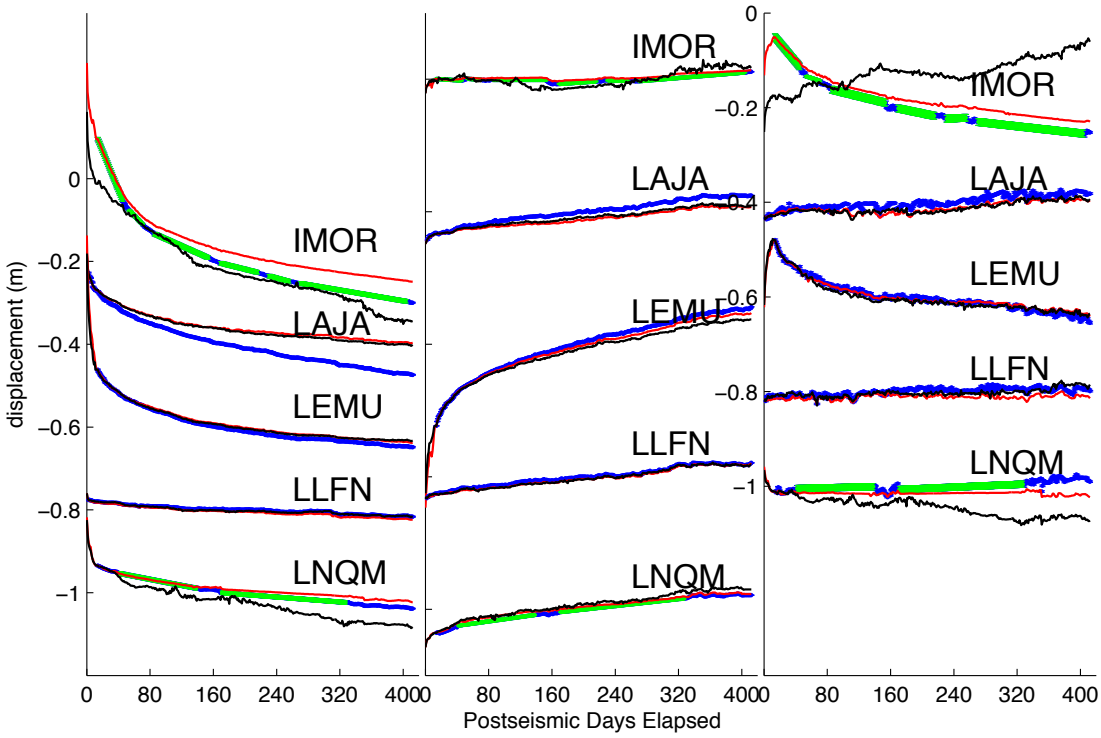

Figure A.6: Continuation of the alphabetically listed timeseries of model predictions and data. Blue, green, and red points represent the data, interpolated data, and the model predictions respectively. Black line represents the model fit to the data when the interpolated points (green) are omitted from the inversion.

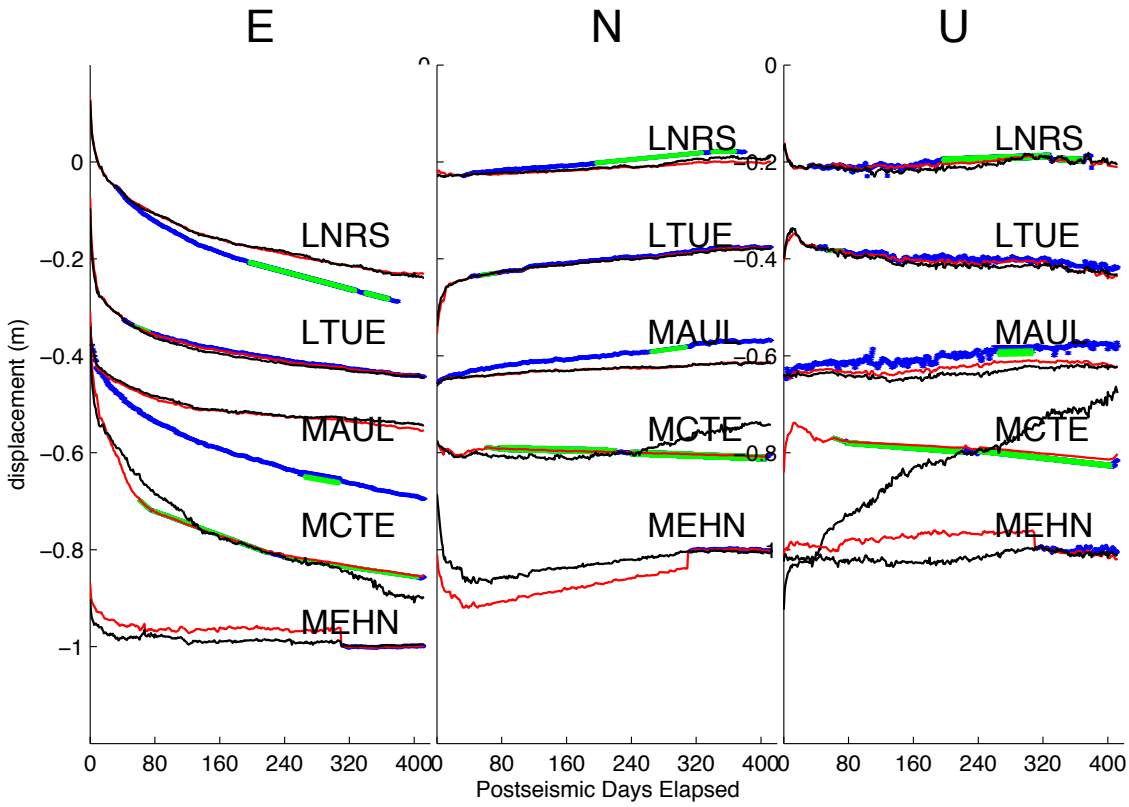

Figure A.7: Continuation of the alphabetically listed timeseries of model predictions and data. Blue, green, and red points represent the data, interpolated data, and the model predictions respectively. Black line represents the model fit to the data when the interpolated points (green) are omitted from the inversion.

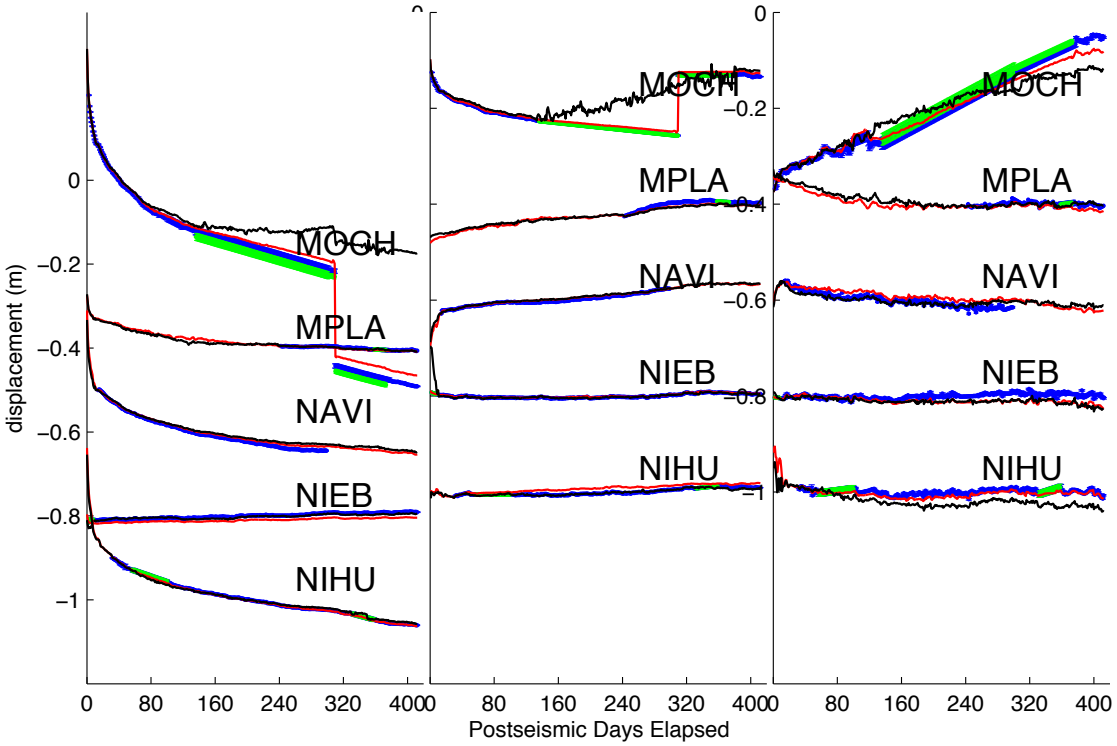

Figure A.8: Continuation of the alphabetically listed timeseries of model predictions and data. Blue, green, and red points represent the data, interpolated data, and the model predictions respectively. Black line represents the model fit to the data when the interpolated points (green) are omitted from the inversion.

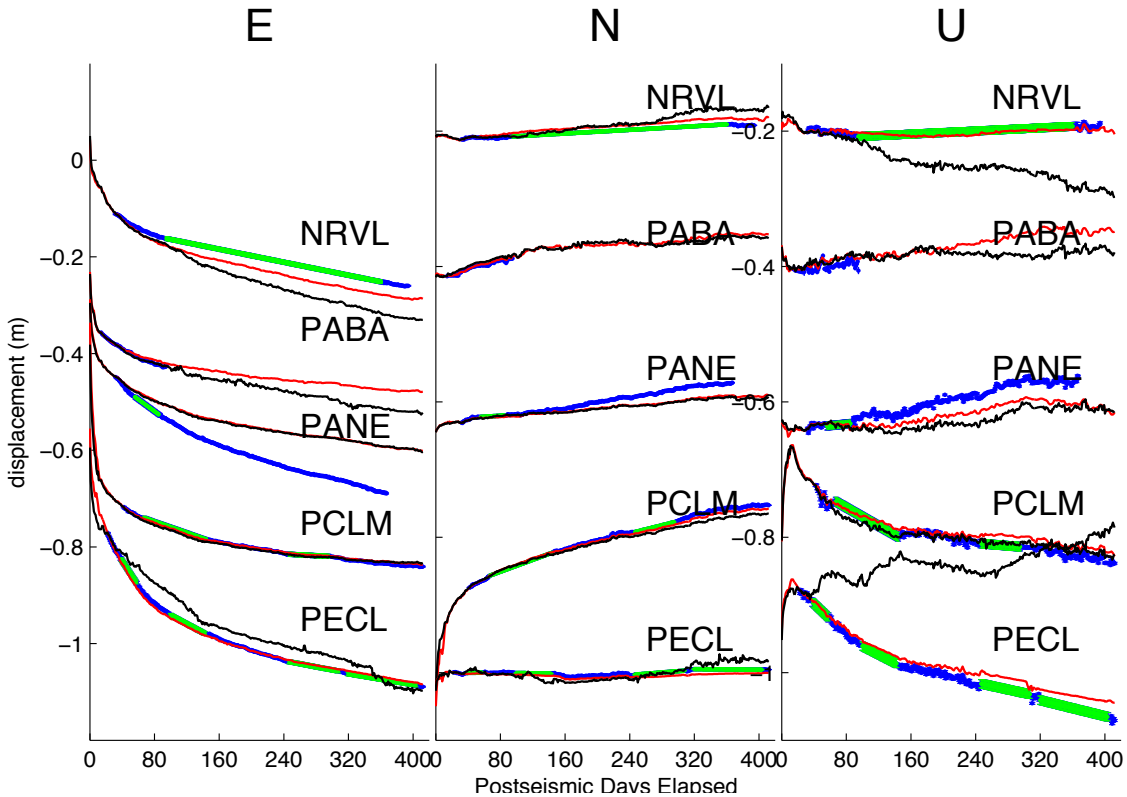

Figure A.9: Continuation of the alphabetically listed timeseries of model predictions and data. Blue, green, and red points represent the data, interpolated data, and the model predictions respectively. Black line represents the model fit to the data when the interpolated points (green) are omitted from the inversion.

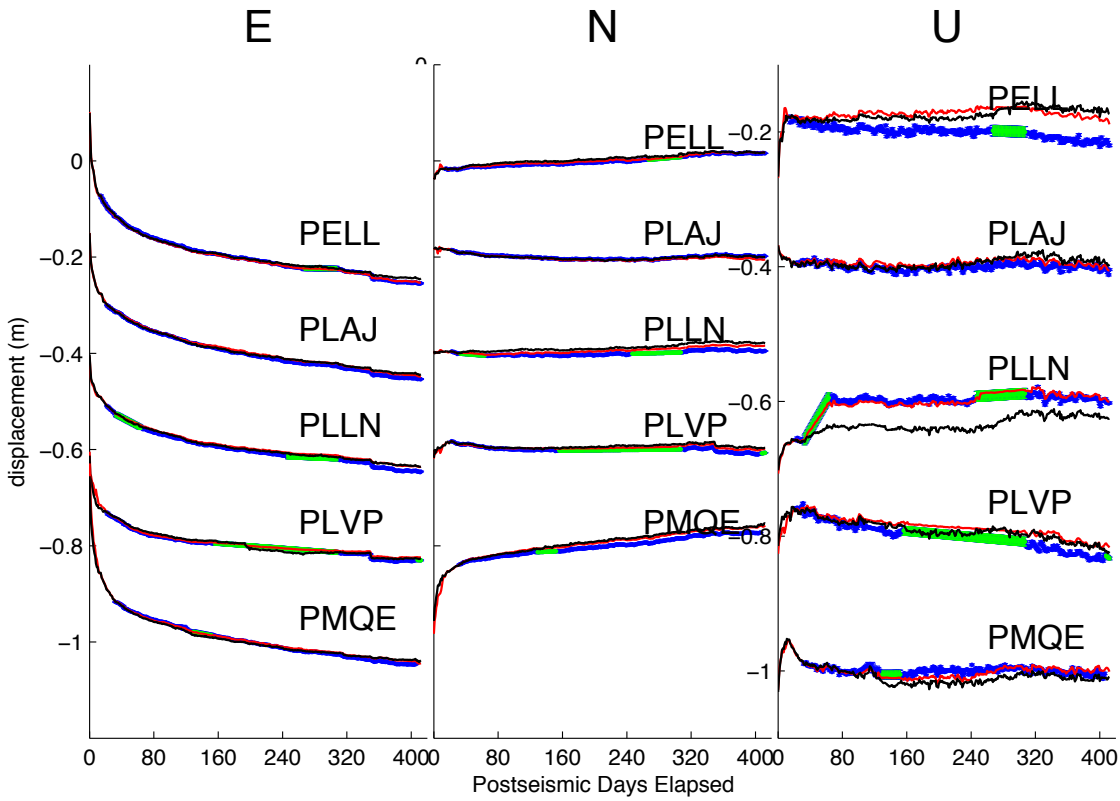

Figure A.10: Continuation of the alphabetically listed timeseries of model predictions and data. Blue, green, and red points represent the data, interpolated data, and the model predictions respectively. Black line represents the model fit to the data when the interpolated points (green) are omitted from the inversion.

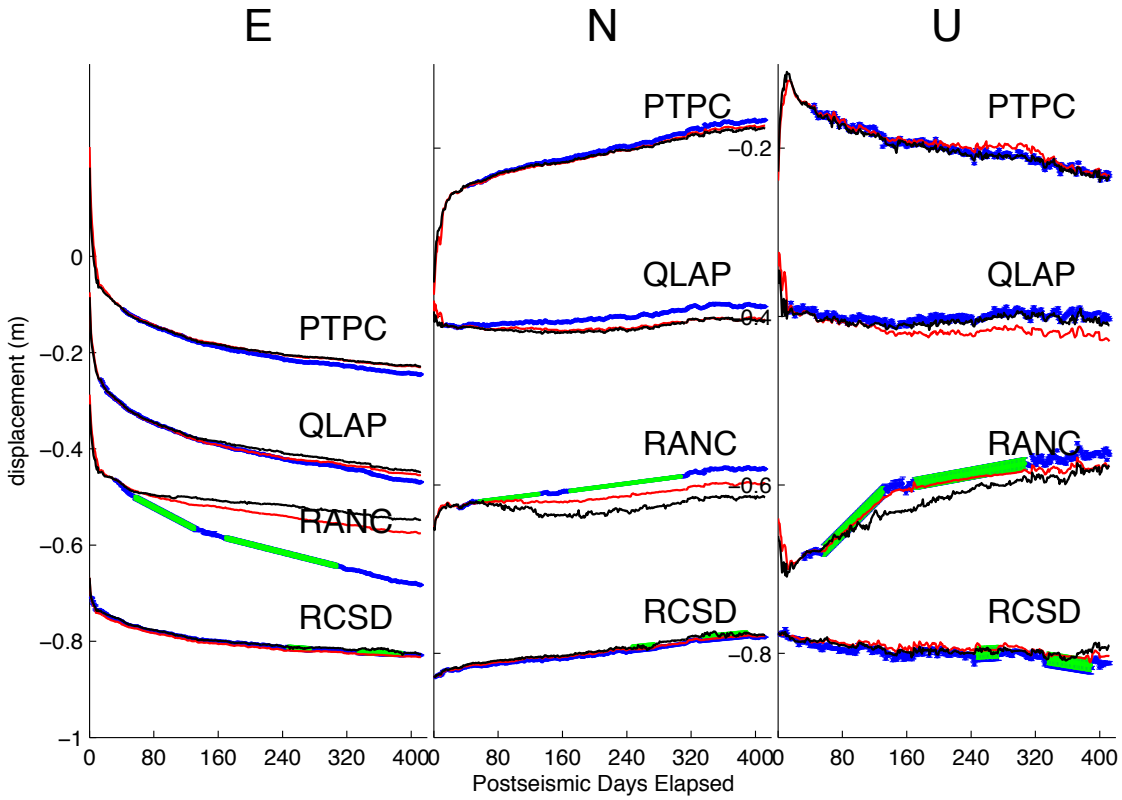

Figure A.11: Continuation of the alphabetically listed timeseries of model predictions and data. Blue, green, and red points represent the data, interpolated data, and the model predictions respectively. Black line represents the model fit to the data when the interpolated points (green) are omitted from the inversion.

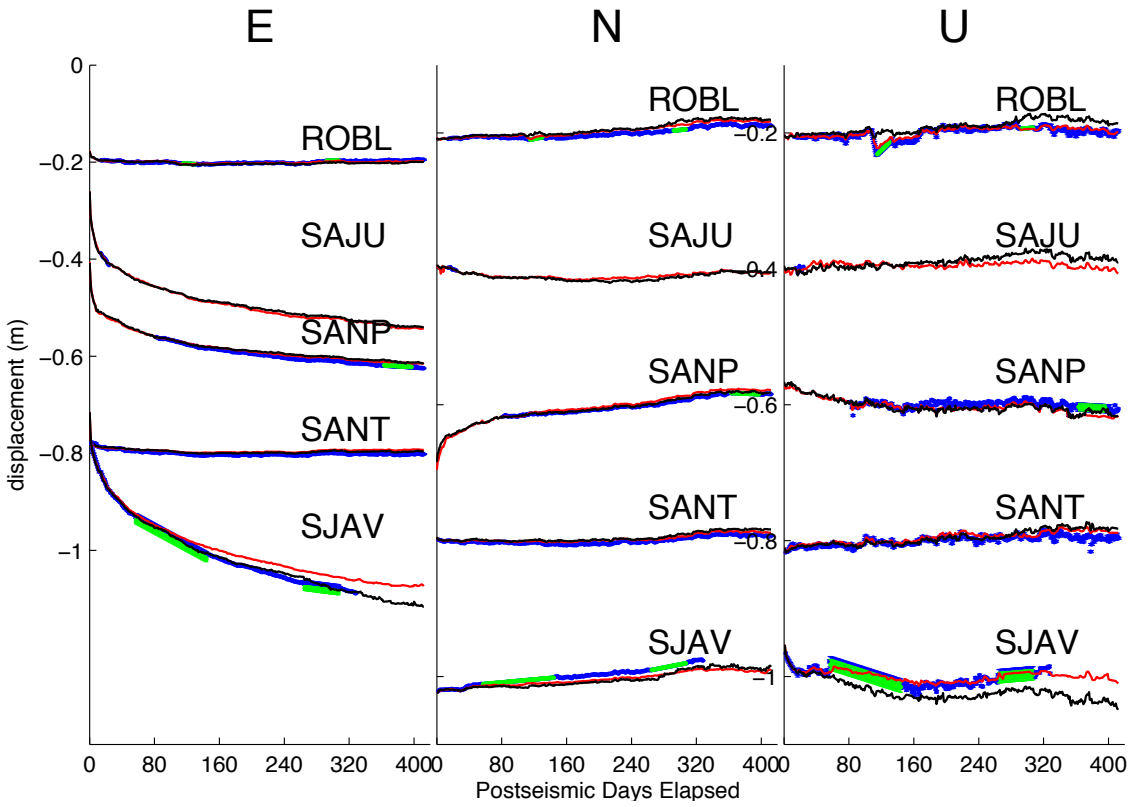

Figure A.12: Continuation of the alphabetically listed timeseries of model predictions and data. Blue, green, and red points represent the data, interpolated data, and the model predictions respectively. Black line represents the model fit to the data when the interpolated points (green) are omitted from the inversion.

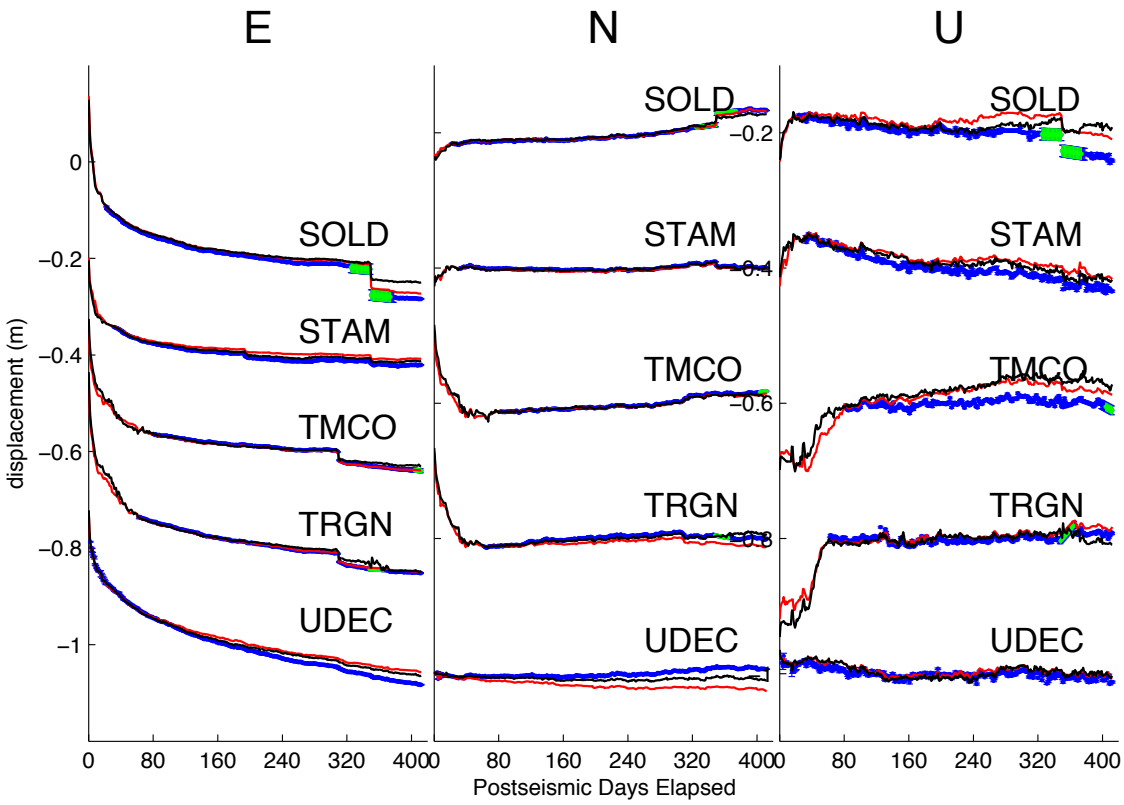

Figure A.13: Continuation of the alphabetically listed timeseries of model predictions and data. Blue, green, and red points represent the data, interpolated data, and the model predictions respectively. Black line represents the model fit to the data when the interpolated points (green) are omitted from the inversion.

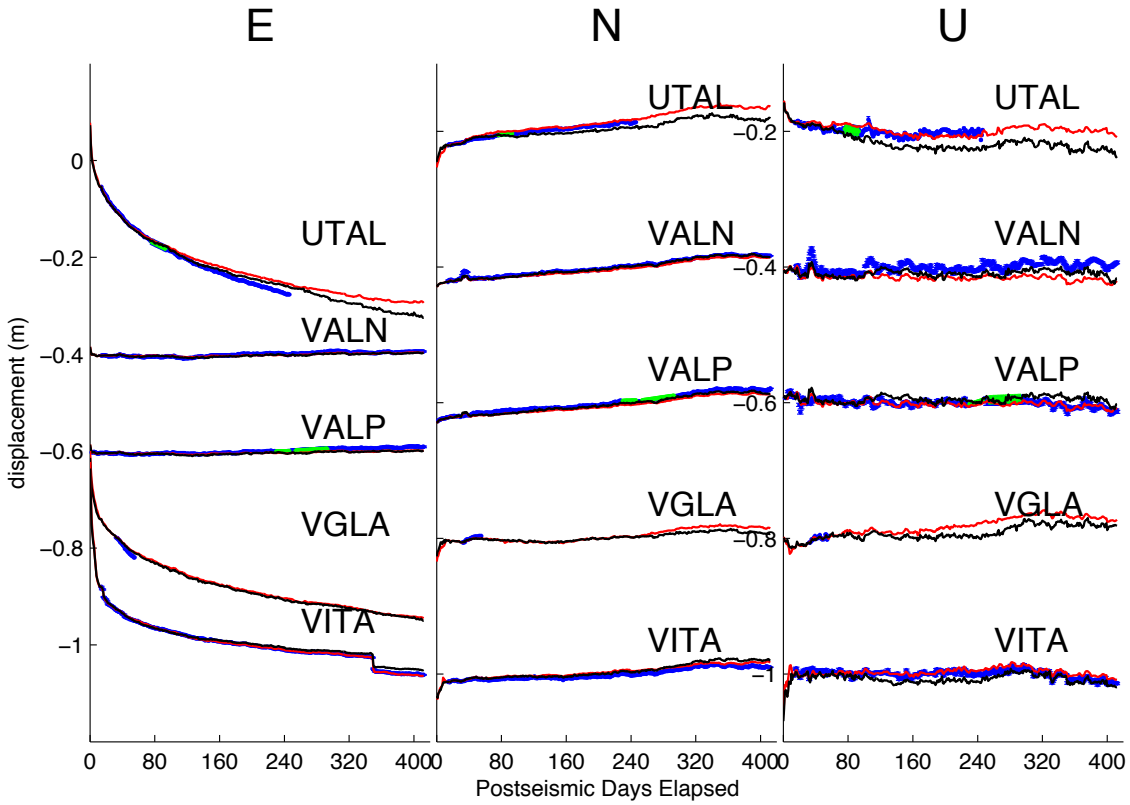

Figure A.14: Continuation of the alphabetically listed timeseries of model predictions and data. Blue, green, and red points represent the data, interpolated data, and the model predictions respectively. Black line represents the model fit to the data when the interpolated points (green) are omitted from the inversion.

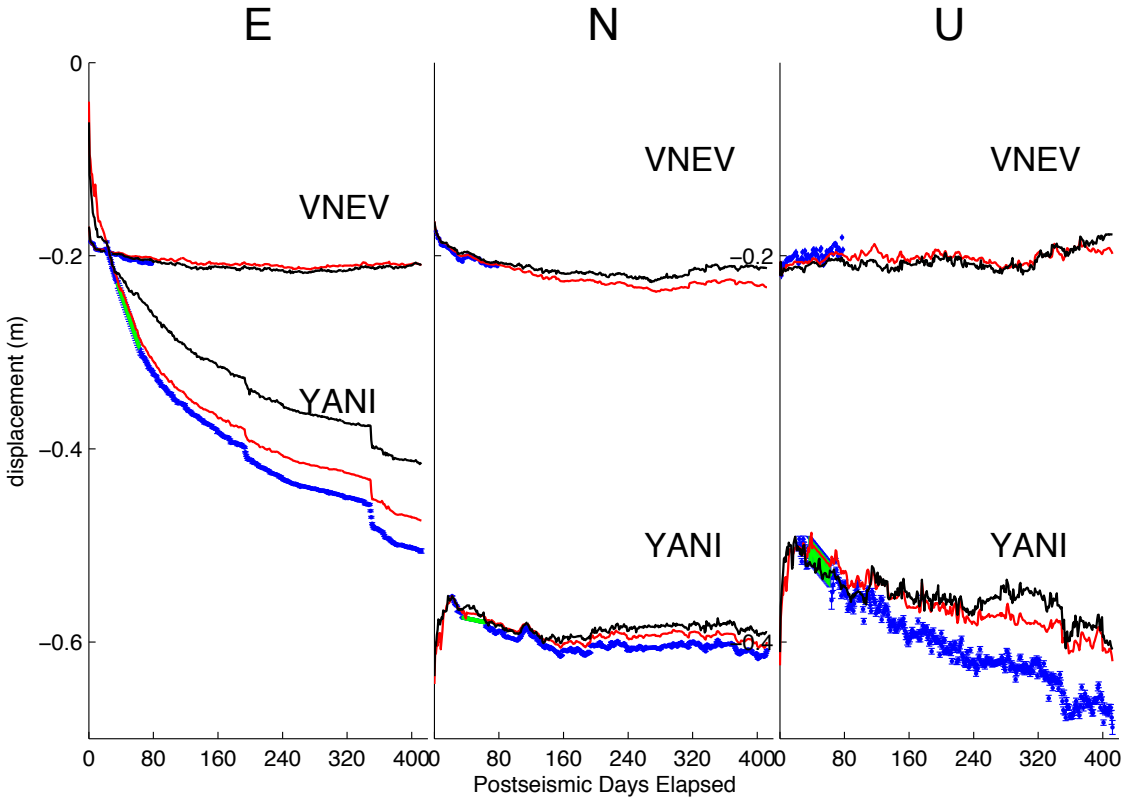

Figure A.15: Continuation of the alphabetically listed timeseries of model predictions and data. Blue, green, and red points represent the data, interpolated data, and the model predictions respectively. Black line represents the model fit to the data when the interpolated points (green) are omitted from the inversion.

Appendix B

Maule Simultaneous Postseismic Processes appendix

- Shown in this appendix chapter are the time series fits to the data for the best fitting models in each ensemble type. An animation of these appendix figures can be found on the CD provided or at this link. The animation file is named *"simultaneous_processes_fits.avi"*.
- The parameters describing time functions for the locking (backslip) can be found on the CD provided in the file *"locking_time_functions.xlsx"* or at this link.

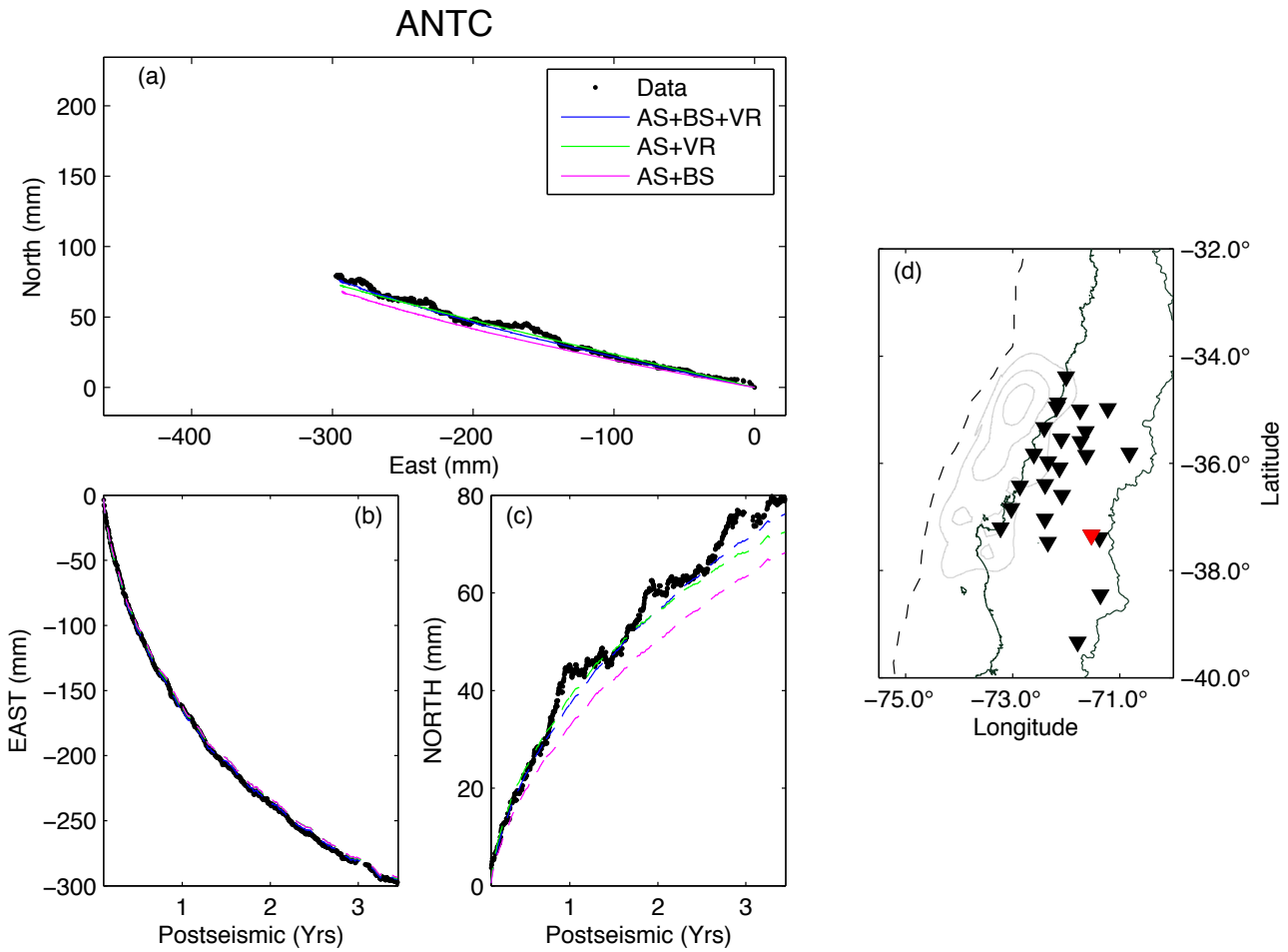

Figure B.1: Panel **(a)** shows the horizontal displacement pathway of the data and the predictions from the model ensembles (colours denoted in the legend). The aspect East and North scale are the same (equal aspect ratio). Panel **(d)** shows the location of the station (red triangle) in the cGPS network (black triangles) and with respect to the coseismic slip distribution (grey contours). Panels **(b)-(c)** show the east and north displacements as a function of time for the data and predictions.

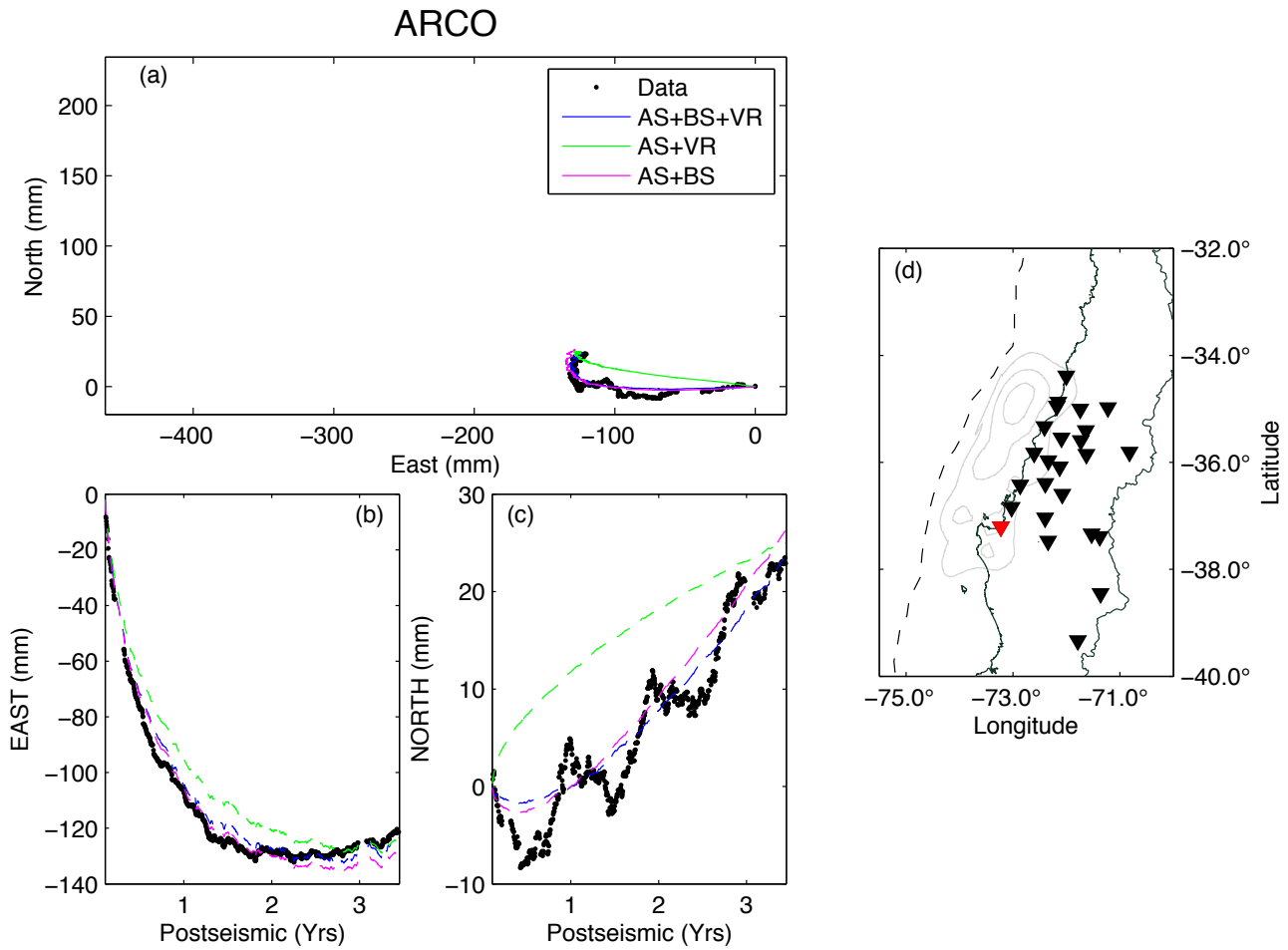

Figure B.2: Panel **(a)** shows the horizontal displacement pathway of the data and the predictions from the model ensembles (colours denoted in the legend). The aspect East and North scale are the same (equal aspect ratio). Panel **(d)** shows the location of the station (red triangle) in the cGPS network (black triangles) and with respect to the coseismic slip distribution (grey contours). Panels **(b)-(c)** show the east and north displacements as a function of time for the data and predictions.

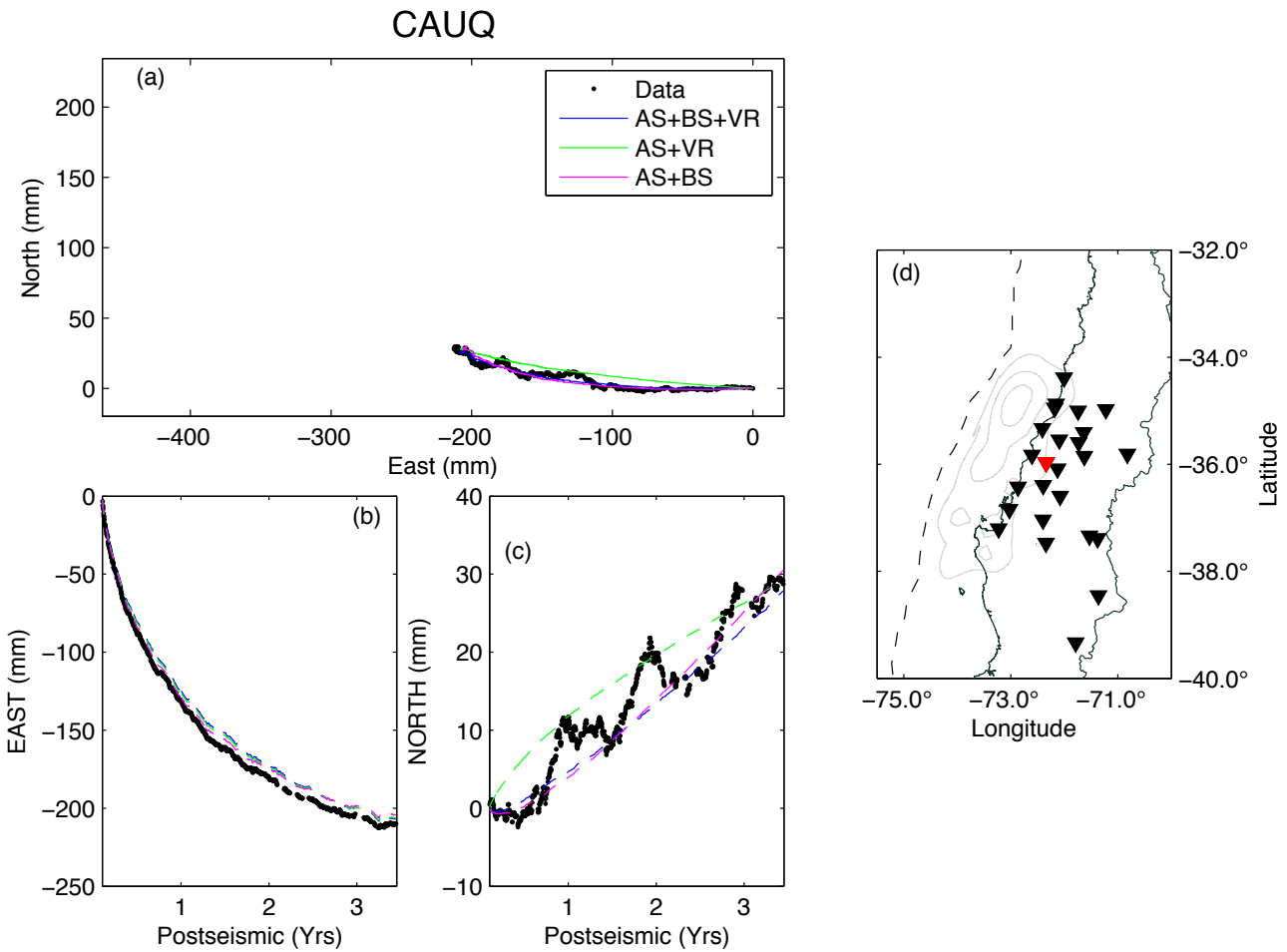

Figure B.3: Panel **(a)** shows the horizontal displacement pathway of the data and the predictions from the model ensembles (colours denoted in the legend). The aspect East and North scale are the same (equal aspect ratio). Panel **(d)** shows the location of the station (red triangle) in the cGPS network (black triangles) and with respect to the coseismic slip distribution (grey contours). Panels **(b)-(c)** show the east and north displacements as a function of time for the data and predictions.

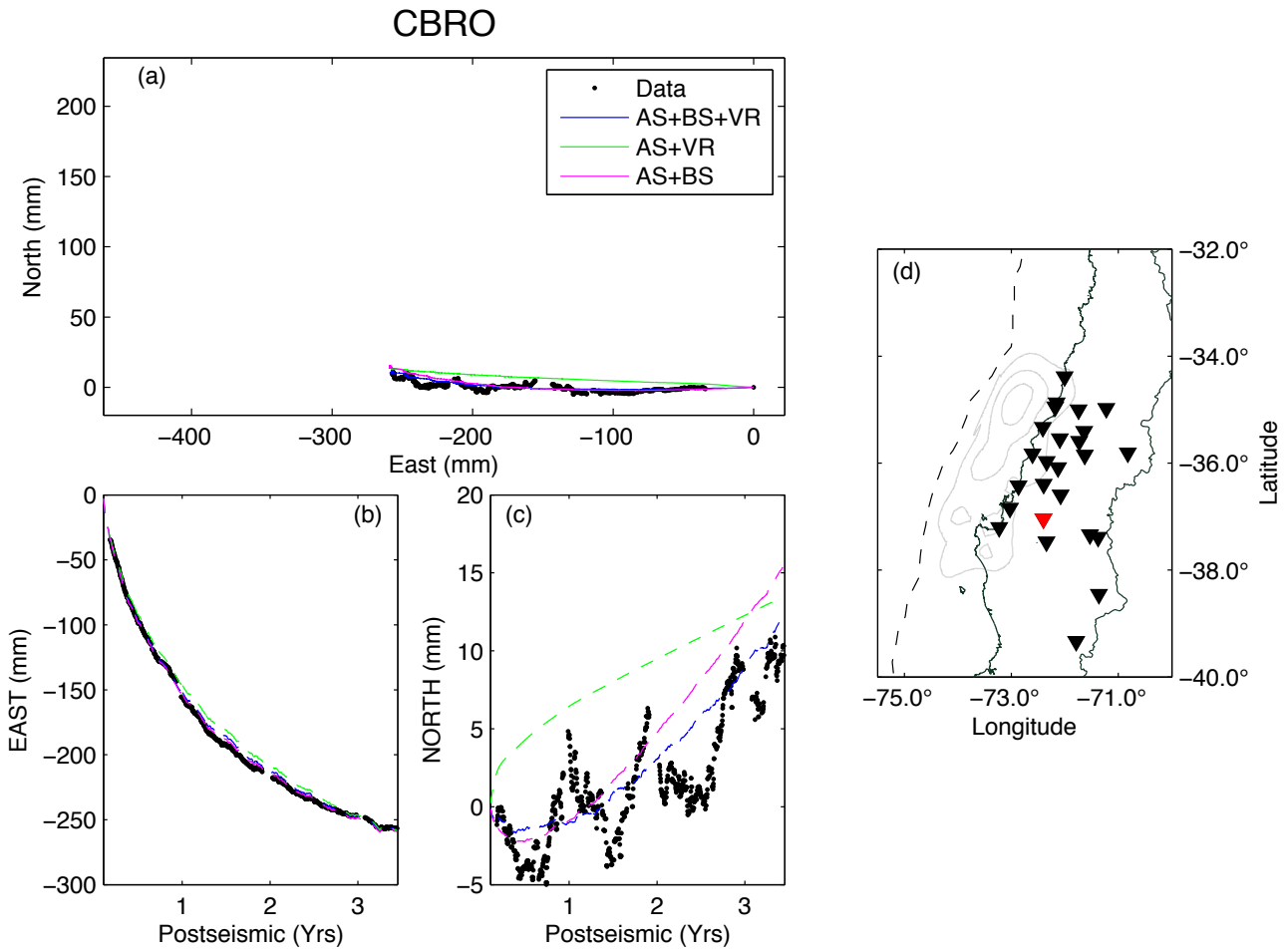

Figure B.4: Panel **(a)** shows the horizontal displacement pathway of the data and the predictions from the model ensembles (colours denoted in the legend). The aspect East and North scale are the same (equal aspect ratio). Panel **(d)** shows the location of the station (red triangle) in the cGPS network (black triangles) and with respect to the coseismic slip distribution (grey contours). Panels **(b)-(c)** show the east and north displacements as a function of time for the data and predictions.

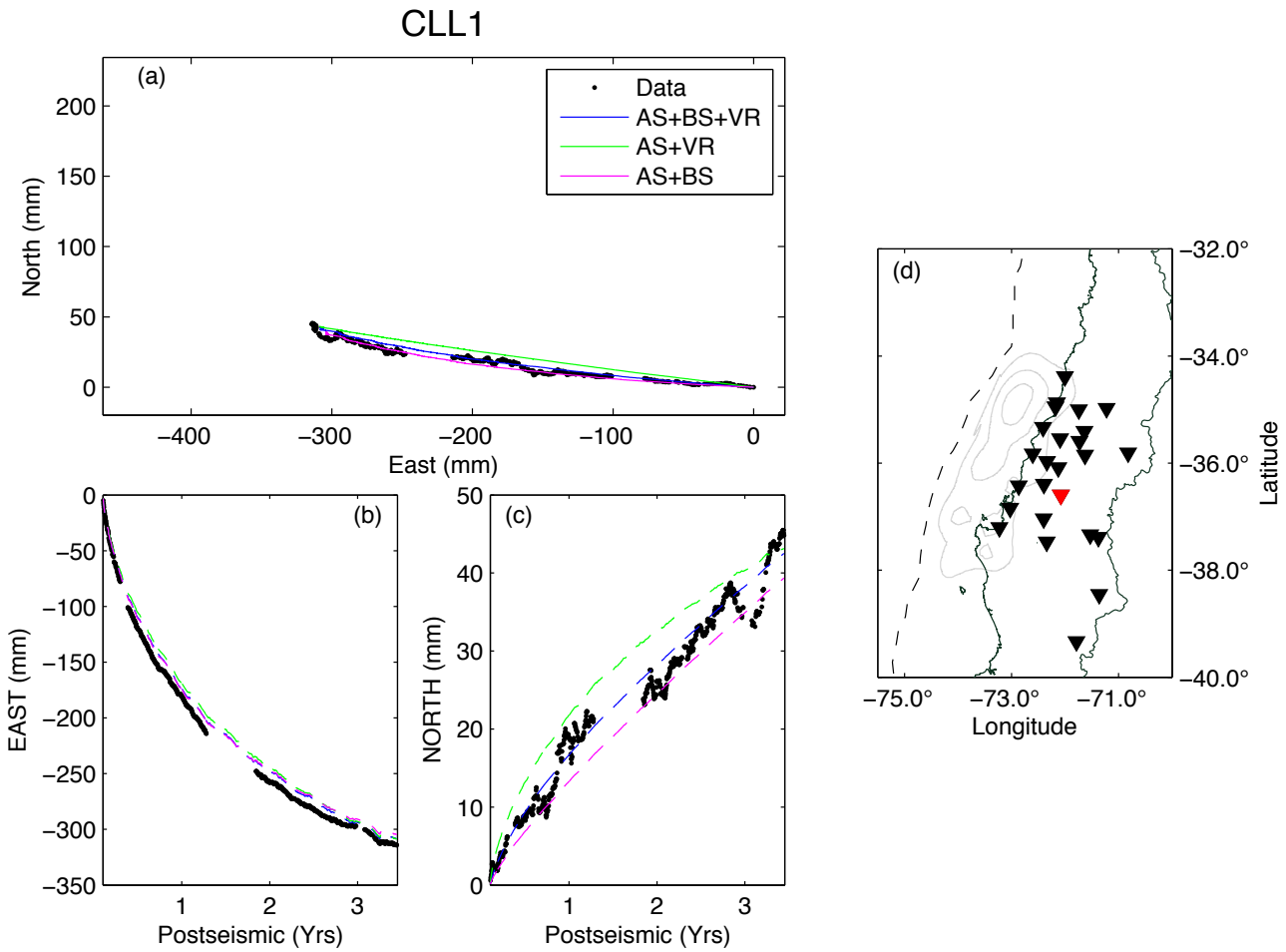

Figure B.5: Panel **(a)** shows the horizontal displacement pathway of the data and the predictions from the model ensembles (colours denoted in the legend). The aspect East and North scale are the same (equal aspect ratio). Panel **(d)** shows the location of the station (red triangle) in the cGPS network (black triangles) and with respect to the coseismic slip distribution (grey contours). Panels **(b)-(c)** show the east and north displacements as a function of time for the data and predictions.

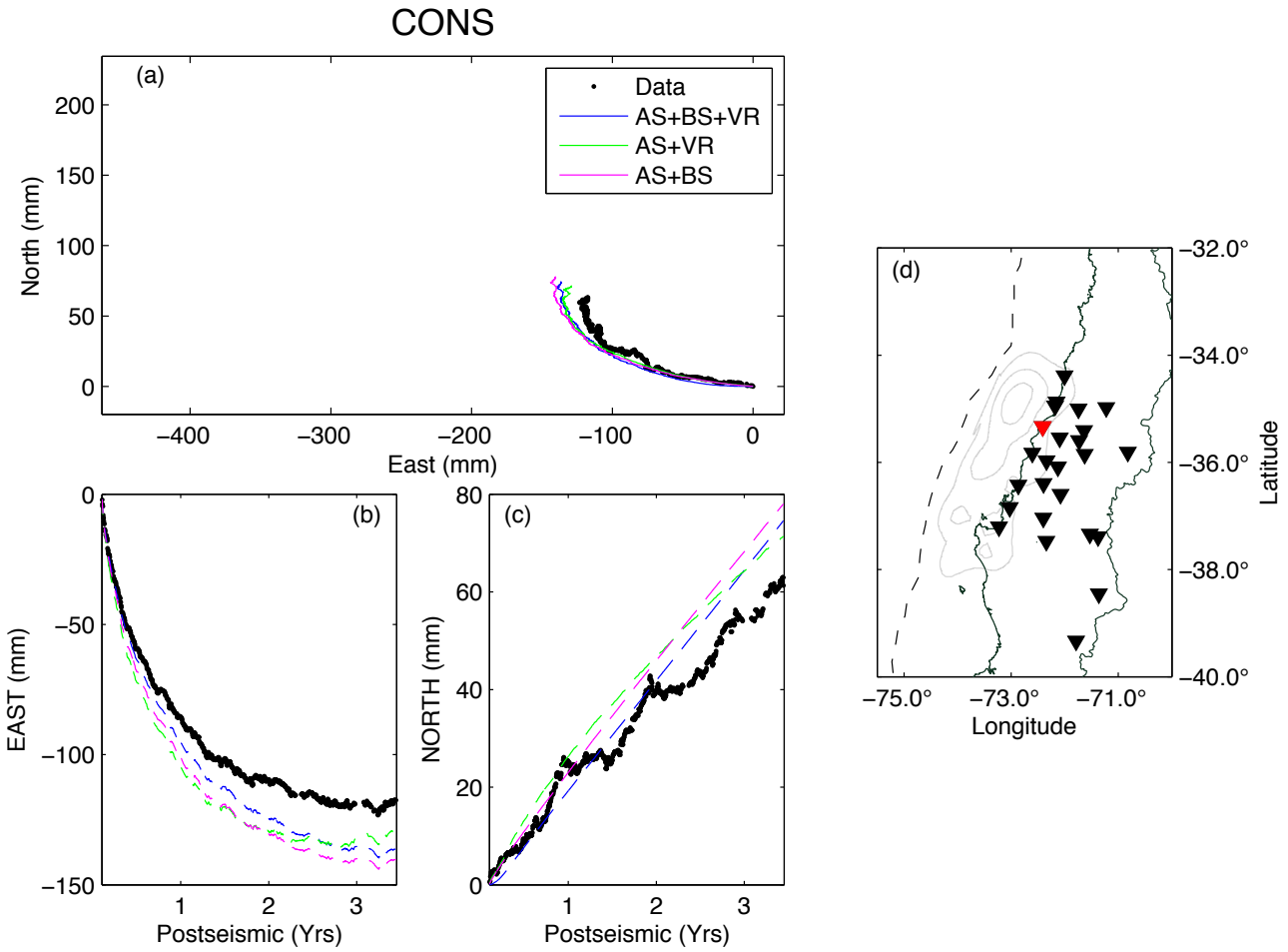

Figure B.6: Panel **(a)** shows the horizontal displacement pathway of the data and the predictions from the model ensembles (colours denoted in the legend). The aspect East and North scale are the same (equal aspect ratio). Panel **(d)** shows the location of the station (red triangle) in the cGPS network (black triangles) and with respect to the coseismic slip distribution (grey contours). Panels **(b)-(c)** show the east and north displacements as a function of time for the data and predictions.

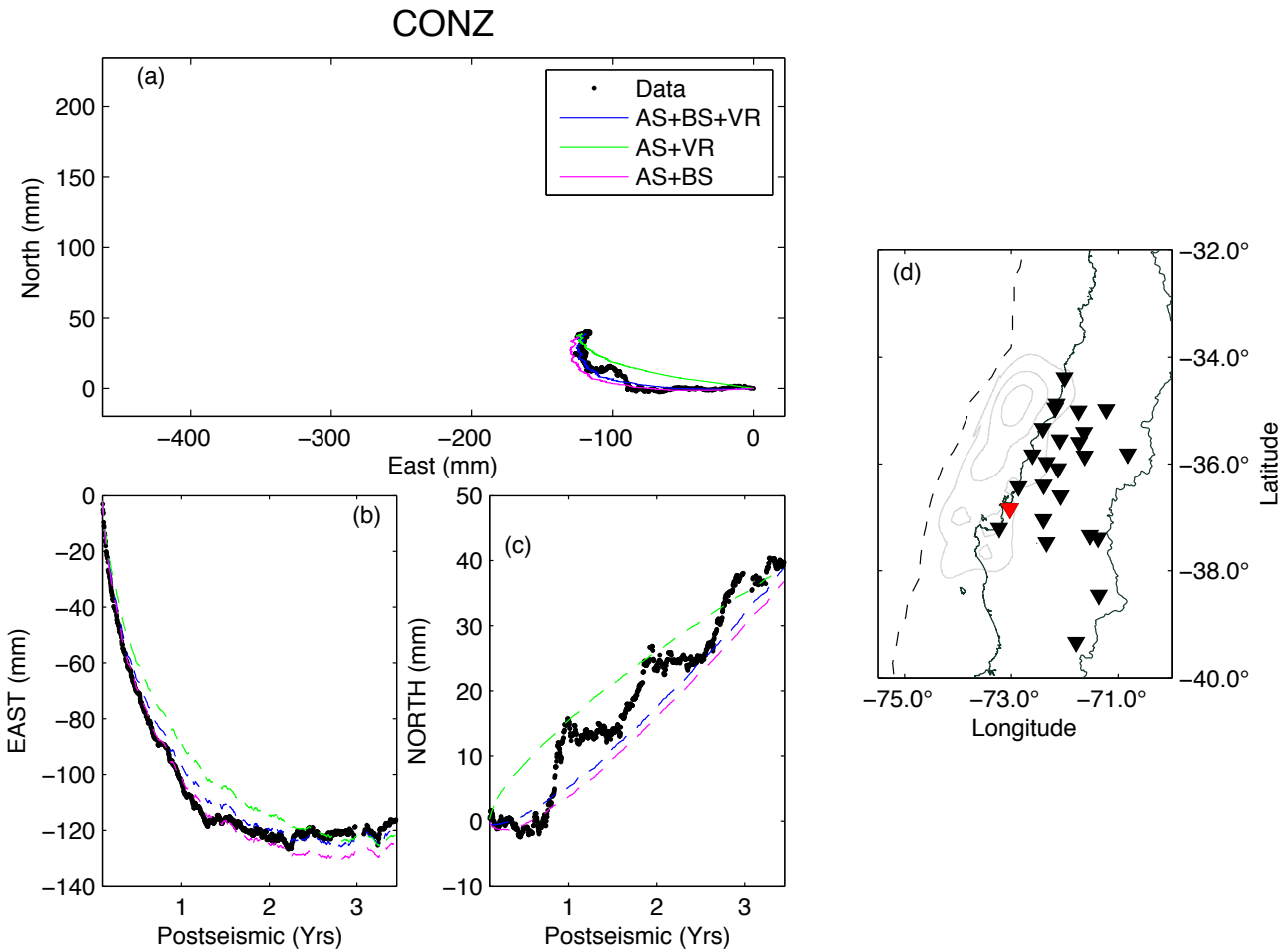

Figure B.7: Panel **(a)** shows the horizontal displacement pathway of the data and the predictions from the model ensembles (colours denoted in the legend). The aspect East and North scale are the same (equal aspect ratio). Panel **(d)** shows the location of the station (red triangle) in the cGPS network (black triangles) and with respect to the coseismic slip distribution (grey contours). Panels **(b)-(c)** show the east and north displacements as a function of time for the data and predictions.

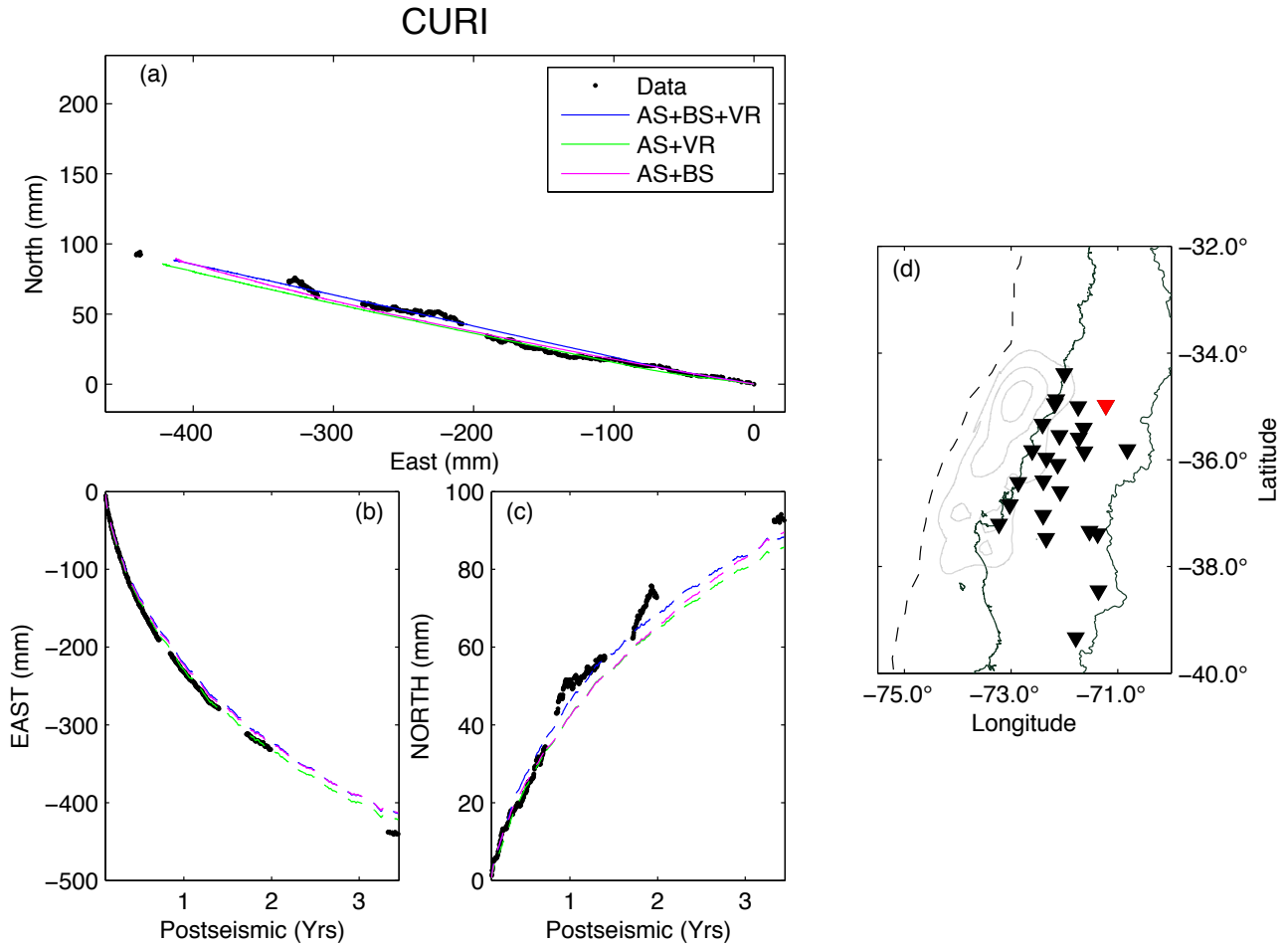

Figure B.8: Panel **(a)** shows the horizontal displacement pathway of the data and the predictions from the model ensembles (colours denoted in the legend). The aspect East and North scale are the same (equal aspect ratio). Panel **(d)** shows the location of the station (red triangle) in the cGPS network (black triangles) and with respect to the coseismic slip distribution (grey contours). Panels **(b)-(c)** show the east and north displacements as a function of time for the data and predictions.

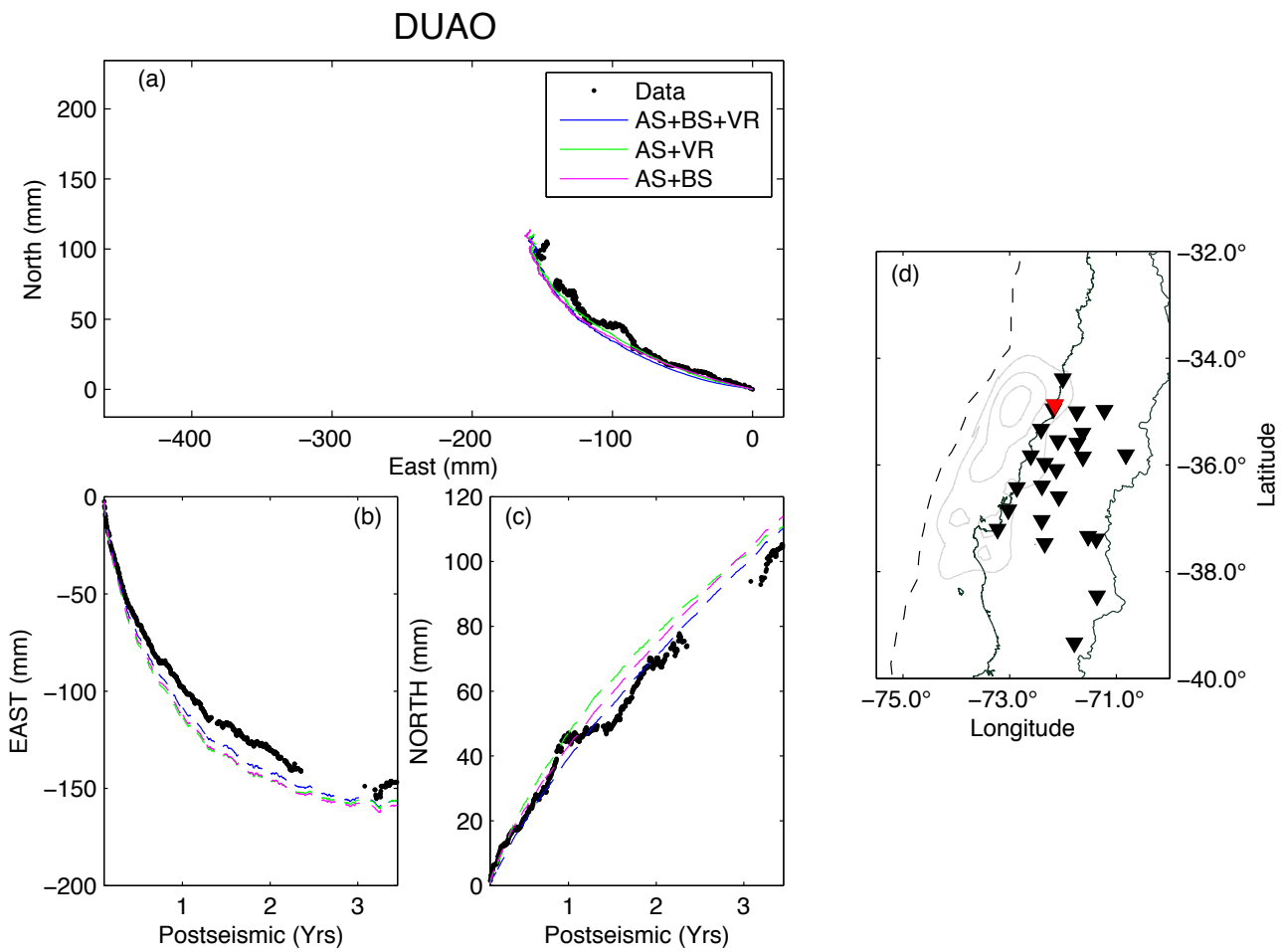

Figure B.9: Panel **(a)** shows the horizontal displacement pathway of the data and the predictions from the model ensembles (colours denoted in the legend). The aspect East and North scale are the same (equal aspect ratio). Panel **(d)** shows the location of the station (red triangle) in the cGPS network (black triangles) and with respect to the coseismic slip distribution (grey contours). Panels **(b)-(c)** show the east and north displacements as a function of time for the data and predictions.

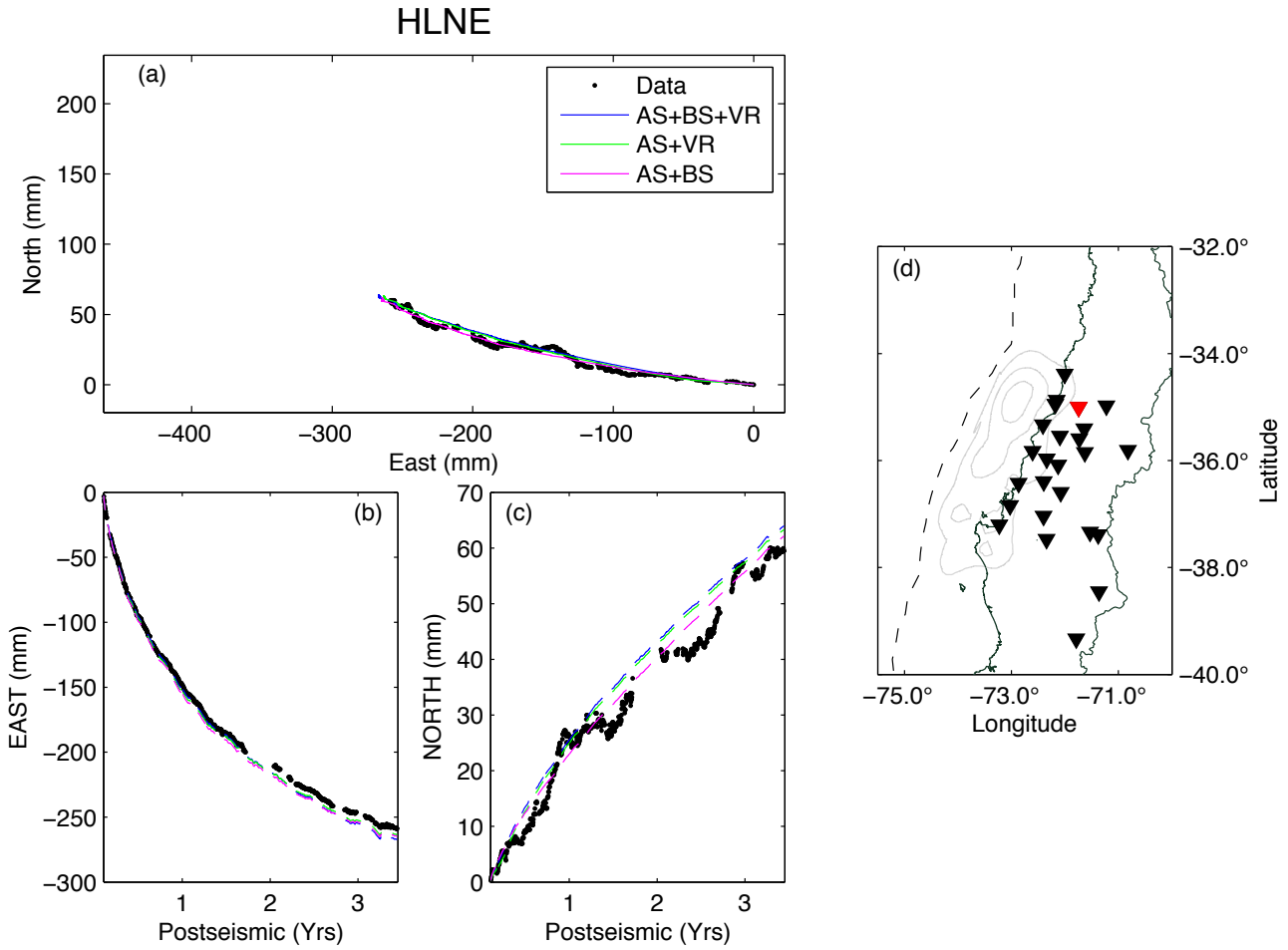

Figure B.10: Panel **(a)** shows the horizontal displacement pathway of the data and the predictions from the model ensembles (colours denoted in the legend). The aspect East and North scale are the same (equal aspect ratio). Panel **(d)** shows the location of the station (red triangle) in the cGPS network (black triangles) and with respect to the coseismic slip distribution (grey contours). Panels **(b)-(c)** show the east and north displacements as a function of time for the data and predictions.

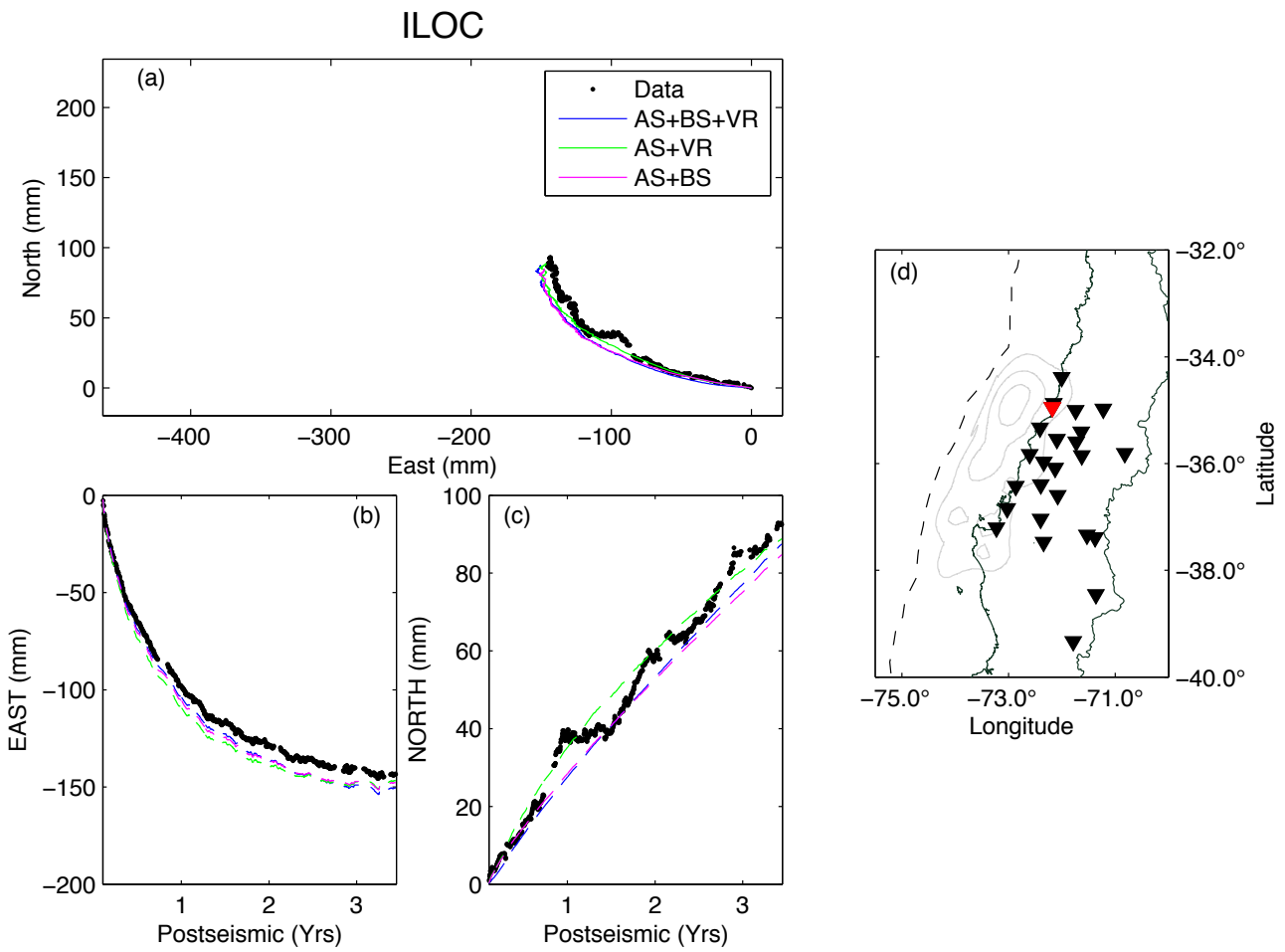

Figure B.11: Panel **(a)** shows the horizontal displacement pathway of the data and the predictions from the model ensembles (colours denoted in the legend). The aspect East and North scale are the same (equal aspect ratio). Panel **(d)** shows the location of the station (red triangle) in the cGPS network (black triangles) and with respect to the coseismic slip distribution (grey contours). Panels **(b)-(c)** show the east and north displacements as a function of time for the data and predictions.

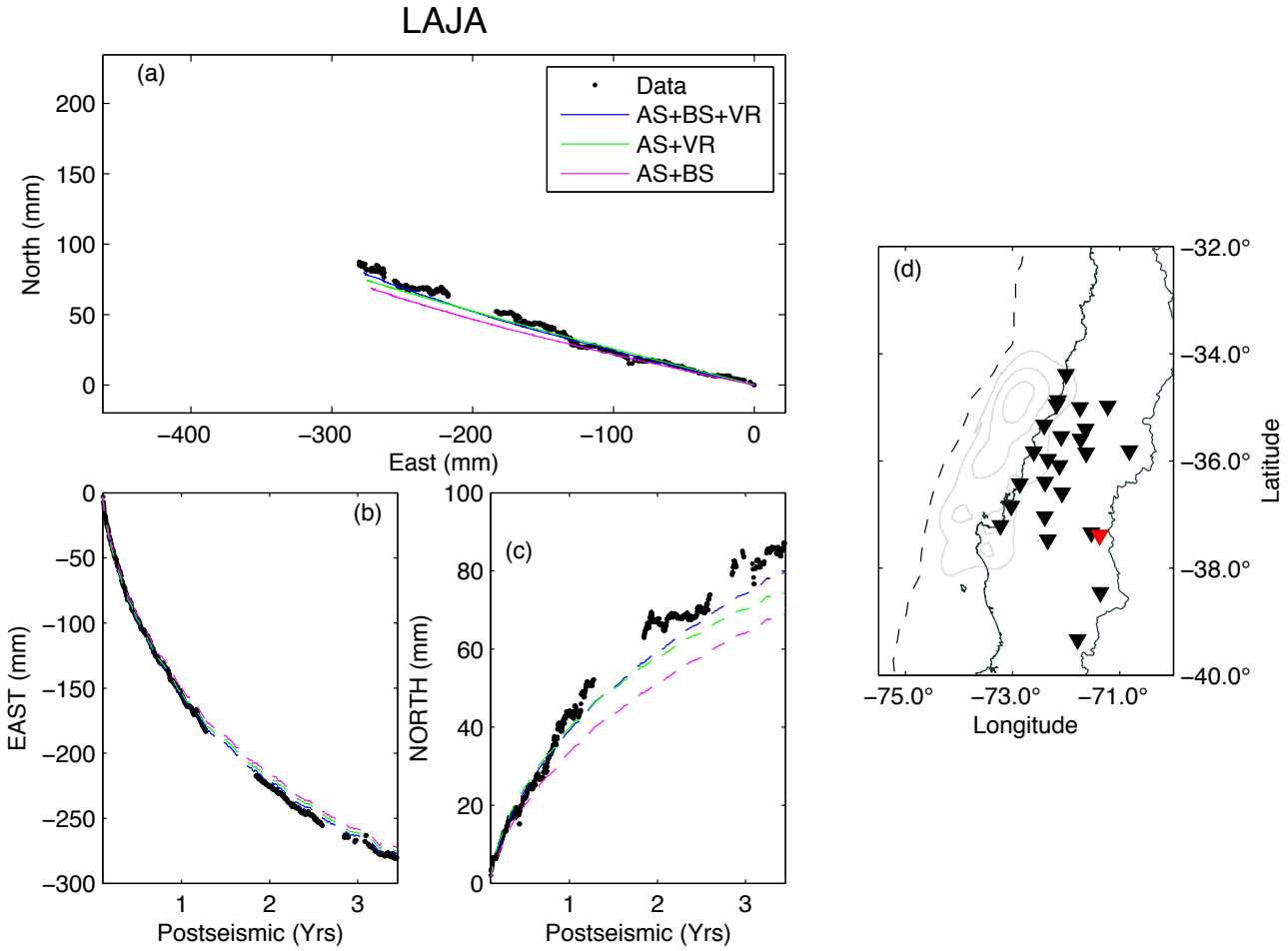

Figure B.12: Panel **(a)** shows the horizontal displacement pathway of the data and the predictions from the model ensembles (colours denoted in the legend). The aspect East and North scale are the same (equal aspect ratio). Panel **(d)** shows the location of the station (red triangle) in the cGPS network (black triangles) and with respect to the coseismic slip distribution (grey contours). Panels **(b)-(c)** show the east and north displacements as a function of time for the data and predictions.

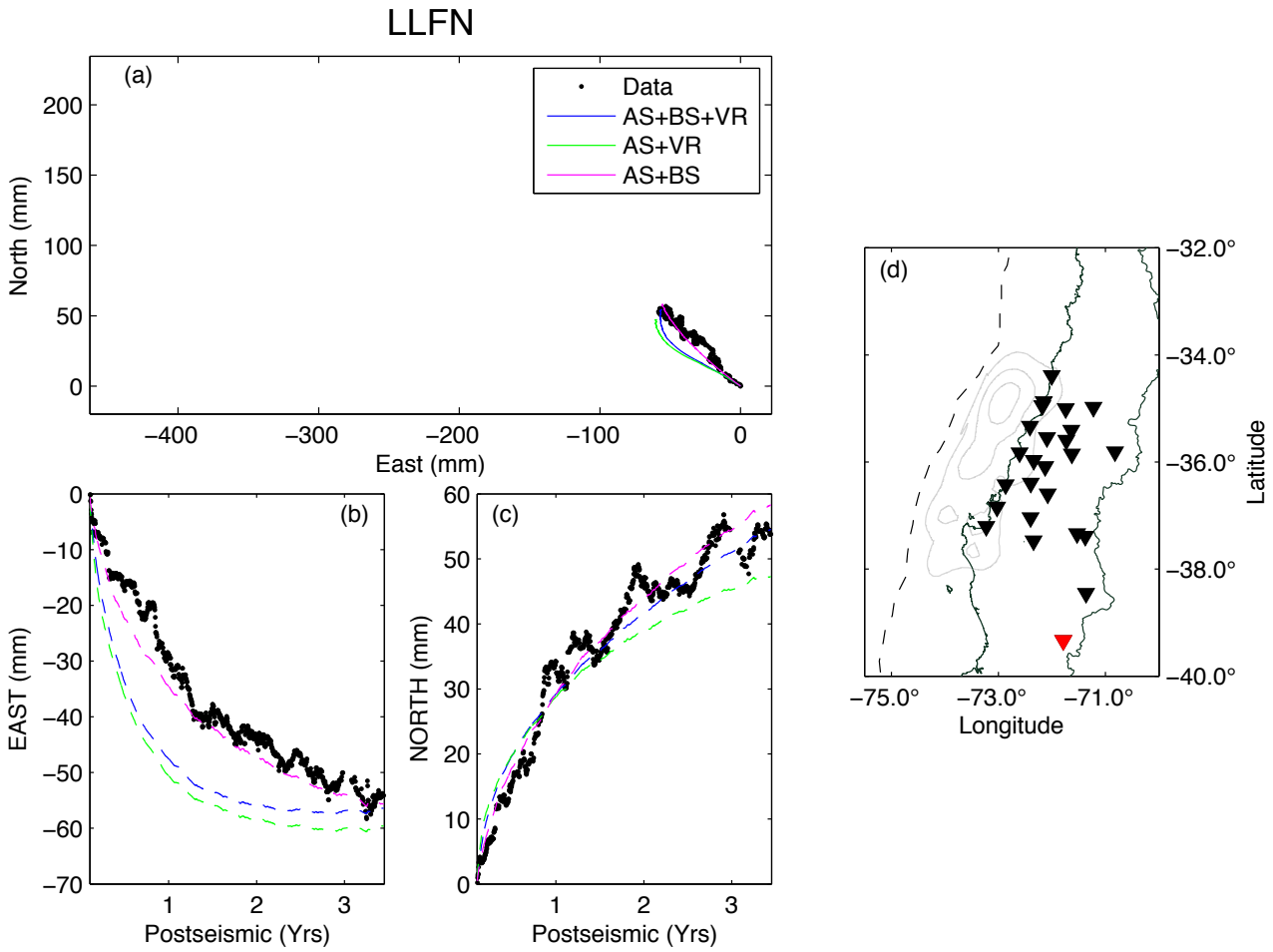

Figure B.13: Panel **(a)** shows the horizontal displacement pathway of the data and the predictions from the model ensembles (colours denoted in the legend). The aspect East and North scale are the same (equal aspect ratio). Panel **(d)** shows the location of the station (red triangle) in the cGPS network (black triangles) and with respect to the coseismic slip distribution (grey contours). Panels **(b)-(c)** show the east and north displacements as a function of time for the data and predictions.

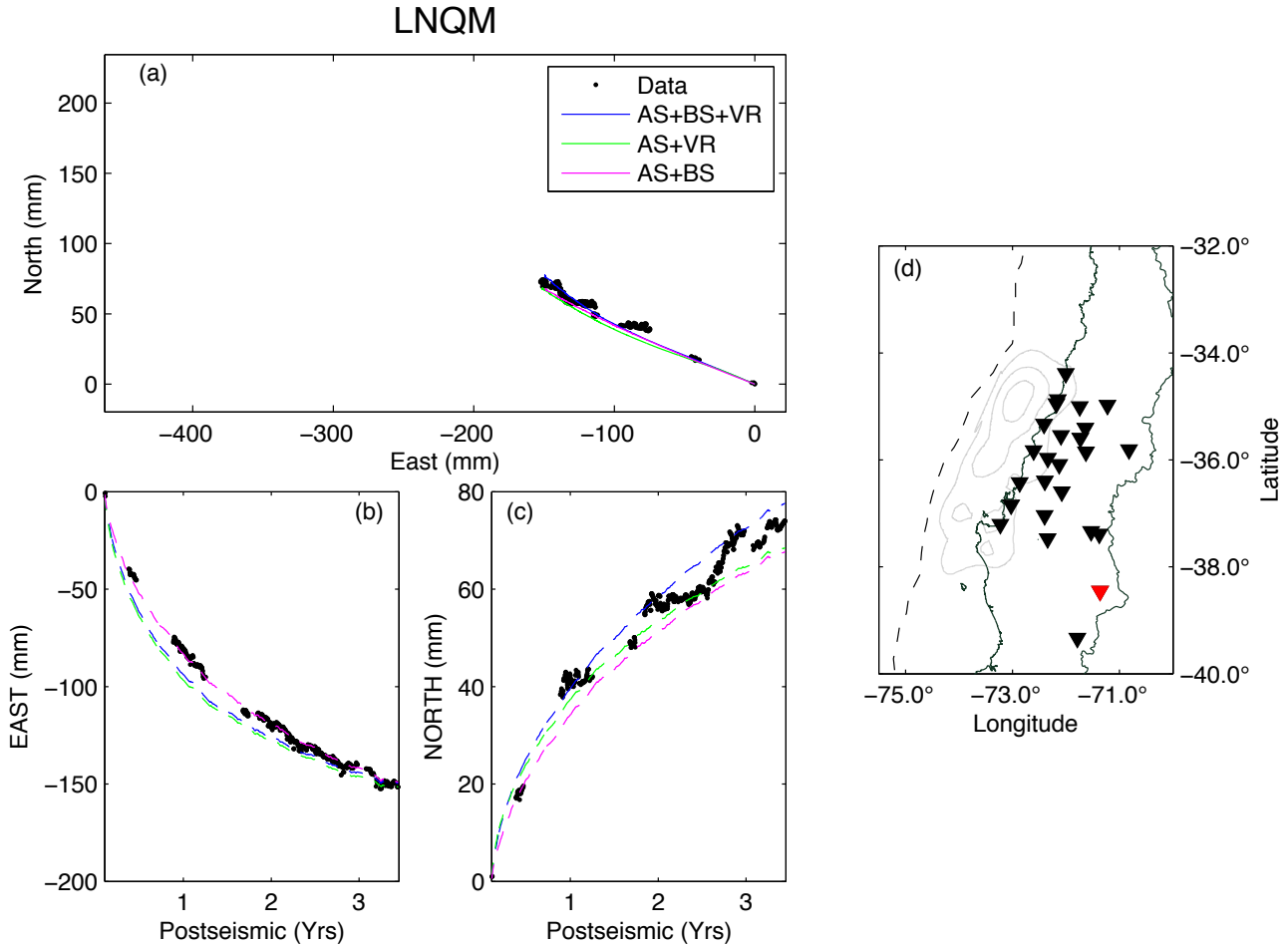

Figure B.14: Panel **(a)** shows the horizontal displacement pathway of the data and the predictions from the model ensembles (colours denoted in the legend). The aspect East and North scale are the same (equal aspect ratio). Panel **(d)** shows the location of the station (red triangle) in the cGPS network (black triangles) and with respect to the coseismic slip distribution (grey contours). Panels **(b)-(c)** show the east and north displacements as a function of time for the data and predictions.

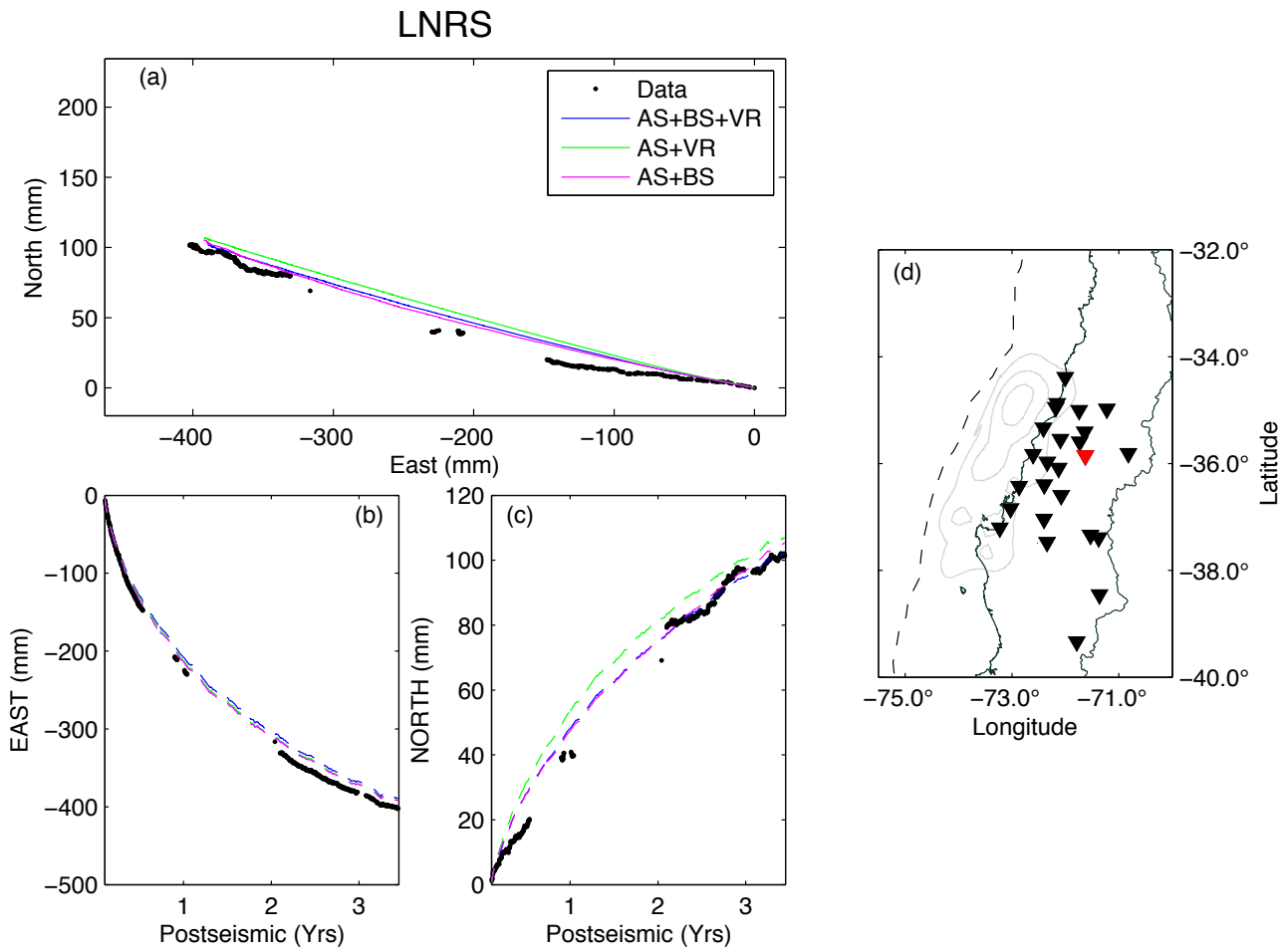

Figure B.15: Panel **(a)** shows the horizontal displacement pathway of the data and the predictions from the model ensembles (colours denoted in the legend). The aspect East and North scale are the same (equal aspect ratio). Panel **(d)** shows the location of the station (red triangle) in the cGPS network (black triangles) and with respect to the coseismic slip distribution (grey contours). Panels **(b)-(c)** show the east and north displacements as a function of time for the data and predictions.

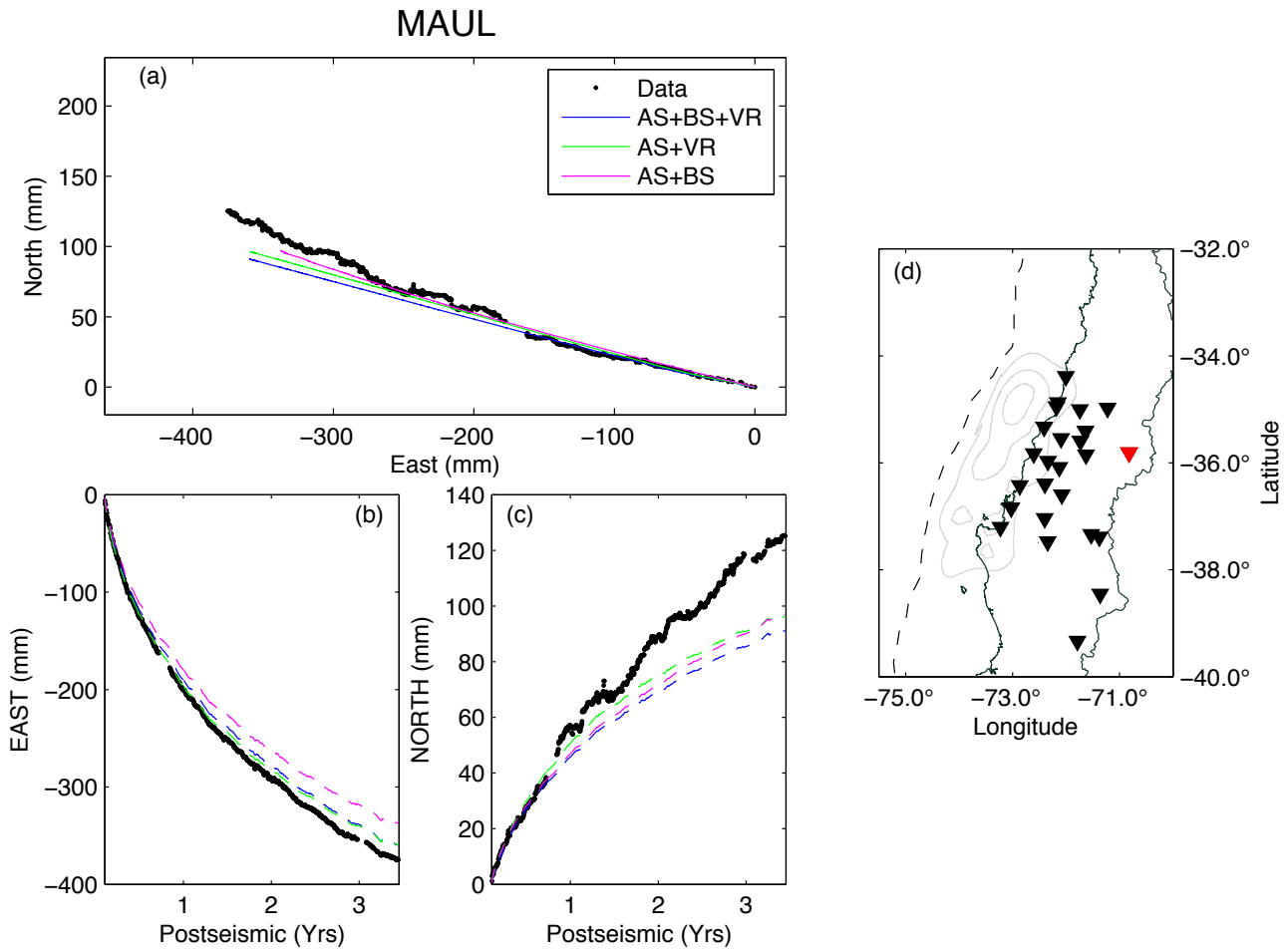

Figure B.16: Panel **(a)** shows the horizontal displacement pathway of the data and the predictions from the model ensembles (colours denoted in the legend). The aspect East and North scale are the same (equal aspect ratio). Panel **(d)** shows the location of the station (red triangle) in the cGPS network (black triangles) and with respect to the coseismic slip distribution (grey contours). Panels **(b)-(c)** show the east and north displacements as a function of time for the data and predictions.

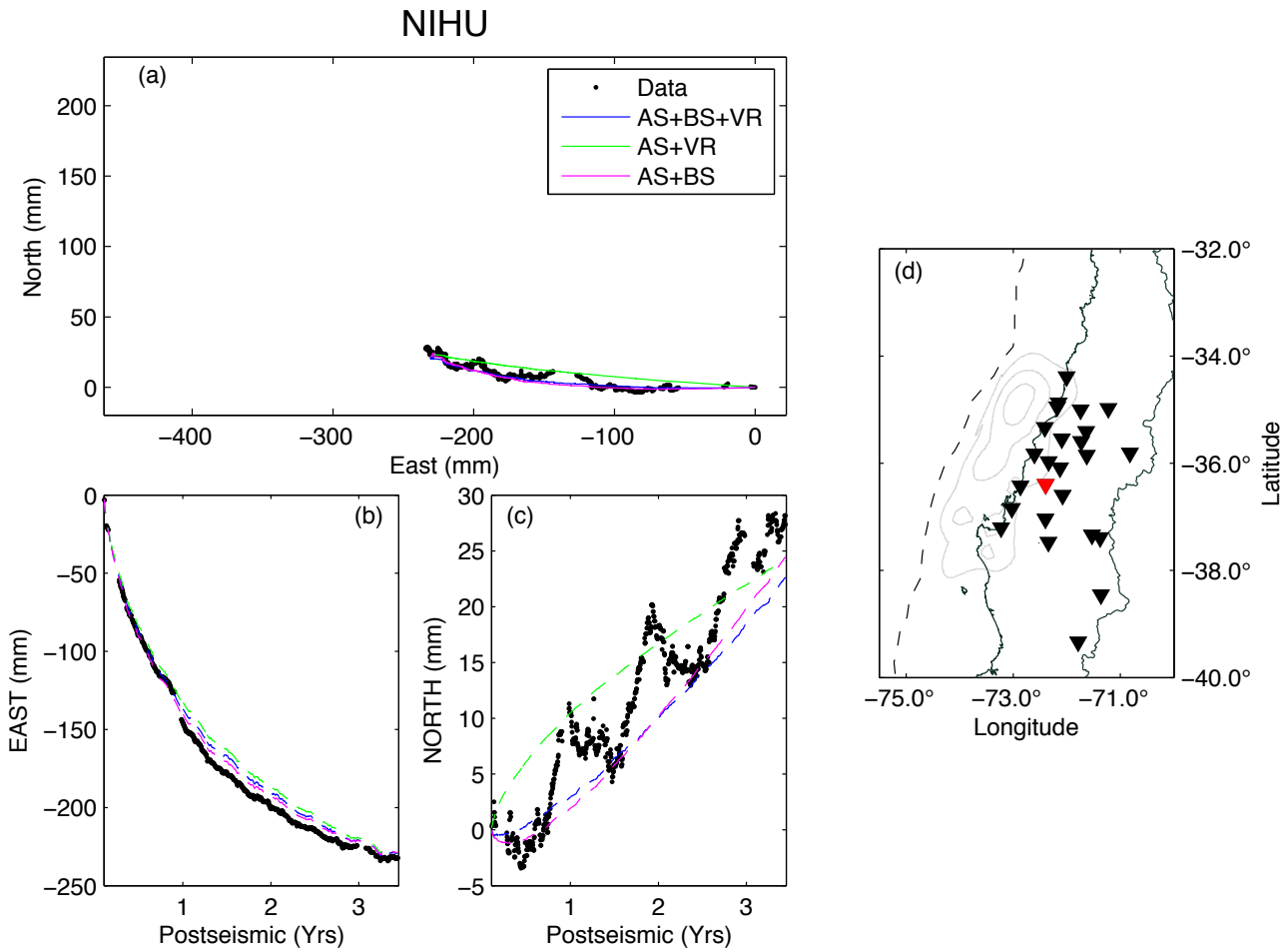

Figure B.17: Panel **(a)** shows the horizontal displacement pathway of the data and the predictions from the model ensembles (colours denoted in the legend). The aspect East and North scale are the same (equal aspect ratio). Panel **(d)** shows the location of the station (red triangle) in the cGPS network (black triangles) and with respect to the coseismic slip distribution (grey contours). Panels **(b)-(c)** show the east and north displacements as a function of time for the data and predictions.

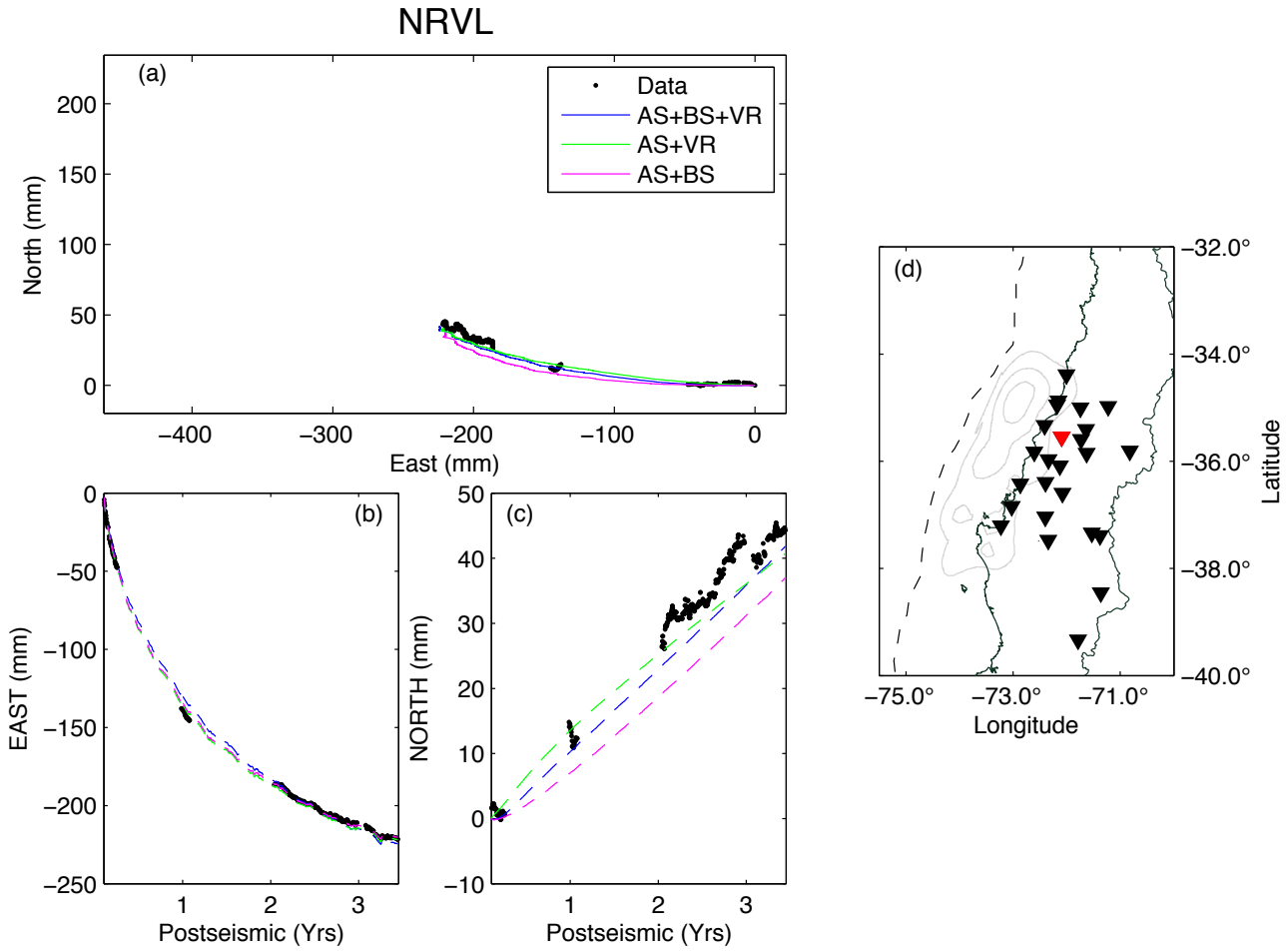

Figure B.18: Panel **(a)** shows the horizontal displacement pathway of the data and the predictions from the model ensembles (colours denoted in the legend). The aspect East and North scale are the same (equal aspect ratio). Panel **(d)** shows the location of the station (red triangle) in the cGPS network (black triangles) and with respect to the coseismic slip distribution (grey contours). Panels **(b)-(c)** show the east and north displacements as a function of time for the data and predictions.

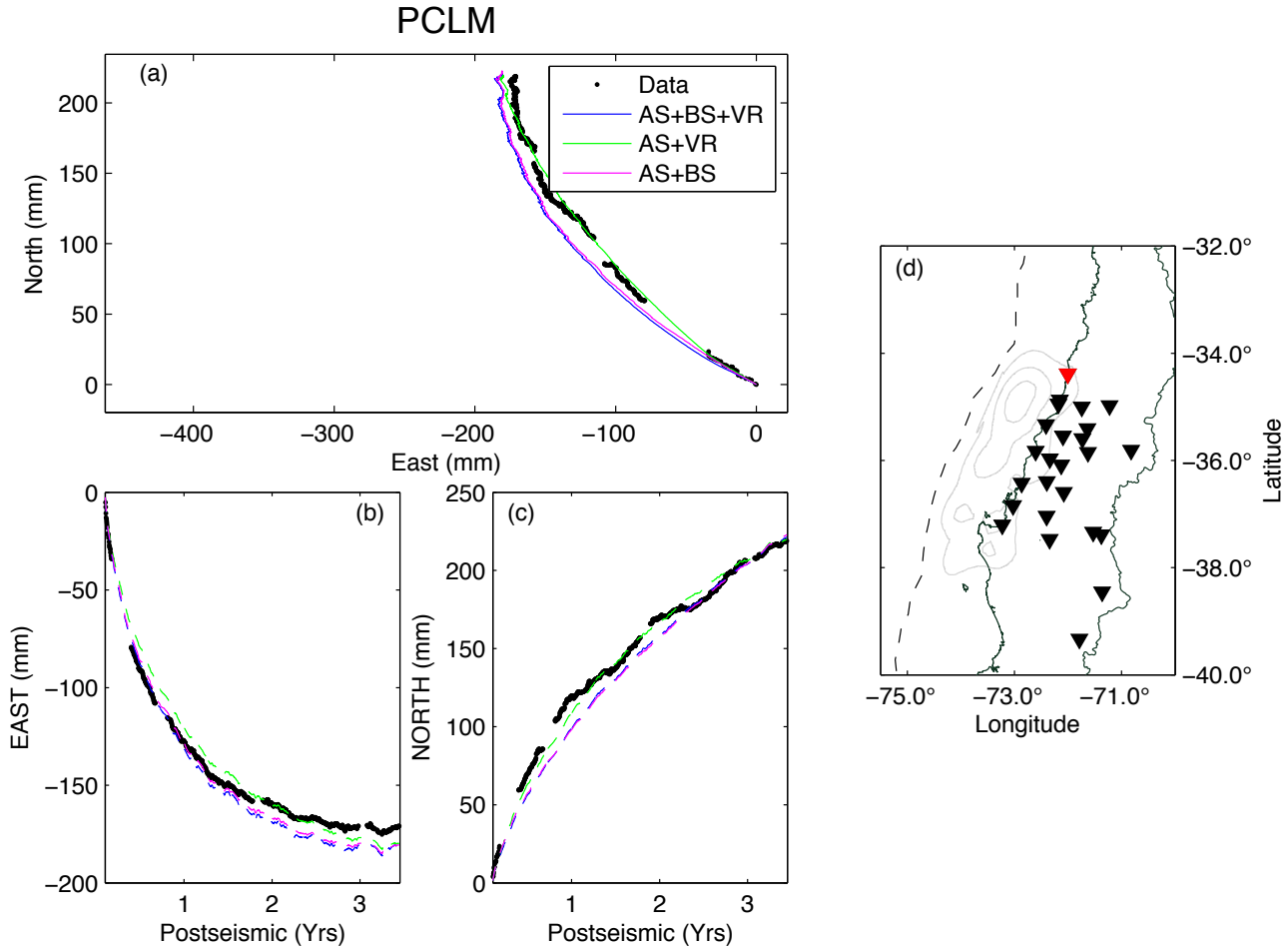

Figure B.19: Panel **(a)** shows the horizontal displacement pathway of the data and the predictions from the model ensembles (colours denoted in the legend). The aspect East and North scale are the same (equal aspect ratio). Panel **(d)** shows the location of the station (red triangle) in the cGPS network (black triangles) and with respect to the coseismic slip distribution (grey contours). Panels **(b)-(c)** show the east and north displacements as a function of time for the data and predictions.

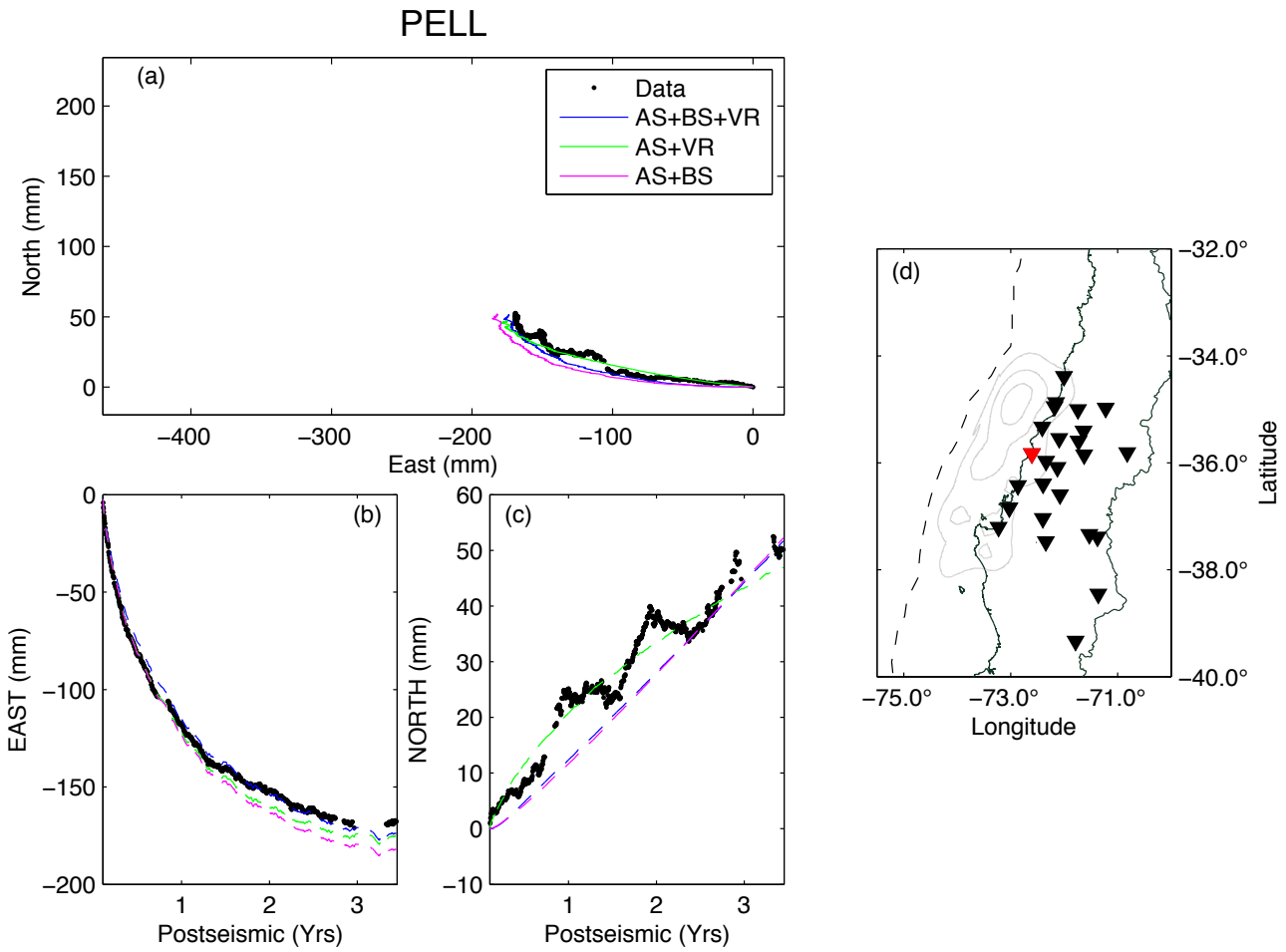

Figure B.20: Panel **(a)** shows the horizontal displacement pathway of the data and the predictions from the model ensembles (colours denoted in the legend). The aspect East and North scale are the same (equal aspect ratio). Panel **(d)** shows the location of the station (red triangle) in the cGPS network (black triangles) and with respect to the coseismic slip distribution (grey contours). Panels **(b)-(c)** show the east and north displacements as a function of time for the data and predictions.

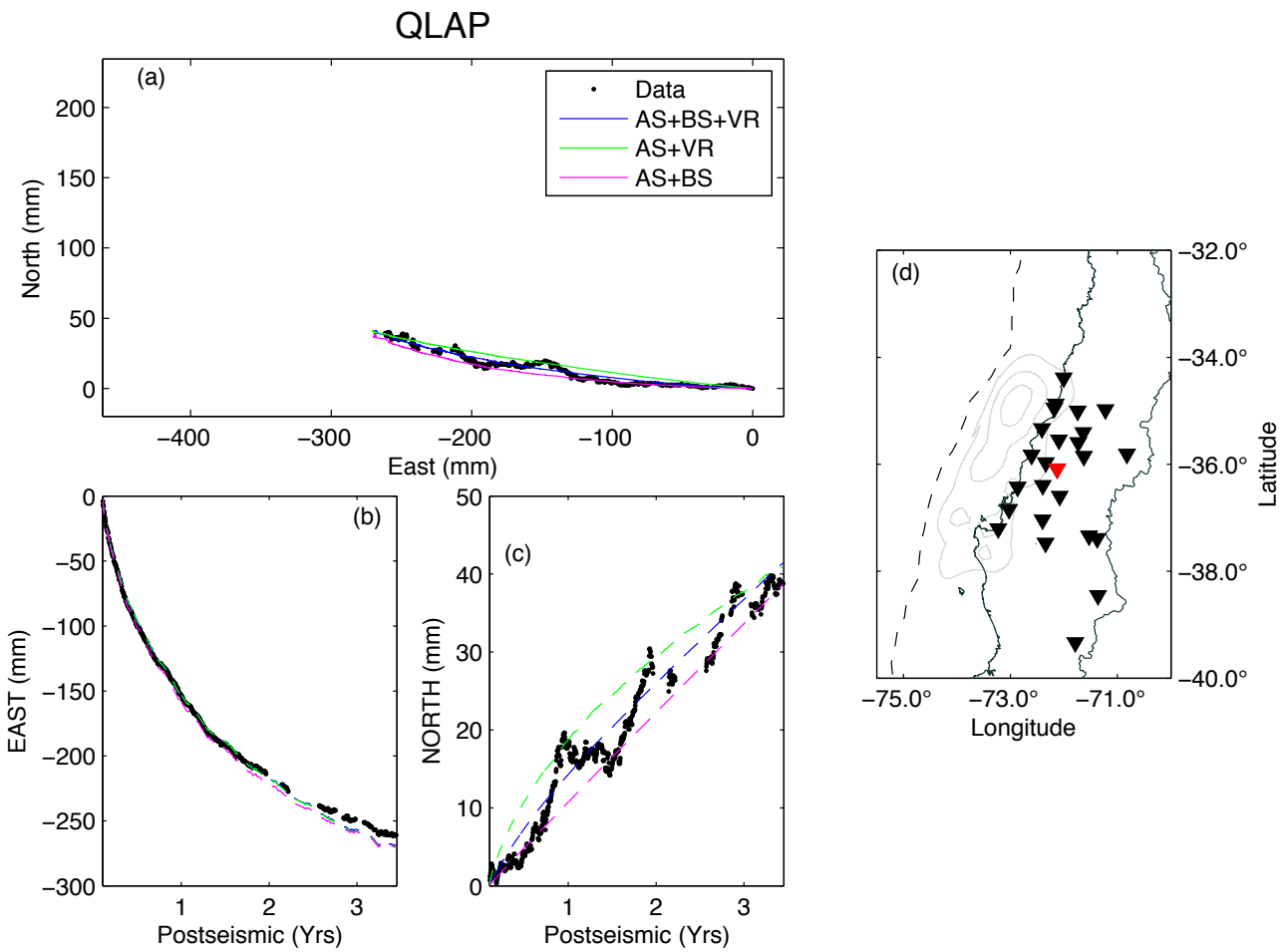

Figure B.21: Panel **(a)** shows the horizontal displacement pathway of the data and the predictions from the model ensembles (colours denoted in the legend). The aspect East and North scale are the same (equal aspect ratio). Panel **(d)** shows the location of the station (red triangle) in the cGPS network (black triangles) and with respect to the coseismic slip distribution (grey contours). Panels **(b)-(c)** show the east and north displacements as a function of time for the data and predictions.

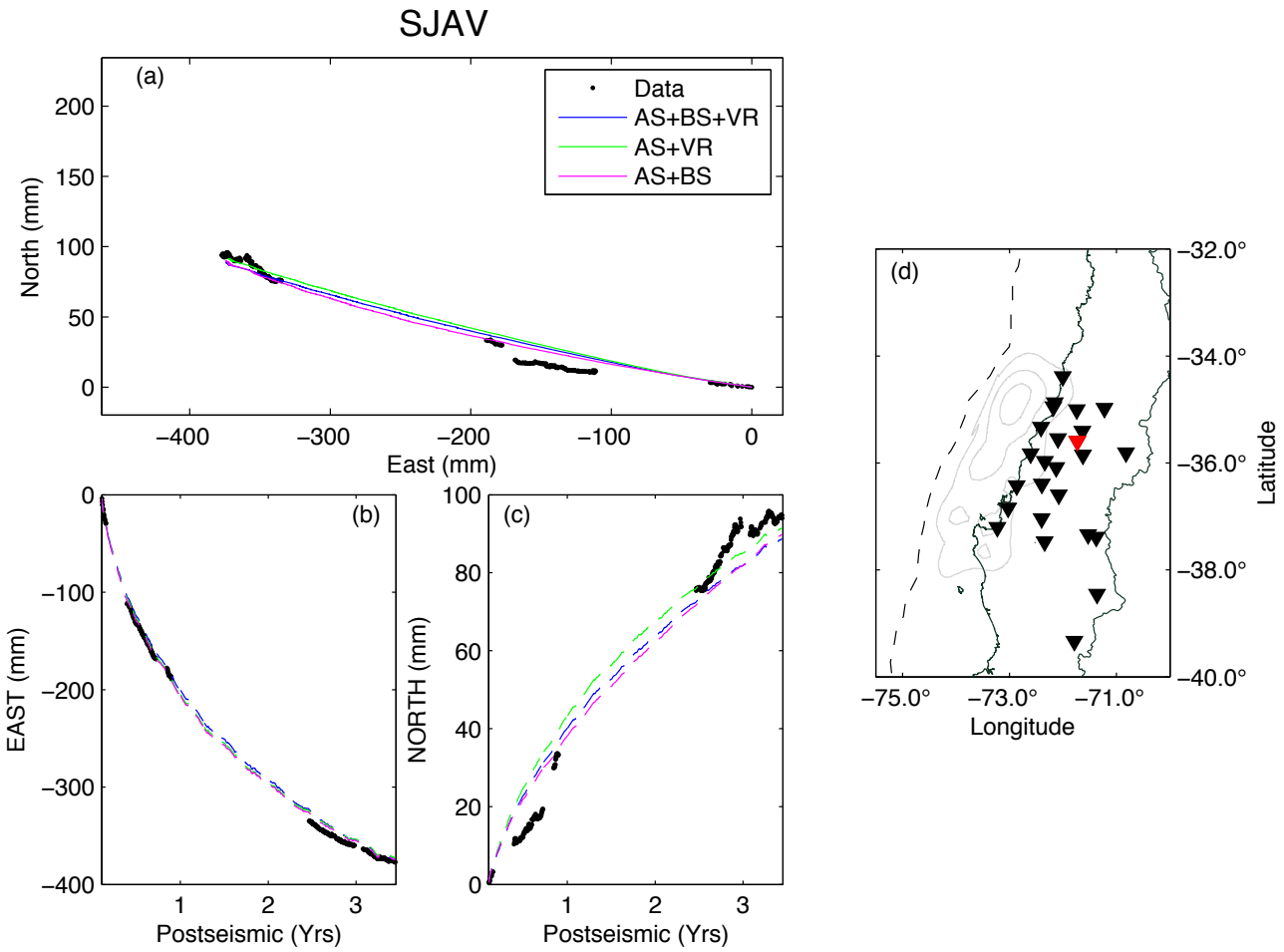

Figure B.22: Panel **(a)** shows the horizontal displacement pathway of the data and the predictions from the model ensembles (colours denoted in the legend). The aspect East and North scale are the same (equal aspect ratio). Panel **(d)** shows the location of the station (red triangle) in the cGPS network (black triangles) and with respect to the coseismic slip distribution (grey contours). Panels **(b)-(c)** show the east and north displacements as a function of time for the data and predictions.

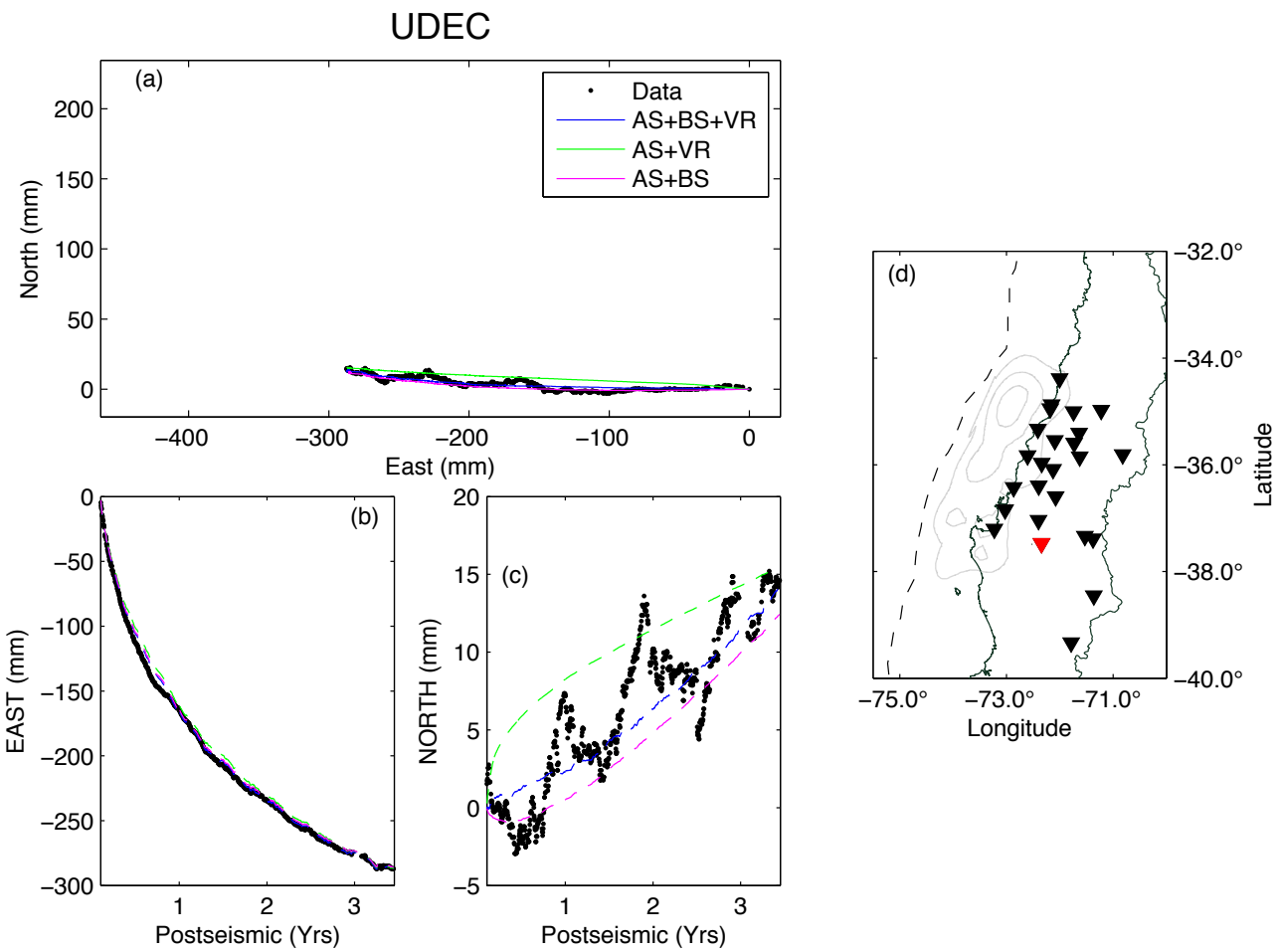

Figure B.23: Panel **(a)** shows the horizontal displacement pathway of the data and the predictions from the model ensembles (colours denoted in the legend). The aspect East and North scale are the same (equal aspect ratio). Panel **(d)** shows the location of the station (red triangle) in the cGPS network (black triangles) and with respect to the coseismic slip distribution (grey contours). Panels **(b)-(c)** show the east and north displacements as a function of time for the data and predictions.

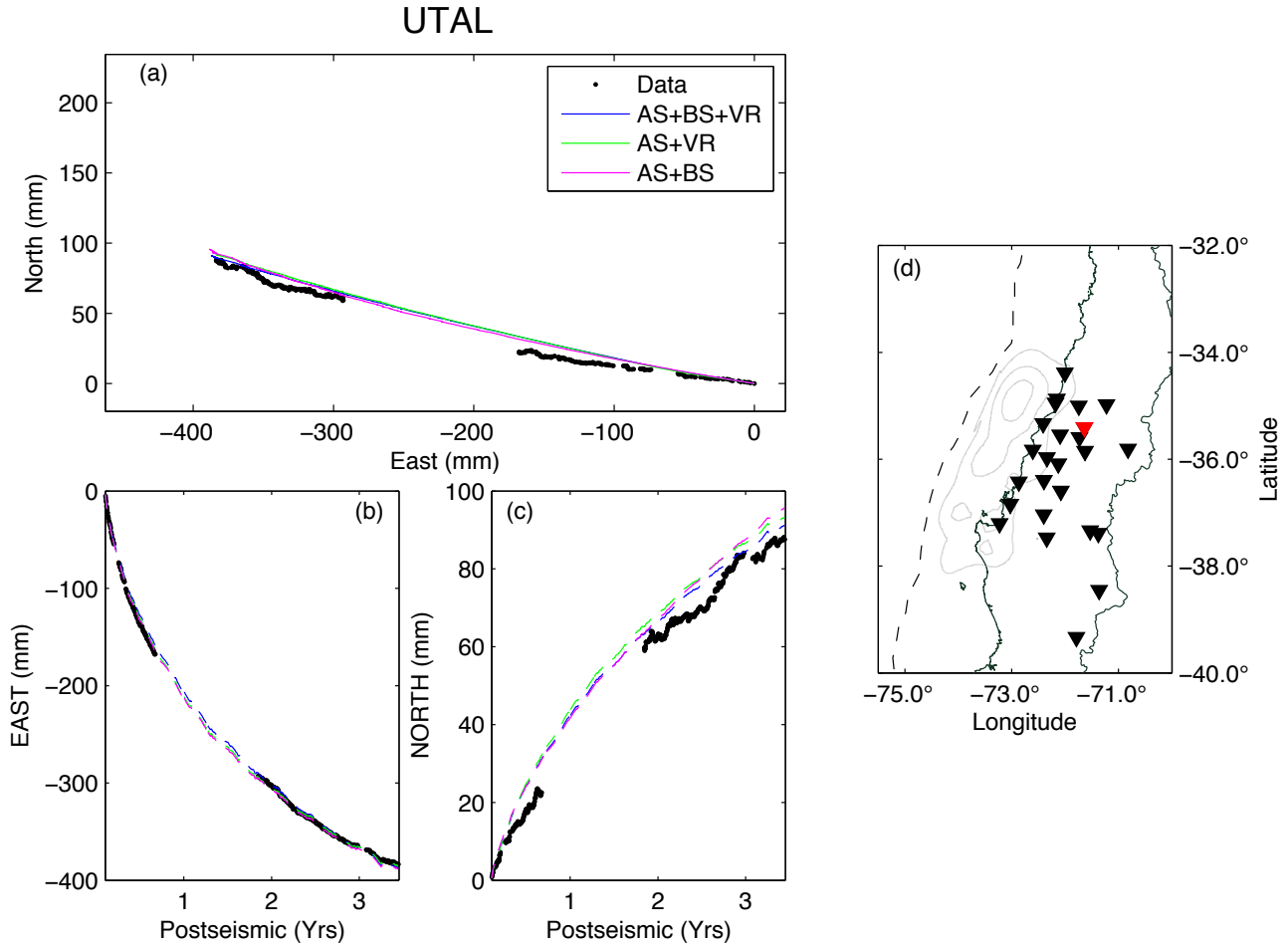

Figure B.24: Panel **(a)** shows the horizontal displacement pathway of the data and the predictions from the model ensembles (colours denoted in the legend). The aspect East and North scale are the same (equal aspect ratio). Panel **(d)** shows the location of the station (red triangle) in the cGPS network (black triangles) and with respect to the coseismic slip distribution (grey contours). Panels **(b)-(c)** show the east and north displacements as a function of time for the data and predictions.

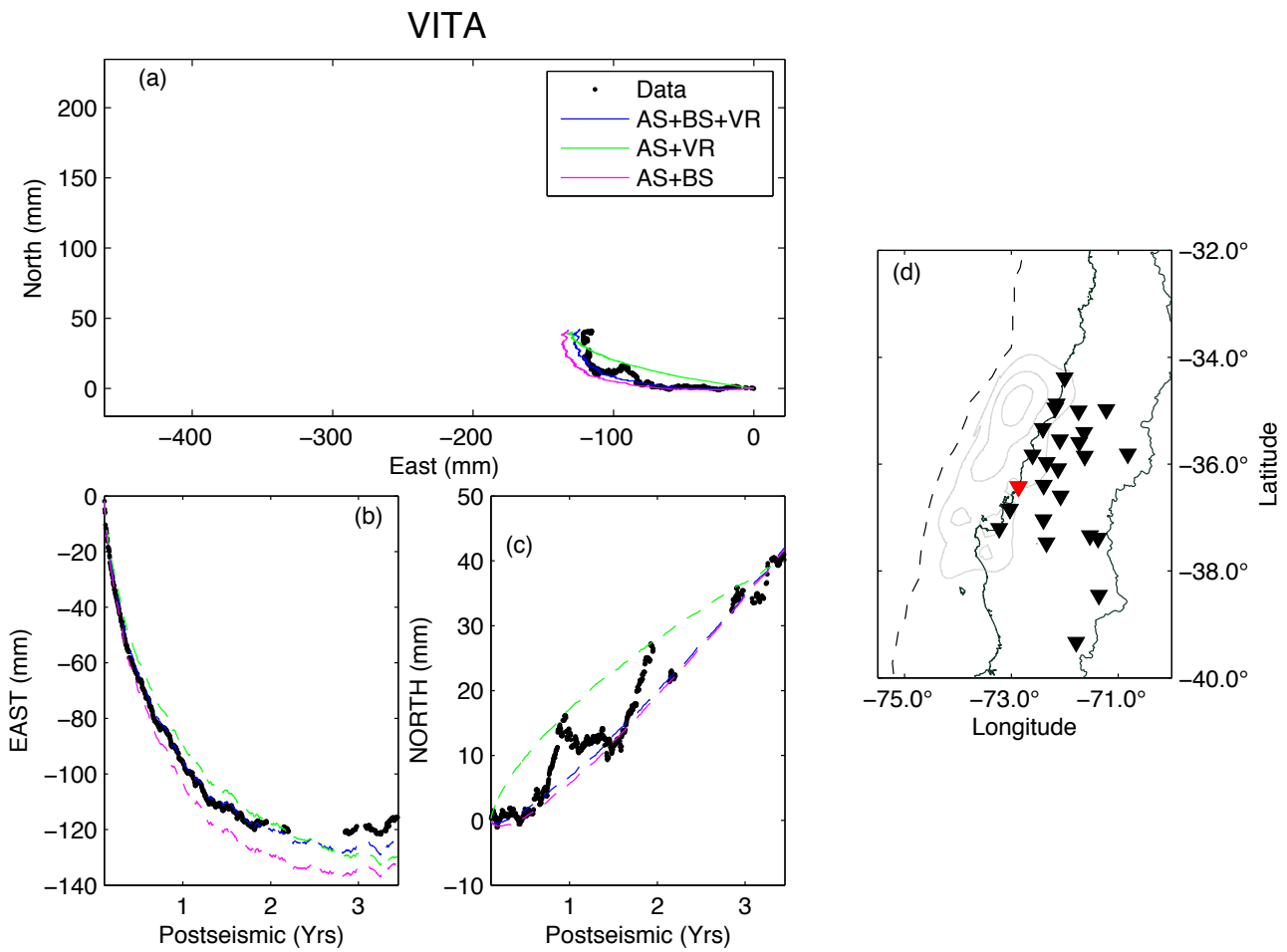

Figure B.25: Panel **(a)** shows the horizontal displacement pathway of the data and the predictions from the model ensembles (colours denoted in the legend). The aspect East and North scale are the same (equal aspect ratio). Panel **(d)** shows the location of the station (red triangle) in the cGPS network (black triangles) and with respect to the coseismic slip distribution (grey contours). Panels **(b)-(c)** show the east and north displacements as a function of time for the data and predictions.

Appendix C

Iquique study appendix

- Animated versions of figures 4.11-4.15 can be found on the CD provided or at the following link. The animation files for each station are named *"gps_seispreds_"* followed by the station name.
- A plan view animation of the GPS data and seismic predictions with the filename *"gps_seispreds_planview.avi"* can be found on the CD or at the following link. The animation shows the cumulative displacement evolution for the mean cGPS data and prediction since March 15th (left hand side), and an estimation of the cumulative aseismic signal from subtraction of these means (right hand side). Error ellipses of the data show the 95% confidence interval, and the contours surrounding mean seismic predictions represent a region where the probability density function $P > 0.004$.

Appendix D

Abstrakt

Die Messung von Oberflächenverschiebungen, die mit Beginn der neuen Ära satellitengestützter Geodäsie verfügbar geworden sind, haben sich als wertvolles ergänzendes Instrument neben der seismischen Überwachung aktiver Subduktionzonen bewährt. Die Möglichkeit, die jeweiligen Plattenbewegungen mit hoher räumlicher und zeitlicher Auflösung genau zu bestimmen, hat viele Initiativen Modellierung untersuchen sowohl heterogene platten Schnittstelle Kinematik und Subduktionszone seismischen Zyklus Dynamik inspiriert. Die Isolierung von Platte Schnittstelle Kinematik von der Oberfläche Signal und dem robusten Modellierung der kinematischen Quelle bieten die Fallstudien, gegen die mechanischen Modelle von Erdbeben Wiederauftreten kann verglichen werden, und ist deshalb von größter Bedeutung für die langfristige Zwischengefährdungsbeurteilung eines Subduktion Marge.

In dieser Dissertation präsentiere ich die Untersuchungen der Subduktionszone seismischen Zyklus platten Schnittstelle Kinematik und Dynamik des viskoelastischen Subduktionszone in Reaktion auf die Überschiebung Erdbeben. Ich vergleiche kinematische Modelle zur Seismizität, um die Heterogenität in seismischen Wirkungsgrad über den Plattenschnittstelle sowohl in der interseismischen und postseismischen Phasen des Erdbebenzyklus zu messen. Ich versuche, die verschiedenen Signale, die von gleichzeitigen postseismischen Prozessen kommen zu trennen und eine Diskussion der Uneindeutigkeit des Parameters Lösungsraum für die getrennten Signale zu erforschen und zu präsentieren.

Für diese Untersuchungen verwende ich die GPS-Daten und veröffentlichte Erdbebenkataloge des Chile Maule 2010 Mw 8,8 und Pisagua-Iquique 2014 Mw 8.1 Ereignisses.

Aus den Maule Untersuchungen, ist erkennbar, dass afterslip ist ein dominanter früh postseismischer Prozess ist (verfallend über 3-4 Jahre), welcher sehr gut durch die hervorragende Berichterstattung über Nahfeld-kontinuierliche GPS (cGPS) erfasst wird. Afterslip räumlich-zeitliche Merkmale sind in bestimmten Regionen gelöst und der Vergleich der afterslip zu koseismische Schlupf Bereiche der Platte-Schnittstelle, die eher mit großen Größenordnung Nachbeben scheitern zu offenbaren. Postseismische Prozesse können getrennt werden, wenn wir einige Annahmen über afterslip Verhalten anstellen: Um das simultane postseismische Signal zu separieren, habe ich das postseismische Richtverfahren entwickelt. Die Trennung berücksichtigt drei postseismische Prozesse: Platte Schnittstelle Wiederverriegelung, afterslip und viskoelastische Entspannung. Plattenwiederverriegelung ist ein traditionell vernachlässigter postseismischer Prozess, wenn es in Kombination

mit viskoelastischem Entspannung modelliert und afterslip verbessert der Modellvorhersage passt in den Zeitreihen deutlich. Der Effekt der Wiederverriegelung, wenn hinzugefügt, um afterslip und viskoelastische Entspannung, ist, damit die horizontalen Verschiebungen mit der Zeit veer. Die afterslip mit der Postseismic Richtverfahren getrennt eine normierte Abklingzeit Funktion, die in guter Übereinstimmung mit der normierten Abfallzeit in Abhängigkeit von den Nachbeben in den ersten 3-4 Jahren ist, was darauf hindeutet, dass die Raumzeit-Beziehung zwischen afterslip und Nachbeben weiterhin besteht lange in der postseismischen Zeitperiode. Die afterslip ist jedoch überwiegend aseismic und pulsierenden in der Natur; die zur Interpretation der afterslip Impulse auf einer postseismisch geschwächtrn Plattenschnittstelle, die von den größeren Größenordnung Nachbeben ausgelöst und mit der Veröffentlichung von Stress afterslip Zuführung wieder in die Scherspannung zwingt der Nachbeben Folge.

Für die Pisagua-Iquique Erdbeben, untersuche ich die seismische Effizienz des vorhergehenden foreshock Schwarm und die Quellparameter der größte foreshock das diesen Schwarm eingeleitet. Die cGPS Bewegungen im Vorfeld der Mw 8.1 mainshock werden hauptsächlich durch seismische Schlupf erklärt, obwohl signifikante aseismic postseismic Antworten können für die größeren Erdbeben im Schwarm gelöst werden. Ähnlich wie bei der Interpretation der Maule afterslip und Nachbeben, interpretiere ich die vorübergehende aseismic Signale als afterslip der Vorbeben.

Während viel versprechende räumlichen Beziehungen zwischen internationalen, Co- und postseismic elastische Versetzungs Kinematik gibt, die Freiheitsgrade für die Schlupf Azimut (rake) müssen weiter untersucht werden, insbesondere für die interseismic Sperr Modelle, die sehr empfindlich auf eine eingeschränkte backslip sein Azimut.

Appendix E

Curriculum Vitae

For reasons of data protection, the Curriculum Vitae is not published in the electronic version.

For reasons of data protection, the Curriculum Vitae is not published in the electronic version.

For reasons of data protection, the Curriculum Vitae is not published in the electronic version.